UNIONE EUROPEA
Fondo Sociale Europeo

Ministero dell'Università e della Ricerca

PON RICERCA E INNOVAZIONE 2014 - 2020

REACT EU

UNIVERSITÀ DEGLI STUDI DI BRESCIA

UNIVERSITÀ
DEGLI STUDI
DI BRESCIA

DOTTORATO DI RICERCA IN INGEGNERIA CIVILE, AMBIENTALE, DELLA COOPERAZIONE INTERNAZIONALE E DI MATEMATICA

Curriculum: Analisi e gestione dei rischi naturali

Settore Scientifico Disciplinare: ICAR/01 Idraulica

CICLO
XXXVII

IMPLEMENTATION OF A MATHEMATICAL MODEL FOR UNSTEADY FLOW IN IRRIGATION CHANNEL NETWORKS WITH APPLICATION TO THE CASE OF MANAGEMENT OF CANALE VACCHELLI, CONSORZIO IRRIGAZIONI CREMONESI

Tesi di dottorato di:

GABRIELE FARINA

Relatore:

Prof. MARCO PILOTTI

Correlatore:

Prof.ssa GIULIA VALERIO

Progetto di ricerca co-finanziato finanziato dall'Unione europea nel quadro del Programma PON R&I 2014-2020 risorse FSE REACT-EU Azione IV.5 "Dottorati su tematiche Green".

Sommario

A scala globale, il 70% dei prelievi di acqua è utilizzato in agricoltura; inoltre, la popolazione che basa il proprio sostentamento sui prodotti dell'agricoltura è in aumento. Tutto ciò in un contesto di conclamato cambiamento climatico. Da queste semplici considerazioni appare evidente come la gestione, il controllo e l'ottimizzazione della distribuzione dei volumi idrici in agricoltura abbia un'importanza fondamentale. In particolare, tale considerazione è rafforzata dal fatto che generalmente i Consorzi Irrigui sono istituzioni antiche che gestiscono la distribuzione delle risorse irrigue attuando soluzioni di "equilibrio" frutto dell'esperienza maturata negli anni, esperienza che potrebbe tuttavia rivelarsi non adatta alle condizioni future imposte dal cambiamento climatico. Uno strumento razionale e fisicamente basato che può essere d'aiuto nell'ottimizzazione del processo di distribuzione è fornito dalle equazioni di Saint-Venant che, affiancato al ruolo del personale esperto, può rendere la gestione delle reti irrigue più efficiente. Il presente studio tratta dell'implementazione di un modello numerico che permetta di risolvere le equazioni di Saint-Venant nella formulazione monodimensionale per una rete di canali a pelo libero interconnessi tra loro secondo una topologia sufficientemente generale. Poiché un modello che abbia come obiettivo la modellazione di una rete irrigua deve integrare mediante opportune condizioni al contorno interne alcuni manufatti idraulici fondamentali, con i quali viene attuata la regolazione delle portate in ingresso alla rete irrigua e delle portate erogate ai canali secondari, tale componente costituisce un aspetto presente nel modello implementato. Particolare attenzione è stata posta nella modellazione dei ponti, infatti, sebbene gli schemi numerici per la modellazione di soglie e paratoie sono relativamente ben definiti la modellazione dei ponti è affrontata in letteratura per mezzo di schemi numerici differernti. Per tale ragione al Capitolo 2 è presentato un approfondimento sugli schemi numerici per la trattazione dei ponti implementati nel codice di calcolo HEC-RAS 2D che è ampiamente utilizzato per la modellazione dei ponti. La definizione della geometria delle sezioni trasversali è un aspetto fondamentale per la realizzazione di qualunque modello idraulico e l'approcio più affidabile per la definizione delle sezioni trasversali è certamente basato su un rilievo topografico diretto. Tuttavia, le sezioni trasversali per un corso d'acqua sono spesso disponibili solo parzialmente. Considerando la crescente disponibilità di rilievi LiDAR con risoluzione e accuratezza sempre maggiori nel Capitolo 4, è stata esplorata una metodologia per la correzione di tali rilievi, che solitamente presentano incongruenze altimetriche nella batimetria del canale sommersa al momento del rilievo. Inoltre, l'attività sperimentale svolta nell'ambito di questa Tesi ha consentito di constatare l'effetto del processo di crescita delle macrofite sulla scabrezza idraulica dei canali nel corso della stagione irrigua. La crescita e sviluppo della vegetazione è governata principalmente dalla radiazione solare, dalla presenza di nutrienti e dalla temperatura dell'acqua. Per tale ragione si è deciso di accoppiare al modello idraulico implementato un modello termico che permetta di modellare la temperatura del corso d'acqua in tutto il dominio considerato e per l'intera stagione irrigua. Nella Tesi sono mostrati i passi percorsi per l'implementazione e validazione delle varie componenti descritte e l'applicazione delle stesse al Canale Vacchelli, il più importante canale gestito dal Consorzio Irrigazioni Cremonesi e uno dei più importanti in nord Italia. Il modello idraulico implementato è stato applicato alle stagioni irrigue del 2022, 2023 e 2024 per il Canale Vacchelli ottenendo dei risultati in linea con le osservazioni e laddove siano presenti delle discordanze rilevanti (e.g. durante la fase iniziale della stagione irrigua) sono stati analizzati i fattori che potrebbero essere responsabili di tale scostamento.

Abstract

On a global scale, 70% of water withdrawals are used in agriculture; furthermore, the population that bases its livelihood on agricultural products is increasing. All this in a context of clear climate change. From these simple considerations it is clear that the management, control and optimization of the distribution of water volumes in agriculture has a fundamental importance. In particular, this consideration is strengthened by the fact that generally the Irrigation Consortia are ancient institutions that manage the distribution of irrigation resources by implementing "equilibrium" solutions resulting from the experience gained over the years, experience that could however prove not suitable for the future conditions imposed by climate change. A rational and physically based tool that can be of help in optimizing the distribution process is provided by the Saint-Venant equations which, combined with the role of expert personnel, can make the management of irrigation networks more efficient. This study deals with the implementation of a numerical model that allows to solve the Saint-Venant equations in the one-dimensional formulation for a network of free-surface channels interconnected according to a sufficiently general topology. Since a model that has as its objective the modeling of an irrigation network must integrate, through appropriate internal boundary conditions, some fundamental hydraulic works, with which the regulation of the incoming flows to the irrigation network and of the flows delivered to the secondary channels is implemented, this component is present in the implemented model. Particular attention has been paid to the modeling of bridges, indeed, although the numerical schemes developed for weirs and gates are relatively well defined, the modeling of bridges is addressed in the literature by means of different numerical schemes. For this reason, in Chapter 2 a detailed study of the numerical schemes for the treatment of bridges implemented in the HEC-RAS 2D is presented, which is widely used for the modeling of bridges. The cross section geometry is a fundamental aspect for the realization of any 1D hydraulic model, the most reliable approach for the definition of the cross sections is certainly based on a direct topographic survey. Sometimes, the cross sections for a watercourse are only partially available. Considering the growing availability of LiDAR surveys with ever-increasing resolution and accuracy, in Chapter 4 a methodology for the correction of LiDAR surveys has been explored, which usually presented inconsistencies in the bathymetry of the channel submerged at the time of the survey. Furthermore, the experimental activity carried out in the context of this Thesis has allowed to observe the effect of the growth of macrophytes on the hydraulic roughness of the channels during the irrigation season. The growth and development of vegetation is mainly governed by solar radiation, the presence of nutrients and the temperature of the water. For this reason, it was decided to couple the implemented hydraulic model with a thermal model that allows modeling the temperature of the canal network for the entire irrigation season. This Thesis shows the steps taken for the implementation and validation of the various components described and their application to the Canale Vacchelli, the most important canal managed by the Consorzio Irrigazioni Cremonesi and one of the most important in northern Italy. The implemented hydraulic model was applied to the irrigation seasons of 2022, 2023 and 2024 for the Canale Vacchelli obtaining results in line with the observations and where there are significant discrepancies between observation and results (e.g. during the initial phase of the irrigation season) the factors influencing the process were analyzed.

Ringraziamenti

Al termine di questo percoso vorrei rigraziare il gruppo di Idraulica dell' Università di Brescia. In particolar modo il mio supervisore, il Professore Marco Pilotti per il costante sostegno, la disponibilità e per la passione che ha saputo trasmettermi durante questi anni. Un sentito grazie alla Prof.ssa Giulia Valerio per la sua disponibilità, a Riccardo, Stella, Payam e Matteo per le esperienze condivise.
Questa ricerca non sarebbe stata possibile senza la collaborazione del Consorzio Irrigazioni Cremonesi e del suo Direttore l' Ing. Luca Milanesi che ringrazio per avermi accolto e per aver condiviso le conoscenze di chi il Consorzio lo gestisce. Un particolare ringraziamento a Gian Franco Manfredini e Alessandro Rigotti per avermi coinvolto nelle attività del Consorzio.
Un sentito ringraziamento a Vito Bacchi per avermi accolto a Chatou al Laboratorio di Ricerca Sviluppo di EDF per i tre mesi di ricerca all' estero durante il percorso di Dottorato.
Ringrazio tutti colleghi che ho conosciuto all' interno dell' Università Paolo, Arianna, Tewelde, Yen e Marco.
Infine, ringrazio la mia famiglia, Tiziana, Giandomenico e Giacomo per il supporto e Giovanni per il supporto da un po' più lontano.

Contents

Introduction **1**

1 A mathematical model for unsteady flow in regulated irrigation channel networks **5**
1.1 Introduction . . . 5
1.2 Governing Equations . . . 5
1.3 A non-linear finite volume model . . . 7
1.3.1 Numerical discretization . . . 7
1.3.2 Boundary Conditions . . . 10
1.3.3 Internal Boundary Conditions . . . 13
1.4 Validation . . . 14
1.4.1 Pre-processing Validation . . . 14
1.4.2 MacDonald's Test Cases . . . 17
1.4.3 Flow over a Bump . . . 29
1.4.4 Sen and Garg (2002) test case . . . 31
1.4.5 Islam et al. (2005) test case . . . 34
1.5 Conclusions . . . 36

2 Numerical tests on the conceptual schemes adopted in the code for bridge modeling **37**
2.1 Introduction . . . 37
2.2 Experimental test and physical model upscaling according to Froude similarity . . . 38
2.3 The Numerical Model: HEC-RAS 2D . . . 41
2.4 Numerical test: Steady state tests . . . 42
2.5 Numerical test: Dam Break tests . . . 45
2.6 Discussion and Conclusions . . . 47

3 Validation of internal boundary conditions **51**
3.1 Introduction . . . 51
3.2 Bridges, Weirs and Gates validation . . . 53
3.3 Conclusions . . . 58

4 Terrain modification to DEM derived from LiDAR surveys **60**
4.1 Introduction . . . 60
4.2 The algorithm . . . 62
4.3 Application to the Mella river . . . 63
4.4 Discussion and conclusions . . . 66

5 Coupling water channel temperature and hydrodynamic: implementation and validation **74**
5.1 Introduction . . . 74
5.2 Heat exchanges at the air-water interface . . . 74
5.3 Numerical model . . . 76
5.4 Comparison with the water quality model implemented in HEC-RAS . . . 77
5.5 Modeling macrophyte biomass dynamics . . . 80
5.6 Conclusions . . . 82

6 Application to the Vacchelli Irrigation Canal **84**
6.1 Introduction 84
6.2 Consorzio Irrigazioni Cremonesi 84
6.3 Monitoring System and field activities accomplished in this study 96
6.4 Mass Balance for the Northern Canal Network of CIC 100
6.5 Application of the Numerical Model to the Vacchelli Canal 105
6.6 Adjustment of the model roughness on the basis of the coupled biomass, hydrodynamic and temperature models 116
6.7 Conclusions 118

Conclusions **120**

List of Research Outputs **123**

References **125**

Introduction

Agricultural water use accounts for the majority of global freshwater consumption, using about 70 percent of the world's available fresh water withdrawals (e.g., Connor, 2015; FAO, 2017), locally with peaks of up to 90 percent, and with negative environmental impacts, such as soil salinization, depletion of aquifers (e.g., Dalin et al., 2017; Döll et al., 2014) and water resources (e.g., Wada et al., 2011). At the same time, the world's growing population drives an inevitable increase in irrigation water consumption so that the demand for irrigated food production is expected to increase by more than 50 percent by 2050 (FAO, 2017). This will happen in the context of climate change, which will change the space-time distribution of rainfall and will increase global levels of evapotranspiration and the frequency of water stress situations (Dai, 2013), that will be no longer confined to arid and semi-arid regions. Regardless of genetic improvements in crop species (e.g., Richards et al., 2002), evidently this situation can only be countered by optimizing current practices (e.g., Levidow et al., 2014), resorting, for example, to the increasing use of precision irrigation, with the use of sensors to determine precisely how much, where and when to irrigate. These measurements, when integrated within a physically-based and space distributed approach to the water balance, will be very important to tune the actual local water requirement. Potentially, the greatest benefit from these techniques will occur where surface irrigation, the practice according to which water is distributed over the field by overland flow, is extensively applied. Actually, the relevance of surface irrigation is considerable: it is thousands of years old, uses energy provided from gravity and represents perhaps as much as 90 percent of common irrigation activities (e.g., Walker, 1989). The broadest field of application of surface irrigation is in situations where water is supplied from water courses onto the adjacent flood plain through simple hydraulic works. Finally, the typical water supply for surface irrigation is provided by a canal distribution network that accordingly plays a crucial role in improving the efficiency of water use in agriculture, by ensuring the optimal distribution and management of water resources.

Although many details can lead to important improvements of the efficiency of surface irrigation, its fundamental disadvantage is that the high temporal and spatial variability of soil properties lead, within an optimized framework, to an engineering and management problem in which at least two of the primary design variables, discharge and time of application should be judged by the irrigator prior to the initiation of every surface irrigation event (Walker, 1989). However, this flexibility collides with the traditional rigidity of multi-users canal-operated water distribution: time-shifts and the allocation of water are generally dictated by customs and water rights that have become established on an empirical basis over time, often with a very limited understanding of the system's hydraulics (Afrasiabikia et al., 2017). Actually, irrigation consortia are often ancient institutions and achieving an equilibrium solution in water distribution by conflict-resolution is the goal of their action. Any change to this equilibrium is regarded with suspicion or even hostility because a fast, rational and shared way to compute new equilibria is usually not known. Accordingly, the empiricism underlying the distribution of water is unable to cope with the dynamism imposed by climate change.

To further emphasize the practical consequence of this gap between optimal management and the *business-as-usual* approach, it must also be said that within an agricultural water distribution and delivery network, operational losses are associated with the improper operation of water level regulation and off-take structures. These losses are related to the mismatch between resource availability and actual water demand. Often operational losses are larger than seepage

losses (e.g., Barkhordari & Hashemy Shahdany, 2022) and by far larger than evaporation driven losses in the network. Accordingly, any improvement of the performance of the distribution system must go through the improvement of the operation methods of dynamic water level regulation and off-take structures, integrating a demand-oriented approach on the on-farm scale and coupling a mathematical model of the network with remote measurements and automation.

The mathematical model that provides the rational and quantitative alternative to manage real-time water distribution is provided by the physically based Saint-Venant equations (Chaudhry, 2008), that, coupled with internal and external boundary conditions, provide an excellent model of the hydraulics of the channel network. Several models are available for this task. In 1993 the ASCE Task Committee on Irrigation Canal System Hydraulic Modeling (see, Clemmens, 1993) provided a wide review of models available at that time for the unsteady flow modeling of irrigation canals, also guiding their improvement.
The optimization of irrigation water resources can be pursued through various methodologies. For example, the management of the irrigation channel network could be based on the manual operation of the sluice gates at the withdrawal points. Consortium operators frequently adjust the gate openings based on the contemporary upstream and downstream water levels in order to ensure the correct delivery of flow into secondary channel, as established by the timetable of the irrigation water shift. Although the offtacking structures are regularly monitored and adjusted by the operators, the ability to adapt dynamically to the variable water level conditions in the main canal is not feasible unless an automatic gate control system is implemented.
Various solutions are available for automating gate movement (e.g., Conde et al., 2021; Wahlin & Zimbelman, 2014), and their effectiveness can be evaluated. In this regard, the optimal choice of automation algorithm can be tested by applying it to a properly calibrated hydraulic model of the network (Wahlin & Zimbelman, 2014).
On the other hand, hydraulic modeling of the irrigation network can provide an overall view of its state and allows to test different irrigation resource distribution scenarios. In this direction, the model can help identify the optimal scheduling of water withdrawals to minimize periods of network stress or to reduce water losses due to infiltration.
In the following years, several algorithms have been proposed (Islam et al., 2008; Islam et al., 2005; Jamal & Bhallamudi, 2020; Sen & Garg, 2002; Zhu et al., 2011). Over the past two decades, a set of commercial models have also been developed that can be effectively used for hydraulic modeling of irrigation channels, for instance:

- HEC-RAS, is primarily used for river hydraulics modeling, but it can also be applied to irrigation channel networks (e.g., Barkhordari & Hashemy Shahdany, 2022; Wanyama & Bwambale, 2024).
- ICSS hydrodynamic model, that was developed to solve both steady and unsteady condition (Karimi Avargani et al., 2023).
- Simulation Irrigation Canals SIC2, where the Saint-Venant Equations are discretized using the Preismann scheme (SIC2 Website). The model has been successfully applied to the Canale Emiliano Romagnolo (CER) in Italy (Luppi et al., 2018) to compute the discharge in ungauged sections of the irrigation channel network.
- SOBEK successfully applied to model the Doroodzan irrigation channels network in Iran (Afrasiabikia et al., 2017).

Although there are many solutions in the literature to model irrigation channel networks and also commercial software, we believe that it is still worthwhile to implement a custom numerical

model. First of all, it is a fundamental and complex exercise of implementation of the Saint-Venant Equations, at the very core of environmental hydraulics. Accordingly, this task responds to an essential task of a University system devoted to research, namely the implementation of autonomous calculation tools and not only the use of commercial software. Regardless of this fundamental aspect, which, however, should never be forgotten, the development of proprietary codes could provide greater flexibility in different aspects. For instance, a non-comprehensive list could include the following considerations: (1) usually irrigation channel networks are ancient, not standardized and characterized by complex structures. Only a custom mathematical model could be adjusted to describe the hydraulics of these structures. (2) A custom mathematical model could be more easily coupled with a customized monitoring system of the irrigated area. (3) A custom mathematical model can easily include specific features of each irrigation district, such as the seasonal variability of roughness that can be customized if the code is open. (4) Similarly, different water stress indexes computed from satellite measurements can be easily coupled with the mathematical model to build an on-demand system. (5) It could be modified to create a digital twin to be used in the training of field operators.
These were some of the reasons that motivated this Thesis, whose original objective was to develop a mathematical model that solve the 1D formulation of the Saint-Venant Equations for a general irrigation channel network. This task is the subject of the Chapter 1 of the Thesis. The main characteristic that should be addressed by the numerical model are: (1) the possibility to deal with compact irregular cross section; (2) the possibility to solve the unsteady 1D Saint-Venant Equations for a general topology of a channel network (both dendritic or looped network); (3) the possibility to introduce internal boundary conditions to model the structures which typical characterizes irrigation channel networks.

Along the way of implementing these goals, several new problems arose, not evident at the beginning, that required important insights. First of all, the implementation of internal boundary conditions required to select the appropriate hydraulic schematization for each structure. Considering that, due to the complexity of bridge modeling, different approaches have been proposed, we eventually decided to test the methodology recently implemented in HEC-RAD 2D to model bridges. This led to the subject of the Chapter 2 of the Thesis, where HEC-RAS 2D has been carefully tested considering the experimental test cases for steady and unsteady presented in the paper of Ratia et al. (2014). Eventually, having concluded positively about the capability of the approach implemented within HEC-RAS 2D to deal with bridges in different flow regimes, we implemented the methodology within the solver but this required exploring the wider field of the implementation of internal boundary conditions at hydraulic works that can be present within an irrigation network: this topic is the subject of the Chapter 3 of the Thesis.

An important stumbling block that arises in the use of a solver for Saint-Venant Equations is related to the description of the topology and geometry of the network. Only in some fortunate cases the different branches that make up the network have been surveyed and cross sections are rarely available. Having encountered this problem also when dealing with the solution of 2D Shallow Water Equations for flooding problems, we considered the possibility of surveying the layout of the network through a LiDAR of the irrigated area. In such a case, a major problem is that of obtaining the actual bathymetry of the channel bed, which is covered and hidden by the water surface. In this direction, we devised an original methodology to accomplish this task: this topic is the subject of the Chapter 4.

The implemented model required a real test case for verification and for knowing and un-

derstanding the relevant features of a complex irrigation system. This was provided by the Consorzio di Irrigazioni Cremonesi. Studying the case of Canale Vacchelli we soon encroached on the problem of the seasonal aquatic weed growth, which made it impossible to model the hydraulics of the irrigation system considering a constant roughness coefficient. In turn, dealing with this problem required modeling the temperature variation within the channel. Having deployed two thermistors 30 kms apart within the Vacchelli channel, we observed the peculiarities of the temperature variation during the transfer from the channel inlet to Tombe Morte station. This led to the conclusion that it was necessary to include a thermal model within the solver that, in turn, could provide a fundamental ingredient to the aquatic weed growth model. This topic was the subject of the Chapter 5.

Here, however, a caveat must be done: the topic of aquatic weed growth proved very complex, requiring a botanic competence beyond the scope of my background and an extensive experimental activity for its calibration: in other words, it could be the subject of another specific research. Here we selected a method that is implemented within a standard problem for water quality modeling (Berger & Wells, 2008) and we used it within a simple conceptual model for the Manning's roughness coefficient variation, after a limited calibration. The model proved very effective but would certainly benefit from further study.

Finally, in the Chapter 6 most of the developed algorithms have been applied to the Vacchelli test case. Beyond exploring the capability of the model to reproduce the space-time variation of water elevation and discharge along the channel, the simulations explored a set of phenomena that can be of practical and theoretical interest in the management of a drainage network: for instance, the possibility of using a simple mass balance in place of the full set of Saint-Venant Equations to have the discharge at a given point in space and time along the network. The comparison with the numerical solution shows pros and cons of this approach. Another fundamental point regards the measurement of the time variation of the stage-discharge curve over the irrigation season and the possibility to model it with the proposed approach. Although affect by uncertainties (e.g. the application of the reduction, the effects of infiltration), the simulations performed for the irrigation season of 2022, 2023 and 2024 show the capabilities of the implemented model to reproduce the discharge at end of the Vacchelli canal.

1 A mathematical model for unsteady flow in regulated irrigation channel networks

1.1 Introduction

In the following sections, the 1D Saint-Venant Equations are presented along with the characteristic analysis which provides the basis for implementing a 1D semi-implicit numerical method to solve the Saint-Venant Equations in their one dimensional formulation. The numerical model was implemented in MATLAB. Moreover, in the numerical model, internal boundary conditions have been implemented to solve the different hydraulic controlling structures that are usually present along an irrigation channel network (e.g. weirs and gates), as well as to take into account the possible presence of bridges. The numerical model has been validated for a set of test cases and compared with the corresponding analytical or numerical solution.

1.2 Governing Equations

The 1D Saint-Venant Equations governing the unsteady flow in an open channel network are based on the conservation of mass and momentum. These equations can be expressed as follows (Casulli, 2023):

$$\begin{aligned} \frac{\partial A}{\partial t} + \frac{\partial (Au)}{\partial x} &= 0 \\ \frac{\partial (Au)}{\partial t} + \frac{\partial (Auu)}{\partial x} &= -gA\frac{\partial \eta}{\partial x} - \gamma u \end{aligned} \tag{1.1}$$

where, t is the time, x is the spatial position along the river path, u and η are the unknown cross-section averaged velocity and water surface elevation, A is the area of the cross-section, γ is the friction term and g is the acceleration of gravity. As well known, there are different possibilities to solve the system of equations (1.1) spacing between implicit and explicit methods, using finite difference, finite volume, and finite element method (Casulli, 2023; Casulli & Zanolli, 2022). Despite the explicit methods are extensively used to solve Shallow Water Equations (SWE in the following), (Bonomelli et al., 2023; Pilotti et al., 2011) they are characterized by the stability restriction imposed by the Courant-Friedrichs-Lewy condition (CFL) requiring a small time step. On the other hand, a complete implicit scheme may be unconditionally stable but requires complex algorithms to solve the whole system of equations (Casulli, 1990). Semi-implicit numerical methods provide a compromise between explicit and implicit methods. To clarify the numerical discretization of the terms of the system of equation (1.1) provided in the following section, the characteristic analysis discussed in (Casulli, 2023) is reported, that was used to identify which terms should be implicitly discretized to relax the CFL condition. Considering a rectangular channel with a unitary width, $z = -h_b(x)$ the function which describes the bottom profile , the total hydraulic depth is expressed as $H(x,\eta) = h_b(x) + \eta(x,t)$ (see Figure 1.1).

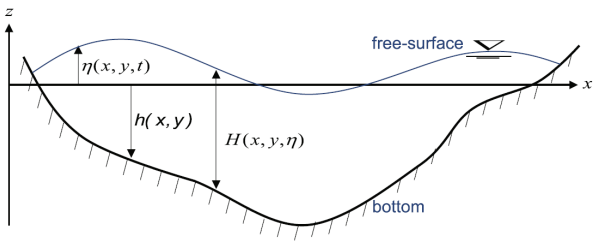

Figure 1.1: x-z section of the flow domain (from Casulli and Zanolli, (2022))

Accordingly, the system of Equations (1.1) can be written in its non-conservative form as follows:

$$\begin{cases} \frac{\partial u}{\partial t} + u\frac{\partial u}{\partial x} + g\frac{\partial \eta}{\partial x} = -\frac{\gamma u}{H} \\ \frac{\partial \eta}{\partial t} + u\frac{\partial \eta}{\partial x} + H\frac{\partial u}{\partial x} = -u\frac{\partial h_b}{\partial x} \end{cases} \tag{1.2}$$

The system of equations (1.2) can be written in matrix notation as follows:

$$\boldsymbol{W}_t + \boldsymbol{A}\boldsymbol{W}_x = \boldsymbol{b} \tag{1.3}$$

Where, $\boldsymbol{W}$ is the vector of two components which are the unknowns, $\boldsymbol{A}$ is a 2x2 matrix composed by the coefficients of the left side spatial derivatives of the system of Equations (1.2) and $\boldsymbol{b}$ is the right-hand side of the system of Equations (1.2):

$$\boldsymbol{W} = \begin{pmatrix} u \\ \eta \end{pmatrix} \quad \boldsymbol{A} = \begin{pmatrix} u & g \\ H & u \end{pmatrix} \quad \boldsymbol{b} = \begin{pmatrix} -\frac{\gamma u}{H} \\ -u h_{b_x} \end{pmatrix} \tag{1.4}$$

since the eigenvalues are real the system of Equations (1.2) it is strictly hyperbolic for a wet bed, and the corresponding characteristic equation is given by:

$$det(\boldsymbol{A} - \lambda \boldsymbol{I}) = 0 \tag{1.5}$$

The solution of Equation (1.5) is given by the eigenvalues of the matrix $\boldsymbol{A}$ $\lambda_{1,2} = u \pm \sqrt{gH}$. These quantities represent the wave celerity and, for instance, under the assumption of subcritical flow $|u| < \sqrt{gH}$ any signal in water can travel in two directions: the positive x-direction and the negative x-direction (Figure 1.2).

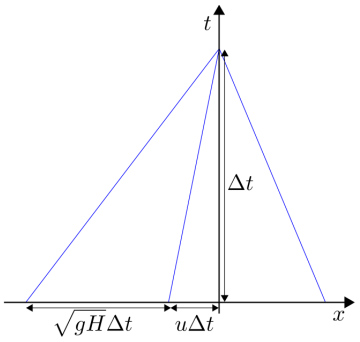

Figure 1.2: Characteristic lines and CFL limitation.

For hyperbolic systems there is a well known stability restriction for any explicit numerical methods (CFL) that requires:

$$\Delta t \leq \frac{\Delta x}{|u| + \sqrt{gH}} \tag{1.6}$$

The CFL represents the necessary condition for any explicit method applied to the system of equations (1.2) to remain stable. This condition is translated into a time step limitation once the spatial discretization is fixed. A way to relax the time restriction provided in Equation (1.6) is to use a method that is not fully explicit and not fully implicit either but a semi-implicit method which requires to discretize implicitly some terms. The terms from which the stability restriction related to $\sqrt{gH}$ arise from matrix $\boldsymbol{A}$ are: the coefficient of $\frac{\partial u}{\partial x}$ in the continuity equation and $\frac{\partial \eta}{\partial x}$ in the momentum equation, meaning that the two partial derivatives should be taken implicitly. Moving to a complete stability analysis the time step limitation is affected by friction:

$$\Delta t \leq \frac{1}{\frac{|u|+\sqrt{gH}}{\Delta x} + \frac{\gamma}{H}} \tag{1.7}$$

For shallow water problems, friction becomes dominant in the stability condition and consequently means that u on the right-hand side should be taken implicitly so that the stability inequality (1.7) can be relaxed. The last term that leads to an unconditionally stable method is the advection: in this case if an Eulerian-Lagrangian discretization is taken for advection the CFL is completely relaxed.

1.3 A non-linear finite volume model

The unsteady flow in an open channel network is based on the conservation of mass and the momentum equation that may be expressed in non-conservative form (e.g., Casulli & Stelling, 2013) as follows:

$$\begin{aligned} \frac{\partial A}{\partial t} + \frac{\partial Au}{\partial x} &= q \\ \frac{\partial u}{\partial t} + u\frac{\partial u}{\partial x} &= -g\frac{\partial \eta}{\partial x} - \Upsilon u \end{aligned} \tag{1.8}$$

Where q represents the source/sink terms, Υ is the friction term and, in this case, is defined as $\Upsilon = \frac{gn^2|u|}{R_h^{4/3}}$.

1.3.1 Numerical discretization

The implemented numerical model is based on the numerical method proposed by Casulli and Stelling (2013) that couples a finite volume, semi-implicit discretization for the equation of the conservation of mass and a finite difference scheme for the momentum equation. The computational domain is discretized using a staggered grid, the velocity and the cross sectional area are defined at the cross section interfaces $j = 1, 2, ..., N_s$, having a distance between two consecutive cell points Δx_j. The water surface elevation is defined at the mid-cell points $i = 1, 2, ..., N_p$ (Figure 1.3).

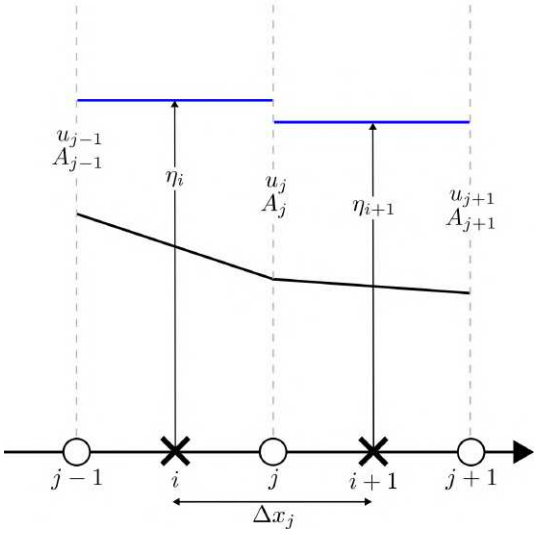

Figure 1.3: Staggered discretization, highlighting the location of the discretized variables A, u, η.

The left and right cell-points of the cross section interface j are defined respectively as $l(j)$ and $r(j)$. To complete the topology of the network, vector S_i contains all the cross sections that share the same point i (Figure 1.4).

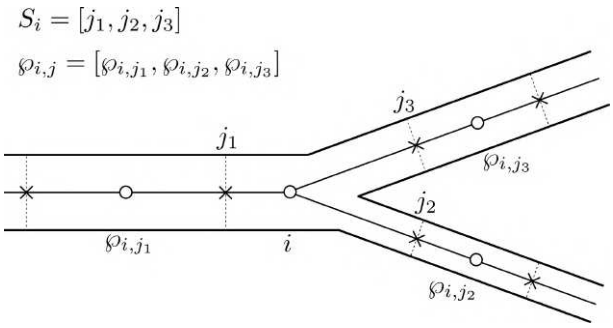

Figure 1.4: Topology of a junction.

Typically, the elements grouped in S_i are two except for junctions where the number of elements in S_i is equal to the branches that converge in the same junction. Additionally, $\wp_{i,j}$ represents the neighbor grid point of the considered grid point i which share the same cross section j (See Figure 1.4 for details).
In order to solve the momentum equation in the system of equations (1.8). The momentum equation is discretized following the finite difference discretization as follows:

$$\frac{u_j^{n+1} - Fu_j^n}{\Delta t} = -g\frac{\eta_{r(j)}^{n+\theta} - \eta_{\ell(j)}^{n+\theta}}{\Delta x_j} - \Upsilon_j^n u_j^{n+1} \quad j = 1, 2, \ldots, N_s \tag{1.9}$$

where Δt is the time step, Fu_j^n is computed according to the Eulerian-Lagrangian discretization, generally, F is a stable explicit finite difference operator, which accounts for the time derivative and for the advective term (Casulli, 1988), θ is the implicitness factor used for the theta method discretization of η: $\eta^{n+\theta} = \theta\eta^{n+1} + (1-\theta)\eta^n$, and of u: $u^{n+\theta} = \theta u^{n+1} + (1-\theta)u^n$. One advantage of this type of discretization is that u^{n+1} can be written explicitly in terms of the other variables. This will be used in the following solution procedure, to obtain a system of solving equations in terms of the water surface elevation η only. Introducing the definition of material derivative:

$$\frac{Du}{Dt} = \frac{\partial u}{\partial t} + u\frac{\partial u}{\partial x} \tag{1.10}$$

Equation (1.10) can be discretized as follows:

$$\frac{Du}{Dt} = \frac{u_j^{n+1} - u_*^n}{\Delta t} \tag{1.11}$$

Where u_*^n is the velocity interpolated at the foot of the Lagrangian trajectory. Its position x_{j*} is computed integrating the velocity backward in time from the node x_j at time t_{n+1} to its original location at time t_n and is defined as follows:

$$x_{j^*} = x_j - \int_0^{\Delta t} u\big(x(t)\big)dt \tag{1.12}$$

In literature, different methods have been proposed to compute the quantity of interest at the foot of the Lagrangian trajectory (Casulli, 1990; Rosatti et al., 2005, 2011). In the implemented numerical model the sub-stepping method proposed Casulli (1990) has been implemented, according to which at each time step a time substep is introduced $\Delta\tau = \frac{\Delta t}{N}$ where N is chosen sufficiently large to satisfy the following stability equation:

$$\Delta\tau \leqslant \min\left(\frac{\Delta s}{\max|u_j^n|}\right) \tag{1.13}$$

for all the j faces of the domain where u is discretized. Considering that the average velocity u is a variable to be computed through the solution process of SWE, the value of u^{n+1} is not known for the computation of the Lagrangian trajectory backward in time. To solve this issue Casulli (1990) proposed to assume that $u^{n+1} = u^n$ and to solve Equation (1.12) using an Euler method for each sub step. Thus, introducing the sub-step time $s^k = t^{n+1} - kd\tau$ for $k = 0, ..., N-1$ the location of Lagrangian trajectory is computed backward as:

$$x^{(k+1)} = x^{(k)} - \Delta\tau u(x^{(k)}) \tag{1.14}$$

Note that during the iterations, the coordinate $x^{(k+1)}$ doesn't match exactly the location of a cross-section; accordingly an interpolation of the velocity field is necessary. To this purpose, different interpolation methods are proposed in the literature (e.g. cubic interpolation Rosatti et al., 2011) in the implemented numerical model a linear interpolation has been chosen. The procedure to compute the Lagrangian trajectory is schematized in Figure 1.5.

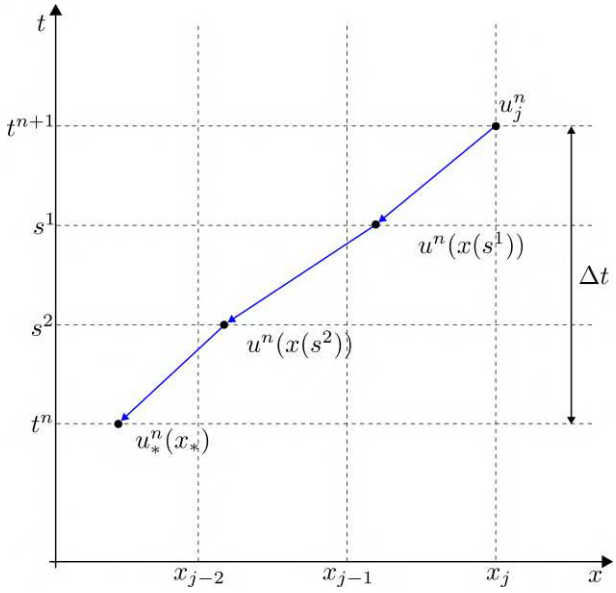

Figure 1.5: Computation of the velocity at the foot of the Lagrangian trajectory

The continuity equation in the system of equations (1.8) is integrated on the control volume of each grid point with a semi-implicit finite volume approximation as follows:

$$V_i\left(\eta_i^{n+1}\right) = V_i\left(\eta_i^n\right) - \Delta t \sum_{j \in S_i} \sigma_{i,j} A_j^n u_j^{n+\theta} + Q_{i,*}\Delta t, \quad i = 1, 2, \ldots, N_p \tag{1.15}$$

where: $u^{n+\theta} = (\theta u^{n+1} + (1-\theta)u^n)$, V_i is the water volume in the cell i, $Q_{i,*}$ is the inflowing/outflowing discharge in/from cell i, $\sigma_{i,j}$ in the flux term is a sign function associated with the orientation of the velocity defined as follows:

$$\sigma_{i,j} = \frac{r(j) - 2i + \ell(j)}{r(j) - \ell(j)} \tag{1.16}$$

The substitution of u_j^{n+1} from Equation (1.9) into Equation (1.15) provides a mildly nonlinear system of N_p equations for the surface elevation η_i^{n+1}:

$$V_i\left(\eta_i^{n+1}\right) - g\theta^2\Delta t^2 \sum_{j \in S_i} \frac{A_j^n}{\Delta x_j \left(1 + \Upsilon_j^n \Delta t\right)} \left[\eta_{\wp(i,j)}^{n+1} - \eta_i^{n+1}\right] = b_i, \quad i = 1, 2, \ldots, N_p \tag{1.17}$$

where:

$$b_i = V_i\left(\eta_i^n\right) - \Delta t \sum_{j \in S_i} \sigma_{i,j} A_j^n \left[\theta G_j^n + (1-\theta) u_j^n\right] + Q_{i,*}\Delta t \tag{1.18}$$

and:

$$G_j^n = \frac{F u_j^n - g(1-\theta)\Delta t \frac{\eta_{r(j)}^n - \eta_{\ell(j)}^n}{\Delta x_j}}{1 + \Upsilon_j^n \Delta t} \tag{1.19}$$

The system of equations (1.17) can be written in the compact vector notation:

$$\mathbf{V}(\boldsymbol{\zeta}) + \mathbf{T}\boldsymbol{\zeta} = \mathbf{b} \tag{1.20}$$

where, $\mathbf{V}(\boldsymbol{\zeta})$ is the vector of N_p elements of the volume of each cell, non-linear function of the water surface elevation $\boldsymbol{\zeta} = (\eta_i^{n+1})_{i=1}^{Np}$, $\mathbf{T}$ is the matrix of N_pxN_p elements that arises from the linear terms in the Equation (1.17) and $\mathbf{b}$ is the vector of N_p elements given by the right-hand side of Equation (1.17) defined in Equation (1.18).
The system of equations (1.17) can be solved iteratively with a Newton type algorithm. Thus, a converging Newton type method for solving the system of equations (1.17) can be formulated as follows:

$$\boldsymbol{\zeta}^{l+1} = \boldsymbol{\zeta}^l - \left[\boldsymbol{C}^l + \boldsymbol{T}\right]^{-1} \left[\boldsymbol{V}(\boldsymbol{\zeta}^l) + \boldsymbol{T}\boldsymbol{\zeta}^l - \boldsymbol{b}\right] \tag{1.21}$$

where the superscript l denotes the iterations step and $[C^l + T]$ is the Jacobian matrix associated with the system of equations (1.20). Once η^{n+1} is computed is substituted in the momentum equation to compute u^{n+1} and consequently moving forward to the next time step.

1.3.2 Boundary Conditions

To solve the system of equations provided by Equations (1.17) appropriate boundary conditions need to be defined at the boundaries of the domain depending on the flow regimes. In the following, the implementation of a set of boundary conditions used in practical applications are provided, considering both subcritical and supercritical flow regime.

Upstream Boundary Condition, Subcritical Flow
In subcritical flow, two types of boundary conditions have been implemented: water surface elevation hydrograph, $\eta_{bc}(t)$, and flow discharge hydrograph, $Q_{bc}(t)$. To implement these boundary conditions a ghost cell was introduced at the beginning of the domain (Figure 1.6), i.e., upstream of the first cell in each branch of the modeled network. Considering that more than one branch can be present in a general channel network, in the following we'll keep the general i subscript for the first physical cell in the branch.

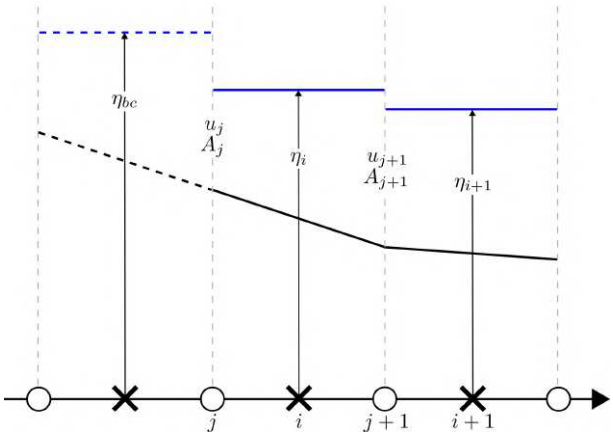

Figure 1.6: Visual representation of the ghost cell for upstream boundary condition for the node i

Regarding the first boundary condition and considering a ghost cell before the beginning of the domain, Equation (1.17) for the node i could be expanded as follows:

$$V_i\left(\eta_i^{n+1}\right)+g\theta^2\Delta t^2\frac{A_j^n}{\Delta x_j\left(1+\Upsilon_j^n\Delta t\right)}\eta_i^{n+1}-g\theta^2\Delta t^2\frac{A_{j+1}^n}{\Delta x_{j+1}\left(1+\Upsilon_{j+1}^n\Delta t\right)}\left[\eta_{i+1}^{n+1}-\eta_i^{n+1}\right]=b_i \quad (1.22)$$

where the right hand side b_i is a function of known quantities only. In particular it is a function of η_{bc}^{n+1} that is known for every time step:

$$\begin{aligned} b_i =& V_i(\eta_i^n)-\Delta tA_j^n\sigma_{i,j}[\theta G_j^n+(1-\theta)u_j^n]-\Delta tA_{j+1}^n\sigma_{i,j+1}[\theta G_{j+1}^n+(1-\theta)u_{j+1}^n] \\ &+g\theta^2\Delta t^2\frac{A_j^n}{\Delta x_j(1+\Upsilon_j^n\Delta t)}\eta_{bc}^{n+1}+Q_{i,*}\Delta t \end{aligned} \quad (1.23)$$

On the other hand, considering a flow hydrograph $Q_{bc}(t)$ as upstream boundary condition and considering the indexing provided in Figure 1.6 the Equation (1.15) for node i at the beginning of the domain could be written as follows:

$$V_i(\eta_i^{n+1})=V_i(\eta_i^n)+\Delta tA_j^n\left(\theta\frac{Q_{\text{bc}}^{n+1}}{A_j^{n+1}}+(1-\theta)u_j^n\right)-\Delta tA_{j+1}^n\left(\theta u_{j+1}^{n+1}+(1-\theta)u_{j+1}^n\right) \quad (1.24)$$

moving in Eq.(1.24) the unknown in the left hand side and replacing the definition of u_{j+1}^{n+1} provided by Equation (1.9):

$$V_i\left(\eta_i^{n+1}\right)-\theta\Delta tA_j^n\frac{Q_{\text{bc}}^{n+1}}{A_j^{n+1}}-g\theta^2\Delta t^2\frac{A_{j+1}^n}{\Delta x_{j+1}\left(1+\Upsilon_{j+1}^n\Delta t\right)}[\eta_{i+1}^{n+1}-\eta_i^{n+1}]=b_i \quad (1.25)$$

where:

$$b_i=V_i(\eta_i^n)-\Delta tA_j^n\sigma_{i,j}(1-\theta)u_j^n-\Delta tA_{j+1}^n\sigma_{i,j+1}\left[\theta G_{j+1}^n+(1-\theta)u_{j+1}^n\right]+Q_{i,*}\Delta t \quad (1.26)$$

note that in Equation (1.25) the non-linear part for this equation is not the term related to the volume only as before, but it includes the quantities that are function of $A_j^{n+1}(\eta_i^{n+1})$. The Jacobian of the system which is used in the solution of the modified Equation (1.20) is changed accordingly. Additionally, A_j^{n+1} is a function of the water level in the ghost cell η_{bc}^{n+1} which is

unknown. Accordingly, for this type of boundary condition it was assumed that the water depth in the ghost cell is equal to the water depth in the cell i at the beginning of the domain.

Upstream Boundary Condition, Supercritical Flow

For supercritical flow regime two upstream boundary conditions are required: for instance, $\eta_{bc}(t)$ and $Q_{bc}(t)$. Accordingly, Equation (1.15) for the node i at the beginning of the domain could be written as follows:

$$V_i\big(\eta_i^{n+1}\big) - \theta\Delta t A_j^n \frac{Q_{\text{bc}}^{n+1}}{A_j^{n+1}} - g\theta^2\Delta t^2 \frac{A_{j+1}^n}{\Delta x_{j+1}\big(1+\Upsilon_{j+1}^n\Delta t\big)}\big[\eta_{i+1}^{n+1} - \eta_i^{n+1}\big] = b_i \tag{1.27}$$

where:

$$b_i = V_i(\eta_i^n) - \Delta t A_j^n \sigma_{i,j}(1-\theta)u_j^n - \Delta t A_{j+1}^n \sigma_{i,j+1}\big[\theta G_{j+1}^n + (1-\theta)u_{j+1}^n\big] + Q_{i,*}\Delta t \tag{1.28}$$

note that in Equation (1.27) in this case A_j^{n+1} is computed as a function of the imposed known values $\eta_{bc}^{n+1}(t)$ and $Q_{bc}^{n+1}(t)$ during the iteration process.

Downstream Boundary Condition, Subcritical Flow

In subcritical flow, two types of boundary conditions have been implemented: water surface elevation hydrograph, $\eta_{bc}(t)$ and normal depth condition. To implement these boundary conditions a ghost cell was added at the end of the domain (Figure 1.7).

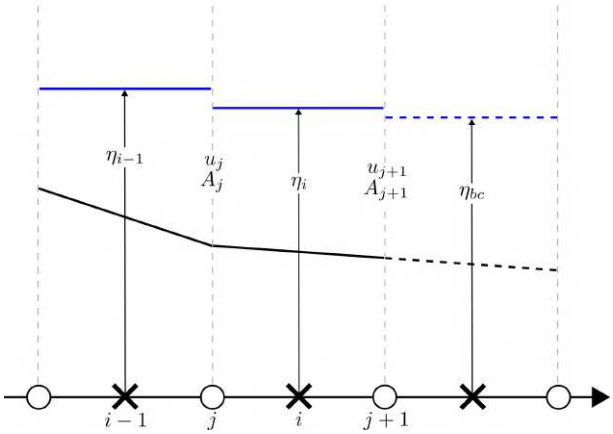

Figure 1.7: Visual representation of the ghost cell for downstream boundary condition for the node i

For the first boundary condition, considering a ghost at the end of the domain, Equation (1.17) for the node i at the end of the branch could be expanded as follows:

$$V_i(\eta_i^{n+1}) - g\theta^2\Delta t^2 \frac{A_j^n}{\Delta x_j(1+\Upsilon_j^n\Delta t)}[\eta_{i-1}^{n+1} - \eta_i^{n+1}] + g\theta^2\Delta t^2 \frac{A_{j+1}^n}{\Delta x_{j+1}(1+\Upsilon_{j+1}^n\Delta t)}\eta_i^{n+1} = b_i \tag{1.29}$$

given that η_{bc}^{n+1} is known, it is moved to the right hand side of equation. Accordingly, the right hand side b_i can be written as follows:

$$\begin{aligned} b_i =& V_i(\eta_i^n) - \Delta t A_j^n \sigma_{i,j}[\theta G_j^n + (1-\theta)u_j^n] - \Delta t A_{j+1}^n \sigma_{i,j+1}[\theta G_{j+1}^n + (1-\theta)u_{j+1}^n] \\ &+ g\theta^2\Delta t^2 \frac{A_{j+1}^n}{\Delta x_{j+1}(1+\Upsilon_{j+1}^n\Delta t)}\eta_{bc}^{n+1} + Q_{i,*}\Delta t \end{aligned} \tag{1.30}$$

The second type of boundary condition implemented for subcritical flow is the one provided by the assumption of normal depth at the end of the domain. Accordingly, the uniform flow equation has to be implemented at the end of the domain that, considering the indexing provided in Figure 1.7, can be defined as follows:

$$Q_{j+1}^{n+1} = \frac{1}{n_{j+1}} \left(R_{h_{j+1}}^{n+1} \right)^{2/3} A_{j+1}^{n+1} \sqrt{S_b} \tag{1.31}$$

where R is the hydraulic radius. Since the slope of the bed S_b is known, Equation (1.15) can be written for the node i at the end of the domain as follows:

$$\begin{aligned} V_i(\eta_i^{n+1}) =& V_i(\eta_i^n) + \Delta t A_j^n \left(\theta u_j^{n+1} + (1-\theta) u_j^n \right) \\ & - \Delta t A_{j+1}^n \left(\theta \frac{1}{n_{j+1}} \left(R_{h_{j+1}}^{n+1} \right)^{2/3} \sqrt{S_b} + (1-\theta) u_{j+1}^n \right) \end{aligned} \tag{1.32}$$

moving in Eq.(1.32) the unknown in the left hand side and replacing the definition of u_{j+1}^{n+1} provided by Equation (1.9):

$$V_i(\eta_i^{n+1}) - g\theta^2 \Delta t^2 \frac{A_j^n}{\Delta x_j (1 + \Upsilon_j^n \Delta t)} [\eta_{i-1}^{n+1} - \eta_i^{n+1}] + \theta \Delta t A_{j+1}^n \frac{1}{n_{j+1}} \left(R_{h_{j+1}}^{n+1} \right)^{2/3} \sqrt{S_b} = b_i \tag{1.33}$$

where b_i is defined as follows:

$$b_i = V_i(\eta_i^n) - \Delta t A_j^n \sigma_{i,j} \left[\theta G_j^n + (1-\theta) u_j^n \right] - \Delta t A_{j+1}^n \sigma_{i,j+1} (1-\theta) u_{j+1}^n + Q_{i,*} \Delta t \tag{1.34}$$

As for flow hydrograph upstream boundary condition $R_{h_{j+1}}^{n+1}$ is a function of η_i^{n+1}, accordingly the non-linear part for this equation is not the term related to the volume only. The Jacobian of the system which is used in the solution of the modified Equation (1.20) is changed accordingly.

Downstream Boundary Condition, Supercritical Flow

As reported by Rosatti et al. (2011) in supercritical regime characteristics analysis requires no boundary conditions at the outlet. However, the system of equations (1.20) requires a boundary condition on η. Accordingly, Equation (1.17) was manipulated in order to impose $\eta_i - z_i = \eta_{bc} - z_{bc}$ where z is the elevation of the bed.

1.3.3 Internal Boundary Conditions

Typically, in an open channel irrigation system there are different control structures along the channel for regulating the flow (e.g. weirs, gates) and other structures as bridges and culvert that could affect the water surface elevation along the channel. Usually, the dynamics of flow through a hydraulic structure is described by a stage-discharge relation based on a suitable local energy balance. Accordingly, in correspondence of these structures Equation (1.9) has been replaced with an appropriate stage-discharge relation. Let's suppose to introduce an internal boundary condition between the cell faces j and $j+1$ (Figure 1.8).

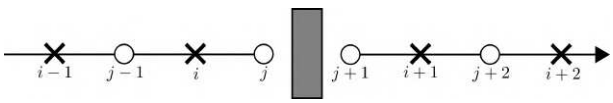

Figure 1.8: Visual representation of the introduction of an internal boundary condition between cell faces j and $j+1$

Consequently, both node i and node $i+1$ are directly affected by the internal boundary condition. In correspondence of these nodes Equations (1.17) needs to be modified in order to incorporate the stage-discharge rating curve of the structure. Considering node i, Equation (1.17) could be written in the following form:

$$V_i(\eta_i^{n+1}) - g\theta^2\Delta t^2 \frac{A_{j-1}^n}{\Delta x_{j-1}(1+\Upsilon_{j-1}^n\Delta t)}[\eta_{i-1}^{n+1} - \eta_i^{n+1}] + \theta\Delta t A_j^n f(\eta_i^{n+1}, \eta_{i+1}^{n+1}) = b_i \qquad (1.35)$$

where $f(\eta_i^{n+1}, \eta_{i+1}^{n+1})$ is a function used to compute the velocity at face j according with the stage-discharge curve used for the internal boundary condition.
b_i^n is expressed as follows:

$$b_i = V_i(\eta_i^n) - \Delta t A_{j-1}^n \sigma_{i,j-1}\Big[\theta G_{j-1}^n + (1-\theta)u_{j-1}^n\Big] - \Delta t A_j^n \sigma_{i,j}(1-\theta)u_j^n + Q_{i,*}\Delta t \qquad (1.36)$$

It has to be considered that $f(\eta_i^{n+1}, \eta_{i+1}^{n+1})$ is a non-linear function of η_i^{n+1} and η_{i+1}^{n+1}; accordingly the Jacobian of the system which is used in the solution of the modified Equation (1.20) is changed accordingly. As far as node $i+1$ is concerned, it is treated as an external boundary condition but in this case the flow discharge at the face $j+1$ is forced to be equal to the flow discharge at the face j. A set of validation test cases for the internal implemented boundary condition are provided in the Chapter 3 following the in-depth analysis of the methodologies used in HEC-RAS 2D to model bridges provided in Chapter 2.

1.4 Validation

The numerical model presented above has been implemented in MATLAB. In order to test the correct implementation and the performance of the presented numerical model several tests have been performed. As a first step, given that the model can handle irregular cross section, a validation of the geometries property pre-processor of the cross section was performed comparing the obtained results with the ones obtained using HEC-RAS (Brunner, 2024b) for an irregular cross section. After the positive conclusion of this preliminary test, the performance of the solver has been verified. The MacDonal test cases (Delestre et al., 2014; Macdonald, 1996) and the flow over a bump test cases have been used to validate the implemented model for steady condition, under the influence of different types of boundary conditions in an open-channel. The test cases proposed for an idealized channel network (Islam et al., 2005; Sen & Garg, 2002) have then been performed to check if the implemented model can handle a system of connected open channels (open and looped network).

1.4.1 Pre-processing Validation

The implemented numerical model can handle irregular cross sections. Accordingly, before solving the Saint-Venant Equations, all the cross sections considered in the numerical model need to be processed in order to compute different geometrical properties (area, wetted perimeter, hydraulic radius, elevation of the centroid) and hydraulic properties (e.g. composed Manning roughness coefficient) for different water levels: the processed information is then stored in look-up tables as function of the water surface elevation and are used to speed up the solution process. A similar pre-processing is performed for the control volumes, which are processed in order to compute the volume and the horizontal water surface area as a function of water surface elevation. As an example, to show the performance of the pre-processing algorithm, the cross section shown in Figure 1.9 whose geometry is reported in Table 1.1 is considered.

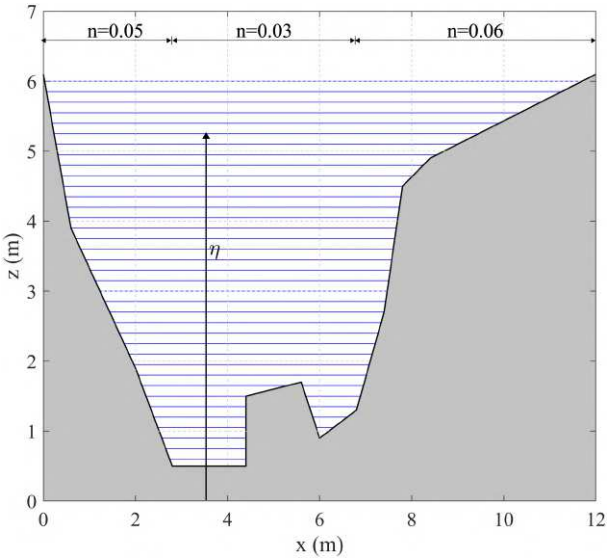

Figure 1.9: Geometry of the cross section used for the validation of the pre-processing of the geometry.

Table 1.1: Geometry of the cross section detailed in the Figure 1.9, along with space distribution of the Manning's n.

x (m)	z (m)	n (s $m^{-1/3}$)	x (m)	z (m)	n (s $m^{-1/3}$)
0	6.1	0.05	6	0.9	0.03
0.6	3.9	0.05	6.8	1.3	0.06
2	1.9	0.05	7.4	2.7	0.06
2.8	0.5	0.05	7.8	4.5	0.06
4.4	0.5	0.03	8.4	4.9	0.06
4.4	1.5	0.03	12	6.1	0.06
5.6	1.7	0.03			

To account for the effect of different values for the Manning roughness coefficient, the section-averaged values of the friction factors can be obtained by the Einstein-Horton method as follows:

$$\overline{n} = \left(\frac{\sum_k P_k n_k^{1.5}}{\sum_k P_k} \right)^{2/3} \tag{1.37}$$

where the index k refers to the sub-section k with constant Manning coefficient and the related P_k wetted perimeter. The pre-processing algorithm of the cross section has been validated using the results provided by HEC-RAS for the same cross section. The comparisons for the area, the wetted perimeter and the Manning roughness coefficient are reported in Figure 1.10.

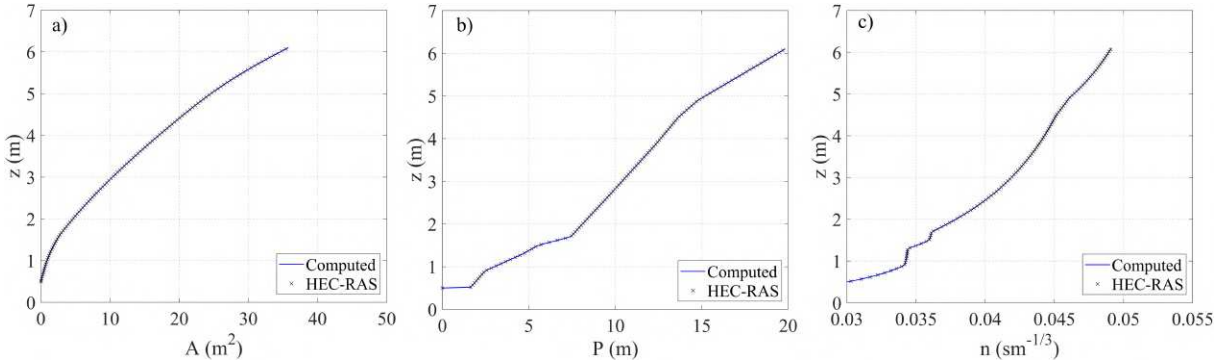

Figure 1.10: Geometrical properties of the cross section, comparison with HEC-RAS. a) Area, b) Wetted perimeter, c) Manning roughness coefficient for different water level η.

To validate the cell pre-processing, a control volume limited by two identical cross sections shown in Figure 1.9 was considered, the distance between the two cross sections was assumed equal to 20 m. The pre-processing of the control volume has been validated with the results provided by HEC-RAS for the same control volume. The comparisons for the volume and the horizontal water surface area are reported in Figure 1.11.

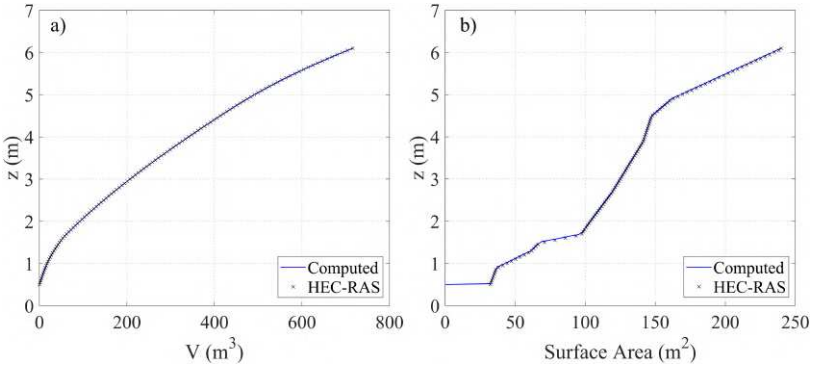

Figure 1.11: Geometrical properties of the cell, comparison with HEC-RAS. a) Volome, b) Horizontal water surface area for different water level η.

As one can observe, the comparison demonstrates the correct implementation of the geometric pre-processing of the channel network. Finally, to pool all the pre-processed properties the uniform flow stage-discharge curves is provided in Figure 1.12 considering a slope of the bed $S_0 = 0.001$.

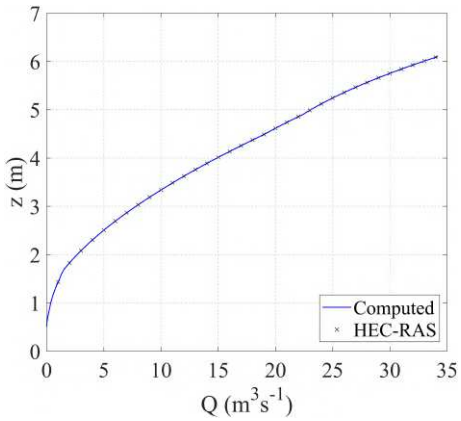

Figure 1.12: Comparison of the uniform flow stage-discharge curve for the considered cross section, compared to the steady state solution provide by HEC-RAS for different discharges in a prismatic channel characterized by the cross section (Table 1.1) and a slope of the bottom $S_0 = 0.001$.

The pre-processing of the cross sections is based on the hypothesis of compact cross section tipically used in irrigation channel network. Although the pre-processor can handles the geometry of irregular cross sections with floodplains, in correspondence of the elevation of the floodplain there is a sharp increase of the wetted perimeter and consequently a sharp reduction of the cross section conveyance. Accordingly, to avoid this problem a further improvement in this direction can be to compute the conveyance of the cross section dividing it in a set of sub-sections that cover respectively the floodplain and the main channel.

1.4.2 MacDonald's Test Cases

In this section, the implemented numerical model is validated for a set of problems with non-prismatic channels in steady state condition introduced by Macdonald (1996) and reported in Delestre et al. (2014). The five considered channels have a variable slope and width in space and they are characterized by a length L. Each channel is defined using the bottom width B computed as a function of the spatial position and the slope of the bottom S_0. The slope of the bottom and, consequently, the elevation of the bottom are functions of the water height. The main characteristics of the cases are summarized in Table 1.2.

Table 1.2: Main features of the test cases.

Case	***Short description***	***B*** ***(m)***	***L*** ***(m)***	***n*** ***(s m$^{-1/3}$)***	***Z*** ***(-)***	***Q*** ***(m^3 s^{-1})***
1	Subcritical flow in a short domain	B_1 (x)	200	0.03	0	20
2	Smooth transition in a short domain	B_1 (x)	200	0.03	0	20
3	Hydraulic jump in a short domain	B_1 (x)	200	0.03	0	20
4	Subcritical flow in a long domain	B_2 (x)	400	0.03	2	20
5	Smooth transition followed by a hydraulic jump in a long domain	B_2 (x)	400	0.03	2	20

The channels for the cases 1, 2, 3 are rectangular and the width is defined by Equation (1.38), on the other hand in the cases 4, 5 the cross section is trapezoidal with a slope of the banks Z as shown in Figure 1.13 and the bottom width is defined by Equation (1.39).

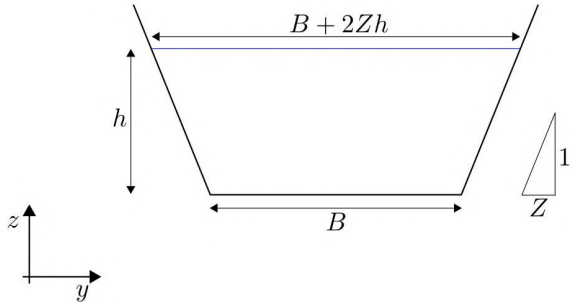

Figure 1.13: Transversal cross section for the MacDonald test cases.

$$B_1(x) = 10 - 5\exp\left(-10\left(\frac{x}{200} - \frac{1}{2}\right)^2\right) \tag{1.38}$$

$$B_2(x) = 10 - 5\exp\left(-50\left(\frac{x}{400} - \frac{1}{3}\right)^2\right) - 5\exp\left(-50\left(\frac{x}{400} - \frac{2}{3}\right)^2\right) \tag{1.39}$$

The base width profiles defined in Equation (1.38) and (1.39) are shown in Figure 1.14.

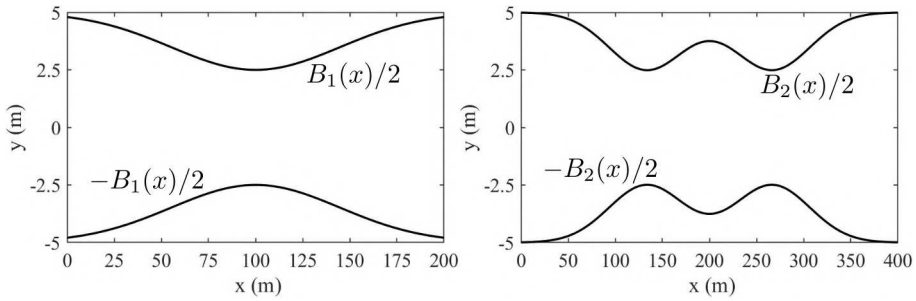

Figure 1.14: Bottom channel width computed using Equation (1.38) for $B_1(x)$ and Equation (1.39) for $B_2(x)$ for the MacDonald test cases.

The slope of the bed is computed according to:

$$S_0(x) = \left(1 - \frac{Q^2\big(B(x) + 2Zh(x)\big)}{gh(x)^3\big(B(x) + Zh(x)\big)^3}\right)\frac{\partial h(x)}{\partial x} + Q^2 n^2 \frac{\big(B(x) + 2h(x)\sqrt{1+Z^2}\big)^{4/3}}{h(x)^{10/3}\big(B(x) + Zh(x)\big)^{10/3}} - \frac{Q^2}{gh(x)^2\big(B(x) + Zh(x)\big)^3}\frac{\partial B(x)}{\partial x} \tag{1.40}$$

Here it is important to observe that the water depth $h\,(x)$ is given. Accordingly, the actual slope of the bed $S_0\,(x)$ to be used in the test can be simply obtained by the equation above and consequently it is possible to compute the elevation of the bottom $z\,(x)$:

$$z(x) = \int_x^L S_0(X)dX \tag{1.41}$$

The accuracy of the results was evaluated using two different measures, the L_1 error given by:

$$L_1 = \frac{1}{N_P}\sum_{i=1}^{N_P} |\hat{\eta}(x_i) - \eta_i| \tag{1.42}$$

and:

$$L_\infty = max|\hat{\eta}(x_i) - \eta_i| \tag{1.43}$$

Where $\hat{\eta}\,(x_i)$ is the exact solution, η_i is the elevation of the water surface computed with the implemented numerical model, i is the i-th node of the discretized domain and N_p is the total number of nodes.

Case 1: Subcritical flow in a short domain

In this case, the flow regime is subcritical for the entire domain; a constant flow hydrograph is used as upstream boundary condition, and the water height is prescribed at outflow:

$$\begin{cases} \text{upstream: } Q = 20\,\text{m}^3\text{s}^{-1} \\ \\ \text{downstream: } h = 0.902921\,\text{m} \end{cases} \tag{1.44}$$

The analytical solution is provided by:

$$h(x) = 0.9 + 0.3\exp\left(-20\left(\frac{x}{200} - \frac{1}{2}\right)^2\right) \tag{1.45}$$

The values of the parameters used in the present test case are reported in Table 1.3, along with L_1 and L_∞ for different space discretization. A constant time step was chosen to satisfy the relaxed condition $C_{vel} = u\Delta t/\Delta x$, assumed in this case equal to 0.9. The implemented numerical scheme should be stable also for C_{vel} greater than one. Accordingly, to test this numerical scheme property, the case test was repeated using a time step that allows to reach a C_{vel} equal to 3. The results are reported in Table 1.4.
Figure 1.15 shows a comparison of the analytical solution with the results computed using cell spacing of 2.5 m for a C_{vel} equal to 0.9 (Figure 1.15a) and for a C_{vel} equal to 3 (Figure 1.15b).

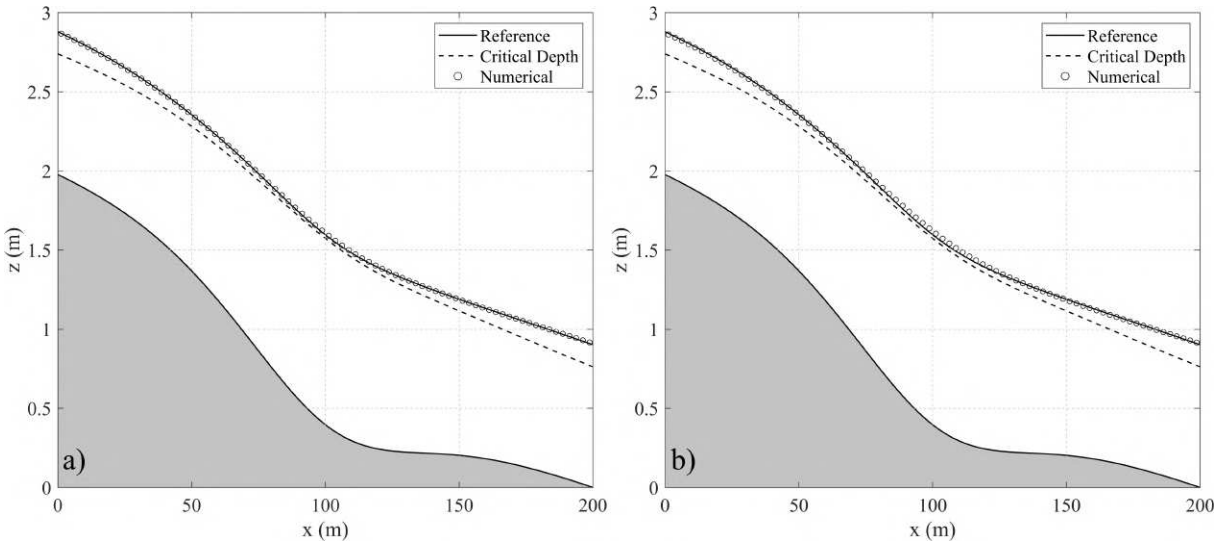

Figure 1.15: Comparison between the numerical results and the analytical solution. a) $C_{vel} \leq 0.9$, b) $C_{vel} \leq 3$.

Table 1.3: Values of the numerical scheme parameters adopted for the numerical test case, the L_1 and L_∞ computed between the analytical solution and the computed one.

Δx (m)	θ (-)	Np (-)	Δt (s)	C_{vel} (-)	L_1 (m)	L_∞ (m)
10	1	20	2.7	0.88	0.0087	0.0277
5	1	40	1.3	0.85	0.0051	0.0168
2.5	1	80	0.65	0.86	0.0028	0.0095
1	1	200	0.27	0.9	0.0012	0.0041
0.5	1	400	0.13	0.87	6.4×10^{-4}	0.0023

Table 1.4: Values of the numerical scheme parameters adopted for the numerical test case, the L_1 and L_∞ computed between the analytical solution and the computed one. In these cases, the maximum C_{vel} has been set to 3.

Δx (m)	θ (-)	Np (-)	Δt (s)	C_{vel} (-)	L_1 (m)	L_∞ (m)
10	1	20	9.5	3.00	0.0214	0.0649
5	1	40	4.6	2.96	0.0126	0.0408
2.5	1	80	2.25	2.94	0.007	0.0240
1	1	200	0.9	2.97	0.0031	0.0112
0.5	1	400	0.45	2.99	0.0016	0.0060

Case 2: Smooth transition in a short domain

In this case, the flow regime is subcritical for the upstream part of the domain, followed by a smooth transition to a supercritical flow regime. A constant flow hydrograph is used as upstream boundary condition, and free flow at outflow:

$$\begin{cases} \text{upstream: } Q = 20\,\text{m}^3\text{s}^{-1} \\ \\ \text{downstream: Free flow} \end{cases} \tag{1.46}$$

The analytical solution is defined as follows:

$$h\left(x\right) = 1 - 0.3\tanh\left(4\left(\frac{x}{200} - \frac{1}{3}\right)\right) \tag{1.47}$$

The values of the parameters used in the present test case are reported in Table 1.5, along with L_1 and L_∞ for different space discretization. The constant time step was chosen to satisfy the C_{vel}, assumed in this case equal to 0.9. As in the previous test cases, the numerical model has been validated for C_{vel} greater than one assuming a C_{vel} equal to 1.5. The results are reported in Table 1.6.
Figure 1.16 shows a comparison of the results of the implemented algorithm and the analytical solution obtained using cell spacing of 2.5 m for the case obtained for a C_{vel} equal to 0.9 (Figure 1.16a) and for a C_{vel} equal to 1.5 (Figure 1.16b).

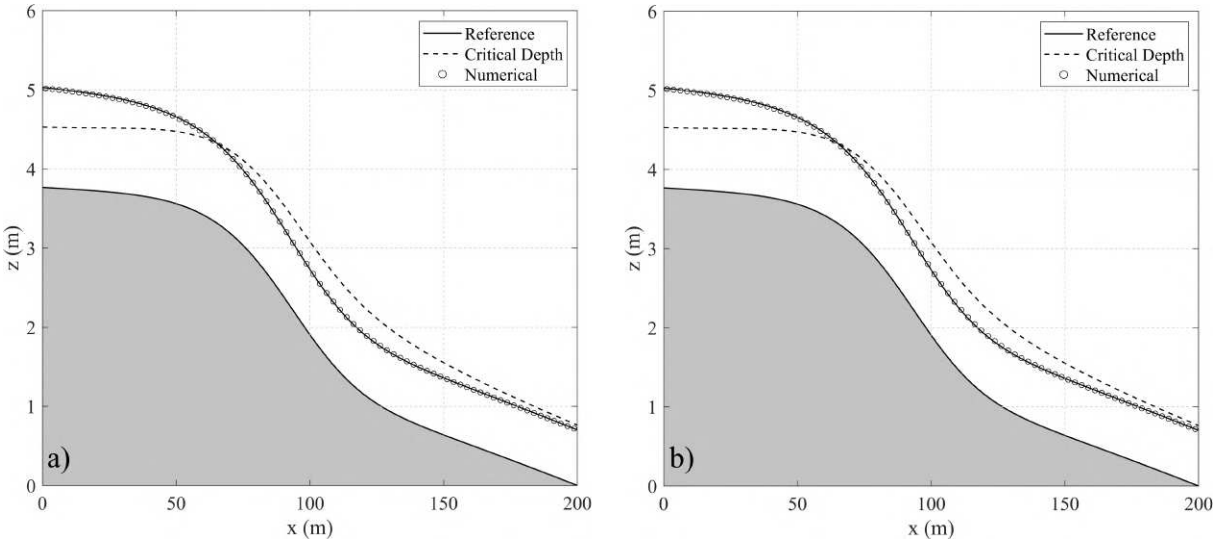

Figure 1.16: Comparison between the numerical results and the analytical solution. a) $C_{vel} \leq 0.9$, b) $C_{vel} \leq 1.5$.

Table 1.5: Values of the numerical scheme parameters adopted for the numerical test case, the L_1 and L_∞ computed between the analytical solution and the computed one.

Δx (m)	θ (-)	Np (-)	Δt (s)	C_{vel} (-)	L_1 (m)	L_∞ (m)
10	1	20	1.88	0.9	0.0127	0.0277
5	1	40	0.92	0.89	0.0081	0.0159
2.5	1	80	0.45	0.88	0.0046	0.0085
1	1	200	0.18	0.89	0.0020	0.0035
0.5	1	400	0.09	0.89	0.0010	0.0018

Table 1.6: Values of the numerical scheme parameters adopted for the numerical test case, the L_1 and L_∞ computed between the analytical solution and the computed one. In these cases, the maximum C_{vel} has been set to 1.5.

Δx (m)	θ (-)	Np (-)	Δt (s)	C_{vel} (-)	L_1 (m)	L_∞ (m)
10	1	20	3.15	1.48	0.0175	0.0323
5	1	40	1.55	1.49	0.0110	0.0212
2.5	1	80	0.76	1.48	0.0061	0.0119
1	1	200	0.3	1.47	0.0026	0.0051
0.5	1	400	0.15	1.48	0.0013	0.0026

Case 3: Hydraulic jump in a short domain

In this case, the flow regime is supercritical upstream and then the flow becomes subcritical for the downstream part of the domain, passing through a hydraulic jump . A constant flow hydrograph coupled with a constant water surface have been used as upstream boundary condition and a costant water height has been used as downstream boundary condition:

$$\begin{cases} \text{upstream: } Q = 20 \text{ m}^3\text{s}^{-1} \text{ and } h = 0.7m \\ \text{downstream: } h = 1.4992\text{m} \end{cases} \tag{1.48}$$

The analytical solution for the water depth is defined as follows:

$$\begin{aligned} h(x) &= 0.7 + 0.3\left(\exp\left(\frac{x}{200}\right) - 1\right) \quad \text{for } 0 \text{ m} \leqslant x \leqslant 120 \text{ m} \\ h(x) &= \exp\left(-p(x - x^\star)\right) \sum_{i=0}^{M} k_i \left(\frac{x - x^\star}{x^{\star\star} - x^\star}\right)^i + \phi(x) \quad \text{for } 120 \text{ m} < x \leqslant 200 \text{ m} \end{aligned} \tag{1.49}$$

Where:

- $x^\star = 120$
- $x^{\star\star} = 200$
- $M = 2$
- $k_0 =$ - 0.154375
- $k_1 =$ - 0.108189
- $k_2 =$ - 2.014310
- $p = 0.1$
- $\phi\left(x\right) = 1.5 \exp\left(0.1\left(\frac{x}{200} - 1\right)\right)$

The values of the code parameters used in the present test case are reported in Table 1.7, along with L_1 and L_∞ for different space discretization. A constant time step was chosen to satisfy the C_{vel}, which was assumed to be equal to 0.9 in this case.
As done for the previous test cases, the numerical model has been validated for C_{vel} greater than one assuming a C_{vel} equal to 1.5. The results are reported in Table 1.8.
Figure 1.17 shows a comparison of the results of the implemented algorithm and the analytical solution obtained using cell spacing of 2.5 m for the case with a C_{vel} equal to 0.9 (Figure 1.17a) and for a C_{vel} equal to 1.5 (Figure 1.17b).

Table 1.7: Values of the numerical scheme parameters adopted for the numerical test case, the L_1 and L_∞ computed between the analytical solution and the computed one. In these cases, the maximum C_{vel} has been set to 0.9.

Δx (m)	θ (-)	Np (-)	Δt (s)	C_{vel} (-)	L_1 (m)	L_∞ (m)
10	1	20	2	0.88	0.0236	0.1189
5	1	40	1	0.89	0.0145	0.1270
2.5	1	80	0.5	0.89	0.0084	0.1326
1	1	200	0.2	0.9	0.0038	0.1369
0.5	1	400	0.1	0.9	0.0020	0.1348

Table 1.8: Values of the numerical scheme parameters adopted for the numerical test case, the L_1 and L_∞ computed between the analytical solution and the computed one. In these cases, the maximum C_{vel} has been set to 1.5.

Δx (m)	θ (-)	Np (-)	Δt (s)	C_{vel} (-)	L_1 (m)	L_∞ (m)
10	1	20	3.4	1.48	0.0291	0.1272
5	1	40	1.7	1.5	0.0178	0.1281
2.5	1	80	0.84	1.5	0.0102	0.1336
1	1	200	0.33	1.48	0.0046	0.1567
0.5	1	400	0.165	1.48	0.0026	0.1941

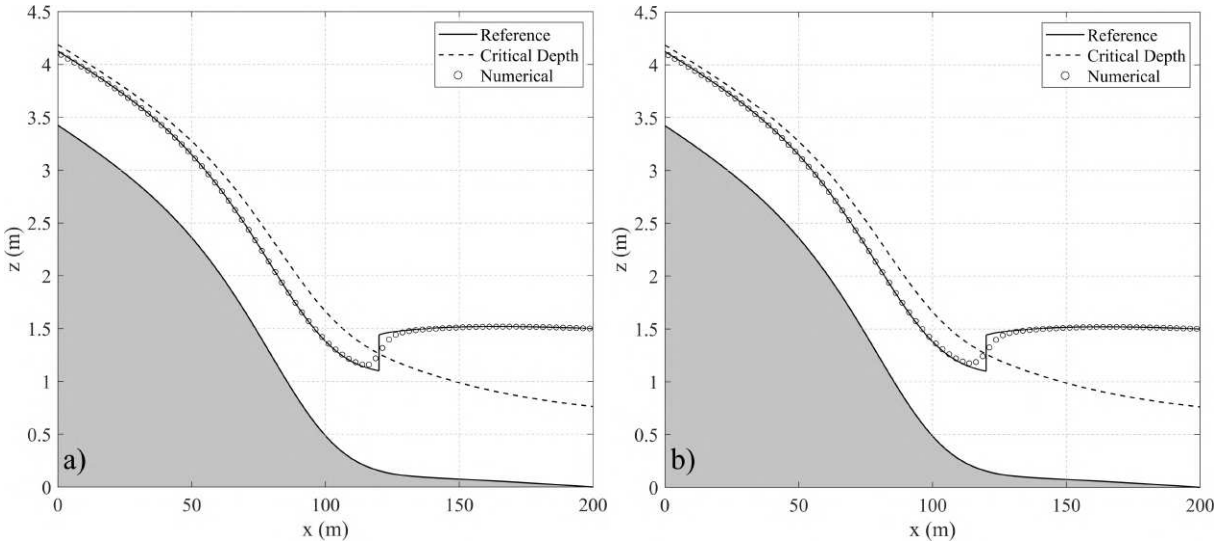

Figure 1.17: Comparison between the numerical results and the analytical solution. a) $C_{vel} \leq 0.9$, b) $C_{vel} \leq 1.5$.

Case 4: Subcritical flow in a long domain

In this case, the flow regime is subcritical for the entire domain. A constant flow hydrograph is used as upstream boundary condition and a constant water height is prescribed at outflow:

$$\begin{cases} \text{upstream: } Q = 20\,\text{m}^3\text{s}^{-1} \\ \\ \text{downstream: } h = 0.904094\,\text{m} \end{cases} \tag{1.50}$$

The analytical solution for the water depth is defined as follows:

$$h(x) = 0.9 + 0.3\exp\left(-40\left(\frac{x}{400} - \frac{1}{3}\right)^2\right) + 0.2\exp\left(-35\left(\frac{x}{400} - \frac{2}{3}\right)^2\right) \tag{1.51}$$

The values of the code parameters used in the present test case are reported in Table 1.9, along with the L_1 and L_∞ for different space discretization. A constant time step was chosen to satisfy the C_{vel}, assumed in this case equal to 0.9.
As done for the previous test cases, the numerical model has been validated for C_{vel} greater than one assuming a C_{vel} equal to 3.0. The results are reported in Table 1.10.
Figure 1.18 shows a comparison of the results of the implemented algorithm and the analytical solution obtained using cell spacing of 5 m for the case obtained for a C_{vel} equal to 0.9 (Figure 1.18a) and for a C_{vel} equal to 3 (Figure 1.18b).

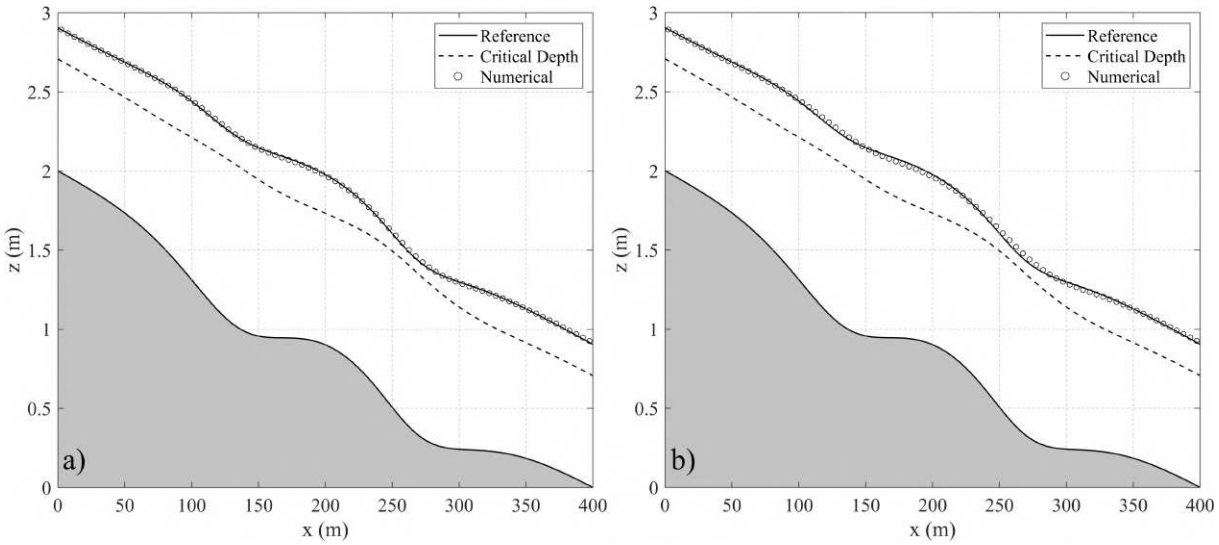

Figure 1.18: Comparison between the numerical results and the analytical solution. a) $C_{vel} \leq 0.9$, b) $C_{vel} \leq 3$.

Table 1.9: Values of the numerical scheme parameters adopted for the numerical test case, the L_1 and L_∞ computed between the analytical solution and the computed one. In these cases, the maximum C_{vel} has been set to 0.9.

Δx (m)	θ (-)	Np (-)	Δt (s)	C_{vel} (-)	L_1 (m)	L_∞ (m)
20	1	20	7.50	0.90	0.0123	0.0333
10	1	40	3.65	0.89	0.0079	0.0228
5	1	80	1.80	0.89	0.0044	0.0136
2	1	200	0.71	0.89	0.0019	0.0061
1	1	400	0.35	0.88	9.97×10^{-4}	0.0032

Table 1.10: Values of the numerical scheme parameters adopted for the numerical test case, the L_1 and L_∞ computed between the analytical solution and the computed one. In these cases, the maximum C_{vel} has been set to 3.0.

Δx (m)	θ (-)	Np (-)	Δt (s)	C_{vel} (-)	L_1 (m)	L_∞ (m)
20	1	20	25.7	2.99	0.0216	0.0688
10	1	40	12.6	2.99	0.0156	0.0497
5	1	80	6.15	2.99	0.0097	0.0320
2	1	200	2.4	2.97	0.0045	0.0159
1	1	400	1.2	3	0.0024	0.0088

Case 5: Smooth transition followed by a hydraulic jump in a long domain

In this case, the flow regime is subcritical upstream followed by a smooth transition to the supercritical flow regime. This regime is terminated by a hydraulic jump and the flow regime becomes subcritical for the remaining part of the domain. A constant flow hydrograph has been used as the upstream boundary condition, and the water height is prescribed at outflow:

$$\begin{cases} \text{upstream: } Q = 20\,\text{m}^3\text{s}^{-1} \\ \\ \text{downstream: } h = 1.2\,\text{m} \end{cases} \tag{1.52}$$

The analytical solution for the water depth is defined as follows:

$$\begin{aligned} h(x) &= 0.9 + 0.25\left(\exp\left(-\frac{x}{40}\right) - 1\right) + 0.25\exp\left(15\left(\frac{x}{400} - \frac{3}{10}\right)\right) \quad \text{for } 0\text{ m} \leqslant x \leqslant 120\text{ m} \\ h(x) &= \exp\left(-p(x - x^*)\right)\sum_{i=0}^{M} k_i \left(\frac{x - x^*}{x^{**} - x^*}\right)^i + \phi(x) \quad \text{for } 120\text{ m} < x \leqslant 400\text{ m} \end{aligned} \tag{1.53}$$

Where:

- $x^\star = 120$
- $x^{\star\star} = 400$
- $M = 2$
- $k_0 =$ - 0.183691
- $k_1 = 1.519577$
- $k_2 =$ - 18.234429
- $p = 0.09$
- $\phi(x) = 1.5\exp\left(0.16\left(\frac{x}{400} - 1\right)\right) - 0.3\exp\left(2\left(\frac{x}{400} - 1\right)\right)$

The values of the code parameters used in this test case are reported in Table 1.11, along with the L_1 and L_∞ for different space discretization. The constant time step was chosen to satisfy the C_{vel}, which was assumed to be equal to 0.9 in this case.

Table 1.11: Values of the numerical scheme parameters adopted for the numerical test case, the L_1 and L_∞ computed between the analytical solution and the computed one. In these cases, the maximum C_{vel} has been set to 0.9.

Δx (m)	θ (-)	Np (-)	Δt (s)	C_{vel} (-)	L_1 (m)	L_∞ (m)
20	1	20	5.90	0.89	0.0170	0.0494
10	1	40	2.88	0.9	0.0102	0.0687
5	1	80	1.41	0.89	0.0061	0.0710
2	1	200	0.56	0.89	0.0029	0.0712
1	1	400	0.28	0.89	0.0016	0.0720

As has been done for the previous test cases, the numerical model has been validated for C_{vel} greater than one assuming a C_{vel} equal to 3.0. The results are reported in Table 1.12.

Table 1.12: Values of the numerical scheme parameters adopted for the numerical test case, the L_1 and L_∞ computed between the analytical solution and the computed one. In these cases, the maximum C_{vel} has been set to 3.

Δx (m)	θ (-)	Np (-)	Δt (s)	C_{vel} (-)	L_1 (m)	L_∞ (m)
20	1	20	20.6	2.98	0.0292	0.1237
10	1	40	10.05	2.99	0.0194	0.1144
5	1	80	4.9	2.99	0.0116	0.0996
2	1	200	1.90	2.98	0.0056	0.0875
1	1	400	0.94	2.98	0.0032	0.0835

Figure 1.19 shows the comparison of the results of the implemented algorithm and the analytical solution obtained using cell spacing of 2.5 m for the case obtained for a C_{vel} equal to 0.9 (Figure 1.19a) and for a C_{vel} equal to 3 (Figure 1.19b).

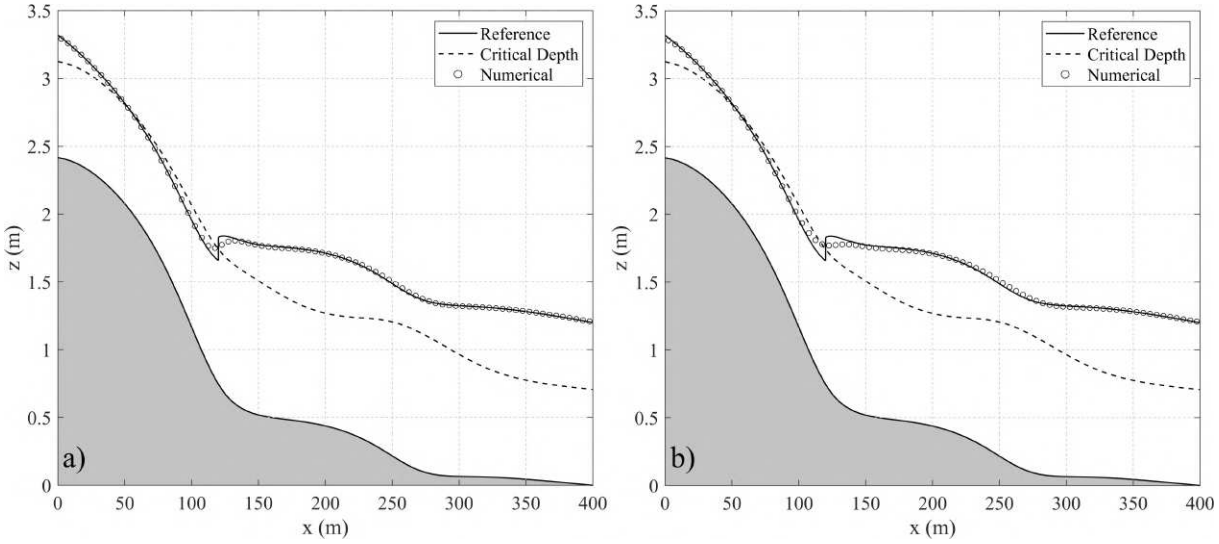

Figure 1.19: Comparison between the numerical results and the analytical solution. a) $C_{vel} \leq 0.9$, b) $C_{vel} \leq 3$.

1.4.3 Flow over a Bump

Steady flow over a parabolic bump is a classical numerical test used by various authors (Catella et al., 2008; Delestre et al., 2014; Rosatti et al., 2011) because it allows testing of different flow regimes across a geometric singularity, with possible occurrence of a hydraulic jump and under different boundary conditions. In the following cases, a rectangular channel 25 m long and 1 m wide has been considered. The bed elevation is given by:

$$z(x) = \begin{cases} 0.2 - 0.05(x-10)^2, & 8 < x < 12 \\ 0 & \text{otherwise} \end{cases} \tag{1.54}$$

Three different cases have been considered with different flow regimes (subcritical, transcritical without shock and transcritical with shock). The boundary conditions adopted for the selected cases are reported in Table 1.13. The flow is frictionless and the analytical solution for the comparison of the numerical results has been computed using the specific energy balance and the conservation of momentum. The results of the numerical tests for the three test cases are reported in Table 1.14. Finally, a visual comparison of the results for a grid spacing of 0.25 m is reported in Figure 1.20.

Table 1.13: Short description of the test cases and their boundary conditions.

Case	***Short description***	***Q*** (m^3s^{-1})	η_{ds} ***(m)***
1	Subcritical	4.42	2
2	Transcritical without steady shock	1.53	-
3	Transcritical with steady shock	0.18	0.33

Table 1.14: Values of the numerical scheme parameters adopted for the numerical test case,the L_1 and L_∞ computed between the analytical solution and the computed one.

Case	Δx ***(m)***	θ ***(-)***	***Np (-)***	Δt ***(s)***	C_{vel} ***(-)***	L_1 ***(m)***	L_∞ ***(m)***
1	0.5	0.65	50	0.172	0.88	0.0044	0.0244
	0.25	0.65	100	0.086	0.89	0.0023	0.0133
	0.125	0.65	200	0.043	0.89	0.0012	0.0069
2	0.5	0.65	50	0.125	0.89	0.0253	0.038
	0.25	0.65	100	0.06	0.88	0.0120	0.0213
	0.125	0.65	200	0.03	0.89	0.0059	0.0112
3	0.5	0.65	50	0.23	0.89	0.0039	0.0260
	0.25	0.65	100	0.1	0.87	0.0037	0.1205
	0.125	0.65	200	0.05	0.88	0.0013	0.0286

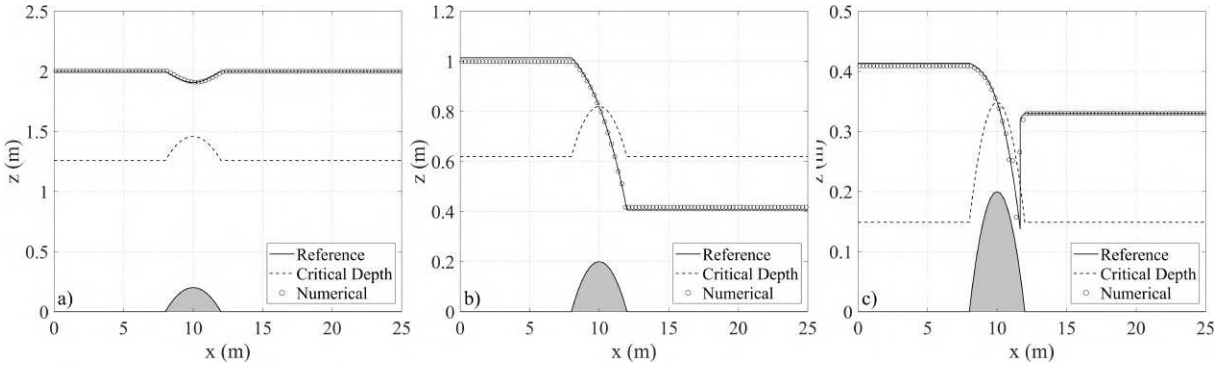

Figure 1.20: Comparison between analytical solutions e numerical solutions for flow over a bump a) subcritical flow, b) transcritical flow without shock, c) transcritical flow with shock.

1.4.4 Sen and Garg (2002) test case

All the situations considered so far are related to a single channel branch and are in steady conditions. The implemented method however is suitable to deal with a generic channel network, where both isolated branches and loops are present. Moreover, it solves the unsteady flow equations. In this direction, the hypothetical channel network proposed by Sen and Garg (2002) has been used in literature for validation of different mathematical models developed for channel networks (Yuan et al., 2020; Zhu et al., 2011) and its layout is schematized in Figure 1.21.
The channels are trapezoidal, and the main characteristics are summarized in Table 1.15. The initial condition was provided by a warm-up simulation in which the inflowing discharges (Q=10 m^3s^{-1}) and the downstream boundary condition were kept constant in order to obtain a steady state condition. The upstream boundary condition used for the canal (8) is shown in Figure 1.22a, the boundary conditions adopted for the channel (4) and (5) are a constant inflow of 10 m^3s^{-1}. The downstream boundary conditions used for the channel (3) and (10) are a constant depth of 5 m.

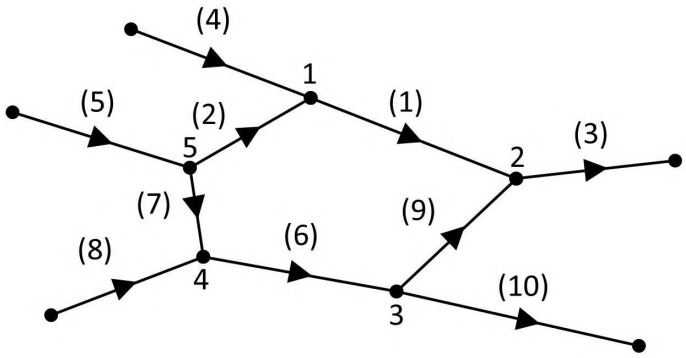

Figure 1.21: Schematic representation of the canal network, Sen and Garg (2002).

Table 1.15: Characteristic of the canal network shown in Figure 1.21 and discharge adopted as initial condition after the warm-up period. The mass balance is rounded to the fourth decimal digit.

Canal Number	***Q_0 (m^3s^{-1})***	***Length (m)***	***Bed width (m)***	***Side slope***	***Bed Slope***	***n ($s\ m^{-1/3}$)***
1	14.8	2000	100	1V:2H	0.0001	0.025
2	4.8	1000	50	1V:2H	0.0002	0.025
3	15.6	1000	75	1V:2H	0.0001	0.025
4	10	1000	50	1V:2H	0.0002	0.025
5	10	1000	50	1V:2H	0.0002	0.025
6	15.2	1000	75	1V:2H	0.0001	0.025
7	5.2	1000	50	1V:2H	0.0002	0.025
8	10	1000	50	1V:2H	0.0002	0.025
9	0.8	1000	75	1V:2H	0.0001	0.025
10	14.4	2000	100	1V:2H	0.0001	0.025

In the work of Sen and Garg (2002) the numerical solution is not provided; accordingly, the results of the implemented algorithm were compared with the results provided by Zhu et al. (2011). The results are shown in Figure 1.22b, 1.22c, 1.22d, 1.22e, 1.22f. The entire channel network was equally discretized in space in 600 cross-section and a constant time step of 120 s.

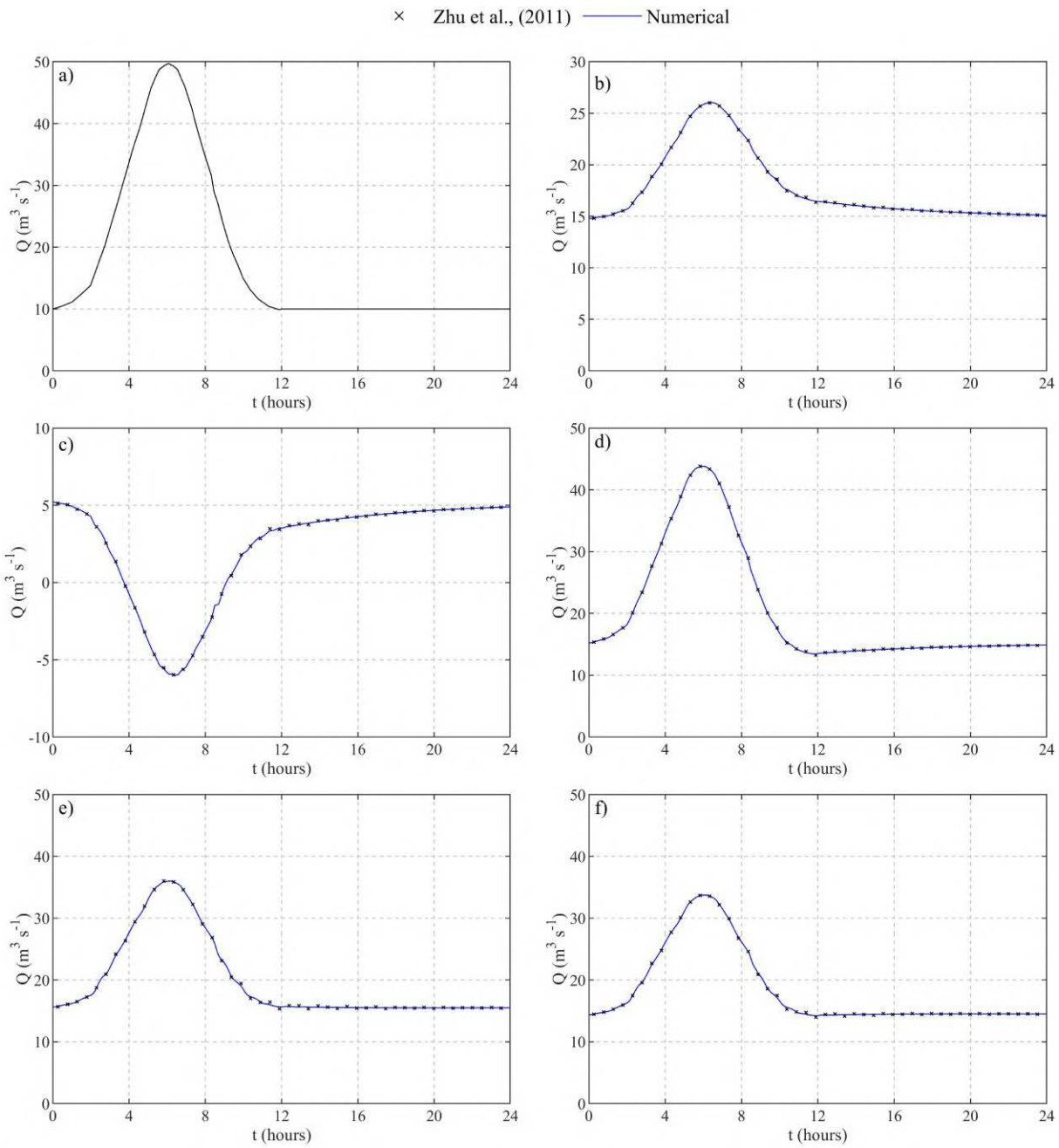

Figure 1.22: a) upstream boundary condition for the upstream cross section of canal (8). Comparison of the results of the implemented model and the data by Zhu et al. (2011) b) upstream canal (1), c) downstream canal (7), d) upstream canal (6), e) downstream canal (3), f) downstream canal (10). For canal numbers see Figure 1.21.

The initial condition, computed performing a warm-up simulation until convergence to the steady state solution, provides the possibility to validate mass conservation at each junction of the channel network. Accordingly, the computed discharges for each junction channel network are reported in Table 1.16.

Table 1.16: Sen and Garg (2002) test case, validation of mass conservation for each junction of the channel network. Incoming discharges are considered positive and outflowing discharges are considered negative. The mass balance in the last column is rounded to the fourth decimal digit.

Junction	***Q*** (m^3s^{-1})			
	Canal 4	***Canal 2***	***Canal 1***	ΔQ
1	10.0000	4.7875	-14.7875	0
	Canal 1	***Canal 3***	***Canal 9***	ΔQ
2	14.7875	-15.6357	0.8482	0
	Canal 6	***Canal 9***	***Canal 10***	ΔQ
3	15.2125	-0.8482	-14.3643	0
	Canal 7	***Canal 8***	***Canal 6***	ΔQ
4	5.2125	10	-15.2125	0
	Canal 5	***Canal 2***	***Canal 7***	ΔQ
5	10.0000	-4.7875	-5.2125	0

1.4.5 Islam et al. (2005) test case

The unsteady flow in the idealized tree-like channel network with a closed path proposed by Islam et al. (2005) has been simulated. The channel network is shown in Figure 1.23 and the main characteristics of each channel are reported in Table 1.17.

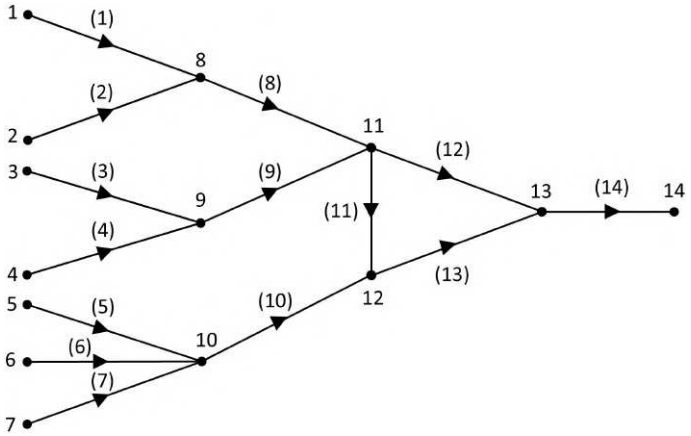

Figure 1.23: Schematic representation of the looped canal network (Islam et al., 2005)

Table 1.17: Characteristics of the canal network shown in Figure 1.23

Canal Number	***Length (m)***	***Bed width (m)***	***Side slope (-)***	***Bed slope (-)***	***n ($s\ m^{-1/3}$)***
1,2,8,9	1500	10	1	0.00027	0.022
3,4	3000	10	1	0.00047	0.025
5,6,7,10	2000	10	1	0.00030	0.022
11	1200	10	Vertical	0.00033	0.022
12	3600	20	Vertical	0.00025	0.022
13	2000	20	Vertical	0.00025	0.022
14	2500	30	Vertical	0.00016	0.022

The hydrograph used as a boundary condition for the upstream cross section of the canals (1) to (7) is shown in Figure 1.24a. In Figure 1.24b the stage hydrograph used as a downstream boundary condition for the Canal (14) is shown. The entire channel network was spatially discretized in 1172 cross sections and a constant time step equal to 10 s was used. A steady state velocity and water surface elevation was used as initial condition. In our model this initial condition was obtained by marching in time the unsteady shallow water equations with constant boundary conditions for a sufficiently long warm-up period. The boundary conditions provided by Zhu et al. (2011) have been used and the implemented algorithm's results were compared with those provided by Zhu et al. (2011) in Figure 1.24c, 1.24d, 1.24e, 1.24f.

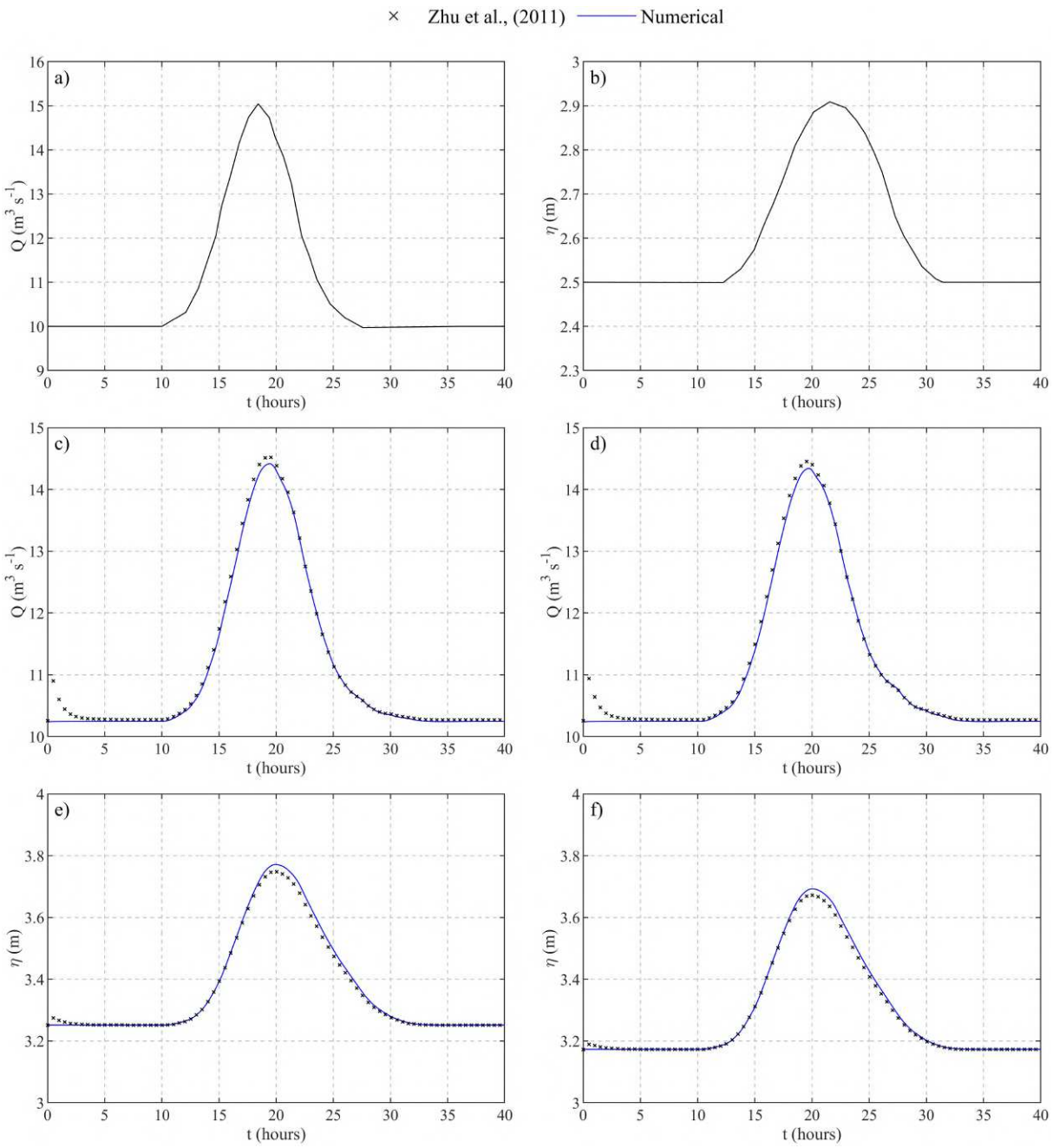

Figure 1.24: a) Upstream boundary condition for the channels (1),(2),(3),(4),(5),(6),(7); b) Downstream boundary condition for the channel (14). Comparison of the results of the implemented algorithm and the results of Zhu et al. (2011); c) discharge Node 11; d) discharge Node 12; e) water surface elevation Node 11; f) water surface elevation Node 12. Node 11 is at the upstream cross section of the canal (11) and Node 12 is at the downstream cross section of the canal (11).

As in the previous test case, mass conservation is verified at each junction of the channel network. Accordingly, the computed discharges for each junction of the channel network are shown in Table 1.18.

Table 1.18: Islam et al. (2005) test case, validation of mass conservation for each node of the channel network. Incoming discharges are considered positive and outflowing discharges are considered negative. The mass balance in the last column is rounded to the fourth decimal digit.

Junction	***Q*** (m^3s^{-1})				
	Canal 1	***Canal 2***	***Canal 8***		$\boldsymbol{\Delta Q}$
8	10.0000	10.0000	-20.0000		0
	Canal 3	***Canal 4***	***Canal 9***		$\boldsymbol{\Delta Q}$
9	10.0000	10.0000	-20.0000		0
	Canal 5	***Canal 6***	***Canal 7***	***Canal 10***	$\boldsymbol{\Delta Q}$
10	10.0000	10.0000	10.0000	-30.0000	0
	Canal 8	***Canal 9***	***Canal 11***	***Canal 12***	$\boldsymbol{\Delta Q}$
11	20.0000	20.0000	-10.2450	-29.7550	0
	Canal 10	***Canal 11***	***Canal 13***		$\boldsymbol{\Delta Q}$
12	30.0000	10.2450	-40.2450		0
	Canal 12	***Canal 13***	***Canal 14***		$\boldsymbol{\Delta Q}$
13	29.7550	40.2450	-70.0000		0

1.5 Conclusions

The presented numerical method was implemented within MATLAB. It can handle irregular cross-sections under the reasonable assumption of compact cross-section; all the geometrical properties of the cross sections and cells are pre-processed and saved in a look-up table in order to speed-up the simulation. The validation of the implemented numerical method both for steady and unsteady test cases provides satisfactory results in terms of accuracy when compared with the analytical solutions (MacDonald test cases, Flow over a bump test cases) or the results provided from other numerical scheme proposed in literature (Sen and Garg (2002) test case and Islam et al. (2005) test case). The numerical scheme solve a system of N_p equations (where N_p is the number of nodes used to discretize the domain), thanks to the possibility to replace the u_j^{n+1} from the momentum equation directly in the mass conservation equation. Accordingly, the system of N_p equation is solved using a Newton-type algorithm until convergence, the solution η_i^{n+1} is then used to compute the velocity u_j^{n+1} and proceeds forward to the next time step. Obviously, the implementation is not exempt from limitations which requires further investigation: a more in depth study of the computation of the Fu_j^n term in correspondence of a junction would be advisable. In the implemented numerical method in the cross-sections that enclose a junction when the Lagrangian trajectory cross a junction Fu_j^n is approximated as u_j^n. Moreover, to complete the model an infiltration source term in the conservation of mass should be introduced, based for instance on the Darcy law. On the other hand, an infiltration law requires more parameters which are difficult to retrieve (e.g., the permeability of the porous media, and of the channel bottom and the level of the groundwater table in time).

2 Numerical tests on the conceptual schemes adopted in the code for bridge modeling

This chapter is based on:
Farina, G., Pilotti, M., Bonomelli, R., Martínez-Aranda, S., García-Navarro, P., Modeling bridges in HEC-RAS 2D: comparison with flume experiments. Technical note under review *Journal of Hydraulic Engineering (ASCE)*

2.1 Introduction

As explained in Chapter 1, the implemented numerical code must be able to effectively compute the flow conditions in unsteady flow for a general layout of channels network used for water irrigation. We have already demonstrated the capability of the code to reproduce exact or numerical solution for steady and unsteady test cases. We have also underlined that a major component of this kind of code is represented by the modeling of hydraulic works used for discharge regulation and for reproducing the effects of bridges on the flow conditions. Both these structures are ubiquitous in irrigation networks and exert a strong influence on the flow conditions. Whereas the numerical schemes used for modeling gates and weirs are relatively well defined, bridge modeling represents a more complex area. This is largely due to the greater geometric variability of bridges, which spans from a simple deck crossing a channel without any interaction whatsoever to very complex, irregular multi-arch structures that deeply affect the flow for any stage of the flow. Moreover, several flow conditions are possible across a bridge (i.e., low flow, pressure flow and overtopping). Accordingly, there is not a standard for the conceptual equations to be used in the modeling. Finally, the actual implementation of the approach for general bridges layout is extremely complex. Accordingly, in the choice of the conceptual schemes to be implemented within our code we eventually decided to include into the code the stage-discharge curve pre-processed by the widely used software HEC-RAS for bridge modeling. Actually HEC-RAS is becoming a worldwide standard for 1D and 2D solution of SWE. It includes different schemes to compute the backwater effect caused by bridges of general layout and provides a detailed reference manual that can be used to understand the way these structures are modeled in the code. However, due to the complexity of the task and to the inevitable arbitrariness of several choices in the modeling process, we felt the importance of testing the actual capability of the adopted schemes in HEC-RAS to reproduce the measured flow field across physical models of bridges in laboratory conditions. For greater generality, we decided to make this test using HEC-RAS 2D, that uses the stage-discharge curves used in 1D simulation but implemented within a 2D grid of the flow field. This chapter presents the results obtained in this extensive and original set of comparisons, that eventually supported our decision of using the stage-discharge curves pre-processed by the widely used software HEC-RAS within our numerical code. To this purpose, the experimental results of flume experiments for bridges provided by the experimental tests by Ratia et al. (2014) were used. In literature, four different types of bridge representation in 2D numerical models were explored (Mckenna et al., 2023; Cea et al., 2022): 1) by mesh discretization (MD), which requires a refinement of the mesh grid around the piers and abutments of the bridge: in this case the pressurized flow regime is not considered and the typical size of the grid refinement around the bridge directly affects the time step, increasing the computational time; 2) by introducing a head loss (HL) as an additional source term in the governing equations (e.g., Ratia et al., 2014); 3) as an internal boundary condition (IBC) (Dazzi et al., 2020) where appropriate discharge formulas which describe the hydraulics of the bridge are imposed at cells boundary along a polyline representing the structure and 4) by the Preissmann slot, that can be extended to 2D SWE to solve the pressurized flow

(Maranzoni and Mignosa, 2018; Cea et al., 2022). Neither the first nor the fourth mode can account for the overflow condition. In this direction, the widely used SWE solver HEC-RAS 2D, was recently released (from version 6.0) with the option to lay out bridges inside a 2D flow area. The novel approach can be used for all flow regimes (low flow, pressure flow, overtopping in the possible combinations; Brunner, 2020). Although this approach relies on the curves for modeling bridges that are computed as in the 1D version of HEC-RAS, the performance of these procedures could be different when they are introduced in a 2D unstructured code, where there are complex problems of coupling with the surrounding cells. For instance, the 1D model relies on two additional user-defined cross sections placed upstream and downstream the bridge where the flow is fully expanded. This step is not present in the 2D model where it is dealt with by the surrounding grid. Moreover, the bridge curves used for unsteady flow are built in steady flow condition. Finally, the choice of a modeling method for bridge hydraulics and of the parameters involved in the computation is required, for which a default value is suggested by the program along with a possible range of variation. Although there is a considerable body of literature that can assist in the selection of the method and in the calibration (e.g., Bradley, 1978), it is sometimes difficult, even for the experienced user, to appreciate in advance the implication of the possible options (Bradley, 1978). HEC-RAS 2D is released along with a set of validation test cases (Brunner et al., 2020) and it is continually tested by comparison with the results of physical models and other SWE solvers to understand the performance of the model in challenging problems (e.g., Pilotti et al., 2020, Milanesi and Pilotti, 2021, Costabile et al., 2021), so contributing to improve its predictive effectiveness. However, until now no systematic test of the novel approach for bridge hydraulics in HEC-RAS 2D has been conducted in the literature. In this chapter a contribution to fill this gap is provided, using the experimental results of a physical model in a flume for fifteen different bridge geometries in steady flow experiments and eight bridge geometries in unsteady flow (Ratia et al., 2014). These two large datasets allow to test the performance of bridge modeling in HEC-RAS 2D for both, steady and unsteady conditions and provide insights on the practical consequences of the different options that can be selected for this task within the program.

2.2 Experimental test and physical model upscaling according to Froude similarity

The experimental results measured by Ratia et al. (2014) have been used in several numerical studies (e.g., Maranzoni and Mignosa, 2018; Cea and López-Núñez, 2021; Dazzi et al., 2020). The experiments were performed in a laboratory flume where the water level upstream and downstream of a bridge were measured for fifteen different geometries in steady flow experiments and for eight bridge geometries in unsteady flow (Ratia et al., 2014).

Steady flow experiments.
Fifteen different bridge geometries were tested by Ratia et al. (2014) in a 6 meter long rectangular flat flume. The rectangular cross-section is 0.24 m wide and 0.16 m high, built in methacrylate with a tested Manning coefficient n=0.011 s m$^{-1/3}$ (Martínez-Aranda et al., 2018). A schematic view of the experimental setup is shown in Figure 2.1, detailing the bridge location from the inlet reservoir, and the upstream and downstream measurement sections. During the steady experiments, water was continuously recirculated from a recovery deposit (downstream of the channel) to an inlet reservoir (upstream of the channel). During the experiments the discharge was measured using an inline flow-meter, and the upstream and downstream water depths were acquired manually once the flow reached the steady state. The final dataset comprises 207 data points obtained using different combinations of bridge geometry and downstream boundary

conditions.

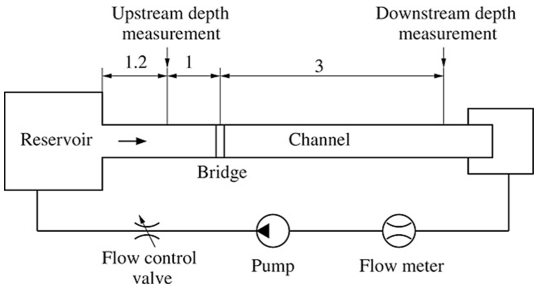

Figure 2.1: Experimental setup of the steady flow experiments, taken from Ratia et al. (2014).

The geometries of the 15 bridges are reported in Figure 2.2.

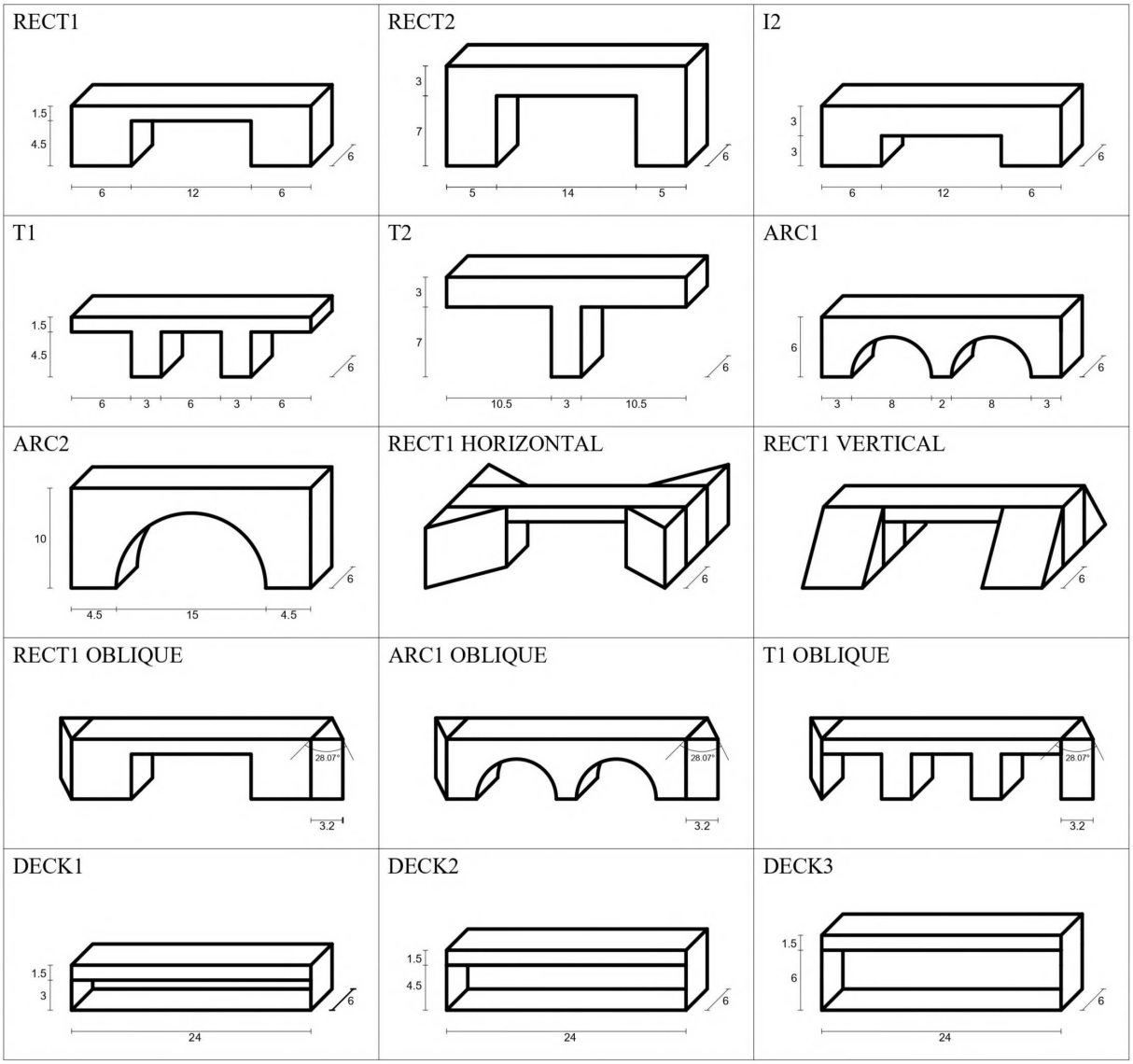

Figure 2.2: Geometry of the bridges used for the flume steady state experiments (all the length dimensions are expressed in centimeters).

Unsteady flow experiments.
A set of dam break experiments with different 8 bridge layouts (Figure 2.4) were also conducted by Ratia et al. (2014). This experimental setup (Figure 2.3) included a pneumatic gate that separated the upstream reservoir from the channel. The reservoir was filled to a certain level and the gate was opened quasi-instantaneously to reproduce a dam break wave. The channel was closed downstream. Two channel cross sections, one upstream and one downstream of the bridge were illuminated with a laser beam. These illuminated cross-sections were filmed, and the resulting movies were processed to obtain continuous measurements of the depth at the center of the sections. A total of 17 experiments were conducted and the upstream and downstream water level time series were measured for a time window of about 25s.

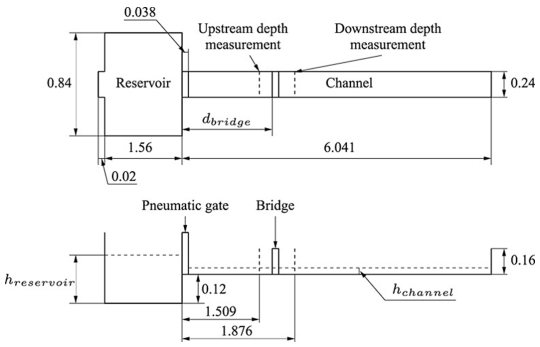

Figure 2.3: Experimental setup of the unsteady flow experiments, taken from Ratia et al. (2014).

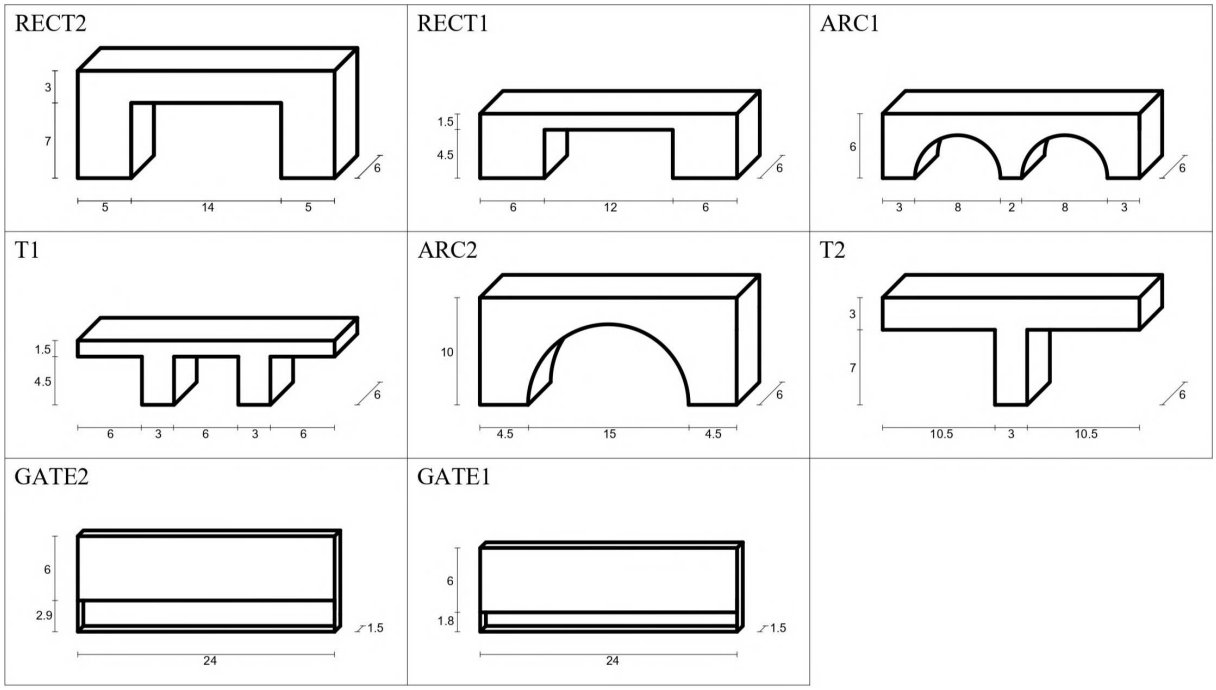

Figure 2.4: Geometry of the bridges used for the Dam Break experiments (all the length dimensions are in centimeters).

Physical model upscaling according to Froude similarity
The typical water depths upstream of the bridges in the rectangular cross-section of the flume used by Ratia et al. (2014) range between 0.014 m and 0.124 m. On the other hand, HEC-RAS 2D has been mainly applied to field-scale cases, and based on our experience, it is uncertain whether it can process input data related to small-scale experiments with discharges less than 1 L s^{-1}. To overcome this stumbling block, the following procedure has been adopted. Considering that 90% of the 207 experiments accomplished by Ratia et al. (2014) are in the range $R_e > 10^4$, $R_e \leq 5000$ for 3% of the cases only, it is adequate (e.g. Chanson, 2004) to rescale the experimental results respecting Froude similarity only:

$$\frac{v_m}{\sqrt{gL_m}} = \frac{v_p}{\sqrt{gL_p}} \tag{2.1}$$

where m refers to the HEC-RAS 2D model and p to the physical model, L is a characteristic length and v the velocity. By introducing the length scale $\lambda_l = L_m/L_p$ adopted for the model geometry, from Equation 2.1 one gets the velocity ratio: $\lambda_v = v_m/v_p = {\lambda_l}^{1/2}$, the time ratio $\lambda_t = t_m/t_p = {\lambda_l}^{1/2}$ and it is eventually possible to define the two scale ratios for the volumetric discharge and the Manning roughness coefficient: $\lambda_Q = Q_m/Q_p = {\lambda_l}^{5/2}$ and $\lambda_n = n_m/n_p = {\lambda_l}^{1/6}$. In conclusion, the geometry of the HEC-RAS 2D model was built assuming a length scale $\lambda_l = 20$ for the undistorted representation of the laboratory flume. The corresponding value of the ratios λ_t, λ_Q and λ_n were used to upscale the geometry and the boundary conditions to be used in all the HEC-RAS 2D simulations. For the final comparison with the experimental results, the HEC-RAS 2D results were downscaled to the physical model scale.

2.3 The Numerical Model: HEC-RAS 2D

HEC-RAS 2D solves the 2D SWE with a combination of finite-difference and finite-volume methods on a structured or unstructured mesh operating with different sets of equations (Brunner, 2020). The Eulerian SWE-EM solver was used for all the simulations because it is more conservative, especially in lab simulations where strict conservation of momentum is important (Brunner, 2020). In the following, HEC-RAS 6.3.1 was used and the analysis for each bridge was conducted using the Energy method approach for low flow conditions, due to its greater generality with respect to Yarnell and Momentum methods. On the other hand, both the Energy method and the Pressure-and-Weir method (Brunner, 2020) were tested for high flow conditions. All the numerical simulations were accomplished using the default value of the parameters (See Table 2.1). In order to detect the flow transition from low flow to pressure flow, two different criteria are available in HEC-RAS: the energy grade line at the upstream cross-section (default option) and the water surface elevation. Whereas the energy grade line is more conservative, the second option was selected in the numerical simulation. In the energy method the curves are computed using the standard step method between two sets of consecutive cross sections placed upstream and downstream of the bridge: the two cross-sections adjacent to the bridge can be modified to take into account the presence of ineffective flow areas and two additional cross sections are taken inside of the bridge structure. The Pressure-and-Weir method for high flow condition combines different equations to model pressure flow (both in free and submerged condition), weir flow and their possible combination. The obtained rating curves for bridges are then used in 2D modeling to compute the difference between upstream and downstream water surface elevation. This difference is then used to compute a force which is distributed to the cells along the bridge centerline, where a special version of the momentum equation is solved. The amount of force given to each cell is based on the percentage of the total flow passing through

that particular set of cells.

Table 2.1: Main default parameters for bridge modeling.

Parameter	***Default value***
Cc (-)	0.30
Ce (-)	0.50
Pressure Flow Criteria	Upstream Energy Grade Line
Number of points for free flow curve (-)	50
Number of submergence curve (-)	50
Number of points on each submerged curve (-)	20
Number of points for free flow curve (-)	50
Weir coefficient ($m^{1/2}$ s^{-1})	1.66
Max submergence (-)	0.98
Weir crest shape	Broad crested

2.4 Numerical test: Steady state tests

A Cartesian mesh was built in the numerical simulations, testing the sensitivity of different mesh sizes on the water depth measured upstream of the bridge. The flume walls were defined as solid walls. Eventually, a mesh with an average linear size of around 0.96 m (0.048 m at the physical model scale) was used, except in correspondence of the bridge where the mesh was adapted to satisfy the requirements for bridge modeling. Provided that the flow is subcritical in the upstream stretch of the flume, the measured constant discharge was used as the upstream boundary condition until convergence to the steady state solution; the depth measured at the end of the channel was used as the downstream boundary condition. The mesh and some of the bridges layout used for the orthogonal bridge set are shown in Figure 2.5.

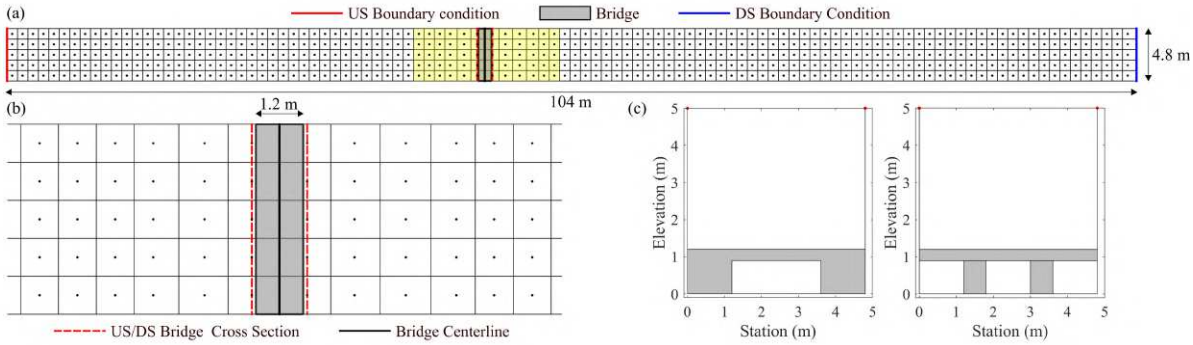

Figure 2.5: Mesh and bridge layout used for the orthogonal set of bridges. (a) Numerical mesh adopted for the simulation, highlighting the location of the bridge and the upstream/downstream boundary condition; (b) details of the mesh around the bridge with the location of the upstream and downstream bridge cross sections used for the computation of the 1D rating curves. (c) Example of two bridge layouts used in the simulation (RECT1 and T1).

In some cases, the geometry and the location of the bridges required a mesh refinement and the introduction of an unstructured grid (Figure 2.6); in particular, for the RECT1 VERTICAL and RECT1 HORIZONTAL cases (Figure 2.2), two fine Digital Elevation Model were built to reproduce the geometry of the vertical and the horizontal abutments; consequently, the mesh cells were aligned to the geometry of the abutments, also respecting the constraints imposed by

the other bridge modeling criteria in HEC-RAS. Furthermore, in the cases RECT1 OBLIQUE, ARC1 OBLIQUE, T1 OBLIQUE (Figure 2.2) the centerline of the bridge is oblique to the walls of the flume, and a mesh alignment was required.

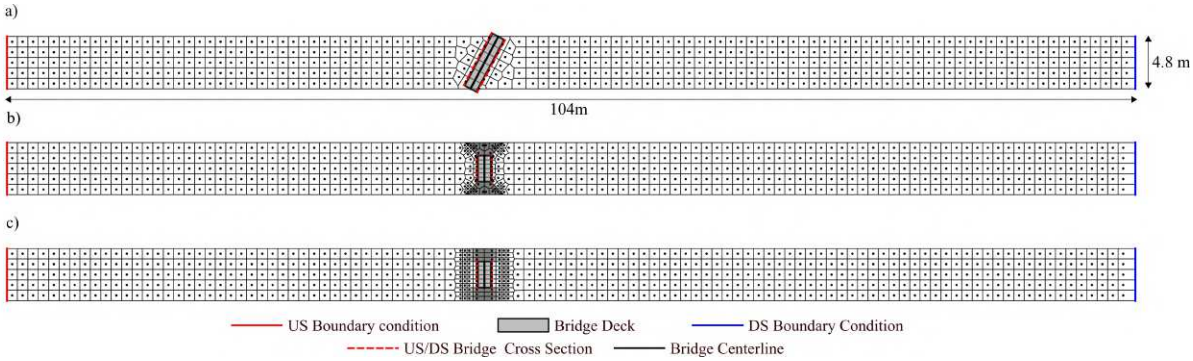

Figure 2.6: Mesh and bridge layout used for: a) oblique bridge set, b) RECT1 Horizontal bridge and c) RECT1 vertical bridge. The shaded areas with the gray scale in b) and c) represent the DTM used to reproduce the presence of the horizontal and vertical abutments

The computed water depths upstream for the different bridge geometries is shown in Figure 2.7, where the label on each Figure refers to the symbols adopted by Ratia et al. (2014). The white, yellow, and green shadings in Figure 2.7 represent the three possible ranges of occurrence of low-flow, pressure, and overtopping conditions at each bridge. The yellow and green shadings are intensified in the areas where the same hydraulic behavior occurs both in the experiments and in the numerical simulations. For the geometries with abutments (RECT1, RECT2, ARC2, see also Figure 2.2), the possibility offered by HEC-RAS to introduce ineffective flow areas near the abutments was tested. In this case, a systematic underestimation of the level upstream especially for low flow condition was observed. An improvement was observed by eliminating the ineffective flow areas as shown in the following where also the effect of the contraction (Cc) and expansion (Ce) energy coefficients is presented. To quantify the matching between the observed data and the numerical results obtained using HEC-RAS 2D for each bridge, the Mean Absolute Percentage Error (MAPE) is computed and shown in Figure 2.7. The MAPE is defined as follows:

$$MAPE = 100 \cdot \frac{1}{N} \sum_{i=1}^{N} \frac{\left| h_i^{HR} - h_i^{EXP} \right|}{h_i^{EXP}} \tag{2.2}$$

where N is the total number of experimental points for each bridge geometry, h_i^{HR} is the upstream water depth computed using HEC-RAS 2D and h_i^{EXP} is the upstream water depth measured during the steady experiments for each bridge.

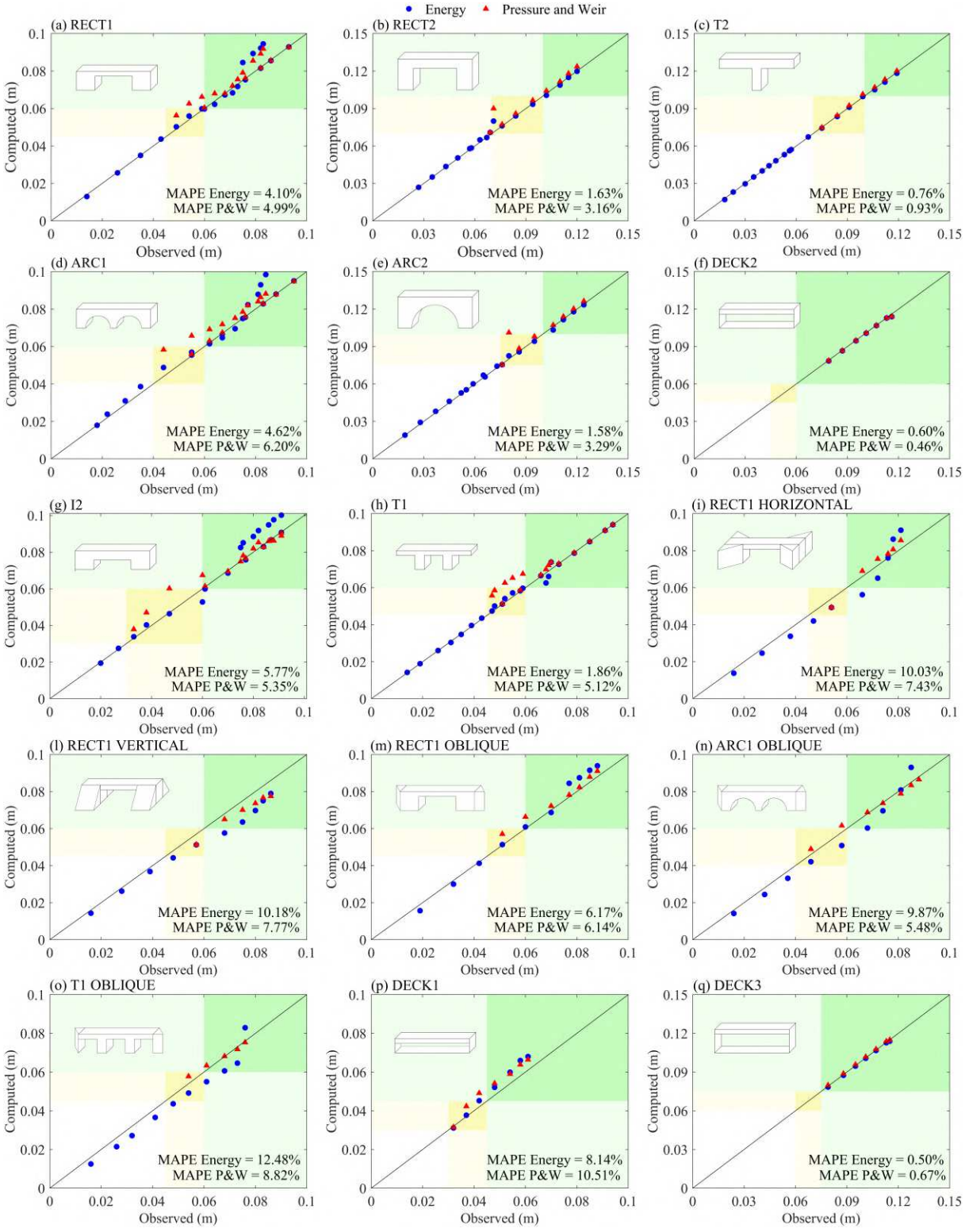

Figure 2.7: Comparison between the observed data from the experiments and the results obtained with the Energy and Pressure-and-Weir methods, using the set of default parameters. See the text for the meaning of the shadings. Note that in the free-surface range the results of the two methods are identical and the red triangles are not shown.

2.5 Numerical test: Dam Break tests

Stoker-like dam breaks were simulated using a Cartesian numerical mesh (Figure 2.8) for the reservoir and the channel, with an average linear size of around 0.40 m (0.02 m at the physical model scale), except in correspondence of the bridge where the mesh was adapted to satisfy the requirements for bridge modeling; a different water level in the reservoir and in the flume was imposed as initial condition. The flume walls were defined as solid walls.

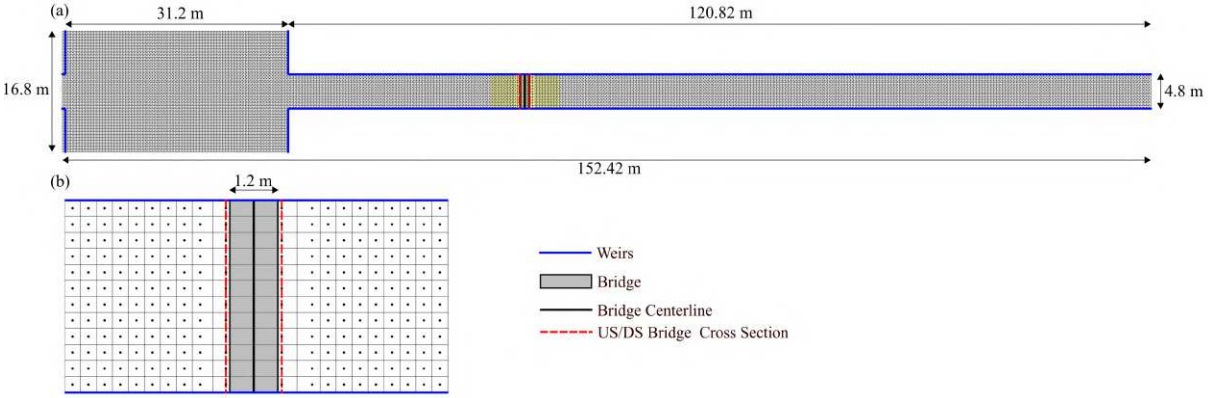

Figure 2.8: Example of mesh and bridge layout used for the dam break test for RECT1 case. (a) Numerical mesh adopted for the simulation, highlighting the location of the bridge; (b) details of the mesh around the bridge with the location of the upstream and downstream bridge cross sections used for the computation of the 1D rating curves. Similar layouts characterize the other test cases.

The results for all the considered cases are shown in Figure 2.9, where the label on each Figure refers to the symbols adopted by Ratia et al. (2014).

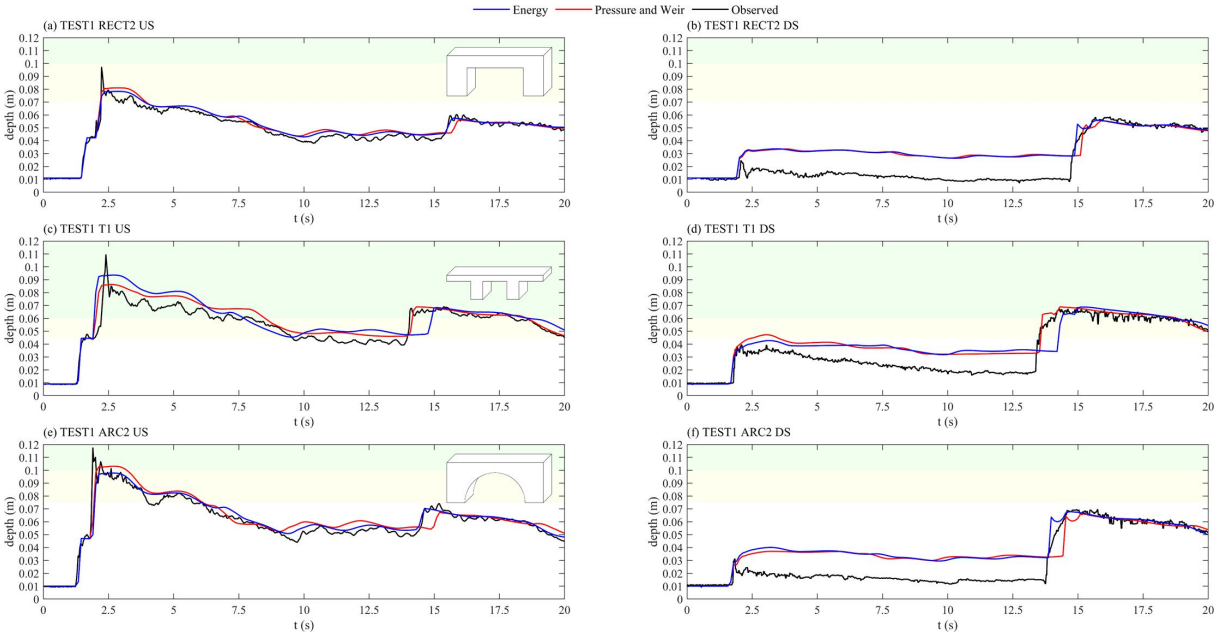

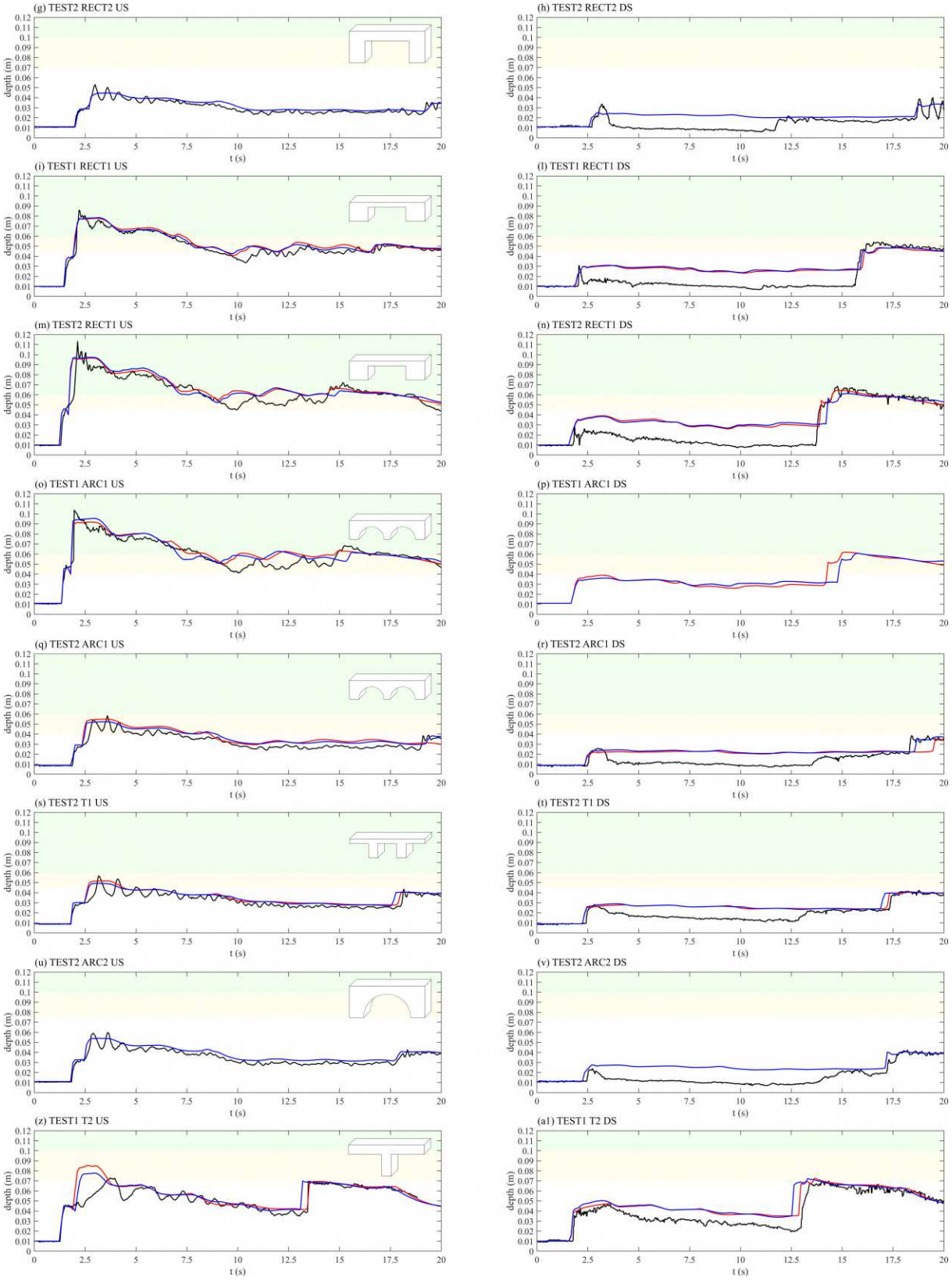
(g) TEST2 RECT2 US
(h) TEST2 RECT2 DS
(i) TEST1 RECT1 US
(l) TEST1 RECT1 DS
(m) TEST2 RECT1 US
(n) TEST2 RECT1 DS
(o) TEST1 ARC1 US
(p) TEST1 ARC1 DS
(q) TEST2 ARC1 US
(r) TEST2 ARC1 DS
(s) TEST2 T1 US
(t) TEST2 T1 DS
(u) TEST2 ARC2 US
(v) TEST2 ARC2 DS
(z) TEST1 T2 US
(a1) TEST1 T2 DS
depth (m)
t (s)

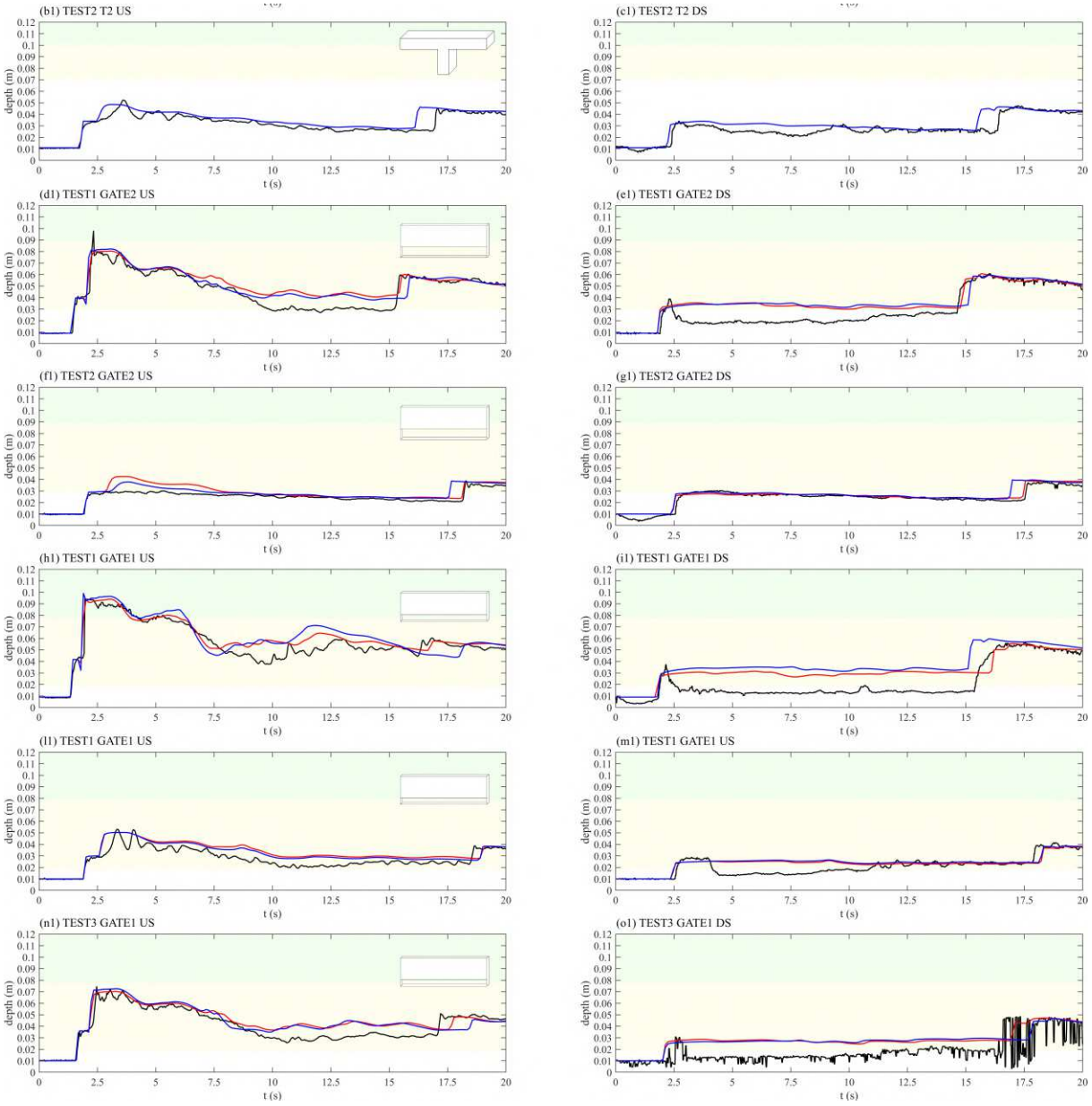

Figure 2.9: Comparison of the results for Dam Break experiments obtained with HEC-RAS 2D, using Energy and Pressure and Weir methods for bridge modeling. The results show the water depth upstream (left) and downstream (right) of the bridge.

2.6 Discussion and Conclusions

The results presented in this chapter confirm that the choice of using the stage-discharge curves computed by HEC-RAS for bridge modeling in the implemented code is well grounded. The tests accomplished using HEC-RAS 2D, that adpots the same stage-discharge curves computed in HEC-RAS 1D, show the capability of this code of reproducing the measured water elevation upstream of many different bridge geometries, both in steady and unsteady case. The obtained results in steady-state show that the backwater profiles are very well-matched for almost all tested cases. Using the default set of coefficients, when the bridge is orthogonal to the main flow and the abutments are vertical, the match between computed and measured water depth

upstream is excellent for low-flow conditions. For pressure conditions and overtopping conditions, the comparison slightly deteriorates. Table 2.2 shows the average error for the three flow conditions. Bridges orthogonal to the flow, oblique and with sloping abutments are considered separately in the table for the Energy method and for the Pressure-and-Weir method.

Table 2.2: Mean absolute percentage error for the different categories of bridge under different flow conditions in steady flow. (1) Energy Method, (2) Pressure-and-Weir Method.

	Bridge type					
	Orthogonal		***Oblique***		***Sloping Abutments***	
Flow condition	***MAPE (1)***	***MAPE (2)***	***MAPE (1)***	***MAPE (2)***	***MAPE (1)***	***MAPE (2)***
Low Flow	1.9%	1.9%	12.6%	12.6%	9.4%	9.4%
Pressure Flow	2.8%	11.4%	6.9%	8.5%	9.3%	9.3%
Overtopping	3.7%	2.6%	8.4%	2.0%	10.8%	5.8%

In general, one can observe a better performance of the Energy method in steady test cases with respect to the Pressure-and-Weir method. The mean MAPE obtained pooling all the cases is 4.60% for the energy method and 4.91% or the Pressure-and-Weir. On average, in the worst case, one can expect a maximum error of the upstream water elevation below 10%, which is very good for practical field applications. Some of the bridges in Figure 2.7 exert a flow contraction caused by their geometry. Accordingly, different expansion and contraction coefficients for energy loss were tested. As reported in the hydraulic reference manual (Brunner, 2020) for 1D bridge modeling, the possible range of variation of the contraction and expansion loss coefficient is between 0 and 1 as an upper value for abrupt transition. Figure 2.10 shows the variation range of the results obtained for the bridges in Figure 2.7a, 2.7b, and 2.7e, by varying the contraction and expansion loss coefficients within the suggested upper and lower bounds. Although the variation of the coefficients can improve the performance, it seems difficult to find out how and when to depart from the default values. Accordingly, also considering the limited error, it seems that using the default value of the parameters can be a priori suggested for all cases.

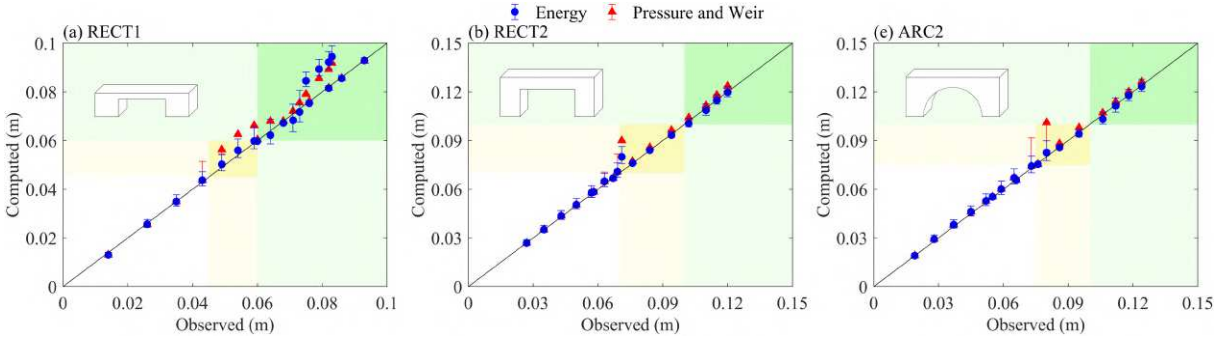

Figure 2.10: Sensitivity of the bridge headwater with different contraction ($0.1 < Cc < 0.6$) and expansion ($0.3 < Ce < 0.8$) loss-coefficients for cases RECT1, RECT2, and ARC2 in Figure 2.7

On the other hand, the combination of the ineffective flow areas (which leads to an underestimation of the upstream water surface for the bridge geometry RECT1, RECT2 and ARC2 when the default values for Cc and Ce are used) and the contraction and expansion loss coefficients which required calibration was investigated. The ineffective flow areas were located

upstream and downstream covering the area occupied by the abutments up to the high chord of the bridge deck. Acting on the values of Cc and Ce a good match with the observed values could be achieved, as shown in Figure 2.11 .

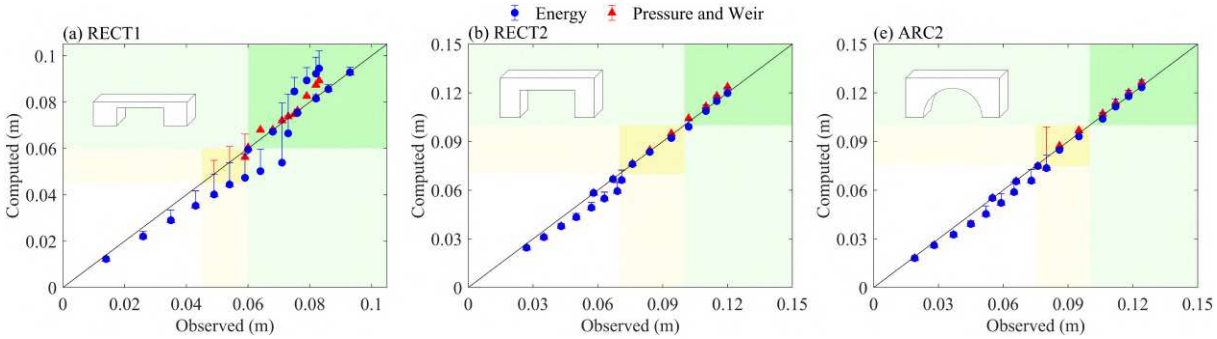

Figure 2.11: Sensitivity of the bridge headwater using ineffective flow area for the cases RECT1, RECT2, and ARC2 in Figure 2.7. The solid dots and triangles represent the results obtained using the ineffective flow areas and the default values for Cc and Ce, whereas the ticks represent the range of improvement obtained acting on Cc and Ce to match the observation (RECT1 Cc=0.8 and Ce=1, RECT2 Cc=0.6 and Ce=0.8, ARC2 Cc=0.6 and Ce=0.8).

Considering pressure flow in Figure 2.7a, 2.7b (RECT1 and RECT2), the Pressure-and-Weir formulation slightly overestimate the upstream water level but on the other hand, the upstream water level is well captured in Fig. 2.7c (T2). Accordingly, the effects of the discharge coefficients for submerged inlet (Cd) and for submerged inlet and outlet (C) adopted in the Pressure-and-Weir method have been explored. In the default procedure Cd is computed as function of the degree of submergence upstream, according to a monotonically growing curve where the min and max values for Cd are respectively 0.27 and 0.5. On the other hand, if a value is defined by the user, Cd remains equal to the user's value for any degree of submergence upstream. Considering that the depth is overestimated, a sensitivity for the maximum value of Cd has been performed. The obtained results show that in the RECT1 and RECT2 cases there are limited improvement if $Cd = 0.5$ is used, without worsening the results for case T2. Finally, the results in unsteady flow confirm the very good reproduction of the water depth upstream of the bridge. However, as one could expect from the hydrostatic nature of SWE, the impulsive elevation peak is almost always underrated, with a maximum error in the order of 20%. Furthermore, the simulations show that the solver does not reproduce the supercritical behavior immediately downstream of the bridge, where the water elevation is overrated until the arrival of the wave reflected from the downstream end of the channel. Note that in the steady-state experiments, the elevation downstream of the bridge is measured only at the end of the flume, far from the area affected by the bridge contraction. Accordingly, the same problem could be present also in steady state. Whereas the correct reproduction of the behavior upstream of the bridge is fundamental for the flood extension, the flow field immediately downstream of the bridge contraction is important when local erosion is a concern. Therefore, it seems that further model validations are required for the application of the HEC-RAS model to predict scour around and downstream of bridge piers. It is difficult to overstate the practical importance of bridge modeling in the overall framework of flood modeling, considering the role played by bridges on floodplain inundation. The presented comparison of experimental data with computed results ranged between steady-state and dam break flows. The main conclusions are as follows:

- Under the assumption that the domain is correctly gridded in correspondence of the bridge, the elevation upstream of the tested bridges is very well reproduced when the bridge is orthogonal to the flow direction, both in steady and unsteady state. The quality of the solution slightly deteriorates when the axis of the bridge is oblique to the channel direction or in the presence of sloping abutments. Here it's important to underline that these bridge layouts introduce a certain degree of subjectivity in all the modeling setup and that the methodology to deal with skewed bridges is still in evolution in HEC-RAS versions.
- In general in steady test cases, the Energy method seems to perform better than the Pressure -and-Weir method. The use of the default set of coefficients and of the standard value of the contraction and expansion coefficient provides a maximum error that, in the different flow conditions and for the different bridge layouts, is documented in Table 2.2. A back-of-the-envelope conservative evaluation of the maximum error is below 15%
- The tests in unsteady flow, where the elevation is measured also downstream and close to the bridge, confirm the very good performance upstream of the bridge and show that the downstream supercritical stretch is not always correctly captured.

3 Validation of internal boundary conditions

3.1 Introduction

In the previous chapters we dealt with two fundamental issues in the implementation of the solver: the first regards bridges modeling, that we validated considering the flume experiments proposed by Ratia et al. (2014). Another fundamental issue for an irrigation system is the correct modeling of the hydraulic works that make water distribution possible. Actually, the best management of an irrigation channel network requires the knowledge of the delivered discharge along the channels and in the secondary channels, in order to guarantee the correct amount of water at each user and correct reduction in case of dry periods. To deliver the correct water amount to the secondary channel two structures are tipically combined: gate and weir or gate and flume schematized in Figure 3.1. Usually, this type of structure is not submerged from downstream and the stage-discharge curve is well-known (e.g., De Marchi, 1977). To regulate the gate at each water withdrawal point, the operator acts on the basis of the contemporary level in the main channel and in the secondary channel: in order to guarantee the correct amount of discharge transferred from the main channel to the secondary channel, the value of the water depth upstream the weir or the flume (modellatore a risalto), is related to the discharge by means of well-known rating curves, that depend on the type of gauging structure.

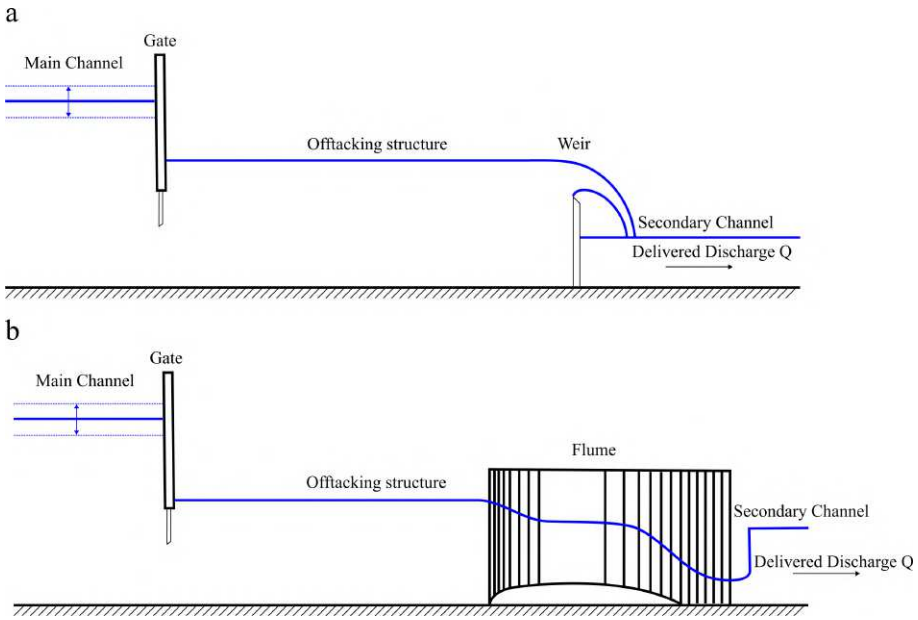

Figure 3.1: Schematization of differnt offtaking structures located along an irrigation channel network, a) Gate-Weir combination and b) Gate-Flume combination.

On the other hand, along each channel other structure can be present: for instance, to increase the specific energy in the main channel and, consequently, improving the delivery of the water at the withdrawal points during dry periods, a suitable backwater effect is caused by the presence of a weir or other specific obstructions. An example of this type of structure is shown in Figure 3.2.

Figure 3.2: Naviglio Grande Pallavicino (Consorzio Irrigazioni Cremonesi) example of a weir structure. A gate is present upstream the weir, on the left of the picture.

Another structure frequently placed along an irrigation channel network is a gate, whose regulation exerts a backwater effect that can be used for different purposes. In particular, gate structure could be located at the inlet of the main channel of an irrigation channel network in order to derive the correct value of discharge from the main river (Figure 3.3a) or in correspondence of a junction to divert the required discharge to the different branches (Figure 3.3b).

Figure 3.3: a) Vacchelli Canal (Consorzio Irrigazioni Cremonesi), inlet structure, picture taken from downstream. b) Canobbia Nuova Canal (Consorzio Irrigazioni Cremonesi) example of a gate at a junction. Note that the gate is submerged from downstream.

Finally, as already underlined in the previous Chapter, the presence of bridges along the channels should be considered in irrigation network modeling in order to capture the backwater effects produced by these structures and their effects, e.g., on the regulation of the gates and on the actual discharge withdrawals at the inlet of the irrigation channels. In this chapter, the governing equations of these structures are presented along with their implementation and validation.

Weirs and Gates are validated for comparison with the results obtained using HEC-RAS 1D for some simplified cases.

3.2 Bridges, Weirs and Gates validation

Ratia et al., (2014) flume experiments

In Chapter 2 we positively tested the accuracy of the conceptual schemes adopted in HEC-RAS to deal with bridges under different conditions. Here we test the actual implementation of these conceptual schemes within the implemented solver. To test the performance of the implemented numerical model to reproduce the effect of a bridge interacting with the flow some of the flume experiences presented in Ratia et al. (2014) have been tested. We focused on the steady state experiments presented in the paper. As explained in Chapter 2, the laboratory setup consists of a 6 m long rectangular channel 24 cm wide and 16 cm high, the estimated Manning's coefficient is n = 0.011 s $m^{-1/3}$. The water level was measured in two points located upstream and downstream and the measured discharge is provided. A full description along with the sketch of the experiments is reported in Chapter 2. To compute the rating curve of a bridge different types of solutions could be adopted: Ratia et al. (2014) proposed an energy loss through the bridge computed as Borda-Carnot energy loss; on the other hand, one of the methodologies proposed in HEC-RAS (Brunner, 2020) is to compute the rating curve of a bridge using an energy balance in order to accounts for the energy loss due to contraction and expansion of the flow through the bridge opening. Another way is using a pressure-and-weir approach coupled with an energy balance for low flow (Brunner, 2020). In the following, for the numerical tests, the rating curves of the bridges have been computed as:

- if the water surface upstream is less than the level of the low chord ($Z_{d,low}$) of the bridge deck the rating curve is computed on the basis of an energy balance accounting for contraction and expansion energy loss through the bridge.
- if the water surface is between the maximum elevation of the low chord ($Z_{d,low}$) and the elevation of the high chord of the deck ($Z_{d,top}$) according to Dazzi et al. (2020) two flow conditions are possible: the free flow condition, described as

$$Q = A_b C_d \sqrt{2g\big(H_u - 0.5\big(Z_{d,low} - z_{bottom}\big)\big)} \tag{3.1}$$

  and for the submerged flow condition:

$$Q = A_b C_Q \sqrt{2g(H_u - \eta_v)} \tag{3.2}$$

  Where A_b is the area of the bridge opening, H_u is the total head upstream, z_{bottom} is the minimum bottom elevation, C_d and C_q are discharge coefficients, respectively with a typical value of 0.5 and 0.8 (Bradley, 1978).
- if the water surface is above the high chord of the deck, the bridge is overtopped and Equation (3.1) or Equation (3.2), depending on the flow condition, are complemented using the weir equation which takes into account the flow on the deck:

$$Q = \phi_b C_w L_b \sqrt{2g}(H_u - Z_{top})^{3/2} \tag{3.3}$$

  where C_w is a weir coefficient, L_b is the bridge width normal to flow and ϕ_b is a flow reduction factor accounting for submergence.

In order to reproduce the steady state experimental test conducted by Ratia et al. (2014) a numerical model of the 5.2 m flume was built using 104 cross sections. The downstream depth measurement for each steady state experimental point was used as the downstream boundary condition coupled with the corresponding constant discharge for the upstream boundary condition. The simulations were run until convergence to the steady state. Using the same symbology adopted by Ratia et al. (2014) the validation was accomplished using the bridges RECT2, T2 and ARC2. The obtained results are shown in Figure 3.4 with the corresponding ones obtained with HEC-RAS 1D with the steady-state solver. The accuracy of the results is measured using the Mean Absolute Percentage Error (MAPE)

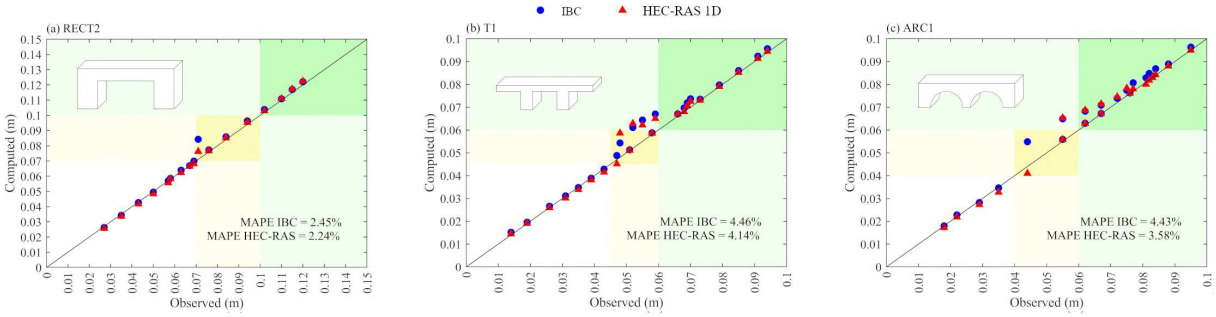

Figure 3.4: Comparison between the observed data from the experiments and the results obtained with the implemented solver and using HEC-RAS 1D.

Weir

The presence of weirs in an irrigation channel network is common, and they are used to measure flow discharge delivered to secondary channel. Sometimes, weir-like structures (see, e.g., Figure 3.2) are introduced along the main channel during dry periods, to cause a backwater profile which increases the efficiency of the lateral structures (e.g., gates) used to deliver discharge on the secondary channel. The equation describing the flow through a weir can be written as (Ghetti, 1998):

$$Q = \Phi_w \mu L_w \sqrt{2g} \left(\eta - p + \frac{u^2}{2g} \right)^{3/2} \tag{3.4}$$

where L_w is the length of the weir, μ is the discharge coefficient and p is the weir crest elevation. Φ_w is the flow reduction factor, a function of the submergence of the weir introduced in order to account for the effect of possible back-water effect from downstream (e.g., Figure 3.5).

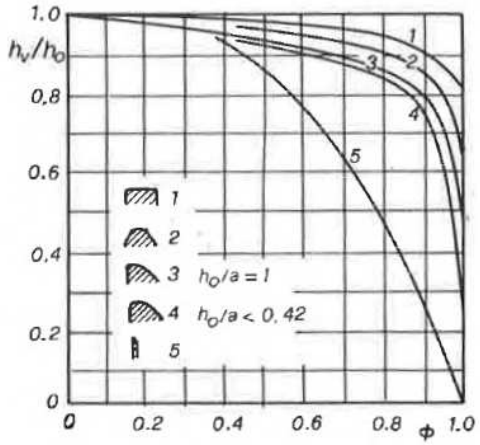

Figure 3.5: Discharge reduction function to account for submergence (Ghetti, 1998), h_0 and h_v are respectively the water depth downstream and upstream the weir measured from the crest of the weir, a is the crest height of the weir.

Also in this case, to validate the implementation of the presented internal boundary condition a comparison with the software HEC-RAS 1D has been made. A 1 km long rectangular channel with a mean slope of the bottom $S_0 = 0.001$ and a weir placed 500 m far from the inlet of the channel has been considered (see Table 3.1) for details of the test case and Figure 3.6 for the inflowing discharge). In order to test the implementation of the weir, an unsteady discharge hydrograph is imposed upstream and, at the same time, the water elevation downstream is varied to consider the development of a submerged condition during the simulation. Overall, although pretty unlikely, the test aims to provide a rather strict verification of the quality of the implementation within the code.

Table 3.1: Summary of the test case.

Length (km)	***Bed width (m)***	***Bed slope (-)***	***n*** $(s\ m^{-1/3})$	μ **(-)**	$\mathbf{p_{weir}}$ **(m)**	**dx (m)**
1	20	0.001	0.04	0.385	1.505	5

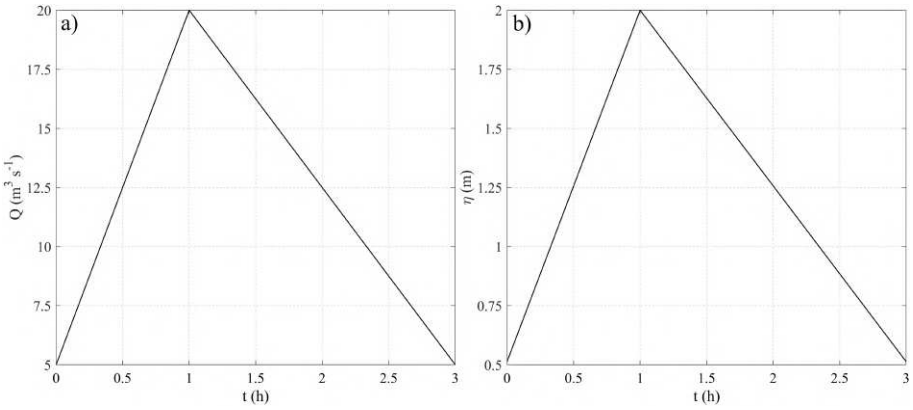

Figure 3.6: a) Upstream inflowing hydrograph; b) Downstream water level hydrograph.

The comparison of the computed results with the ones provided by HEC-RAS 1D are reported

in Figure 3.7 for the node upstream and downstream the weir along with the flow reduction factor Φ_w where, to account for the submergence of the weir, in this specific case the curve (1) presented in Figure 3.5 was used.

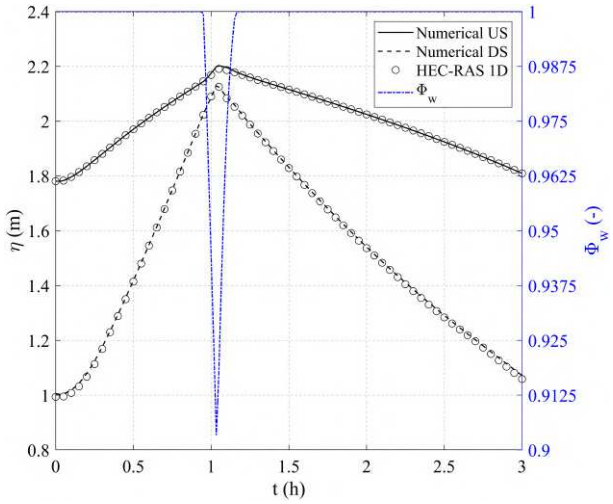

Figure 3.7: Computed free surface elevation for the nodes upstream and downstream of the weir and the computed flow reduction factor, to be read on the right axis.

As shown in Figure 3.7 there is a very good match between the numerical results and the results obtained using HEC-RAS 1D, confirming the correct implementation of this specific internal boundary condition. The major differences for the free surface elevation upstream are in correspondence of the higher level of submergence, because HEC-RAS uses a different curve to compute the flow reduction factor (for details see Brunner, 2020).

Gate

The outflow through a gate is defined free when the supercritical jet downstream is not influenced by the tailwater downstream (Figure 3.8a).

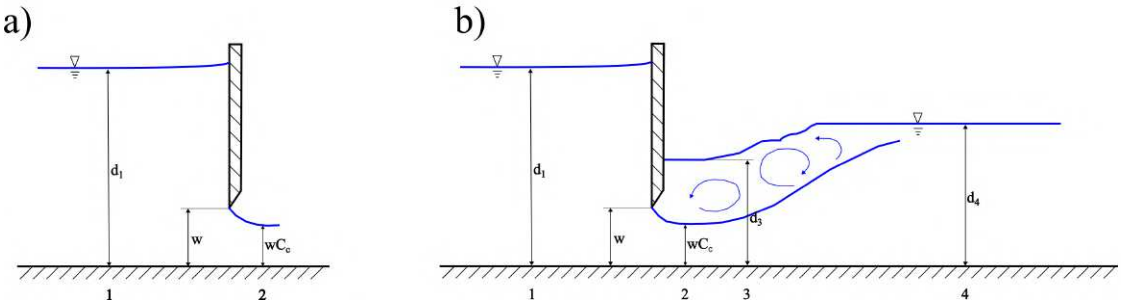

Figure 3.8: a) Free flow from a vertical sluice gate, b) Drowned flow from a vertical sluice gate.

Provided that the contraction coefficient (C_c) is known, the outflowing discharge through the gate is computed by means of the energy equation as follows:

$$Q = \sqrt{\frac{2g(d_1 - wC_c)}{\left(\frac{1}{A_2^2} - \frac{1}{A_1^2}\right)}} \tag{3.5}$$

where d_1 is the water depth measured at cross section 1, w is the gate opening, A_1 and A_2 are respectively the wetted area for the cross section 1 and in the vena-contracta at cross section 2. On the other hand, when the water depth downstream of the gate is greater than the conjugate depth of wC_c the gate outflow becomes "drowned", as shown in Figure 3.8b. Following the methodology proposed by Henderson (1966), it is assumed that the flow in cross section 3 is "divided" in a part of the cross section that is occupied by moving water (wC_c) and a part where water is recirculating and, in average terms, stagnant (above wC_c). Assuming that the energy loss between cross section 1 and cross section 2 is negligible with respect to the energy loss between section 2 and section 4, it is possible to write an energy balance between cross section 1 and cross section 2:

$$Q = \sqrt{\frac{2g(d_1 - d_3)}{\left(\frac{1}{A_2^2} - \frac{1}{A_1^2}\right)}} \tag{3.6}$$

where d_3 is not known and A_2 is computed considering the vena-contracta only; d_3 can be computed using the momentum equation to balance the total thrust between cross section 4 and cross section 2 as follows:

$$gA_4Y_{g,4} + \beta A_4 u_4^2 = gA_3Y_{g,3} + \beta\frac{Q^2}{wCcB_g} \tag{3.7}$$

where, Y_g is the the vertical distance of the centroid from the free surface of the water, and β is the momentum flux correction factor and B_g is the width of the gate opening. Although free flow can happens in real-world application for small opening of the gate, it is pretty unusual in field applications and only the submerged condition has been implemented in the numerical model. Actually, in our experience this type of condition is typical in lowland irrigation channel network characterized by small bottom slope. To evaluate the performance of the described internal boundary condition a comparison with the software HEC-RAS 1D in unsteady conditions was performed considering a 1 km long rectangular channel with a mean slope of the bottom $S_0 = 0.001$ and a gate placed 500 m far from the inlet of the channel (see Table 3.2 for details of the test case and Figure 3.9 for the inflowing discharge along with the time series of the gate opening). For the downstream boundary condition the normal depth was imposed at the end of the channel.

Table 3.2: Summary of the test case.

Length (km)	***Bed width (m)***	***Bed slope (-)***	***n*** ***(s m$^{-1/3}$)***	*Cc* **(-)**	**dx (m)**
1	20	0.001	0.04	0.611	5

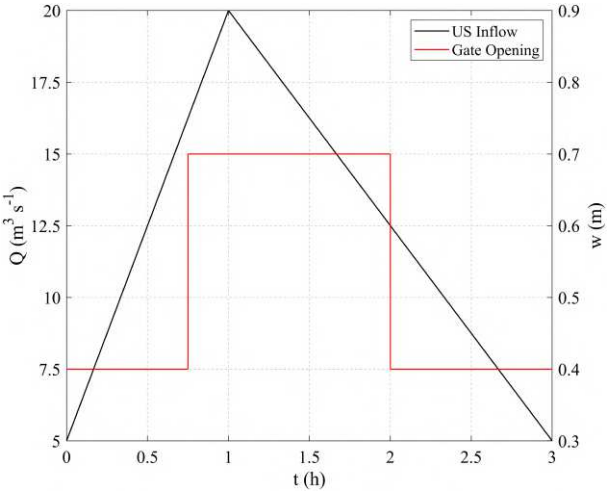

Figure 3.9: Upstream inflowing hydrograph and time series of the gate opening.

The comparison of the obtained results compared with HEC-RAS 1D are reported in Figure 3.10 for the node upstream and downstream the gate. In order to explain the slight observed differences it is here worth mentioning that in HEC-RAS this type of structure is solved using a different equation based on orifice equation, and the default value of the discharge coefficient suggested for orifice flow is C=0.8 (Brunner, 2016), although a variation between 0.7 and 0.9 is accepted for fully submerged bridges. Acting on this parameter a better match between the numerical results could be achieved: the red continuous line shown the HEC-RAS results when the discharge coefficient is C=0.9.

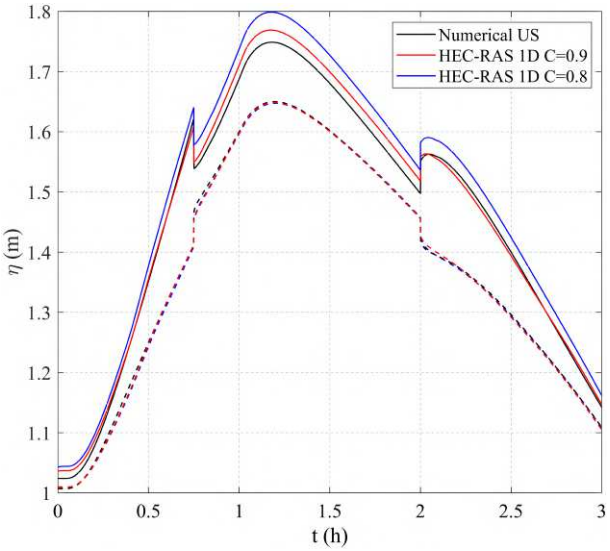

Figure 3.10: Computed free surface elevation for the nodes upstream and downstream the gate. The dashed lines represent the water surface elevation downstream.

3.3 Conclusions

A fundamental aspect required by the modeling of an irrigation channel network is the implementation of internal boundary condition that describes the hydraulic of structures along the irrigation network. An irrigation channel network is managed by means of hydraulic structures:

gates are regulated in order to guarantee the correct intake discharge from the main rivers into the irrigation network; secondary channels are fed by means of gates, weirs and flumes used to regulate the outflow from the main channel. Moreover the presence of bridges that cross the irrigation channel should be integrated in the model when they interact with the flow. Accordingly a set of internal boundary condition has been introduced in the implemented mathematical model that can be used to model weirs, gate and bridges. Regarding the first two types of structures the presented equations are directly implemented in the model. On the other hand, as far as the implementation of bridges is concerned, that are characterized by complex geometry, their stage discharge curve (described for instance by Equation 3.1, 3.2, 3.3) are computed for discrete values of water surface elevation upstream (η_{us}) and downstream (η_v); these curves are then interpolated in a surface $f(\eta_{us},\eta_v)$ and are used in the algorithm to compute the discharge as function of the water surface elevation upstream and downstream. The choice to use a surface built starting from a set of discharge curves was guided by the idea of using the curves already computed with other software (e.g. HEC-RAS) due to the potentially heterogeneity of bridge geometries. The implemented Internal Boundary Condition related to bridges has been validated using the data set provided by Ratia et al. (2014). In this case, the Mean Absolute Percentage Error (MAPE) is less than 5% pooling all the three case, a value which is comparable with the one as obtained using commercial software. Regarding weirs and gates, their validation has been done comparing the results obtained with the implemented solver and HEC-RAS 1D. The results obtained for weirs are comparable with the ones obtained with HEC-RAS. Some difference can be found for high submerged condition because HEC-RAS uses different formulation of Φ_w to account the effect of submergence caused by the tailwater.

4 Terrain modification to DEM derived from LiDAR surveys

This chapter is based on:
Farina, G., Pilotti, M., Milanesi, L. and Valerio G., (2025). A simple method for the enhancement of river bathymetry in LiDAR DEM, *Environmental Modelling & Software*, Volume 186, March 2025, 106354

4.1 Introduction

Another considerable stumbling block in the implementation of the hydraulic model of an irrigation network is related to the description of the topology of the network and, even more, to the description of the cross sections of different branches that make up the network. Whereas the most reliable approach is certainly based on direct land survey, in most situation this piece of information is only partially available. Considering the growing availability of LiDAR survey of wide regions, we believe it is worthwhile to explore the possibility of acquiring this information from the ground signal that can be obtained by LiDAR survey. The area scope (with linear dimension in the order of dozens of km) and the resolution of LiDAR (often in the order of 0.1 m), coupled with the vertical accuracy that is currently in the order of 0.1-0.15 m, ideally make this source of information perfect for the purpose. On such a wide representation of the studied region it is easily possible to detect and trace the topologic connection of the different branches and the high resolution make it possible to single out channels as small as ditches. Moreover, it is theoretically possible to obtain cross-section profiles from a LiDAR survey. However, all that glitters is not gold and, after a preliminary evaluation, we eventually decided to explore better the limitations and the possible strategies to be applied. In particular, it turned out that, whereas the LiDAR survey can be effectively used to identify the topology of the irrigation network and also the average slope along sufficiently long stretches of the canals by measuring the relief of the surrounding ground, it is much more difficult to obtain accurate cross-sections of the canals by intersecting the vertical profile of the LiDAR surface, mostly due to water presence and vegetation sheltering. On the other hand it turned out that the topic is of great interest also in the more general area of flood propagation modeling with 2D SWE solvers. Actually, an accurate bathymetric description of the floodplain, the watercourse, and the transversal hydraulic structures are fundamental requirements for the careful reproduction for simulation using the SWE (e.g., Bures et al., 2019; Pilotti, 2016), and the preparation of a good bathymetry is often the most time-consuming effort in the whole modeling process. The approach currently used for producing high resolution DEM is Light Detection and Ranging, (LiDAR) that, along watercourses, is hindered by the presence of vegetation and water (Mazzoleni et al., 2020). In order to limit the hiding effect of vegetation on the underlying terrain, aerial surveys should be accomplished in non-vegetative period and ground reflection from the first signal must be singled out using filtering algorithms. However, LiDAR sensors typically used for fluvial application operate with near-infrared radiation mostly absorbed by the water column (Kinzel et al., 2013). Accordingly, the survey should be carried out during low-flow periods along with the preferential use of green light laser, capable of penetrating shallow clear water. Finally, also steep banks of artificial canals could hide the actual bottom of the LiDAR beam. Accordingly, in spite of all the precautions, ordinary LiDAR can still misrepresent the bathymetry of watercourses, and a naïve use of LiDAR data could show up unrealistically low watercourses conveyance. In literature, several methods are proposed to tackle the problem of river bathymetry enhancement, sometimes requiring complex post-processing with proprietary codes. Mainly, there are two possibilities, which rely on the availability of surveyed cross section (CS_{sur}, in the following) whose optimal location for river modelling purposes can be selected

according to different criteria that have been proposed in the literature (e.g., Castellarin et al., 2009; Conner & Tonina, 2014). If a set of CS_{sur} is available, the standard solution to LiDAR enhancement consists in creating a DEM of the river bed by interpolating CS_{sur} and substituting it into the original DEM. In literature, different methods for the interpolation of surveyed cross sections were proposed (e.g., Caviedes-Voullième et al., 2014; Dysarz, 2018; Lai et al., 2018; Merwade et al., 2008). The interpolation of the cross sections along the river centerline can also be effectively implemented in 2D hydraulic modelling software (e.g. Brunner,2024a that we successfully used in many cases, e.g. Pilotti et al., 2020; Milanesi and Pilotti, 2021) to assist the user in the bathymetry reconstruction, reducing the number of operations, time and potential errors. Although these algorithms in many situations can be very effective, providing a careful reproduction of the channel bed, in other situations they could lead to an inaccurate reconstruction of the intermediate bathymetry. For instance, 1) when an intermediate island is not accounted by two following cross sections, it is missed in the reconstructed bathymetry if not integrated with a specific technique (Merwade et al., 2008); conversely, 2) if a cross section intersects the profile of elevated ground emerging from water, this is interpolated as far as the following CS in the recreated bathymetry, extending a local morphological feature to the whole reach between the 2 CSs; 3) the interpolation uses an average bed slope between two CSs, so neglecting the local slope variation and creating interpolated CSs that could be above or below the local thalweg. Sometimes the modification can be hydraulically relevant (e.g., when a bed drop is present between two CSs or the two CSs are separated by a long river stretch, maybe characterized by variable slope) creating CSs that do not fit the surrounding floodplain; 4) in some algorithms, the CSs interpolation can create void regions or regions superimposed to the river bed banks, creating inconsistencies between the interpolated surface and the surrounding DEM that must be suitably dealt with (Caviedes-Voullième et al., 2014; Merwade et al., 2008). In other algorithms (e.g., HEC-RAS), the user can select polylines corresponding to the banks to guide the interpolation but, however, the elevation of the CS end-points is determined by the interpolation, recreating a potential inconsistency similar to the one described in 3). On the other hand, although LiDAR intensity returns could be used to distinguish accurately between water (weak signal) and non-water (strong signal), this information is often not available to the final user of a DEM and, accordingly, cannot practically be used to devise a procedure that identifies the water edge boundaries (e.g., Legleiter, 2012); similarly, the use of satellite images that could theoretically be used to this purpose (e.g., Lai et al., 2021), is conditioned, among others, by space resolution issues and by the synchronicity between the survey and the satellite images. When CS_{sur} are not available, some bathymetric correction procedures are based on estimates of the water normal depth using Manning equation, coupled with simplified transversal geometry and a guess discharge value (e.g., Bhuyian et al., 2015; Roub et al., 2012). Although this method can sometimes be effective (e.g., Bures et al., 2019; Reil et al., 2018), it is limited by the arbitrary hypothesis of normal flow, by knowledge of the Manning's coefficient and of the river discharge at the time of the survey, that could be loosely estimated as a function of the drained area (e.g., Knighton, 1998; Leopold & Maddock, 1953) or from measured stage-discharge curves (Bhuyian et al., 2015) or remote sensing observations (e.g., Tarpanelli et al., 2021). Theoretically, the water depth could also be estimated on the basis of some satellite survey (e.g., Mersel et al., 2013), but these should be synchronous to the LiDAR survey, reducing the practical applicability of this methodology to very few cases. In this chapter we provide an alternative method to improve the description of the river bathymetry that endeavors to exploit all the morphological information contained in the original DEM, to the point that the advantage of the proposed method grows with the morphological complexity of the river bed. Accordingly, the method is suitable for braided rivers too, where it can automatically single out sandbars

as inner boundaries, a notoriously challenging task for any existing automatic tool (e.g., Lai et al., 2021). The proposed method requires 1) a DEM properly filtered from vegetation; 2) a set of topographically-surveyed CS_{sur}, to be manipulated using a GIS software; 3) a 2D SWE solver. A reasonable guess on a suitable low-flow discharge value is also needed. The procedure modifies the DEM on the basis of the "true" information contained in the surveyed CS_{sur}. The comparison of CS_{sur} with the corresponding ones extracted from the original DEM provides the local offset of the actual bottom, offset that is linearly interpolated and re-introduced into the DEM using the perimeter of a 2D hydraulic simulation of a suitably low-flow along the river. In this way, the real local width of the river is reproduced even in case that the CS_{sur} missed local enlargements or restrictions or even in presence of a braided pattern of the river. The final result is an enhanced representation of the 3D geometry of the river bed that leads to a more reliable estimates of the actual conveyance K of the river.

4.2 The algorithm

The proposed algorithm for the improvement of the bathymetry of a river crossing an original raster DEM (DEM_{ori}, in the following) requires the use of a GIS software and a 2D SWE solver along with a set of n_{cs} rectilinear CS_{sur} of the watercourse. A simple educated guess on a low-flow discharge is also required. In the following, the procedure is first summarized in 4 steps described in lay and visual language. The purpose of the first step (Figure 4.1) is to identify the subset of cells of DEM_{ori} representing the river bed occupied by water during the LiDAR survey and whose elevation must be lowered. Considering the potentially arbitrarily complex outline of this area, a physically based method can work best: accordingly, a 2D simulation is performed with a suitably chosen low flow Q, such that only the riverbed as present on DEM_{ori} is flooded and the surrounding floodplain is not inundated. This step may require some simple trials. Indeed, too small discharge values would lead to the emergence of unnatural dry areas on the bed, that in case can be eliminated by post-processing, whereas too high Q values would lead to include floodplain cells that were not covered by water at the time of the LiDAR survey. Using the results of this simulation, the shapefile of the outline of the flooded domain (SHP_{fld}) is obtained.

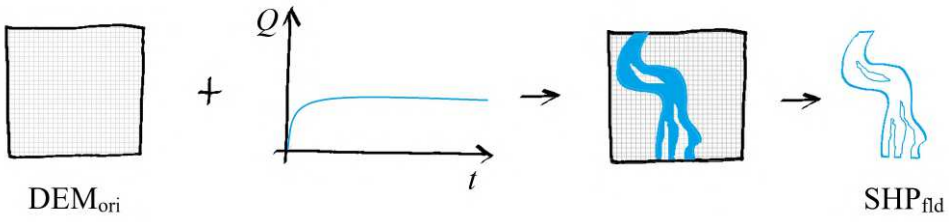

Figure 4.1: Schematic of the first step of the algorithm.

In the second step (Figure 4.2) a set of n_{cs} cross-sections (CS_{ori}) is extracted from DEM_{ori} in correspondence with the surveyed rectilinear CS_{sur} set, limiting their transversal extent l_j (where j is the index of the CS) to the external outline of the previously identified flooded domain. Note that extending the field survey of CS_{sur} as far as the floodplain, in order to capture the levees and floodplain elevations, is a best practice: accordingly, the CS_{sur} width $L_j > l_j$. If an island is present along the cross-section, it is excluded from the computation of l_j. Then, for each cross

section j, the average vertical offset Δz_j over l_j is computed as:

$$\Delta z_j = \frac{\int_{l_j}(z_{ori} - z_{sur})d\xi}{l_j} \quad j = 1, 2, .., n_{cs} \tag{4.1}$$

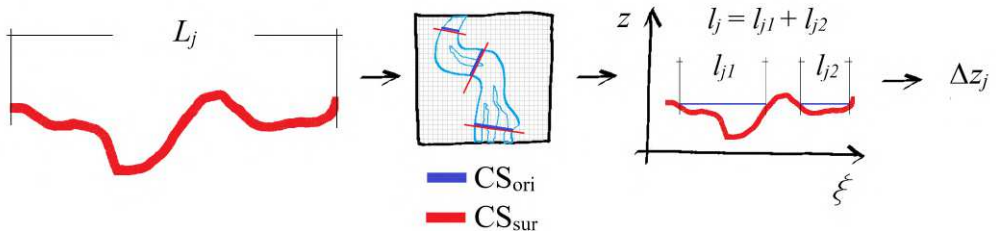

Figure 4.2: Schematic of the second step of the algorithm. The blue solid segment is the outline of CS_{ori}

In the third step (Figure 4.3), a fictitious channel is built, made up of rectangular cross sections of depth Δz_j with the same width L_j and position of the CS_{sur} set. In order to cover the actual extent of the watercourse between two consecutive CSs, these cross sections can be linearly interpolated. Then, the geometry of the fictitious offset channel is converted to a raster file, called DEM_{offset}.

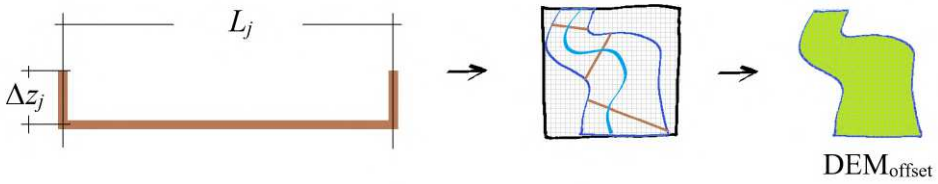

Figure 4.3: Schematic of the third step of the algorithm.

Considering that the width of the channel in DEM_{offset} is larger than the area effectively occupied by water during the LiDAR survey, in the fourth step (Figure 4.4) DEM_{offset} is clipped using the polygon SHP_{fld}. Then the final corrected DEM (DEM_{corr}, in the following) is built as the difference between the elevations of DEM_{ori} and the clipped DEM_{offset}.

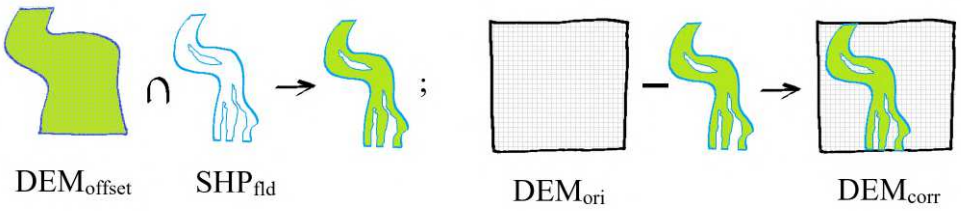

Figure 4.4: Schematic of the fourth step of the algorithm.

4.3 Application to the Mella river

The Mella river is a pre-alpine river in the province of Brescia, one of the most strongly urbanized areas of northern Italy. The 37-km long stretch from the village of Sarezzo as far as the village

of Dello will be studied in the following. The overall river relief in the considered stretch is 230.5 m and its longitudinal profile is shown in (Figure 4.5). Probabilistic peak discharges at the Sarezzo station are Q_{20} = 240 m^3s^{-1} and Q_{200} = 375 m^3s^{-1} where the subscripts indicate the return period.

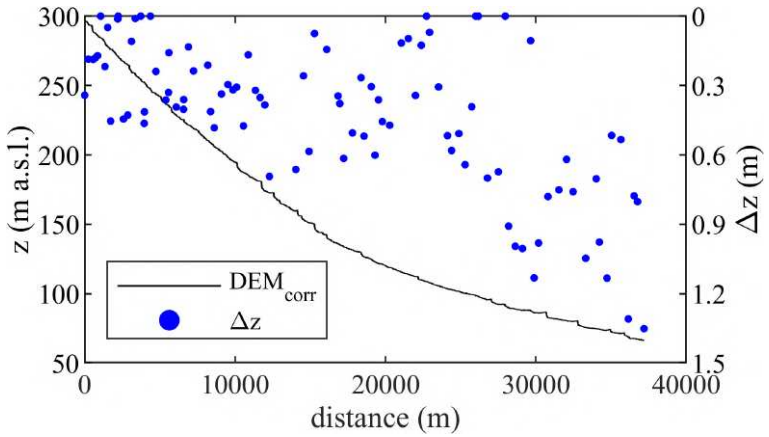

Figure 4.5: Longitudinal profile of the Mella river in the investigated stretch along with computed offset Δz in correspondence of the CS_{sur} set.

The Mella river and the surrounding floodplain is covered by a 0.8-m grid LiDAR DEM measured in 2008-2009, with a planimetric and vertical accuracy of ± 0.30 m and ± 0.15 m respectively. Along the same stretch of the river, 120 CS_{sur} were surveyed in 2002, with a lateral extension that typically covers the floodplain for a width 4 times larger than the river bed; 26 CSs represent weirs and drop structures. Considering that the LiDAR survey was accomplished in low-flow period, after a few trials, eventually a 2D simulation with a constant discharge Q= 20 m^3s^{-1} was performed with HEC-RAS 2D in order to capture the bed of the river covered by water in DEM_{ori}. A computational mesh with an average cell's area of 86 m^2 is built with local refinement up to 5 m in correspondence of levees and other singularities. On the basis of field surveys, the Manning coefficient was set in the range 0.022-0.04 $sm^{-1/3}$. The simulation was performed for 10 hours in order to converge to the steady state solution. Using HEC-RAS Mapper, the shapefile of the flooded domain was obtained and a set of CS_{ori} in the same position of the 120 CS_{sur} with transversal width limited by the flooded domain shapefile was extracted from the DEM_{ori}. The comparison of the two sets of CSs allowed to compute the offset of the river bed for each CS (Equation (4.1) and Figure 4.5), with average value 0.42 m. This value and the following statistics do not account for the offset computed at the 26 CSs representing sudden drop structures where the elevation averaging over the 0.8-m grid and a little planimetric misalignment with CS_{sur} and CS_{ori} could introduce considerable errors in terms of offset and, consequently, in elevation. Considering the small discharge in the river presumably present at the time of the LiDAR survey, here the critical depth of the flow over the sill was approximated to 0. Note that a small value of discharge does not imply a negligible value of the offset at other stations along the river, due to backwater effects or even local negative slopes. At the same time, the method allows different choices to be made based on the specific condition. Although in the period 2002-2009 modifications in the thalweg profile due to sediment erosion/aggradation cannot be totally excluded, considering the limited river Mella morphodynamics it is reasonable to assume that the observed offset is mostly explained by the presence of water along the river. As one can observe, the offset increases moving downstream (Figure 4.5), reflecting the decrease of the average bed slope S_b of the river and its meandering pattern in the floodplain. The interpolation

of the CS_{off} and the conversion to raster file were accomplished using HEC-RAS Mapper and the DEM_{offset} was embedded in DEM_{ori} using QGIS. Figure 4.6 shows the comparison between some cross sections extracted from DEM_{ori} and DEM_{corr} (CS_{ori} and CS_{corr}, respectively) in correspondence of CS_{sur}. The geometry of CS_{corr} is very close to the corresponding CS_{sur} one, with a very good agreement of the stage-K curves, where the conveyance K curves are computed using the software HEC-RAS as follows:

$$K(z) = \frac{1}{n} A R_h^{2/3} \tag{4.2}$$

where n is the Manning roughness coefficient, A and R_h are respectively the wetted area and the hydraulic radius for a fixed elevation z. As shown by the comparison of the stage-K curves in Figure 4.6, the effects of the DEM correction become more relevant as the offset increases, as typically happens where the average slope of the stretch decreases. Moreover, as one could expect, the hydraulic effect of the correction relatively decreases for growing values of the water stage.

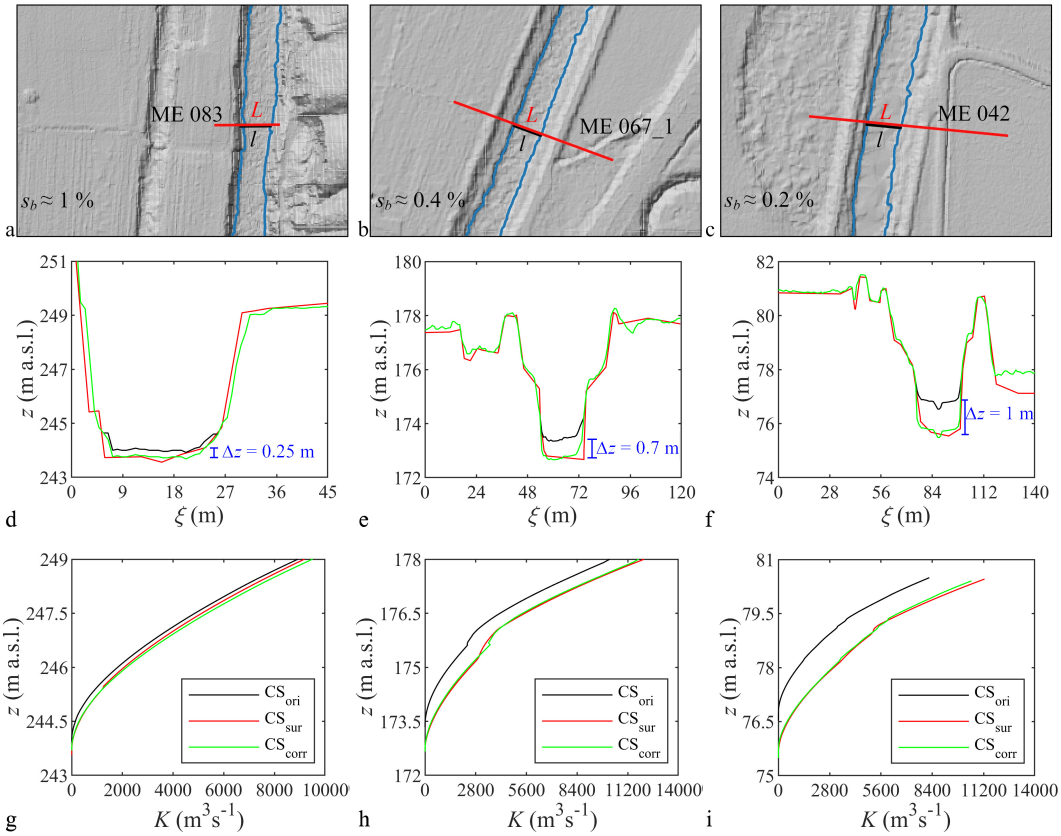

Figure 4.6: Plan view of CSs ME 083 (a), ME 067_ 1 (b), and ME 042 (c) from the Mella river test case with indication of the flooded area and of the part of the CS representing the riverbed. The second row shows an example of the CSs geometry extracted from DEM_{ori} and DEM_{corr} and CS_{sur}; in the third row the stage-K curves are compared to the data from CS_{sur} (d, g: CS ME 083; e, h: CS ME 067_1; f, i: CS ME 042).

In order to measure the quality of the reconstructed CSs, the most relevant quantity in the hydraulics of each CS, i.e. the conveyance, was used as a metric. Assuming the CS_{sur} as ground

truth, the Root Mean Square Error (RMSE) of the conveyance has been computed for the cross sections CS_{ori} (drops excluded) as follows:

$$RMSE_{ori,j} = \sqrt{\frac{\sum_i \left(K_{ori_{i,j}} - K_{sur_{i,j}}\right)^2}{N}} \quad j = 1, 2, .., n_{cs} \tag{4.3}$$

where, j=1,2,..,n_{cs} is the cross section and i=1,2,..,N is the number of the elevation point. In a similar way $RMSE_{corr}$ has been computed for the CS_{corr} set. Figure 4.7 shows the RMSE of the conveyance for the two sets of CSs. Figure 4.7 shows that at some stations the RMSE is greater for CS_{corr}. This problem is not related to the bottom correction but to some inconsistencies between the surveyed cross-section and the original DEM. An example is shown in Figure 4.6d, where CS_{ori} is shallower than the surveyed one, as one could expect, but also was a bit wider. Accordingly, the wetted area of CS_{ori} for a given stage was closer to the area of CS_{sur} before the depth correction. Having corrected the bed bottom in CS_{corr}, its conveyance (see Figure 4.6g) becomes larger than the real one. However, these "pathological" situations that cannot be accounted by any method, simply underline, if needed, the importance of the quality of the original data in the whole modeling process.

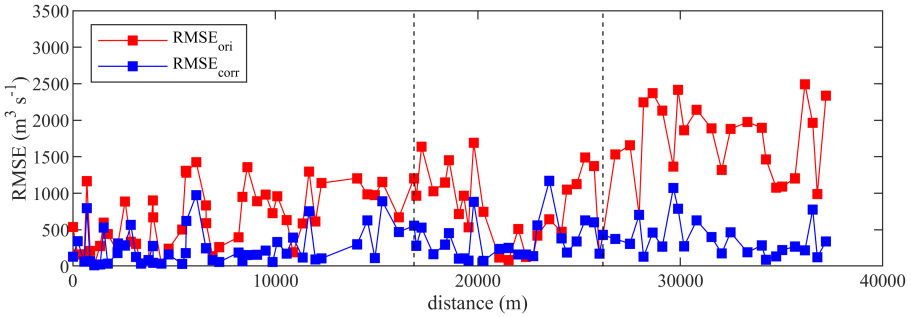

Figure 4.7: RMSE of the conveyance along the Mella River for DEM_{ori} and DEM_{corr} (the vertical dashed lines enclose the stretch of the Mella River analyzed for the cross-validation).

As a cross-validation of the proposed method, moving along the river one cross section at a time was removed and the offset was computed by linear interpolation along the river centerline between the upstream and downstream offset of the removed CS. Lastly, the RMSE was computed for the removed CS for the following comparison. To this purpose, the analysis was limited to the stretch without CS_{sur} in correspondence of sudden bed drops between 16850 and 26180 m. The adopted indicator of goodness of the cross-validation is the mean RMSE computed for the considered stretch of the river, obtaining a mean RMSE computed for CS_{ori} of 809 m^3s^{-1}, a mean RMSE for CS_{corr} of 359 m^3s^{-1} and a mean RMSE for the cross validated offset of 545 m^3s^{-1}. Accordingly, even reducing the available information the method improves the existing geometry.

4.4 Discussion and conclusions

The Mella River case is characterized by a relatively simple shape of the cross sections and by the absence of islands that lead to the presence of parallel riverbeds. To evaluate the performance of the proposed methodology for a different type of river, we applied the procedure to a 2.6 km stretch (See Figure 4.8) of the mountain reach of the Oglio river, in the Valle Camonica valley (Northern Italy). The investigated area is covered with a DEM with a spatial resolution

of 0.8 m derived from a LiDAR survey carried out in 2008 and a set of 7 surveyed CS in 2002 (Figure 4.9). The considered stretch of the river is characterized by the presence of islands in correspondence of the CSs OGS 058 02 and OGS 059, as shown in Figure 4.8a.

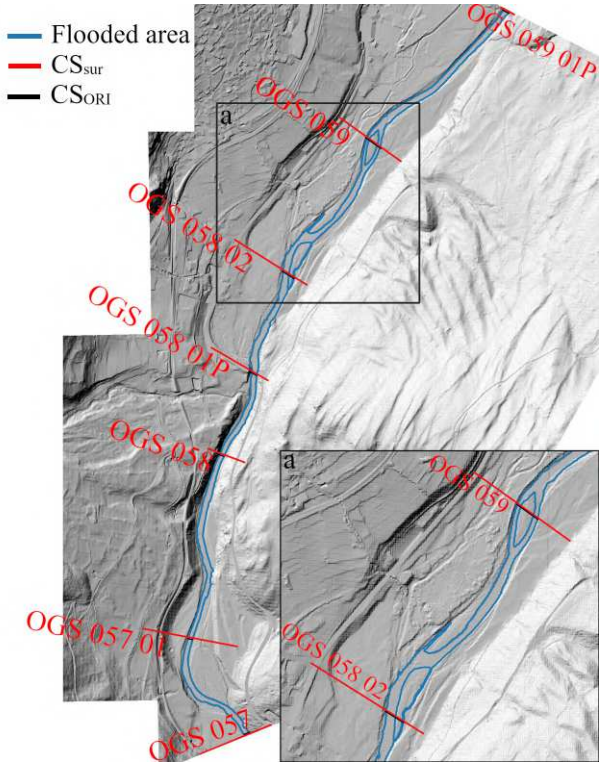

Figure 4.8: Stretch of the Oglio river, highlighting the flooded area (SHP_{fld} obtained in step 1 of the procedure), the planimetric view of CS_{sur} and CS_{ori}.

The DEM of the Oglio river was used as a bathymetric support to prepare a computational mesh with a grid size of 20 m, refined up to 5 m in correspondence of the river. The Manning coefficient for the river bed was set in the range 0.05-0.067 s $m^{-1/3}$ on the basis of a local survey. As boundary conditions, a low-flow hydrograph with a constant discharge of 5 m^3s^{-1} was introduced upstream and a normal depth boundary condition with local slope of 0.02 m/m was set downstream. A 2D SWE simulation was finally accomplished using HEC-RAS 2D along the 2.6 km stretch of the Oglio river that provided the submerged part of the LiDAR only, excluding the emerging islands: from this the CSs offsets (Δz) was computed. Figure 4.9 shows the comparison between CS_{sur} and the cross section CS_{corr} extracted from corrected DEM, along with the computed offset Δz. As one can observe, the procedure, based on a 2D simulation, corrects the DEM in the submerged part only (see CS OGS 059 and OGS 058 02), preserving the "true" morphology provided by the LiDAR survey and respecting the original shape of the islands.

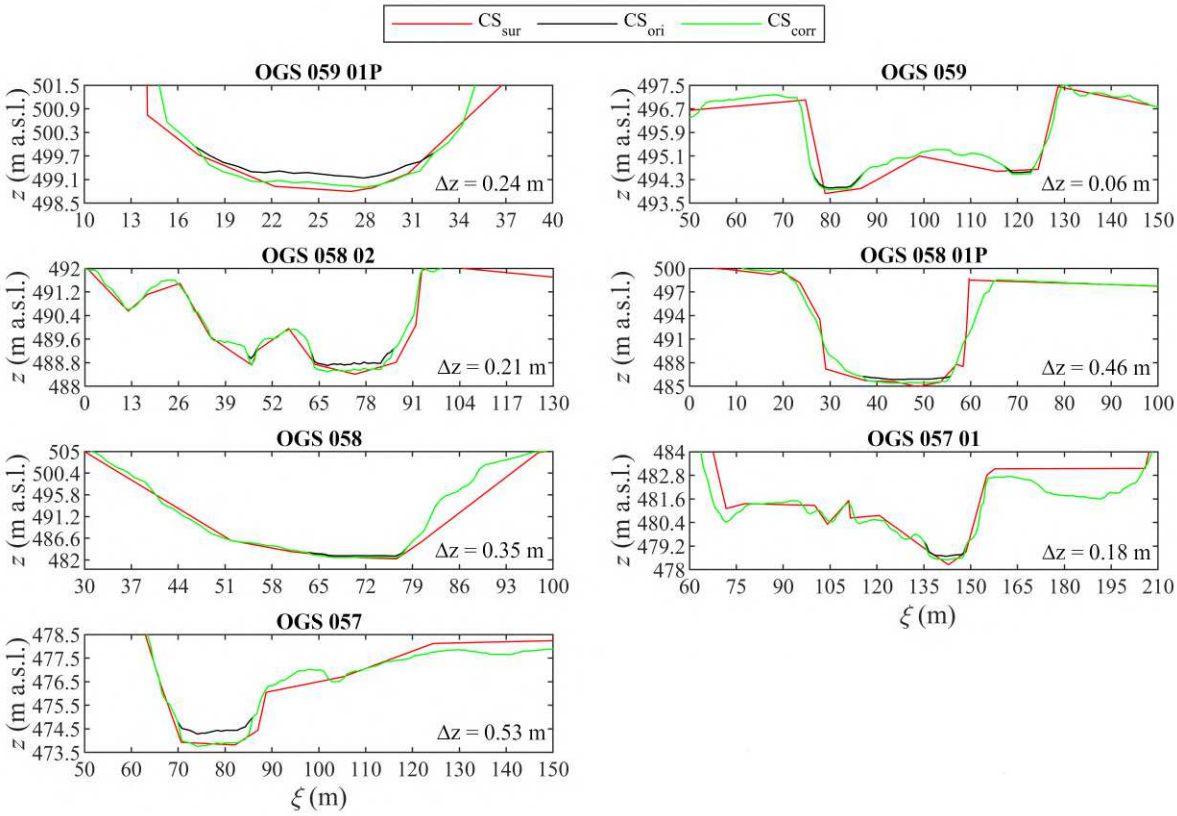

Figure 4.9: Comparison between CS_{sur}, CS_{ori} and CS_{corr} for the Oglio River test case. The horizontal and vertical extent of some CSs is limited to better show the actual DEM correction.

Finally, to further emphasize the capability of the procedure to correct the bathymetry in a complex situation like that of a braided river, where any interpolation between consecutive CSs would fail, we applied it to two idealized test cases. In the first case the bathymetry shown in Figure 4.10 was created, with a length of 1 km and a 0.001 m/m slope of the bottom. We used a 0.25 m grid size DEM, assuming a water depth of 0.5 m during the LiDAR survey. Figure 4.10a shows the DEM of the investigated areas and the position of the 5 idealized surveyed CSs (CS_{sur}). According to the proposed procedure, a HEC-RAS 2D model of the river was built using the idealized LiDAR survey as a bathymetric support, using a computational mesh with a grid size of 2.5 m and a Manning coefficient $n = 0.03$ s $m^{-1/3}$. As boundary conditions, a low-flow hydrograph with a constant discharge of 5 m^3s^{-1} was introduced upstream and a normal depth boundary condition with local slope of 0.001 m/m was set downstream. The comparison between CS_{sur} and the cross section CS_{corr} extracted from the corrected DEM is shown in Figure 4.11. The second paradoxical bathymetry, shown in Figure 4.10b along with 6 surveyed CS (CS_{sur}), was devised to demonstrate that the advantages of the proposed procedure grow with the complexity of the river morphology. The square 50 m x 50 m domain is characterized by a 0.05 m grid size and contains a constant water surface elevation of 1 m. Using the same boundary conditions as before, a 2D HEC-RAS model of the stretch of the river was built using the idealized LiDAR survey as a bathymetric support and a computational mesh with a grid size of 0.5 m. Figure 4.12 shows the comparison between CS_{sur} and the cross section CS_{corr} extracted from the corrected DEM. In this case, the ability of the proposed methodology to handle complex morphologies is evident. The solution provided by the SWE solver, whose

streamlines are shown in Figure 4.13, allows to detect automatically all the obstacles along the river and to limit the correction to the area covered by water at the time of the LiDAR survey. Note that this correction is totally unaffected by the complexity of the islands outline and by the presence of recirculation zones.

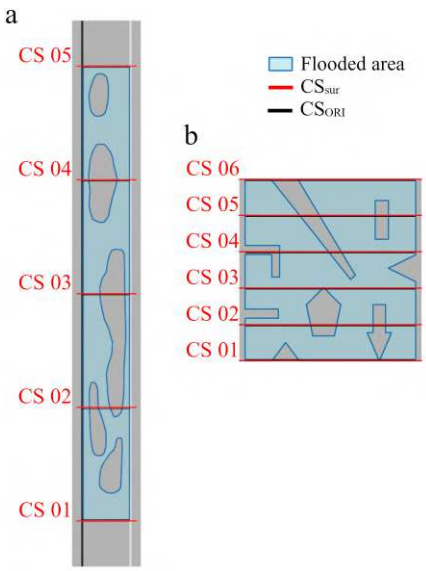

Figure 4.10: Two idealized complex domains, highlighting the flooded area (SHP_{fld} obtained in step 1 of the procedure) along with the planimetric view of CS_{sur} and CS_{ori}.

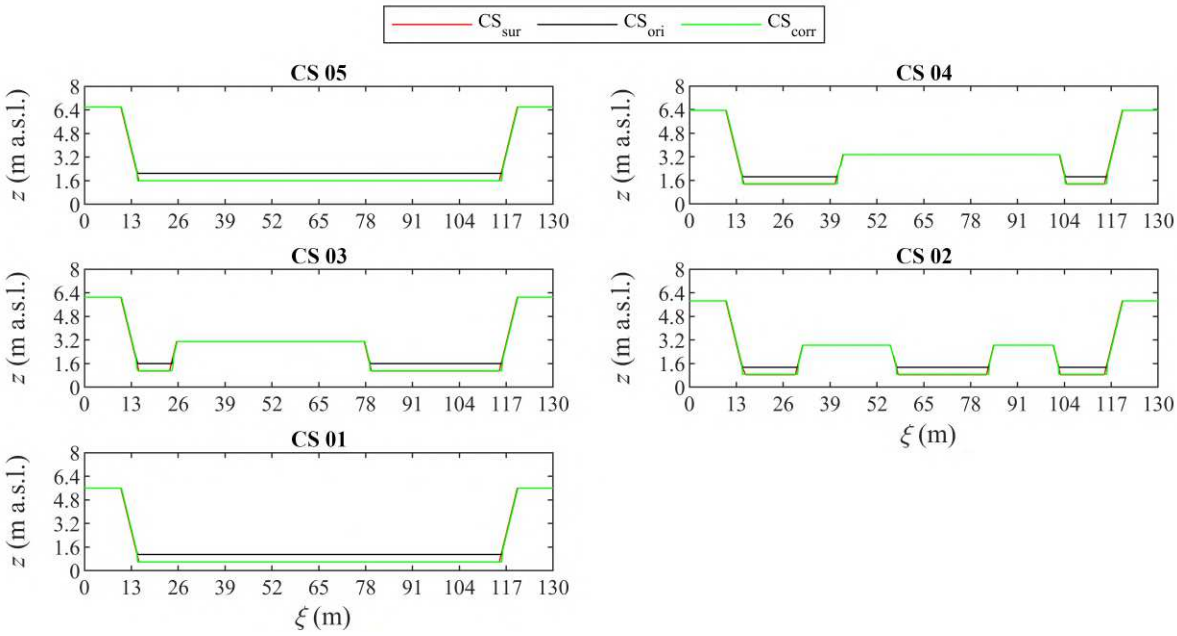

Figure 4.11: Comparison between CS_{sur}, CS_{ori} and CS_{corr} for the idealized braided river test case of Figure 4.10a

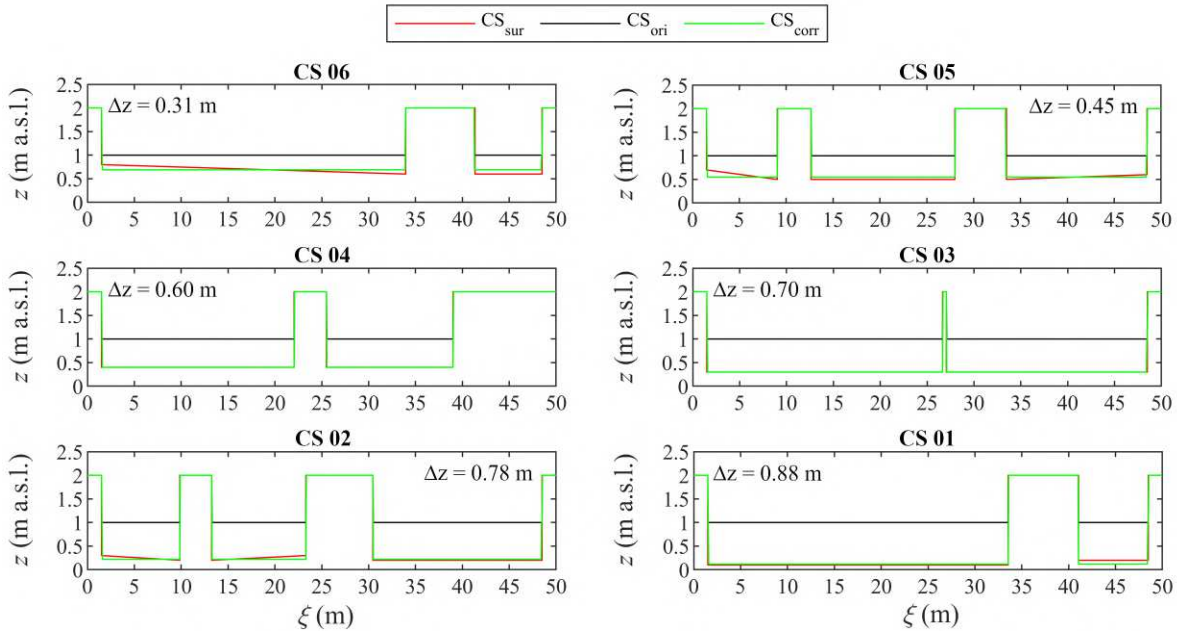

Figure 4.12: Comparison between CS_{sur}, CS_{ori} and CS_{corr} for the idealized braided river test case of Figure 4.10b

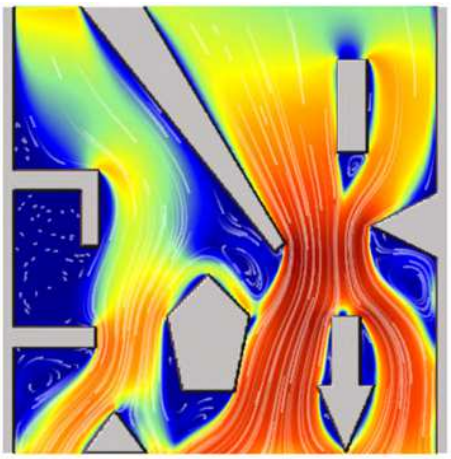

Figure 4.13: Computed streamlines of the flow field for the bathymetry in the right panel of Figure 4.10b. Flow from north to south.

So far, the methodology for the enhancement of river bathymetry for LiDAR derived DEM is presented for river application only. However, as mentioned in the introduction, a stumbling block in the implementation of the hydraulic model of an irrigation network is the description of the cross sections of different branches that make up the network. Here, we argue that that if a high resolution DEM derived from LiDAR survey is available, the proposed methodolgy can be effectively applied also for an irrigation channel network. Accordingly, in order to show this application, a stretch of the Naviglio Nuovo and the Suppeditazione Canal managed by Consorzio Irrigazioni Cremonesi was selected to test the proposed method (for the location and characteristics of these channels see Chapter 6 of this Thesis). The choice of the study area was suggested by the availability of LiDAR derived DEM. Actually being the stretch of these

irrigation channels close to the Oglio River, they are partially covered by a 1 m resolution LiDAR DEM surveyed in 2008-2009.

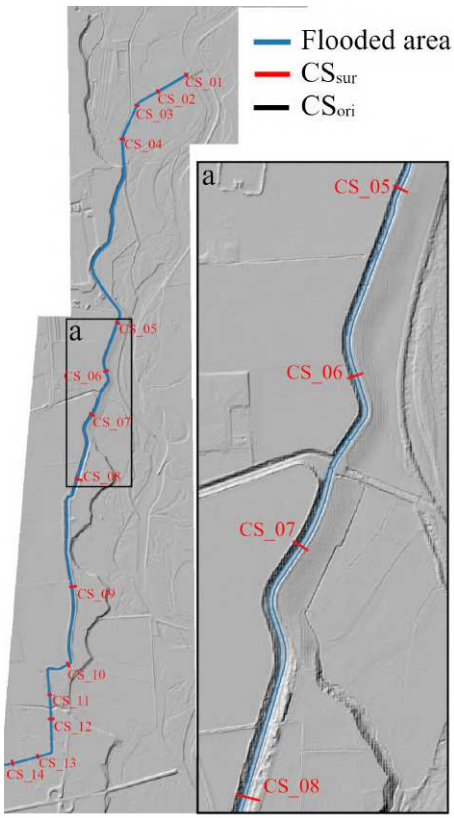

Figure 4.14: Stretch of the Naviglio Nuovo canal Canale di Suppeditazione managed by Consorzio Irrigazioni Cremonesi, highlighting the flooded area (SHP_{fld} obtained in step 1 of the procedure) and planimetric view of CS_{sur} and CS_{ori}.

The proposed procedure was applied to this test case: a HEC-RAS 2D model of the river was built using the bathymetry provided by the LiDAR survey as a bathymetric support, using a computational mesh with a grid size of 5 m (refined up to 2.5 in correspondence of the canal) and a Manning coefficient $n = 0.03$ s $m^{-1/3}$. As boundary conditions, a low-flow hydrograph with a constant discharge of 0.4 m^3s^{-1} was introduced upstream and a normal depth boundary condition was set downstream. The comparison between CS_{sur} and the cross section CS_{corr} extracted from the corrected DEM is shown in Figure 4.15. In this area, for the 5.2 km of the irrigation canal 14 CSs are available (Figure 4.14) surveyed with classical topographic surveys and by means of a GNSS device. In this case, the LiDAR description of the river bed is mainly in good agreement with the surveyed cross sections. Significant differences between LiDAR and ground survey data are evident in CSs 01, 02, 03 and 04 requiring a correction. Generally there is a clear improvement of the channel conveyance in the critical CSs. However, for the cross section CS 02 and CS 04 there are some differences in the geometry of the cross sections. These differences are caused for two different reasons: (1) the small discharge used for the 2D simulation is not sufficiently large to cover the entire river bed cover by the water during the LiDAR survey, on the other hand an increase in the discharge would cause the flooding of some areas not well described the LiDAR survey; (2) the resolution of the DEM (1m) is not sufficient to describe the geometry of the channel.

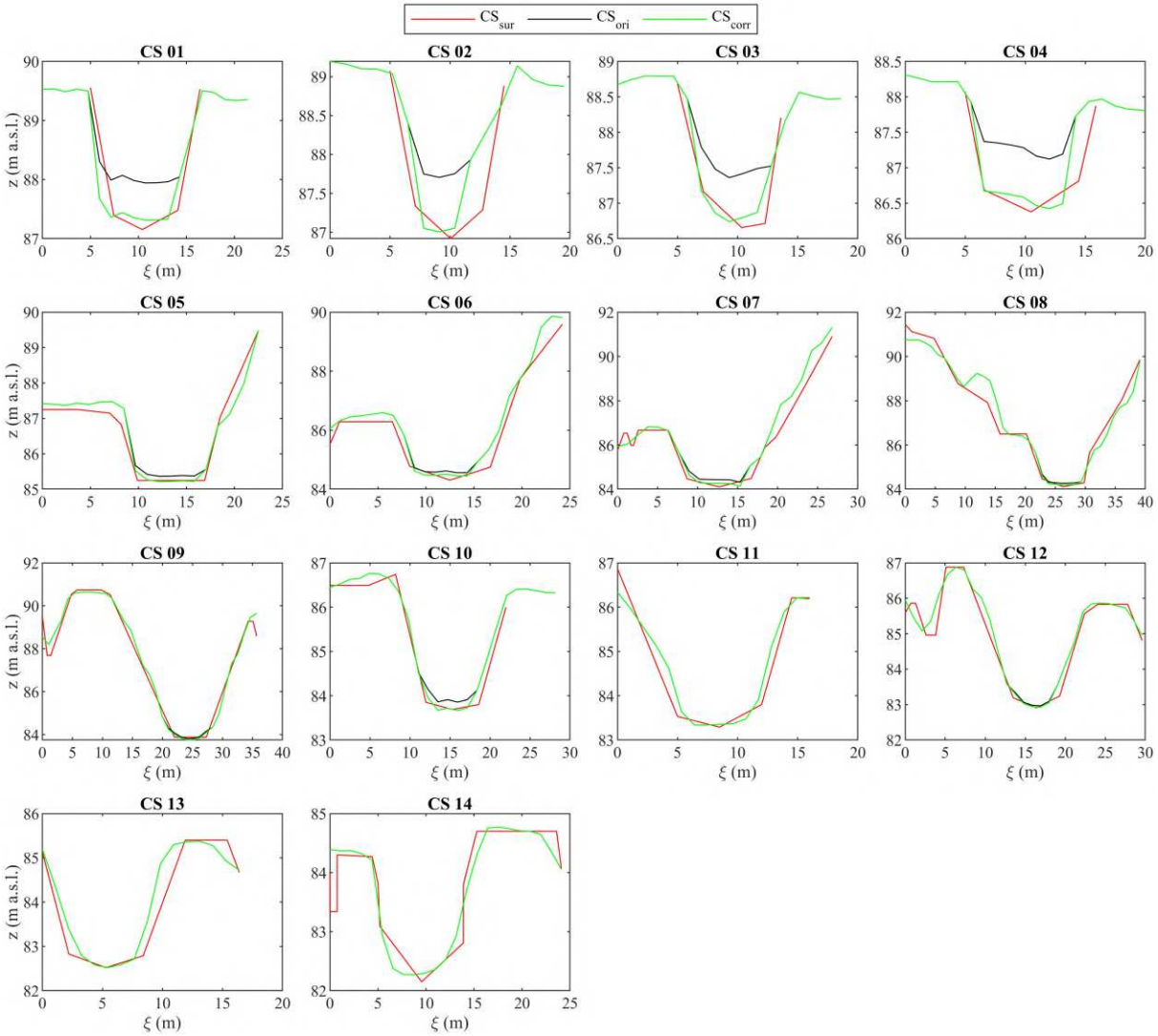

Figure 4.15: Comparison between CS_{sur}, CS_{ori} and CS_{corr} for the irrigation channel test case of Figure 4.14

In conclusion, several methods for CS interpolation available in widely used software are excellent. For instance, HEC-RAS provides superb utilities to manage the bed bathymetry. However, as shown in the introduction, these methods are not perfect. Considering that it is a common experience of hydraulic modelers that the definition of accurate bathymetry is one of the most relevant and engaging steps in the whole modeling effort, we believe it is important to keep improving the available methodologies, in order to devise a method that can eventually incorporate all the constructive contributions coming from the scientific and technical discussion. The procedure requires only measured geometric data, a reasonable guess on the value of the discharge, and uses the simplest possible assumption on the shape of the cross-section below the water level (i.e., rectangular). This could be a limitation if the real bathymetry significantly differs from the rectangular assumption because all the portions of CS_{ori} covered by water are translated of the same quantity Δz. On the other hand, this assumption is also the most reasonable, considering that for low stages most CSs are hydraulically wide, in the sense that their hydraulic radius tends to the water depth, as in an infinitely wide rectangular CS.

As a confirmation of the validity of this assumption, the mean RMSE of the conveyance for the whole Mella river stretch considering only the submerged part of each CS was computed. In this case, the mean RMSE of the conveyance computed for the CSs extracted from DEM_{corr} is 23 m^3s^{-1}. The methodology relies on the availability of surveyed CSs and of a DEM carefully filtered from vegetation. A reasonable density of LiDAR points inside the wetted area is also needed in order to avoid a bad representation of the water surface, that has an influence on the final shape of the reconstructed submerged part of the CS, emphasizing the importance of the good quality of the input data, without which every method is almost inevitably unsuccessful. Moreover, the importance of measuring the DEM and CSs at a short temporal distance is here underlined, in order to limit inconsistencies due to sediment transport and human modification of the riverbed. The original DEM is modified using a 2D flood model that is also the final goal of the overall DEM improvement activities. Accordingly, this preliminary modeling effort is not to be considered as an overburden and simplified SWE models (e.g., kinematic or diffusive approximation) could well be used to this purpose. On the contrary, the 2D simulation gives a sound physical basis to the methodology and captures the river planimetric variability between two consecutive CS_{sur}, providing a reconstruction of the riverbed that preserves all the morphological information available above the water surface at the time of the survey. For instance, using the results of a 2D simulation preserves the presence of islands along the river as demonstrated by the application on a stretch of the Oglio river and on the idealized cases. Provided that there is no silver bullet to solve the problem, by adding an interpolated offset to the local elevation in place of an interpolated elevation, this algorithm does not produce a uniform slope between two consecutive CS_{sur}, because it follows the measured local water surface elevation. Moreover, a 1D reconstruction of the watercourse, based on the interpolation of the CS_{sur} set only, would arbitrarily modify the CS geometry and slope between two consecutive CS_{sur}. Accordingly, we believe that the idea of "digging" the DEM inside the flooded area at the basis of the proposed methodology ensures a better consistency between the excavated area and the surrounding DEM. As a final comment to this chapter, it is important to underline that, although the correction methodologies analyzed have focused on the more complex case of the correction of a natural riverbed in the context of flooding problems, the same methodologies can be used to obtain the cross sections to be adopted within a one-dimensional scheme, both in the case in which it is assumed that there are few measured sections or, even, that these are absent. In this second case, it will be necessary to estimate the values of Δz at different points along the channel network measuring the water depth probably present at the time of LiDAR survey. In this case, the whole presented algorithm should be simplified. Indeed, the second step of the algorithm is already satisfied by the evaluation of Δz in the field.

5 Coupling water channel temperature and hydrodynamic: implementation and validation

5.1 Introduction

In the logical scheme outlined in this Thesis, the hydrodynamic model is imagined as the quantitative engine to be used for the operational choices of water distribution management within a network of channels of arbitrary complexity. The functioning of this model is not designed to determine the stationary state of the system but to model its dynamic evolution over the seasonal period.
When the hydrodynamic modeling of a channel network is accomplished over a relatively long time span, a dominant effect is played by water temperature. Which has a major influence on the biophysical processes that govern macrophyte growth, that, in turn, governs the time variation of the roughness in the channel. Actually, roughness is largely caused by aquatic vegetation whose growth is controlled by temperature with a maximum rate at some optimal temperature (Carr et al., 1997). Accordingly, a fundamental component of a hydrodynamic model for an irrigation network that has to operate over a relatively long time span, would be a component for water temperature computation and, eventually, for weed growth.
Although the dynamics of the water temperature is, in principle, traceable through the use of temperature sensors placed inside a network of channels, within a complex network, the temperature should be measured at several points, with a significant instrumental and operational burden. Furthermore, a setting of this type would prevent the use of the model in a predictive way for knowing the effect of climate change scenarios and their potentially adverse consequences for the water ecosystem. For instance, it would not be possible to forecast the increase in the channel water temperature that would turn out from an increase of air temperature or air humidity. On the other hand, the path constituted by the inclusion, within the hydrodynamic model, of a local physically based energy balance scheme, would allow the determination of the local water temperature on the basis of external information (air temperature, long and short wave radiation, ...) that can be obtained in a reasonably accurate way by meteorological stations in the same area of the channel network and by dynamic quantities provided by the hydrodynamic module (speed and depth in each section). This second approach has the additional advantage of including variables that can strongly influence macrophyte growth, such as water depth and velocity or shortwave radiation, which could be locally inhibited or reduced, for example, by the presence of vegetation along the banks. Accordingly it can provide fundamental insights on the impacts of some operative choices. Finally, as mentioned above, the inclusion of temperature dynamics can provide a link to water quality modeling and to the analysis of climate change on the water ecosystem. For these reasons an energy balance model has been implemented within the hydrodynamic model. In this chapter, we present the implementation of the energy balance method (Pilotti et al., 2019) and the macrophyte biomass evolution model (Berger & Wells, 2008). The overall channel model and the critical evaluation of the results obtained during a long measuring campaign along the main branch of the Vacchelli irrigation channel is then presented in Chapter 6.

5.2 Heat exchanges at the air-water interface

The surface heat exchanges, schematized in Figure 5.1, could be modeled as a combination of five radiative and not radiative processes (Chapra, 1997):

- Φ_{SW} is the net solar shortwave radiation, and the magnitude of this term is dependent of several factors (solar altitude, scattering and absorption, reflection and shading). Usually

the incoming shortwave radiation is measured using suitable pyranometers. If these instruments aren't available, it could be estimated using climate reanalysis datasets (Mihalevich et al., 2022) or it can be computed using equations based on astronomical calculation which are function of the time, position and cloud cover (Chapra, 1997).

- Φ_{LW} is the longwave radiation emitted from the atmosphere. It originates as emission from molecules (mostly CO_2 and water vapor) in the free atmosphere, and from liquid water in cloud (Henderson-Sellers, 1986).
- Φ_{bLW} is the longwave back radiation emitted from the water and it is function of the water temperature.
- Φ_{LH} is a non radiative flux called latent heat. It is linked to convection and conduction. Conduction is the heat exchange between molecules at different temperatures, on the other hand, convection is the heat exchange due to fluid mass movement.
- Φ_{SH} is the sensible heat and it is the heat loss due to evaporation.

Finally, the total heat flux at the water surface interface can be expressed as follows:

$$\Phi = \Phi_{SW} + \Phi_{LW} - (\Phi_{bLW} + \Phi_{SH} + \Phi_{LH}) \tag{5.1}$$

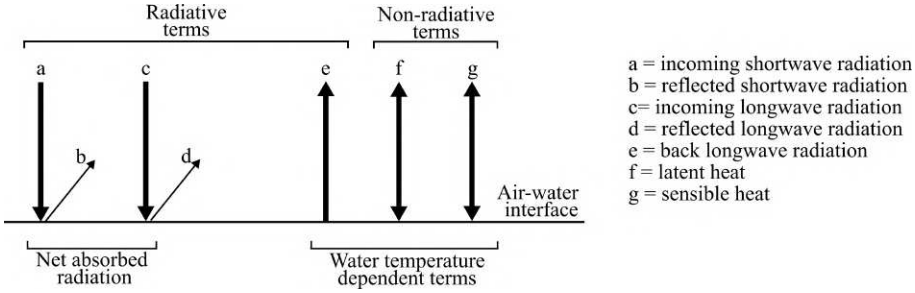

Figure 5.1: The components of surface heat exchanges, discriminating the radiative terms and non-radiative terms and the water temperature dependent terms.

The atmospheric longwave Φ_{LW} radiation can be estimated using a modified Stefan-Boltzmann law considering the atmospheric attenuation and reflection as proposed in Chapra (1997):

$$\Phi_{LW} = (1 - r)(A + 0.031\sqrt{e_{air}})\sigma(T_a + 273)^4 \tag{5.2}$$

where, r is the reflection coefficient (generally, r=0.03) and σ is the Stefan-Boltzmann coefficient (5.67×10^{-8} W m^{-2} K^{-4}), A is a coefficient (0.5 to 0.7), T_a (°C) is the air temperature and e_{air} (mmHg) is the air vapor pressure. Equation (5.2) doesn't account explicitly the effect of the cloud cover, that is present in the law used in Octavio (1977) and implemented in one of the heat model of DELFT-3D FLOW (Deltares, 2024) as follows:

$$\Phi_{LW} = (1 - r)\epsilon_a\sigma(T_a + 273)^4(1 + 0.17F_c^2) \tag{5.3}$$

where ϵ_a is the emissivity of the atmosphere (0.7 for clear sky and low temperature to 1) and F_c which is the cloud cover factor (0-1).
The back radiation from the water surface can be computed using the Stefan-Boltzmann law, expressed as follows:

$$\Phi_{bLW} = \epsilon_w\sigma(T_w + 273)^4 \tag{5.4}$$

where ϵ_w is the emissivity of water (typically 0.97) and T_w is the water surface temperature. The sensible heat represents convective and conductive heat exchanges between the water surface and the air and can be described as follows:

$$\Phi_{SH} = c_1 f(U_w)(T_w - T_a) \tag{5.5}$$

where c_1 is the Bowen's coefficient (typically 0.47 mmHg °C^{-1}) where $f(U_w)$, is an empirical function of the wind velocity U_w at a fixed height. Finally the last term is the latent heat and it can be expressed as follows:

$$\Phi_{LH} = f(U_w)(e_s - e_{air}) \tag{5.6}$$

where e_s is the saturation vapor pressure corresponding to the surface temperature of water (°C). Typically, the range of water content in the air is expressed by the percent relative humidity $R = 100 e_{air}/e_{sat}$ where e_{sat} is the saturation vapor pressure:

$$e_{sat} = 4.596 e^{\frac{(17.27 T_a)}{237.3 + T_a}} \tag{5.7}$$

Equation (5.7) can be used to compute the saturation vapor pressure in correspondence of the water surface using the temperature of the water T_w instead of the air temperature T_a.

5.3 Numerical model

Following the approach proposed by Pilotti et al. (2019) the channels network is discretized as a series of connected completely stirred-tank reactors (CSTR) that can exchange mass and energy (Figure 5.2). Each *i-th* CSTR is connected upstream to the *k-th* CSTR that converge in the CSTR $_{\text{i}}$ and downstream with the *w-th* CSTR.

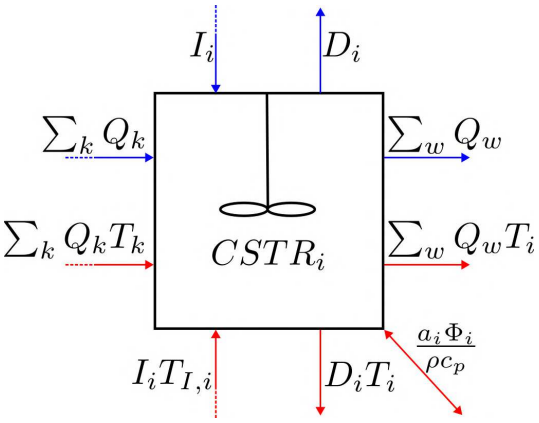

Figure 5.2: Visual representation of the volumetric water balance (blue arrows) and mass-energy balance (red arrows) for the CSTR$_{\text{i}}$.

.

Accordingly, for the CSTR$_{\text{i}}$, the volumetric water balance for the CSTR$_{\text{i}}$ is defined as follows:

$$\frac{dV_{CSTR_i}}{dt} = \sum_k Q_k - \sum_w Q_w + I_i - D_i \tag{5.8}$$

where, V_{CSTR_i} is the water volume of the *i-th* well mixed reactor, $\sum_k Q_k$ is the sum of the incoming discharges for the *i-th* reactor from upstream reactors, $\sum_w Q_w$ is the sum of the out-flowing discharges to the downstream reactors, I_i is a possible localized input and D_i a

possible withdrawal from the *i-th* reactor. Consequently, for each CSTR the mass-averaged energy balance equation can be written as follows:

$$\frac{d(V_{CSTR_i}T_{CSTR_i})}{dt} = \sum_k Q_k T_k - \sum_w Q_w T_i - T_i D_i + T_{I,i} I_i + \frac{a_i \Phi_i}{\rho C_p} \tag{5.9}$$

where, T_i is the temperature of the *i-th* reactor, T_k is the temperature of the upstream reactors, $T_{I,i}$ is the temperature of the localized immission, Φ_i represents both the radiative and non-radiative surface heat exchanges (Equation 5.1), a_i is the surface area of the *i-th* reactor, ρ is the density of water and Cp is the specific heat at constant pressure of water. Equation 5.9 can be discretized explicitly in time for the *i-th* CSTR as follows:

$$(T^{n+1}_{CSTR_i}) = \frac{V^n_{CSTR_i} T^n}{V^{n+1}_{CSTR_i}} + \frac{\Delta t}{V^{n+1}_{CSTR_i}} \left(\sum_k Q^n_k T^n_k - \sum_w Q^n_w T^n_i - T^n_i D^n_i + T^n_{I,i} I^n_i + \frac{a^n_i \Phi^n_i}{\rho C_p} \right) \tag{5.10}$$

Equation (5.10) is coupled with the hydrodynamic solver which provides $V^{n+1}_{CSTR_i}$ and all the discharges between the different CSTRs. The discretization of the CSTRs along the channel network could be performed considering the same discretization adopted for the hydraulic model although sometimes this discretization is finer than the one required for temperature modeling: for instance in a sudden enlargement the hydraulic model requires two cross section upstream and downstream the local variation in the channel and this is not necessary for the purposes of the temperature model. Moreover, Equation (5.10) is discretized using the Euler method and for small cell this could require very small time step to remain stable. To solve these issues, the temperature model discretizes the channel network into a set of control volumes (CSTRs) which joins the consecutive cells used by the hydrodynamic model (Figure 5.3) in order to have larger control volume and consequently relax the stability condition imposed by the explicit discretization of Equation (5.9).

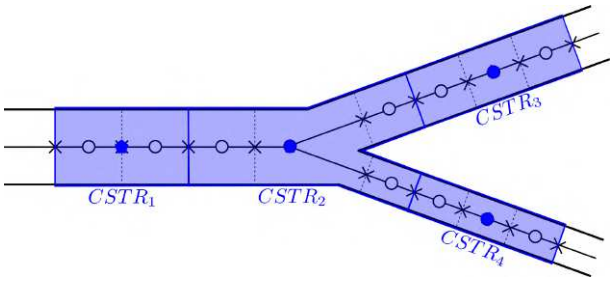

Figure 5.3: CSTRs discretization used in the temperature model overlapped to the classical discretization used in the hydraulic model.

5.4 Comparison with the water quality model implemented in HEC-RAS

In the software HEC-RAS an explicit numerical scheme for water quality model which solve the 1D advection-dispersion equation is implemented. The water quality model could be used to model the water temperature in addition to the dynamics of generic conservative and non-conservative constituents, dissolved nitrogen, dissolved phosphorus, algae, CBOD and dissolved oxygen (Brunner, 2016). As a validation of the numerical model we compared the obtained model output against the output of HEC-RAS considered as a ground truth using the same hydrodynamic condition and the same boundary condition and initial condition for the temperature model. Two converging trapezoidal channels have been considered and the system is

schematized in Figure 5.4. The characteristics of the channels are reported in Table 5.1. Regarding the hydraulic model, the channel network has been discretized using 1003 cross sections with an average distance of 20 m. The inflowing discharge for channel (1) is 10 m^3 s^{-1} and for channel (2) was set to 15 m^3 s^{-1}.

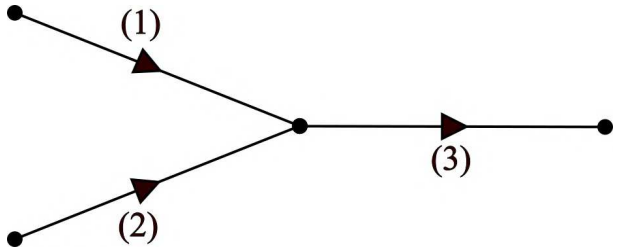

Figure 5.4: Test case for the temperature model.

Table 5.1: Characteristics of the channels shown in Figure 5.4

Canal Number	***Length (km)***	***Bed width (m)***	***Side slope (-)***	***Bed slope (-)***	***n ($s\ m^{-1/3}$)***
1,2	5.0	10	1	0.002	0.033
3	10.0	20	1	0.001	0.033

The model has been run for 7 days using as meteorological data the measured average values for June 2023 for the city of Crema (Northern Italy), shown in Figure 5.5. The wind velocity was assumed equal to zero, as well as the cloud cover factor. For the computation of the longwave radiation Equation (5.3) was considered calibrating the emissivity of the atmosphere $\epsilon_a = 0.9$. Considering the regular grid used to discretize the domain the control volume for the temperature model (CSTR) was selected equal to the control volumes used for the hydrodynamic model. The initial temperature for the whole system was set equal to the temperature of the water used as upstream boundary condition at the first time step.

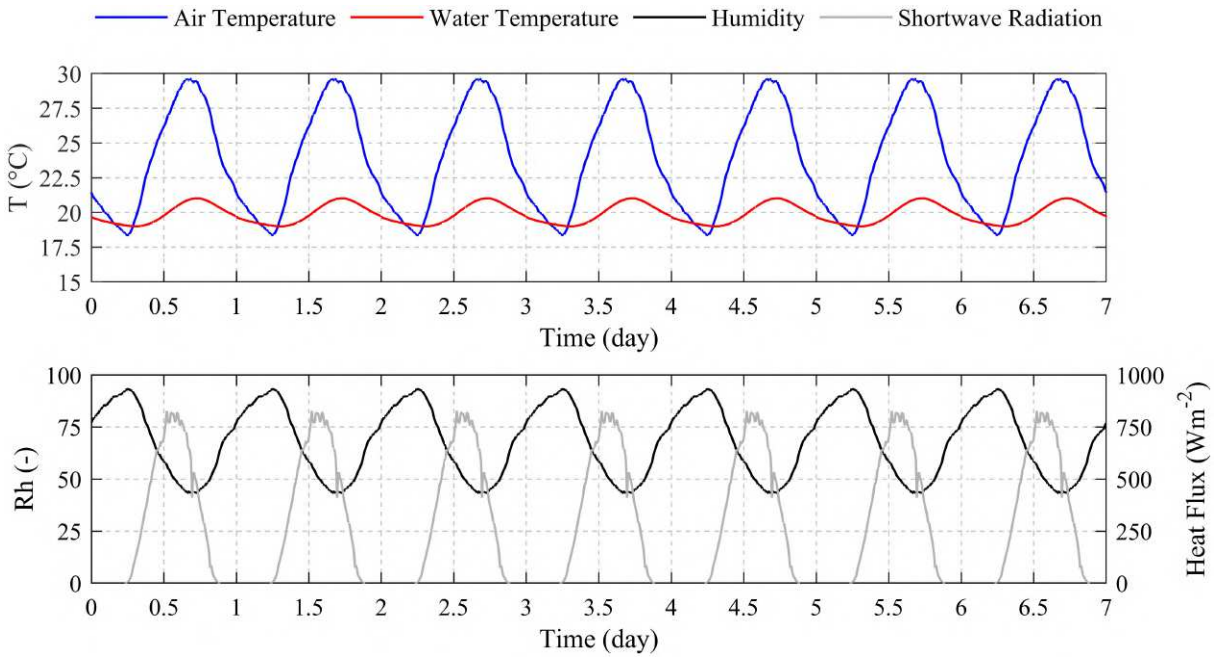

Figure 5.5: Input data for the numerical test for the implemented temperature model: the water temperature represents the upstream boundary condition used for the channels (1) and (2).

The results obtained using the implemented model are shown in the Figure (5.6) comparing the water temperature for the downstream cell of reach (1), (2) and (3) against the results obtained using HEC-RAS.

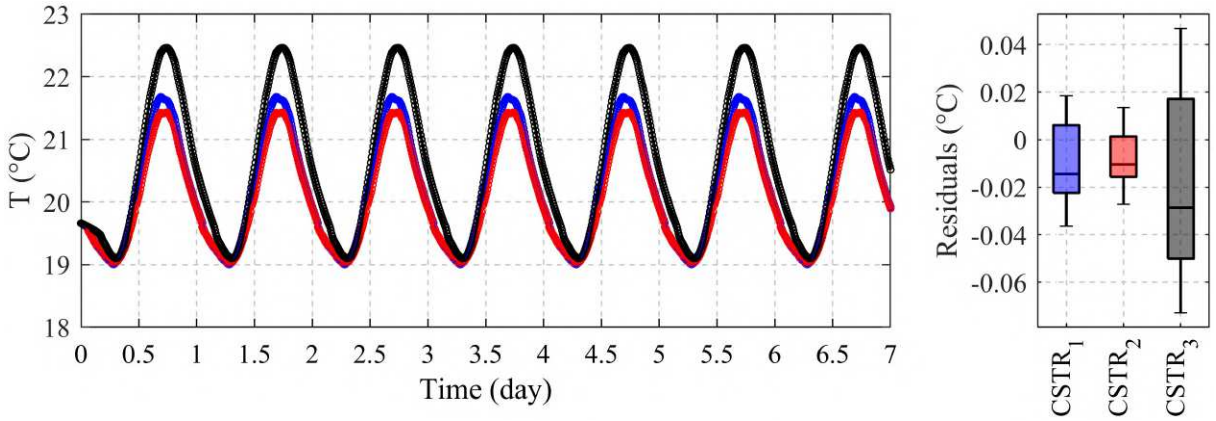

Figure 5.6: Comparison of the results obtained with the implemented model (points) and HEC-RAS (solid line). The results are almost perfectly superimposed. $CSTR_1$ (blue), $CSTR_2$ (red), $CSTR_3$ (black) corresponds respectively to the downstream control volume for channel (1), (2) and (3). The residuals are computed from the difference between the temperature computed by HEC-RAS and the temperature computed using the implemented model.

5.5 Modeling macrophyte biomass dynamics

The effect of seasonal vegetation growth on river roughness is documented in literature; for instance, in the paper of Keupers et al. (2015) the Authors have shown the effects of the seasonal growth of vegetation along the river branches of the Note Grote catchment in Belgium. The Authors have shown the variation of the Manning's roughness coefficient in the warm season. After the start of aquatic macrophytes growth in May, the roughness strongly increases and reach a peak in August, after which a quick decrease is observed down to the value for a river bed with little vegetation. They also underlined the effect of the discharge in the calibration of the Manning's roughness coefficient, and they observe that during peak flow the Manning's coefficient becomes smaller due to the deflection of the vegetation. Perret et al. (2021) have presented a model which couples a temporal vegetation development model (Yin et al., 2003) and a resistance law for emergent or just submerged vegetation (Järvelä, 2004) to correct stage-discharge curves accounting the effects of vegetation on stage discharge "shift". These papers, however, consider only some parts of the overall problem: they do not couple a model for vegetation growth and variation of Manning's coefficient within a hydrodynamic model applied to a complex real case. On one hand, there are simplified models which account for the macrophytes growth in streams as a function of time (e.g. Yin et al., 2003 efficaciously used in Perret et al., 2021). On the other hand, as shown by Carr et al. (1997) the vegetation growth is influenced by different physical parameters such as the water temperature, the solar radiation, and the availability of nutrients. Although different models have been developed with different levels of difficulty and processes included (Dietterich et al., 2024), as reported in (Scheffer et al., 1993) a model incorporating all the important dynamics is necessarily very complex and multi-parametric. As well known by the Von Neumann statement "With four parameters I can fit an elephant, and with five I can make him wiggle his trunk", a multi-parametric model involves the risk of obtaining an impressively good fit of the results without guaranteeing any realism of parameter values. In other words, the risk is that a good fit of the results can be obtained from different parameter sets. This topic is very complex and would require competencies in the biological and botanic areas that go beyond this work. Eventually, after considering several models, in the following the model proposed by Berger and Wells (2008) and implemented in CE-QUAL-W2 is presented. The model has been implemented and coupled with the hydraulic and temperature model with some simplifications. According to Carr et al. (1997) in the framework of macrophyte productivity models, the approach follows a mass balance assuming that the rate of change of biomass concentration S_m is function of the rate of biomass production through gross photosynthesis (P_b), biomass loss due to respiration (R_m) and plant decay (L_m):

$$S_m = P_m - R_m - L_m \tag{5.11}$$

Accordingly, the macrophyte growth rate can be described as follows (Berger & Wells, 2008):

$$dC_{\text{mac}}/dt = \gamma_1 C_{\text{mac}}[\mu_{\text{m,max}} f(I,N,P,C)\gamma_2 - K_{mr} - K_{mm}] \tag{5.12}$$

where, $\mu_{\text{m,max}}$ is the maximum macrophyte growth rate, $f(I,N,P,C)$ is a growth limitation factor related to I (solar radiation), N (nitrogen), P (phosphorus) and C (carbon), γ_1 and γ_2 are the rising and falling limb temperature multipliers of the multiplier function proposed by Thornton and Lessem (1978) for biological processes, C_{mac} is the macrophyte concentration, K_{mr} is the maximum respiration rate and K_{mm} is the maximum mortality rate. All the processes (growth rate, respiration rate and mortality rate) are governed by water temperature: to account this aspect the temperature multipliers proposed by Thornton and Lessem (1978) are introduced in the mass balance equation. The equation proposed by Thornton and Lessem (1978) is based

on the assumption that biological processes have a maximum reaction rate at some optimum temperature or range of temperatures. Accordingly, the reaction rate is the product of the maximum reaction rate with a multiplier that ranges from 0 to 1, depending on the temperature. The multiplier γ_1 is expressed as:

$$\gamma_1(T) = \frac{K_1 e^{\gamma_a (T - T_1)}}{1 + K_1 \left(e^{\gamma_a (T - T_1)} - 1\right)} \tag{5.13}$$

where T is the temperature, K_1 is the reaction rate near the lower threshold temperature, T_1 is the lower threshold temperature, γ_a is a specific rate coefficient computed as:

$$\gamma_a = \frac{1}{T_2 - T_1} \ln \frac{K_2(1 - K_1)}{K_1(1 - K_2)} \tag{5.14}$$

where T_2 is the temperature at maximum reaction rate and K_2=0.98.
The multiplier curve from the characteristic temperature to the higher temperatures is expressed as:

$$\gamma_2(T) = \frac{K_4 \, e^{\gamma_b (T_4 - T)}}{1 + K_4 \left(e^{\gamma_b (T_4 - T)} - 1\right)} \tag{5.15}$$

where K_4 is the reaction rate multiplier at the upper threshold temperature, T_4 is upper threshold temperature and γ_b is a specific rate coefficient expressed as:

$$\gamma_b = \frac{1}{T_4 - T_3} \ln \frac{K_3(1 - K_4)}{K_4(1 - K_3)} \tag{5.16}$$

where T_3 is the temperature at maximum reaction rate and K_3=0.98.
Finally, the reaction rate multiplier curve can be computed for the general temperature T by the equation:

$$K(T) = \gamma_1(T) \cdot \gamma_2(T), \tag{5.17}$$

An example of the reaction rate multiplier expressed in Equation (5.17) is shown in Figure 5.7.

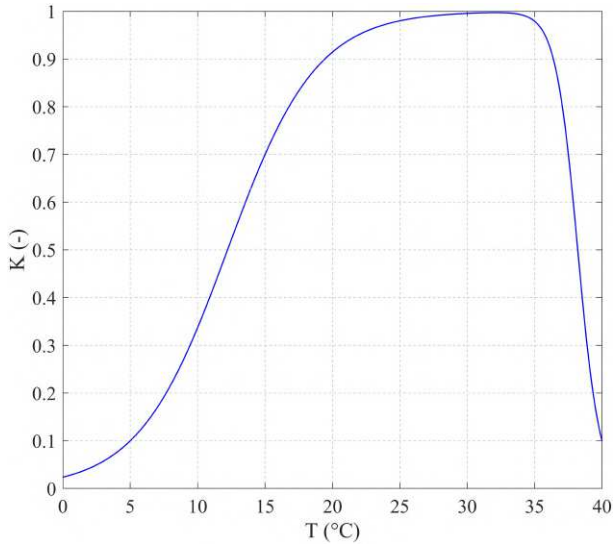

Figure 5.7: Temperature rate multiplier function (T_1=5, T_2=25, T_3=35, T_4=40, k_1=0.1, K_2=0.98, K_3=0.98, K_4=0.1).

Another limiting function which affects the growth rate is related to the availability of nutrients and to the light limitation $f(I, N, P, C)$ and is defined as follows

$$f(I, N, P, C) = min(f(I), f(N), f(P), f(C)) \tag{5.18}$$

The limitation due to the availability of nutrient is described by the Michaelis–Menten equation and considering, for instance the Nitrogen, is expressed as:

$$f(N) = \frac{N}{N + K_N} \tag{5.19}$$

where N is the nutrient concentration and K_N is the half saturation concentration. In the simplified case of infinite availability of nutrients the half-saturation concentration could be taken zero in order to have $f(N)$=1, for instance.
The light limitation function is modeled using the Michaelis–Menten equation as for the nutrient limitation function:

$$f(I) = \frac{I}{I + I_h} \tag{5.20}$$

where, I solar radiation and I_h is the half saturation coefficient for solar radiation. It's important to underline here that the solar radiation I should be estimated at the plant depth and considering the effect of light attenuation in water. The first assumption is that a fraction (β) of the incoming short-wave radiation is absorbed at the water surface layer. Moreover the attenuation of light below the water surface could be estimated using the Beer-Lambert law as follows:

$$I(z_w) = (1 - \beta) I_0 e^{-k_e z_w} \tag{5.21}$$

where I_0 is the incoming short-wave radiation and k_e is the extinction coefficient and z_w is the water depth measured from the surface. Accordingly, $I(z_W)$ should be computed at the plant height but this estimate could be difficult in particular in river where, as reported by Carr et al. (1997) biomass is constantly displaced by water movements. Accordingly, one acceptable hypothesis could be to compute the available short-wave radiation at the mid-point of the water column instead of the bottom to better reflect the light conditions in the area where maximum photosynthesis occurs (Carr et al., 1997).
Equation (5.12) has been discretized explicitly for each *i-th* where the energy balance is solved to compute the temperature as follows:

$$C^{n+1}_{mac,CSTR_i} = (1 + \Delta t(\mu_{\mathrm{m,max}} f(I, N, P, C)\gamma_1\gamma_2 - K_{mr}\gamma_1 - K_{mm}\gamma_1)) C^{n}_{mac,CSTR_i} \tag{5.22}$$

This equation is used to evaluate the evolution of the biomass concentration in each CTSR during the simulation period.

5.6 Conclusions

As will be shown in the next Chapter of this Thesis, the effects of macrophyte growth on the roughness coefficient for the bottom of the channel can't be neglected for long time-span simulation. There are several methods to consider this effect during an hydraulic simulation, for instance by changing dynamically the Manning coefficient in time considering its seasonal variation. This method was applied for the simulation of the irrigation seasons presented in the next Chapter. On the other hand, the vegetation growth and its effects on roughness are primarily governed by some physical forcing as the water temperature, the solar radiation and the availability of nutrients. Although the dynamics of the water temperature can be measured

using a set of temperature sensors installed along the channel network, it requires an additional instrumental and operational burden and of course the direct measure can not be used in a predictive way. Accordingly, we decided to implement the numerical method presented by Pilotti et al. (2019) which solves the mass-averaged energy balance for a set of interconnected well mixed reactors that can share mass between each others. The mass-averaged energy balance considers both the radiative and non-radiative surface heat exchanges. The implemented model was then validated against the well-known software HEC-RAS 1D which incorporates a water quality model, providing very similar results despite different equations are implemented in HEC-RAS (e.g., long-wave radiation, sensible heat and latent heat). Finally, the results of the temperature model provides the input data for the macrophyte growth model proposed by Berger and Wells (2008) which was implemented after some simplification (e.g., extinction coefficient for light attenuation, infinite availability of nutrients). This aspect is very complex and to be improved, further investigation will be inevitable for its future improvement, requiring a botanic competence.

6 Application to the Vacchelli Irrigation Canal

6.1 Introduction

In the previous Chapters a hydrodynamic and thermal model of flow in a general channel network has been proposed and implemented. The model includes a coupled distributed module for computing weeds growth that, in turn, could be linked to a roughness variation model. Every separate component has been tested with simplified cases. In this Chapter we now consider the application of the whole model to a complex real case. To this purpose we selected the test case provided by one of the most important irrigation network in northern Italy, Consorzio Irrigazioni Cremonesi (CIC). Although the model can solve a network with a complex topology, only the main channel operated by CIC, the 34.5 km long Vacchelli canal, has been studied. The Vacchelli case is extremely important and interesting: its study will show the complexities of water shifts at the different withdrawal points, the dynamics of measured water temperature in the transfer along the canal and the time-variation of the stage-discharge curve over the irrigation period, under the effect of the water weeds growth along the canal. Another process that could emerge from the comparison between measured data and modeled results is the possible occurrence of infiltration through the bed of the canal. However, due to the lack of measured data on this process, it has been excluded from the present research.

6.2 Consorzio Irrigazioni Cremonesi

A peculiarity of northern Italy and, in particular, of Lombardy is the presence of large pre-alpine lakes that store several dozens of billions of cubic meters of water. In this area, since ancient time irrigation has exploited this water source and, more recently, from 1933 for Lake Iseo and later for other lakes, irrigation has taken advantage of the systematic regulation of pre-alpine lakes Maggiore, Como, Iseo, Idro and Garda, whose management rules and structure allow to store rain and snowmelt in winter and early spring and distribute it among the downstream users during late spring and summer when the water demand for irrigation purpose is higher. In this area, Consorzio Irrigazioni Cremonesi (CIC in the following) is one of the most important Irrigation consortium in the province of Cremona. It was founded in 1883 with the aim to build the Vacchelli canal (at the time called Marzano Canal), devised to divert water from the Adda watershed, in order to satisfy the water demand of the Cremona's lowland which was supplied by an insufficient amount of water (around 20 m^3s^{-1}) derived from the Oglio River. A collection of old photos of the Vacchelli canal is shown in Figure 6.1 showing some of the most important structures located along the canal.

Figure 6.1: Collection of old pictures of the Vacchelli canal. a) View of the intake structure, picture taken from downstream; b) Lagazzone structure (km 0.938); c) and d) stretch of the Vacchelli Canal; e) withdrawal structure of the Naviglio Civico Pallavicino at Salvirola (km 27.4) and f) The hydraulic structure located in Tombe Morte upstream the end of the Vacchelli Canal (Source: Archivio Consorzio Irrigazioni Cremonesi).

Currently, the maximum discharge derived by CIC is 57.779 m^3s^{-1} (38.5 m^3s^{-1} from the Adda River through the Vacchelli canal and around 16.379 m^3s^{-1} from the Oglio River and the remaining 2.9 m^3s^{-1} are provided from the spring-fed irrigation channels). However, according to the experience of the manager of the consortium, the last contribution is going to run out in the middle term due to over-exploitation of the aquifers. This overall discharge is distributed at many offtaking points by a network of open channels that is approximately 261 km long (Figure 6.2).

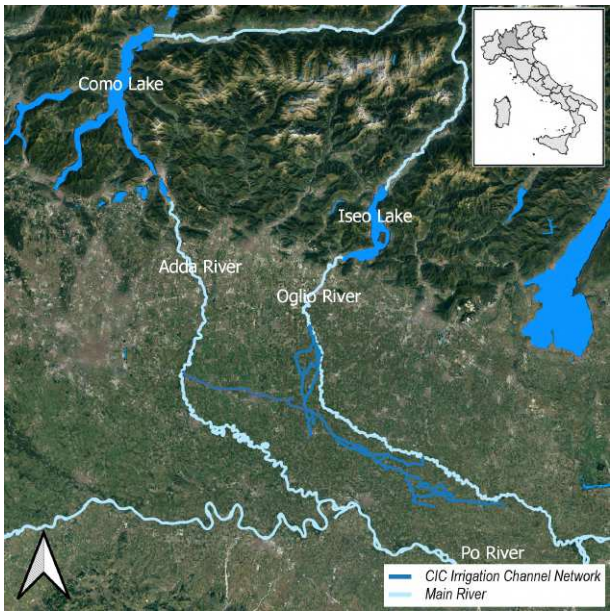

Figure 6.2: Satellite view of the study area highlighting the channel network (dark blue lines) managed by CIC.

The intakes of the channel network are provided by the regulation of pre-alpine Lake Iseo and Lake Como, whose level regulation dates back to 1930 and was defined by law considering a set of conflicting constraints as well as the water demand of the irrigated areas. CIC derives discharge from the Oglio and the Adda river, that are the effluents of Iseo and Como Lake, respectively. Four river intake structures are present along the Oglio river to convey discharges to four different branches of the channel network. On the other hand, the intake of the Pietro Vacchelli channel, the most important channel managed by CIC, is located along the Adda River. CIC is in charge of: 1) maintenance of the channels in the network 2) the control of the intake structures in accordance with the regulation of the upstream lakes 3) regulation of the delivery points according to the scheduled timetable of the water distribution. To regulate the gate at each water withdrawal points, the operators of CIC act on the basis of the contemporary level in the main channel, in order to guarantee the correct amount of discharge transferred from the main channel to the secondary channels. The channel network managed by CIC can be divided into two main districts: 1) the northern part of the channel network, composed by the channels Vacchelli, Geronda, Diramatore Bruno Loffi, Naviglio Grande Pallavicino, Naviglio Nuovo, Cavo Calciana, Molinara and Canale di Suppeditazione and the spring-fed channels. By means of these channels the water is derived from the main rivers (Oglio River and Adda River), along the route delivered from the main channel to the secondary channels at the different withdrawals points. Finally, the water coming from the Adda River and the Oglio River is conveyed to the node of Tombe Morte, where the remaining water from the Adda River conveyed by means of the Vacchelli canal fed the Naviglio Grande Pallavicino canal to satisfy the agricultural water demand of the southern part of the district. 2) The southern part of the district is composed by the main channels Naviglio Grande Pallavicino, Ciria Nuova, Canobbia Vecchia, Ciria Vecchia, Canobbia Nuova, Cavo Bolla, Diversivo Magio and Nuovo Delmona. A schematic representation of the Irrigation channel network managed by CIC is provided in Figure 6.3.

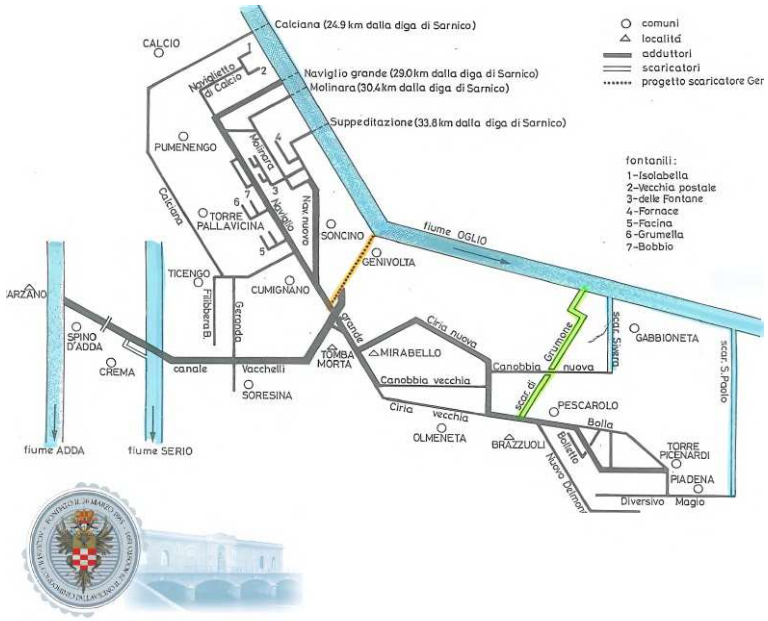

Figure 6.3: Schematization of the irrigation channel network managed by CIC (source: Archivio Consorzio Irrigazioni Cremonesi).

As mentioned above the water discharge is derived at different withdrawal points to supply the secondary channels: their functioning is described in Chapter 3 and two typical examples are shown in Figure 3.1. The discharge derived at each withdrawal points is specified in the timetable of the water distribution. This complex document, that is the final outcome of agreements accomplished over centuries of operation, provides the discharge, the duration of the withdrawals, the beginning and consequently the end of each water withdrawals, so called "turno d'acqua". Mainly, there are two types of regulation of the withdrawals points: 1) continuous withdrawals and 2) hourly withdrawals. In the first type of withdrawal point the gates are kept open during the whole irrigation season in order to derive the discharge as prescribed in the timetable of the water distribution. Daily, or even more frequently, the gates are regulated by the operator of the consortium in order to deliver the prescribed discharge in accordance to the level fluctuation in the main channel upstream of each gate. Fluctuations of the water level in the main channel can occur and are related to reduction or increase of the discharge at the inlet of the channel; otherwise, they can be the possible effect of the operation at different withdrawal points. To introduce the second category of withdrawals, some further definitions should be provided:

- The duration of the water shift (Du) which represents the number of hours during which the gate of a specific withdrawal point is kept open to derive the prescribed discharge;
- The shift (T), usually expressed in days which represents the number of days between two consecutive opening of the same gate.

An example of a hourly withdrawal is presented in Figure (6.4).

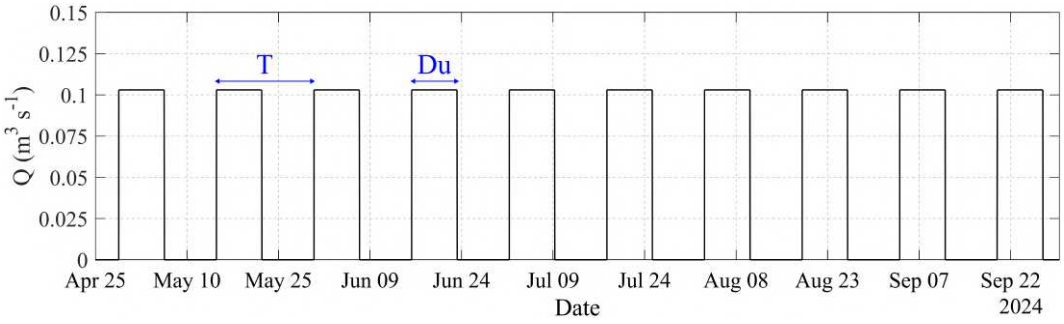

Figure 6.4: Example of an hourly water turn, Vacchelli Canal, Fiesca, T=16 days and Du= 179 hours.

Mainly, CIC adopts two different hourly water turns: in the first case the opening of the gate along with the duration and the shift is provided by a date (e.g. withdrawal Fiesca (Vacchelli Canal), opening 28th April at 20:00, Du=179 hours, T=16 days); on the other hand for some cases the opening is not provided with a date but using the day of the week (e.g. withdrawal Domenicani (Naviglio Grande Pallavicino), opening every Friday at 11:00, Du=6 hours). It's important to observe that due to this type of water shift, the combination of the water shifts in the management of the irrigation channel network over the year changes every year. Moreover, the incoming discharge of the irrigation channel network is related to the water availability of the water volume stored in the pre-alpine lakes. Accordingly, the consortium adopts a reduction coefficient ($0 < r < 1$) applied at each withdrawal and reduces the discharge supplied to the secondary channels according to the same reduction coefficient imposed upstream. In the following, to show the complexity of the water withdrawals in the CIC irrigation channel network, for each channel the location and the delivered discharge at each withdrawals points are shown. This data set is a fundamental requirement for modeling the irrigation channel and is made up of a digital description of the timetable of the water shifts along with the georeferenced location of each withdrawal point. We produced this data set starting from the corresponding written documents.

Vacchelli Canal

The Vacchelli Canal (Figure 6.5) is the most important channel managed by CIC and dates back to 1892. The length of this 25 m-wide trapezoidal channel is 34.5 km and it transfers 38.5 m^3s^{-1} outside from the Adda River watershed to the CIC irrigation area. Along the route the discharge is distributed to several secondary channels by means of 32 withdrawal points (22 continuous withdrawal and 10 hourly withdrawal, see Figure 6.6 and Figure 6.7 for details).

Figure 6.5: Withdrawal points along the Vacchelli Canal.

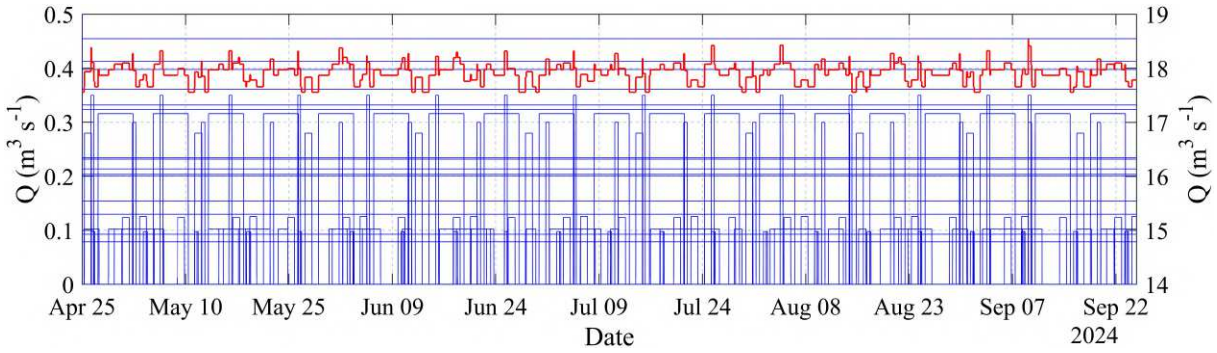

Figure 6.6: Timetable of the water shifts for the Vacchelli Canal: the solid red line represents the sum of the delivered discharge along the channel. Note that for visualization purposes the timetable of the water shift is limited to minor withdrawal points with Q< 0.5 m^3s^{-1}

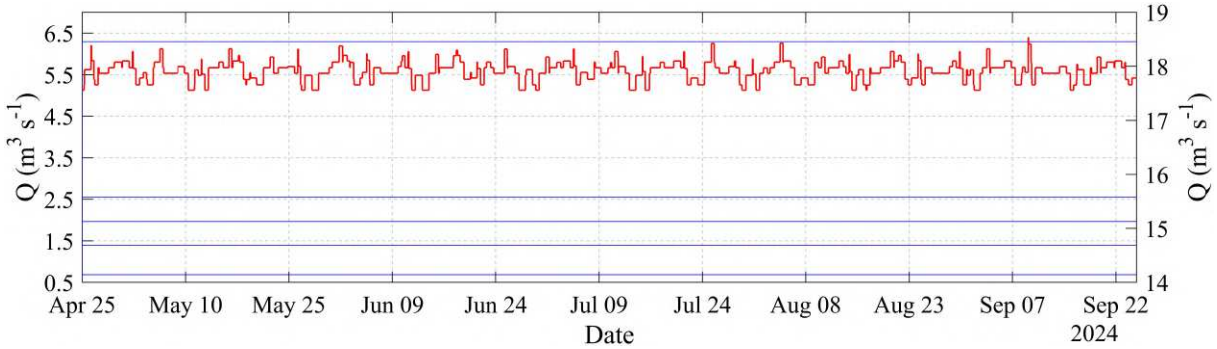

Figure 6.7: Timetable of the water shifts for the Vacchelli Canal: the solid red line represents the sum of the delivered discharge along the channel and the blue lines are the major withdrawals (Q>0.5 m^3s^{-1}), that are steady over the season in absence of reduction.

Geronda Canal

The Geronda Canal (Figure 6.8) is a channel which is fed by the Vacchelli Canal. The length of the Geronda Canal is around 7.5 km and 12 withdrawal points are located along its route (9 continuous withdrawals and 3 hourly withdrawals, Figure 6.9).

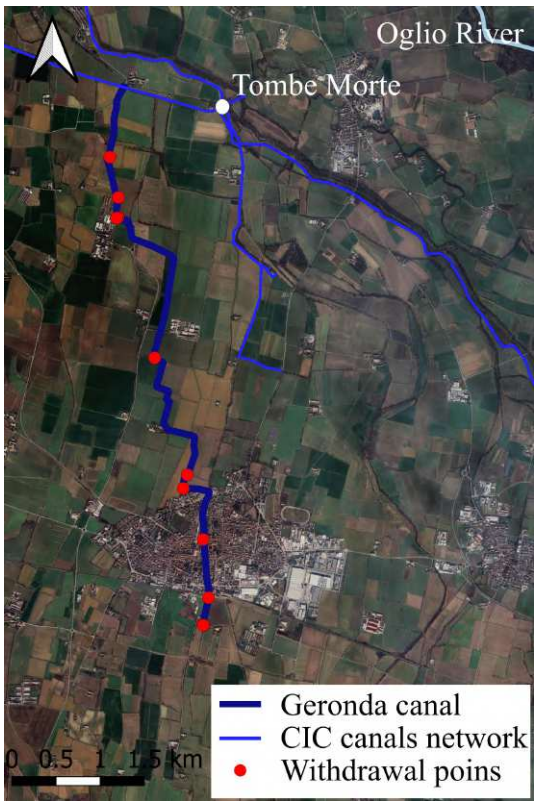

Figure 6.8: Withdrawal points along the Geronda Canal.

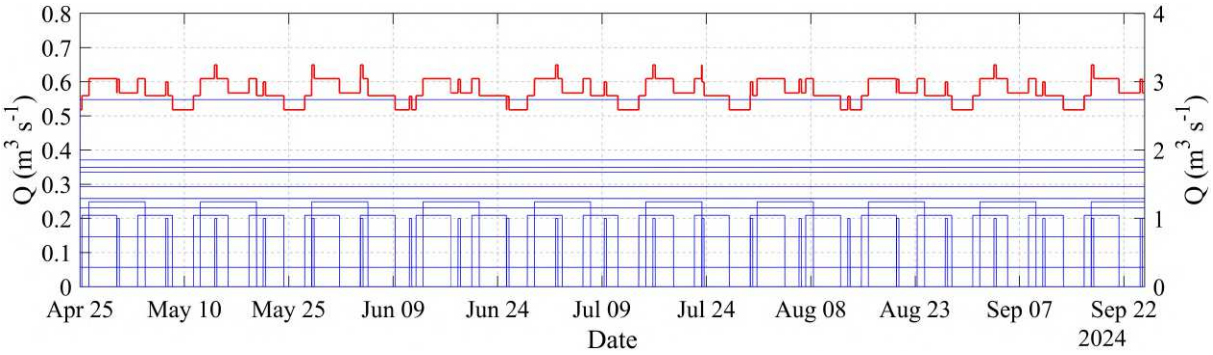

Figure 6.9: Timetable of the water shifts for the Geronda Canal. The solid red line represents the sum of the delivered discharge along the channel.

Diramatore Bruno Loffi

The Diramatore Bruno Loffi canal derives its discharge from the Vacchelli canal by means of a gate close to the Tombe Morte node (Figure 6.10); it is around 3.6 km long and along its route there are 12 withdrawal points (6 continuous water withdrawals and 6 hourly water withdrawals, Figure 6.11).

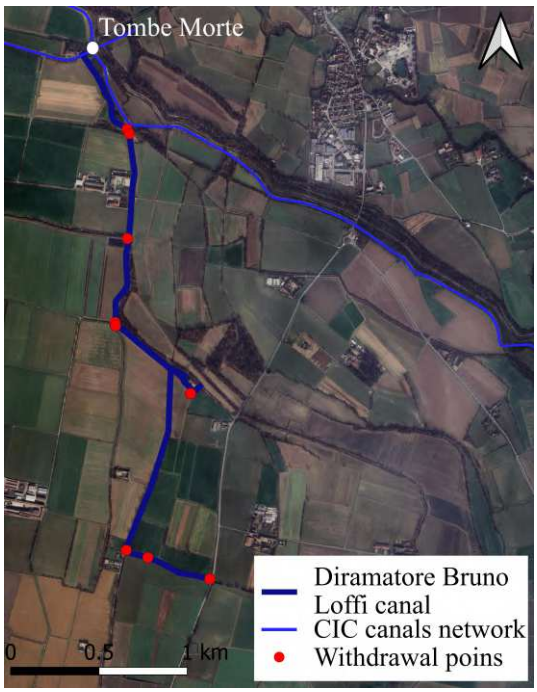

Figure 6.10: Withdrawal points along the Diramatore Bruno Loffi Canal.

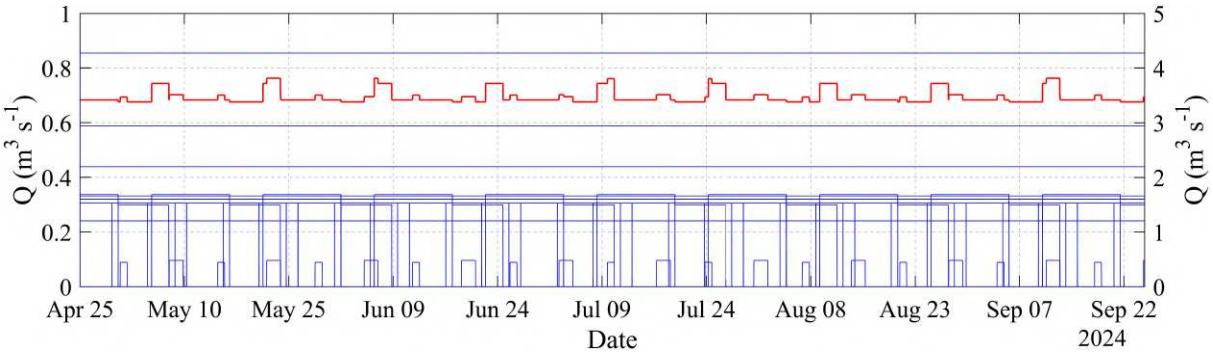

Figure 6.11: Timetable of the water shifts for the Diramatore Bruno Loffi Canal. The solid red line represents the sum of the delivered discharge along the channel.

Naviglio Grande Pallavicino Canal (upstream Tombe Morte)

Naviglio Grande Pallavicino (Figure 6.12) is one of the oldest canal managed by CIC, dating back to the middle age. It is one of the four channels which derive discharge from the Oglio River. Along its route upstream the node of Tombe Morte 26 withdrawal points (11 continuous withdrawal and 15 hourly withdrawal, Figure 6.13 for details) are placed.

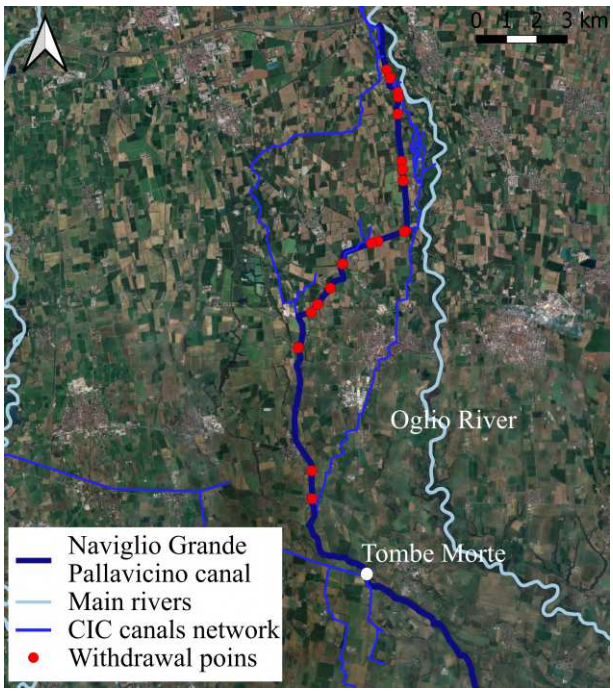

Figure 6.12: Withdrawal points along the Naviglio Grande Pallavicino upstream the node of Tombe Morte.

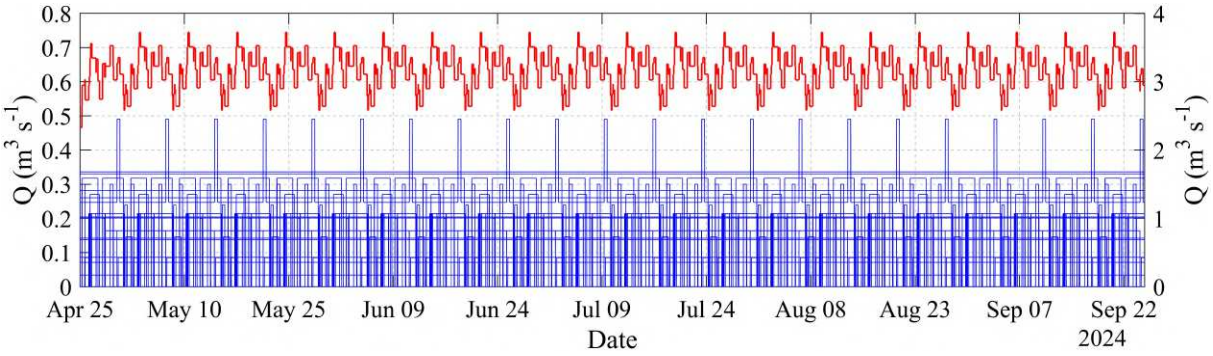

Figure 6.13: Timetable of the water shifts for the Naviglio Grande Pallavicino. The solid red line represents the sum of the delivered discharge along the channel.

Cavo Calciana

Cavo Calciana (Figure 6.14) canal is managed by CIC and derives its discharge from the Oglio River. Along its route 12 withdrawal points (7 continuous withdrawal and 5 hourly withdrawal, Figure 6.15 for details) are located. The residual discharge not supplied to the secondary channel by means of the withdrawal points is eventually conveyed into the Naviglio Grande Pallavicino Canal.

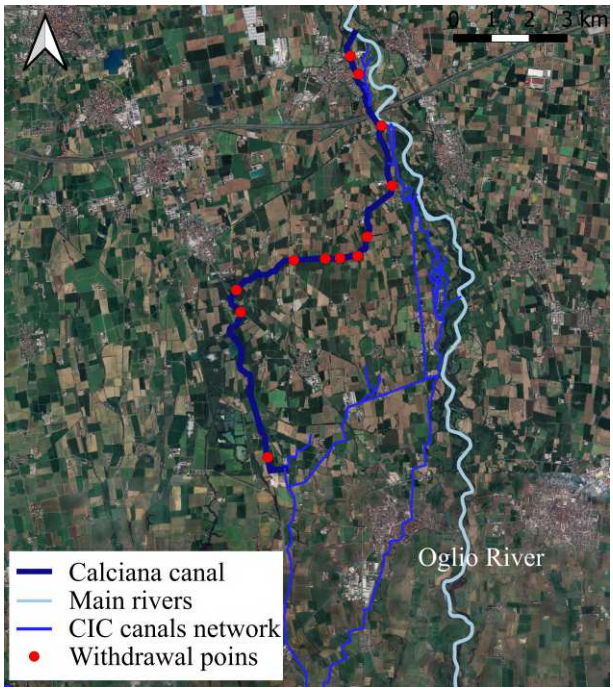

Figure 6.14: Withdrawal points along the Cavo Calciana canal.

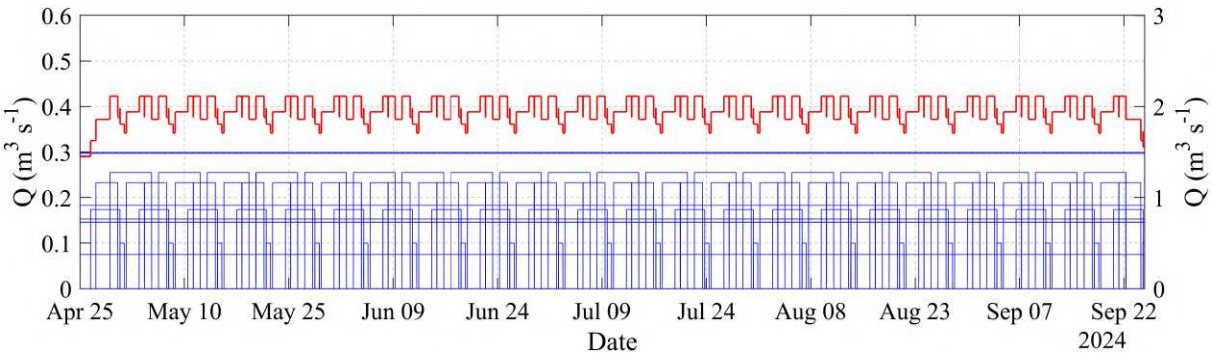

Figure 6.15: Timetable of the water shifts for the Cavo calciana canal. The solid red line represents the sum of the delivered discharge along the channel.

Molinara Canal

The Molinara Canal is fed by the Oglio River (Figure 6.16); it is around 4 km long and along its route only two withdrawal points are located (2 hourly water withdrawals, Figure 6.17). The residual discharge is conveyed into the Naviglio Nuovo canal and consequently into the Naviglio Grande Pallavicino canal.

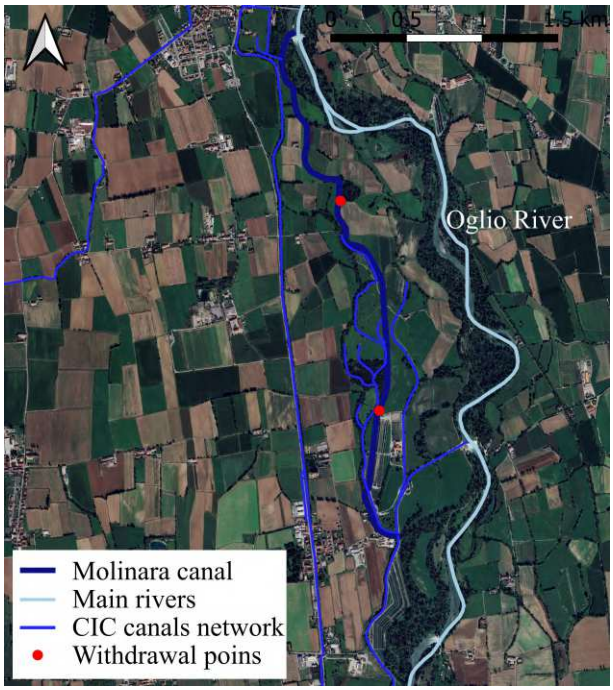

Figure 6.16: Withdrawal points along the Molinara canal.

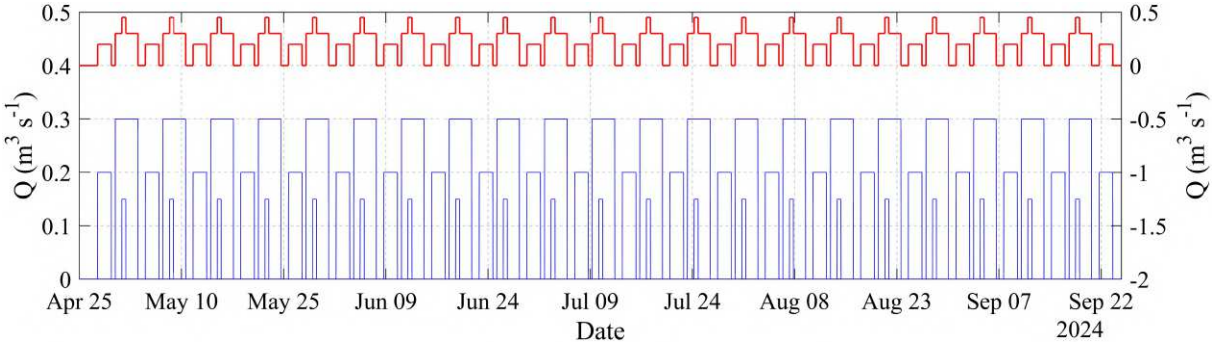

Figure 6.17: Timetable of the water shifts for the Molinara canal. The solid red line represents the sum of the delivered discharge along the channel.

Naviglio Nuovo

The Naviglio Nuovo canal derives discharge from the Oglio River by means of the Suppeditazione Canal (Figure 6.18); it is around 13 km long and along its route six withdrawal points are located (5 continuous water withdrawals and 1 hourly water withdrawals, Figure 6.19). The residual discharge is conveyed into the Naviglio Grande Pallavicino canal.

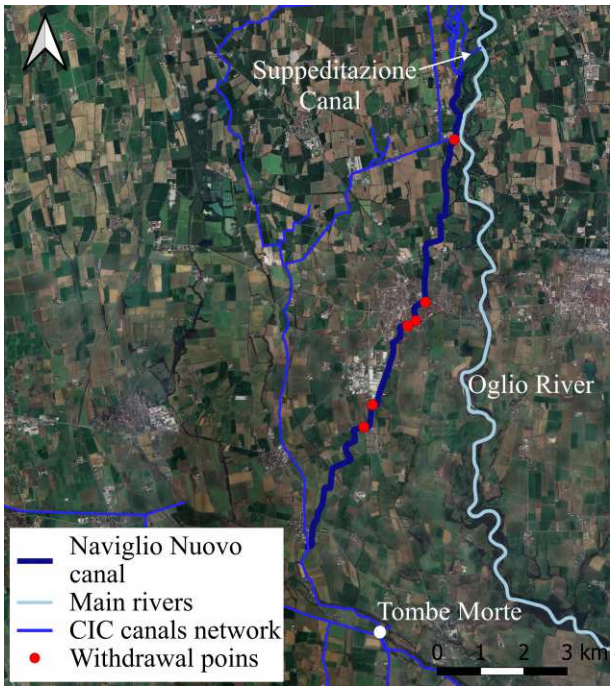

Figure 6.18: Withdrawal points along the Naviglio Nuovo canal.

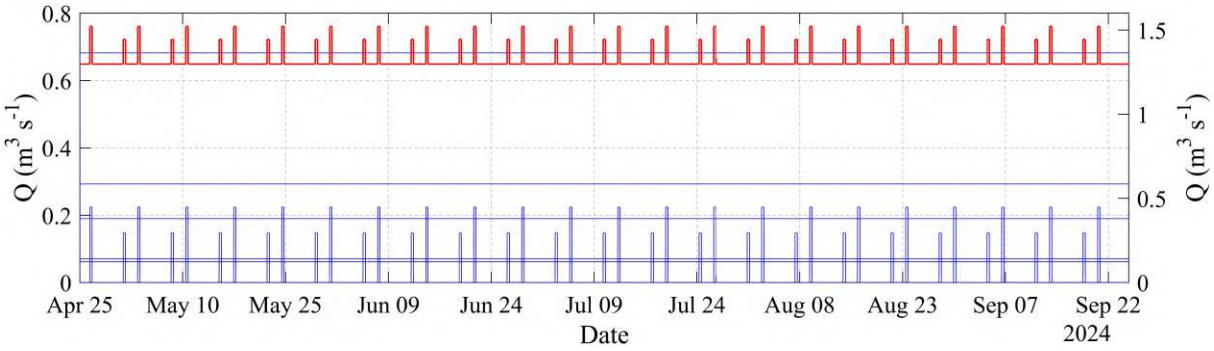

Figure 6.19: Timetable of the water shifts for the Naviglio Nuovo canal. The solid red line represents the sum of the delivered discharge along the channel.

6.3 Monitoring System and field activities accomplished in this study

The management of Consorzio Irrigazione Cremonesi takes advantages from a dense monitoring network managed by HORTUS which allows to monitor the channel network in real time. The main variables measured at different strategic points (the location of the monitoring points is shown in Figure 6.20) are reported in Table 6.1.

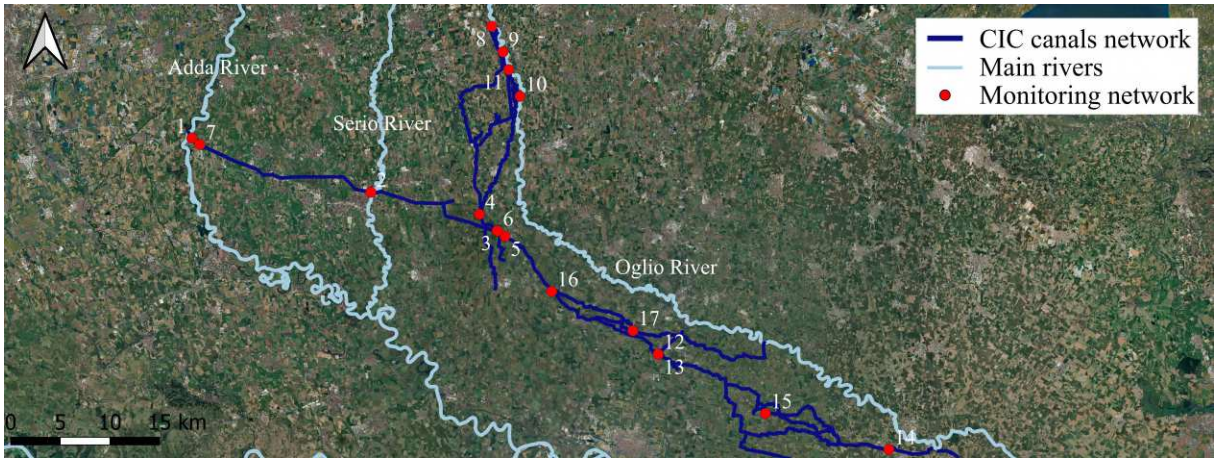

Figure 6.20: Location of the monitoring station along the Channel Network Managed by CIC.

Table 6.1: Time interval, acquisition frequency of the different monitoring stations installed along the Irrigation Channel Network managed by CIC.
* The discharge is computed considering the measured surface velocity.
** The discharge computed by means of the surface velocity is under calibration.

ID	***Measured Parameters***	***Frequency***	***Canal***
1	Water Depth	1 / 30 minutes	Pietro Vacchelli
2	Water Depth	1 / 30 minutes	Pietro Vacchelli
3	Water Depth	1 / 10 minutes	Pietro Vacchelli
4	Water Depth	1 / 30 minutes	Naviglio Grande
5	Water Depth, Velocity, Discharge*	1 / 10 minutes	Naviglio Grande
6	Water Depth	1 /10 minutes	Naviglio Grande
7	Water Depth, Velocity, Discharge**	1 / 10 minutes	Pietro Vacchelli
8	Water Depth	1 / 30 minutes	Cavo Calciana
9	Water Depth	1/10 minutes	Naviglio Grande
10	Water Depth, Velocity, Discharge*	1 / 10 minutes	Canale di Suppeditazione
11	Water Depth, Discharge	1/ 5 minutes (Water Depth) 1/ 10 minutes (Discharge)	Roggia Molinara
12	Water Depth	1/ 30 minutes	Ciria Vecchia
13	Water Depth	1 /30 minutes	Ciria Vecchia
14	Water Depth	1 / 30 minutes	Diversivo Magio
15	Water Depth	1/ 30 minutes	Ciria Vecchia
16	Water Depth	1/ 10 minutes	Naviglio Grande
17	Water Depth	1 /10 minutes	Canobbia Nuova

In addition to the large amount of data provided by the monitoring system of CIC, during

the irrigation season some discharge measurements are performed along the irrigation channel network (e.g. to test whether the measured discharge matches the measurement provided by the monitoring network or if the discharges are correctly diverted along the different branches). To this purpose, CIC measures the discharge by means of the ADCP StreamPro 2 MHz (Figure 6.21) that is one of the favorite solution for making discharge measurements for medium and small streams in practical situations (Lee et al., 2014).

Figure 6.21: ADCP StreamPro 2 MHz used by CIC

StreamPro ADCP 2 Mhz is designed for small and medium-size stream with a depth up to 6 m. The discharge measurements are performed slowly moving along the considered cross section from bank to bank until the measured mean discharge is considered stable. The StreamPro ADCP 2 Mhz divides the water column in a set of bins or cells (1-30) and with a cell size of 2 up to 20 cm, by means of the doppler effect the ADCP measure the velocity for multiple bins along the vertical (ensemble). To track the location of the ADCP along the cross section two options are available: by bottom tracking or by means of the GPS. The first option was used for all the measurement, considering that the GPS tracking is particularly useful in case of moving bed (Mueller et al., 2013), that is negligible for the Vacchelli canal. The discharge measurements performed using ADCP StreamPro 2 MHz can't measure the discharge for the whole water column. Actually, the following factors should be taken into account that lead to unmeasured areas: the immersion of the transducer (transducer depth); the blanking distance where the data cannot be measured; an additional area due the measurement mode and due the dimensions of the bins. Additionally, the discharge near the bed cannot be measured by the ADCP due to the potential side-lobe reflection effect (Teledyne RD Instruments, 2021) so excluding 6% of the distance between the transducer and the bottom. Lastly, when the water depth is shallow in correspondence of the banks, the ADCP is unable to make a valid measurement of the discharge. Accordingly, the total discharge is computed by the sum of the measured discharge in the cross section and the estimated discharge for the unmeasured areas (Figure 6.22):

$$Q_{ADCP} = Q_{Left} + Q_{Top} + Q_{Measured} + Q_{Bottom} + Q_{Right} \tag{6.1}$$

where, Q_{ADCP} is the total discharge, Q_{Left} is the estimated discharge for the left edge, Q_{Top} is the estimated discharge for the area close to the water surface, Q_{Right} is the estimated discharge

for the right edge, Q_{Bottom} is the estimated discharge at the stream bed and $Q_{Measured}$ is the measured discharge.

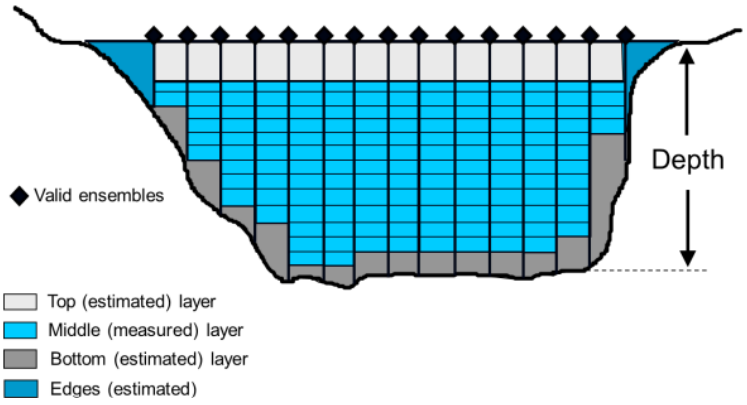

Figure 6.22: Measured and unmeasured areas of an ADCP (from Mueller, 2016).

With reference to the measured discharge ($Q_{Measured}$), the discharge for a cell is defined as follows:

$$Q_{bin} = A_{bin} V_{f,bin} \tag{6.2}$$

where A_{bin} is the area of a single bin and $V_{f,bin}$ is the mean water velocity perpendicular to the area of the bin. The area of each bin can be computed by:

$$A_{bin} = W dz = |\vec{V}_{boat}| dt dz \tag{6.3}$$

where W is the width of the bin and dz is the cell height defined during the configuration of the ADCP. Considering that the ADCP is moving from one bank to the opposite one, the width of each bin is defined by the product of the magnitude of the velocity vector of the boat ($|\vec{V}_{boat}|$) and the time between two consecutive ensembles. The velocity perpendicular to the bin can be computed as follow:

$$V_{f,bin} = \vec{V}_w \cdot \vec{\mathbf{n}} \tag{6.4}$$

where $\vec{V}_w$ if the water velocity vector and $\vec{\mathbf{n}}$ is the unit normal vector to the velocity vector of the boat. Combining Equation 6.4 and Equation 6.3 into Equation 6.2 the discharge across each bin is computed as follow:

$$Q_{bin} = (\vec{V}_w \cdot \vec{\mathbf{n}}) |\vec{V}_{boat}| dt dz \tag{6.5}$$

Equation 6.5 can be manipulate in order to obtain an expression of Q_{bin} in terms of the water and boat velocity component (Teledyne RD Instruments, 2021):

$$Q_{bin} = ((\vec{V}_w \times \vec{V}_{boat}) \cdot \hat{\mathbf{k}}) dt dz = (V_{w,x} V_{boat,y} - V_{w,y} V_{boat,x}) dt dt \tag{6.6}$$

where $\hat{\mathbf{k}}$ is the vertical versor. Finally, $Q_{Measured}$ can be written as the sum for all the bins in the measured zone:

$$Q_{Measured} = \sum_{j=1}^{Ensembles} \sum_{i=1}^{Bins} Q_{bin} \tag{6.7}$$

The analysis and the post-processing of the discharge measurements are performed by means of WinRiver II. This software provides different options to estimate the discharge in the unmeasured zone. Accordingly, the bottom discharge can be computed considering two options (Teledyne RD Instruments, 2021):

- No slip: using this method the software use the lower 20 % of the valid bins to fit a power law and force it through zero at the riverbed;
- Power Method: in this case the software compute the bottom discharge fitting Chen power law proposed for open channel (See Teledyne RD Instruments, 2021 for details).

For the estimate of the discharge at the top layer (Q_{Top}) three options are available:

- Constant: using this method the software use the upper valid bin to compute the discharge assuming the velocity constant in the unmeasured layer;
- three point slope: this method uses the top three bin to estimate a slope used from the top of the bin to the water surface;
- Power Method.

The discharge for the edges is estimated using the following equation:

$$Q_{edges} = CV_m L d_m \tag{6.8}$$

Where C is a coefficient whose value is defined according to the assumed shape of the edge area (triangular or rectangular), V_m is the mean velocity in the first or last segment, d_m is the depth of the first or last ensemble and L is the distance from the banks.
As mentioned above, the macrophyte growth in channel is governed by some physical parameters (e.g. the water temperature and the short wave radiation) and accordingly was measured at the inlet of the Vacchelli Canal and at the end of the Vacchelli Canal (respectively, ID 1 and 3 in Figure 6.20). The temperature was monitored by means of the HOBO U20L-04 Water Level Data Logger probe (Accuracy: ±0.44°C, Response time: 10 minutes in water) and the probe HOBO Water Temp Pro v2 Data Logger probe (Accuracy: ±0.21°C, Response time: 5 minutes in water). The probes were placed at the bottom of the canal, the acquisition frequency has been set in the range 1 / 10 minutes or 1 / 5 minutes. Figure 6.23 shows the periods of time when the temperature probes were working and the days of the discharge measurements.

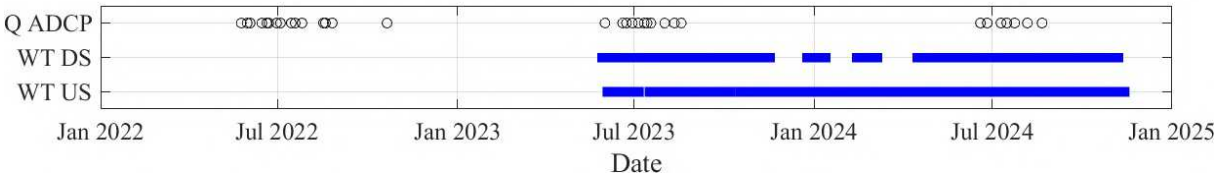

Figure 6.23: Periods of time when the temperature probes were working and the days of the discharge measurements (WT= Water Temperature, Q=Discharge).Some discharge measurements were conducted by the operators of Consorzio dell'Adda.

6.4 Mass Balance for the Northern Canal Network of CIC

The timetables shown above can provide a clear insight on the complexity of the actual spatial and time variability of the discharge flowing in each branch of the network. Managing this complexity is challenging and can't be done on the basis of the simple visual observation of the different timetables. A first step toward a growing level of control is obtained by integrating the different timetables, along with the corresponding reductions, within a code that provides the algebraic sums of the discharges at each point of the network on the basis of the scheduled water supplies and withdrawals. In this way, one could obtain a theoretical curve that provides the discharge availability at each point of the network over time. This would provide a simplified model, based on the conservation of mass only and on the assumption of a constant inflow and instantaneous transfer of the flowing discharge along the canal. Actually, this model doesn't account for the time necessary for a given operation (e.g. reduction of discharge, opening/closing of a gate) to become effective at a specific point. However every infinitesimal discharge variation in a free surface flow is propagated as a level perturbation that propagates with a relative celerity

$$\sqrt{gy} \tag{6.9}$$

where y is the water depth. Accordingly, a finite discharge variation does not propagate immediately. Another reason of approximation is because the timetable does not account for any mutual interaction between the different water withdrawals: in other words, it assumes that at the withdrawal points the delivered discharge to the secondary channels is precisely as prescribed in the timetable. In reality, the withdrawal is governed by the gate regulation on the basis of the contemporary water levels upstream and downstream the gate. However, the upstream level is affected by the withdrawal adjustment at the other secondary channels, whose effects propagate along the Vacchelli channel with different celerities. Accordingly, in reality a progressive adjustment of the gate opening is needed. However, in our experience even this methodology, that would provide a first glimpse of the current water distribution in a network, is not usually available. The correct answer to the problem must take into account both mass and momentum balances, having imposed as boundary conditions the inputs and the withdrawals scheduled by the different timetables. However, one may wonder what is the gap between these two description of the process: accordingly, we believe it can be of operative interest to compare the distribution provided by the simplified mass-based approach with the distribution obtained on the basis of the Saint-Venant Equations, as done in the following where we show the Q(t) curves obtained at the Tombe Morte section operating with the two approaches described above. To show a clear picture of the process we considered a simplified upstream boundary condition of the Vacchelli Canal, with an operation of the gates at the inlet that varies the entering flow discharge from 35 m^3s^{-1} to 38.5 m^3s^{-1} and then goes back to 35 m^3s^{-1} after 1 week, as reported in Figure 6.24.

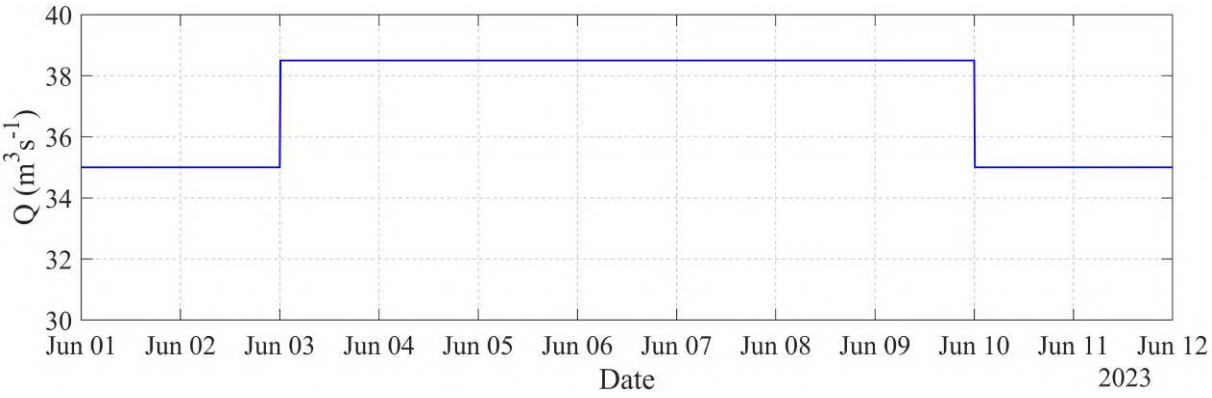

Figure 6.24: Discharge time series used as upstream boundary condition

The digitized time table of the water shift was added as source term in the conservation of mass equation of the Saint-Venant Equations. The comparison at the Tombe Morte node between the results for the hydraulic simulation compared with the ones provided by the mass balance only are reported in Figure 6.25

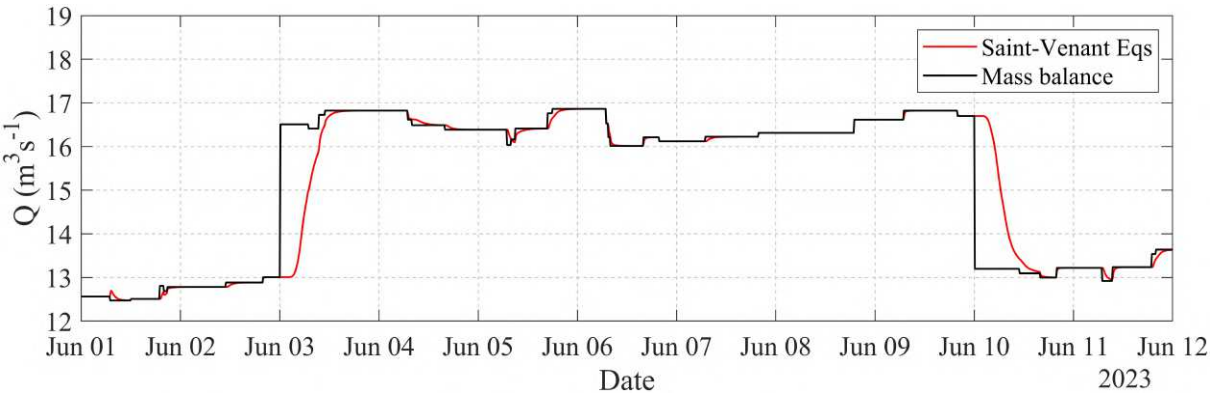

Figure 6.25: Comparison of the discharge variation over time obtained using the Saint-Venant Equations and the mass balance approach at the end of the domain (Tombe Morte)

As one can expect, the two solutions are identical only when they converge to a steady state because the simple mass balance completely misses the change travel time of each discharge variation and has the disadvantages of overestimating/underestimating the flowing discharge for a specific node of the hydraulic network. As shown in Figure 6.25, at Tombe Morte, a simple mass balance would anticipate an increase of discharge that, in reality, happens with 10 hours of delay. The actual amount of error on volume depends on the discharge variation and the relative location, as one can observe by comparing, for example, the gap on the first discharge increase on June 3 with the following smaller increase on June 5. In this case, the overestimation of discharge availability at Tombe Morte on June 3 amounts to a volume of about 60 000 cubic meters. If a discharge increase is anticipated by the simple mass balance, the opposite is true for the reduction. Accordingly, the volume "lost" at Tombe Morte during the rising limb is made available now. Since water distribution is not a matter of volumes only but also of timings, there might be a practical difference for the end users. Accordingly, a monitoring system based on mass balance only has misses all the transient flows due to operations at the upstream cross sections (increase or decrease of discharge) and at the withdrawals point related to the timetable

of the water assignment. These type of considerations are also valid with reference to the regulation of the gates which feed the secondary channels along the main channel. The opening, closure or regulation of a gate in accordance with the timetable of the irrigation water shift corresponds in a reduction/increase of the discharge in the main channel that is immediately transferred downstream if a mass-balance approach is considered. Indeed, the mass balance approach completely misses the discharge change travel time of each gate operation along the channel. Focusing in the period from June 3 to June 6 reported in Figure 6.26 it's possible to draw some insights regarding the discharge change delay for gate operation and their respective combination along the irrigation channel:

- Considering the period highlighted in A in Figure 6.26, two gates were moved. The gate located at km 32.637 closed on June 3 at 9.30; the gate located at km 33.500 delivered the discharge to the secondary channel on June 3 from 7.00 to 11.00. Additionally, during this period the discharge variation imposed upstream is traveling to the node of Tombe Morte. It's interesting to observe how the gate opening and closure combine with the discharge variation imposed upstream.
- Considering the period highlighted in B in Figure 6.26, three gates are opened. The gate located at km 32.944 opens on June 4 at 7.00; the gate at km 20.630 opens at 8.00 and the gate at km 27.396 opens at 16.00. As expected the discharge variation arrives at Tombe Morte as function of the withdrawal point distance.
- In the period highlighted in C in Figure 6.26, three gates are opened. The gate at km 29.845 starts delivering discharge to the secondary channel on June 5 at 7.00. The gates at km 32.944 and km 27.396 stop delivering discharge respectively on June 5 at 9.00 and 8.00. It's worth to observe how the combination of these operations arrives at Tombe Morte node.

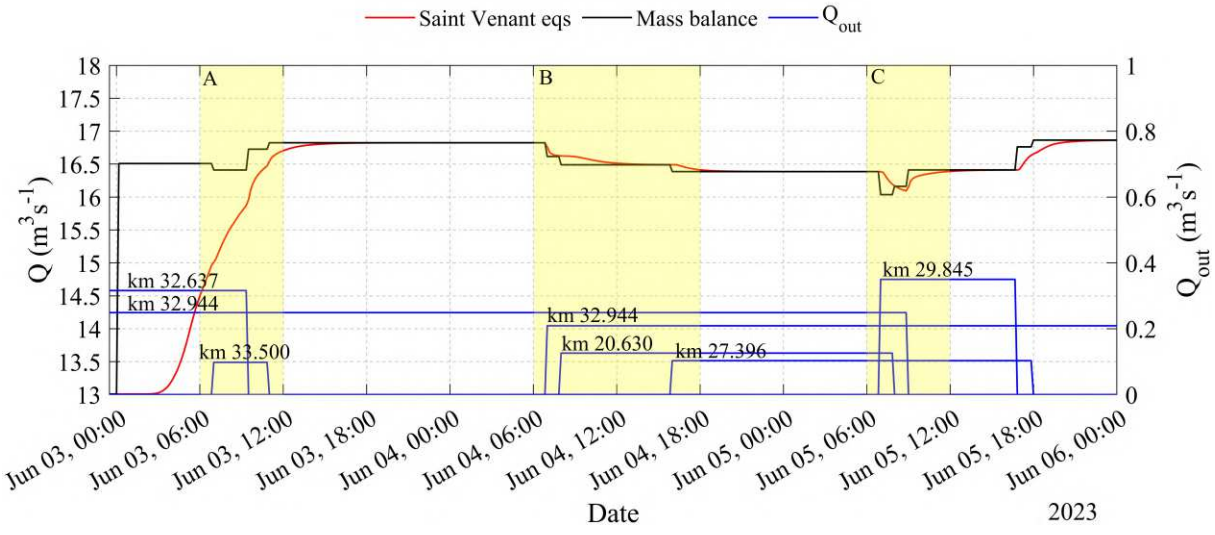

Figure 6.26: Comparison of the discharge variation over time obtained using the Saint-Venant Equations and the mass balance approach at the end of the domain (Tombe Morte) in the period from from June 3 to June 6. Note that two water whithdrwals points are placed at same transect km 32.944 because the gates are placed on the secondary channel Geronda Canal.

This simple consideration provides a clear evidence that using a model based on the Saint-Venant Equation is the accurate and necessary option to be followed whenever the delay and the combination of the discharge variation along the channel is the purpose of the study. The error depends on the magnitude of the discharge variation and on the distance from the check point. The advantages on the use a model based on the solution of the Saint-Venant Equations can be clerly highlighted considering the propagation of the gate regulation in the space-time plane (Figure 6.27). For instance, let us consider a channel characterized by three offtaking points located at (x_1,x_3 and x_5) characterized by the water shifts provided in Figure 6.27c. As can be seen in Figure 6.27b using the simple mass-balance, the regulation at each gate is instantaneously propagated downstream in the domain (blue arrows in Figure 6.27b). On the other hand, if Saint-Venant Equations are considered the gate regulation is propagated according with its celerity (red arrows in Figure 6.27b; for simplicity the celerity is considered constant in this example) providing the area in the space-time that are affected by the regulation.

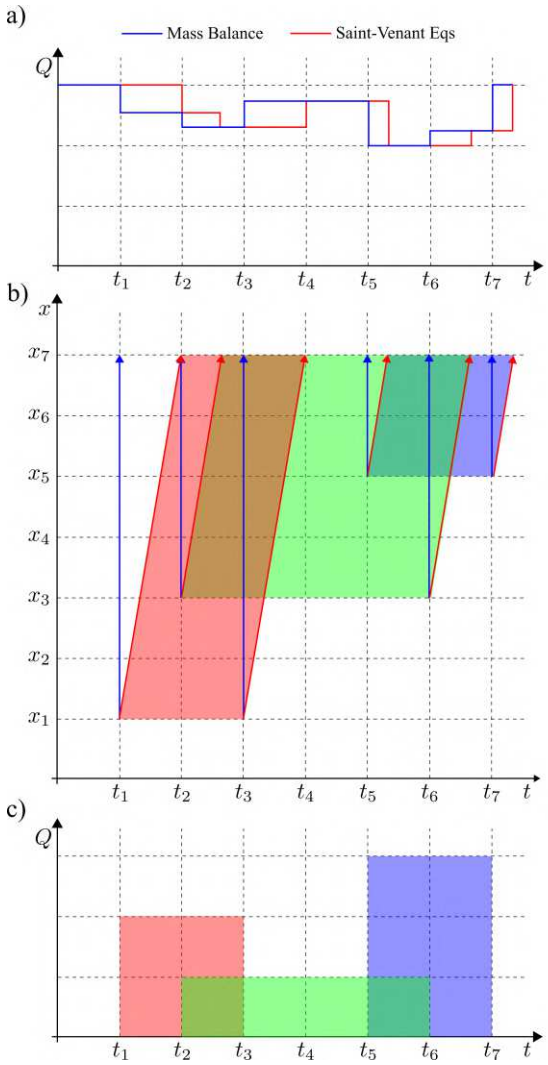

Figure 6.27: a) Comparison of the time series of the discharge at location x_7 computed using mass balance only and considering the gate regulation propagation celerity. b) Celerity of the gates regulation in the space-time plane. c) Timetable of the water shift for the offtacking points located at x_1 (red), x_3 (green) and x_5 (blue).

From Figure 6.27b it is also evident that the actual offtake at x_3 will be affected by the offtake when $t > t_2$. Accordingly, the inital opening at x_3 will have to be changed in order to respect the scheduled discharge at x_3. The space-time plane can be used to compare the mass balance model with the model based on the Saint-Venant Equations. The difference between the two models in terms of discharge shows clearly the propagation in time and space of the different regulations of the gate and the area where the steady state is reached . The comparison for the case of Figure 6.26 is shown in Figure 6.28.

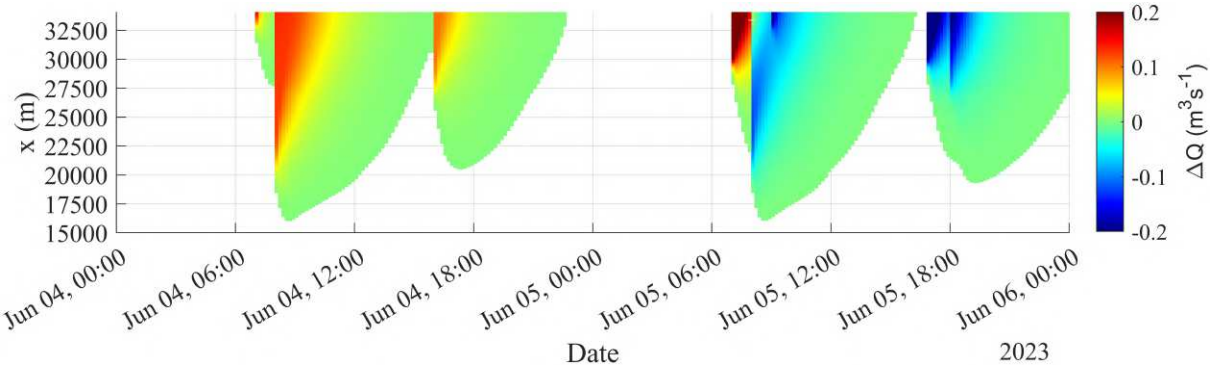

Figure 6.28: Discharge difference between the model based on mass balance only and the model based on the Saint-Venant Equations in the space-time plane.

6.5 Application of the Numerical Model to the Vacchelli Canal

As seen before, the Vacchelli canal, shown in Figure 6.29, distributes its discharge along its route to secondary channels by means of 32 withdrawal points. Along the channel 3 water level gauges are located (Figure 6.29) which measure the water level in time:

- **G01**, located at the beginning of the canal.
- **G02**, located in Crema, upstream the bridge-canal which crosses the Serio River.
- **G03**, located at the end of the channel, upstream of Tombe Morte node.

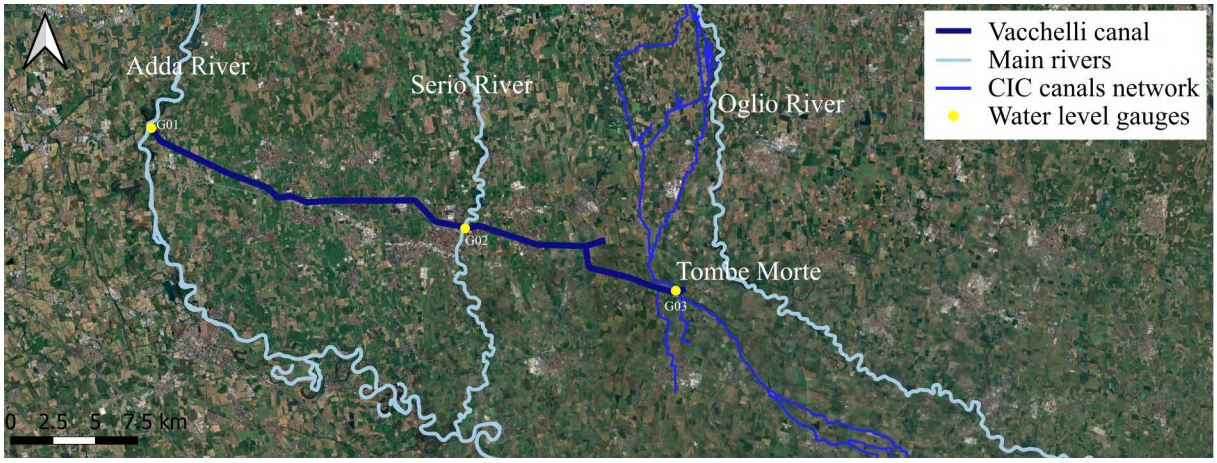

Figure 6.29: Satellite view of the study area highlighting the irrigation channel network managed by CIC and the Vacchelli canal and the location of the gauge (yellow dots) used to measure the water depth.

At the gauge station, G01 a stage-discharge curve was calibrated over the year to compute discharge of the Vacchelli canal on the basis of the measured water level. Usually, the water gauge and the corresponding stage-discharge curve should be located in a control section where there is a biunivocal relation between the water level and the discharge. Typically it happens upstream of a sufficiently long stretch of subcritical flow where the boundary condition along the channel and the other forcing that determine the water profile (e.g., the roughness) do not change over time, so that a biunivocal relation between stage and discharge can be established, possibly also empirically (WMO, 2010). However, in some cases, there might be an issue related to the aquatic vegetation, whose growth on the banks or on the bottom of the bed over the year, strongly affects the roughness, so that the channel stage increases for a given discharge (e.g. Perret et al., 2021; WMO, 2010). This is a well known and important stumbling block, that is often ignored or neglected but, as we'll see in the following, has a fundamental role in changing the stage-discharge relation. The consortium, well-aware of this issue conducts weekly or even more frequently discharge measurements during the irrigation seasons to evaluate the effect of vegetation. On the basis of these measurements, acquatic vegetation is eventually removed from the channel. Moreover a SVR (surface velocity radar) was recently installed at the inlet of the Vacchelli Canal to continuously monitor the discharge. Accordingly, during the irrigation season in the years from 2010 to 2024 a set of discharge measurements have been conducted by the Consortium. The measurements were conducted at the transect km 1.287 and were combined with the water level measured continuously at the gauge station. Between these two points no

water inlets or outlets are present and, neglecting the infiltration losses that are deemed minor, the discharge is assumed to be the same. During the years of measurements no changes that could affect the level at the gauge station (sedimentation on the bed or hydraulic structure construction) were observed. The stage-discharge measured data are shown in Figure 6.30.

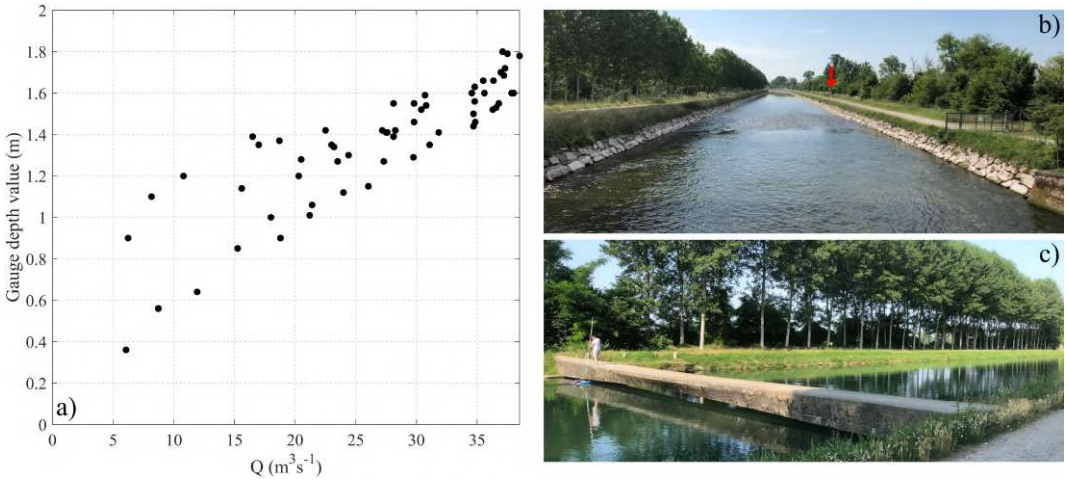

Figure 6.30: a) Discharge measurement data in the period 2010 - 2024, b) location of the gauge station c) location where the flow discharge is measured (km 1.287).

As can be seen in Figure 6.30a there is clear evidence that the water depth at this location is affected from downstream, because the same discharge can flow with different depths over the season. To understand the effect of vegetation on roughness a steady state simulation of the Vacchelli Canal was accomplished with HEC-RAS. The model was limited to the stretch between the inlet and Crema, after numerically proving that the effect of the downstream boundary condition does not affect the investigated stage-discharge curve. This model was used to calibrate the roughness of the channel when it is not affected by the vegetation at the beginning of the irrigation season when the bottom is still reasonably clear and the high discharges lead to conditions of high submergence and, accordingly, of low relative roughness of the vegetation. From a technical point of view in the following the zero of the stage-discharge curve is the elevation of the bottom at the inlet of the channel. On the other hand, the measurements are accomplished at the gauge station, located 200 m downstream where the bottom elevation is 0.15 m lower. In conclusion, the stage level is converted in elevation a.s.l. by adding 0.15 m. In Figure 6.31 the stage discharge curve obtained using the Manning's roughness coefficient n= 0.035 s $m^{-1/3}$ for the banks and 0.021 s $m^{-1/3}$ for the bottom is shown.

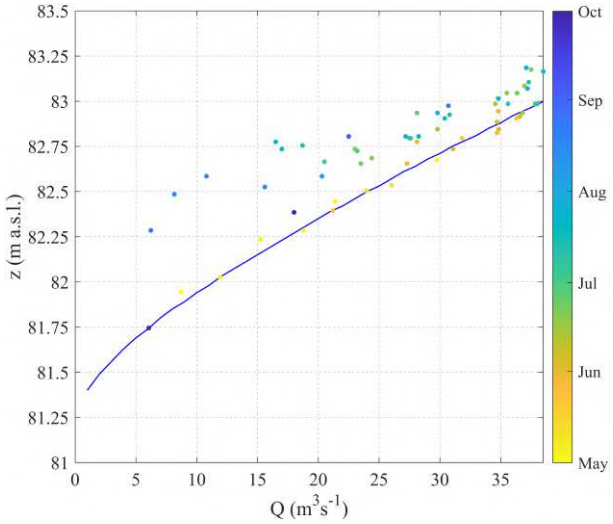

Figure 6.31: The blue solid line represents the computed stage-discharge curve (n= 0.035 s $m^{-1/3}$ for the banks and 0.021 s $m^{-1/3}$ for the bottom) and the points are the stage-discharge measurements during the year. Note that for graphical purposes the color ramp is limited to the period between May and October.

As can be seen from Figure 6.31 the measured stage for a fixed discharge increases as the irrigation season progresses, detaching from the curve. Accordingly, it is clear that the hypothesis of a stationary "clean channel configuration" is violated. Note that usually, due to this effect, the consortium removes the vegetation from the bottom of the channel between the end of June and July. Accordingly, due to the effect of vegetation, the classical approach based on stage-discharge curve, cannot be used to compute the inflowing boundary condition to perform a simulation that covers the whole irrigation season. To solve this issue, first of all a set of 1D steady state simulations using HEC-RAS for the years 2022, 2023 and 2024 were performed for each set of stage-discharge measurements, in order to calibrate the Manning's roughness coefficient. Considering that the banks of the channel are covered with boulders cast within a concrete lining (See Figure 6.30b), the value of the Manning's coefficient for the banks was kept constant (n= 0.035 s $m^{-1/3}$) in time and the calibration has been performed for the bottom only. The results for the 2022, 2023, 2024 irrigation seasons are shown respectively in Figure 6.32, Figure 6.33, Figure 6.34. The 2022 irrigation season was a dry season: consequently, the availability of water resources stored in the lakes (in our case, Como Lake and Iseo Lake) was limited and the downstream irrigation consortia had to adjust their management to the limits imposed by the regulation of the lakes. Due to the limited volumes available and the reduced discharge derived from the main rivers (River Oglio and River Adda), CIC had to equally reduce the discharge supplied to the secondary channels at the offtaking structures. Furthermore, the usual removal of vegetation that grew on the channel bottom, usually done at the end of June, was avoided for management purposes. Indeed, due to the limited water depth in the channel, and the small opening of the gates at the withdrawal points the removal of vegetation, could increase the risk of clogging the opening. The openings had to be reduced also because as shown from the measurements, the vegetation growth affects roughness and leads to an increase of the water level. This increases the water supply at the withdrawal points to the secondary channels because of the greater specific energy upstream of the gate in the Vacchelli channel. During the 2023 and 2024 irrigation seasons this natural process was strongly limited because the vegetation was removed in the second half of June, as shown in Figure 6.33 and Figure 6.34. In reality, the

"clean" channel configuration was not achieved due to the presence of water in the canal that did not allow the operators to remove completely the vegetation. Accordingly, after an increase of the Manning roughness coefficient at the beginning of June, the Manning's roughness coefficient of the bottom remains stable until the end of July when it starts to increase.

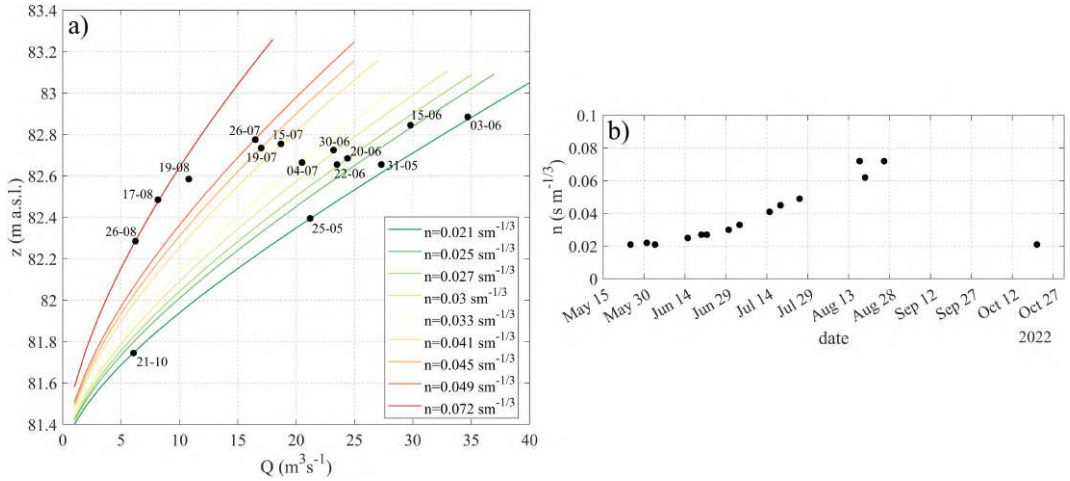

Figure 6.32: Calibration of the Manning's coefficient for the 2022 irrigation season. a) Calibration of stage discharge curves for the cross section where G01 is located and b) time series of the calibrated Manning's coefficient for the 2022 irrigation season.

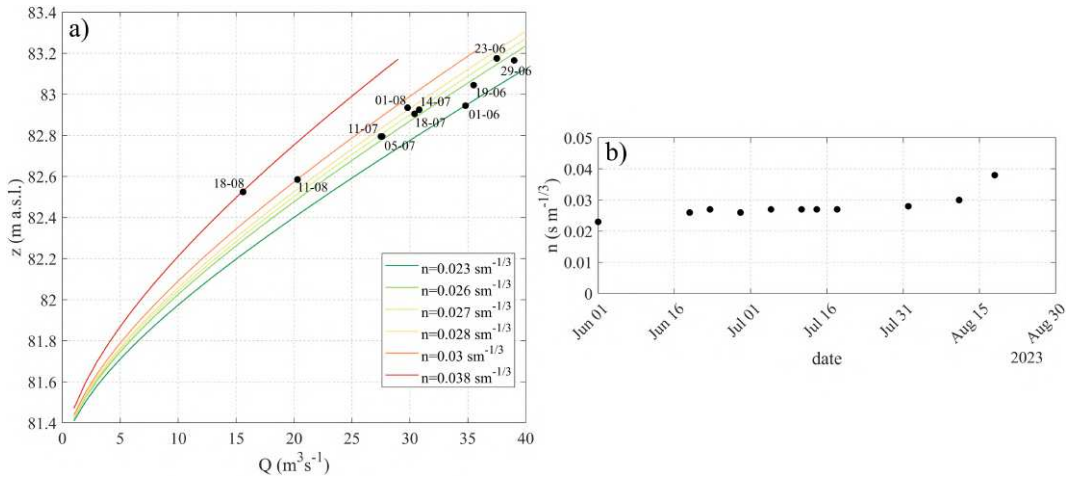

Figure 6.33: Calibration of the Manning's coefficient for the 2023 irrigation season. a) Calibration of stage discharge curves for the cross section where G01 is located and b) time series of the calibrated Manning's coefficient for the 2023 irrigation season.

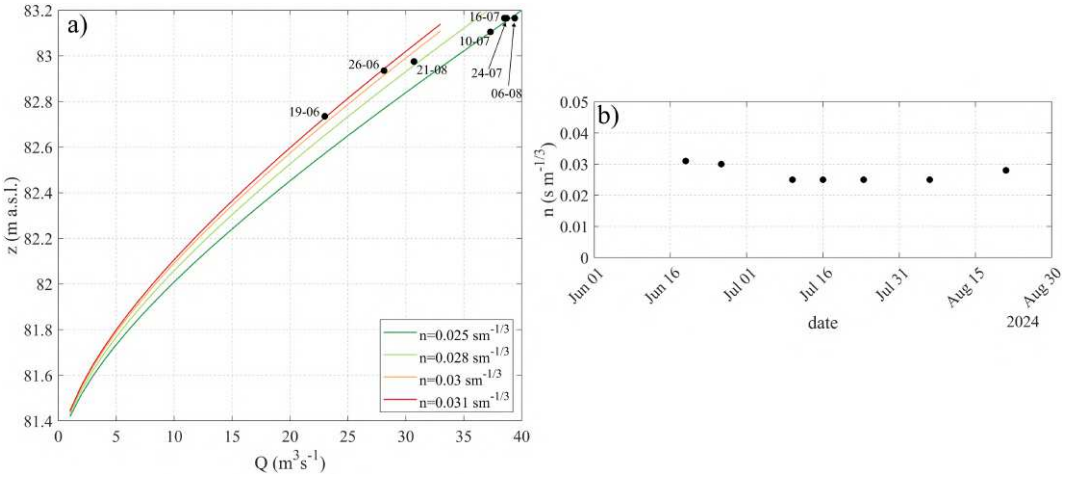

Figure 6.34: Calibration of the Manning's coefficient for the 2024 irrigation season. a) Calibration of stage discharge curves for the cross section where G01 is located and b) time series of the calibrated Manning's coefficient for the 2024 irrigation season.

The stage-discharge curves presented in Figure 6.32, 6.33, 6.34 are very interesting because they quantitatively show the effect of the vegetation growth on the channel conveyance. Moreover, they provide the data needed to build an interpolated surface $Q = f(depth, day)$ to be used to convert the measured water level time series in discharge used in the following as upstream boundary condition in the numerical model, as done in the simulation shown in Figure 6.35. Finally, they provide the fundamental information to calibrate a vegetation growth model, based also on the developed temperature model.

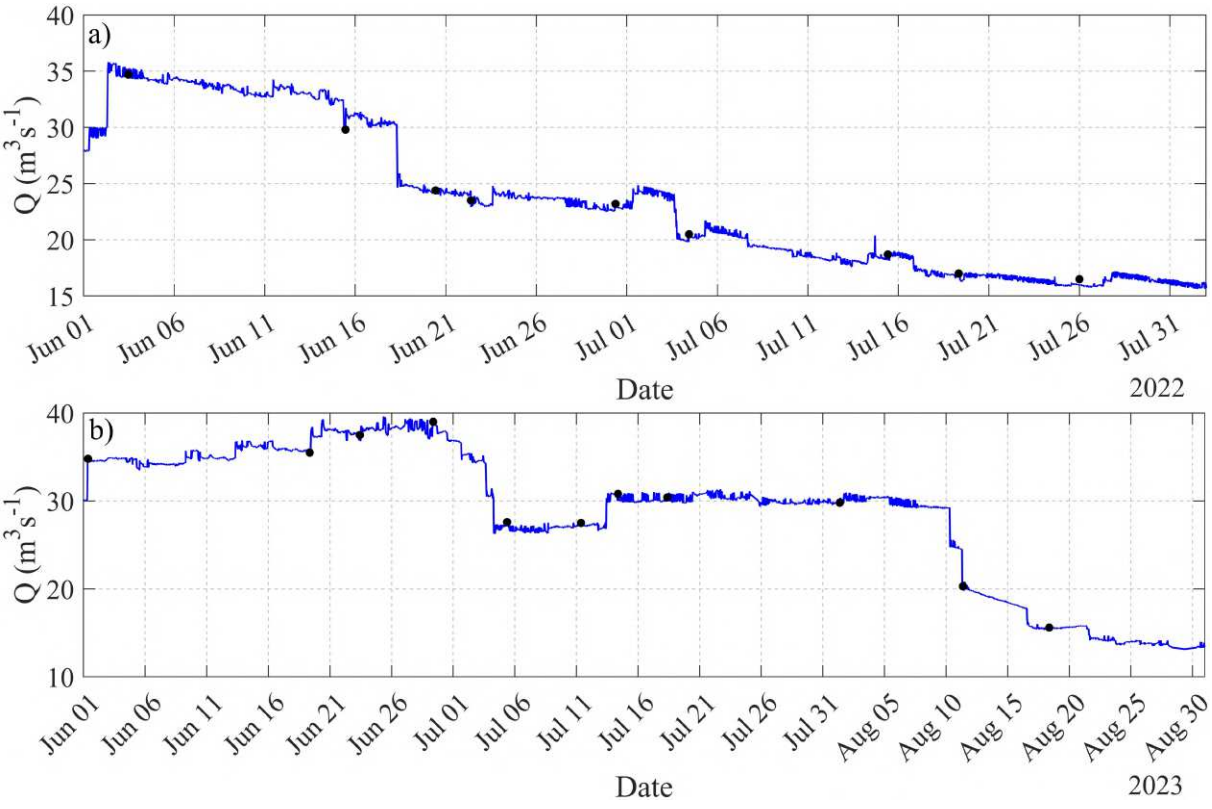

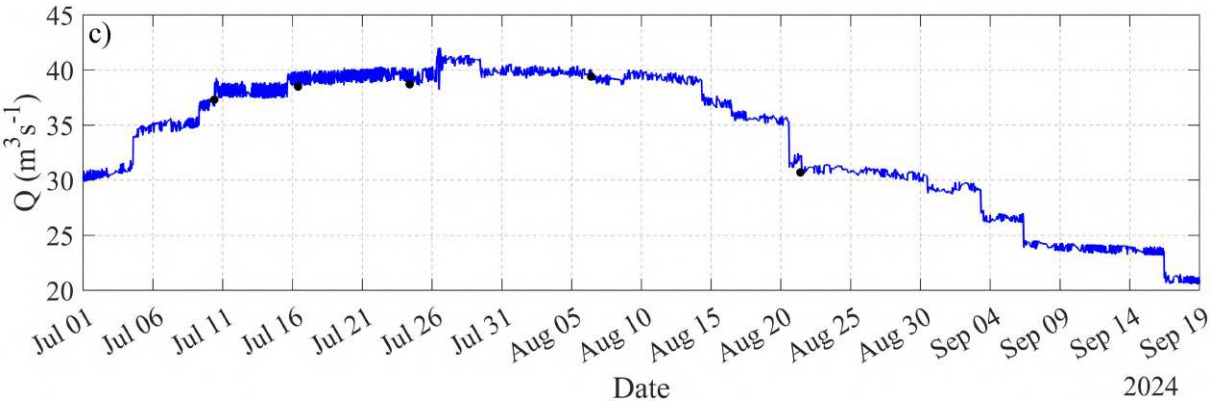

Figure 6.35: Incoming discharge computed at G01 station using the stage-discharge curve presented in Figure 6.32, Figure 6.33, Figure 6.34 for the irrigation season a) 2022, b) 2023 and c) 2024. The black dots represent the measured discharge during the irrigation seasons.

Additionally, in order to validate the implemented numerical model the final discharge entering at Tombe Morte G03 (Figure 6.29 and 6.36) is necessary. Although at this location no direct discharge measurements are available, the incoming discharge to the Tombe Morte node can be evaluated using an overall mass balance. First of all (see Figure 6.36), before entering the Tombe Morte node part of the incoming discharge from the Vacchelli canal is conveyed into the Bruno Loffi Canal. Part of this discharge (Q_{06}) is transferred upstream of station G05 to the Naviglio Grande Pallavicno and is estimated on a daily basis of the water level over a broad crested weir. Moreover, at section G04 (Gorgo Rotondo, Naviglio Grande Pallavicino; see Figure 6.36) upstream of the Tombe Morte node, a water level gauge is present upstream of a bed-drop where the flow becomes critical. Accordingly, the water level measured at this station can be reliably used to compute the discharge (Q_{G04}). Note that the Naviglio Grande Pallavicino underpasses the Tombe Morte bridge-canal and is partially fed by with the entering and unmeasured discharge Q_{TM}. Moreover, along the same canal but downstream the Tombe Morte node, the discharge (Q_{G05}) is measured continuously in time at G05 station (Gabriela, Naviglio Grande Pallavicino). It could be assumed that the discharge ($Q_{DS,TM}$) flowing north-east downstream the Tombe Morte node is equal to the discharge necessary to satisfy the water demand at the withdrawal points (red points in Figure 6.36):

$$Q_{DS,TM}(t) = \sum_i Q_{out,i}(t) \tag{6.10}$$

where $Q_{out,i}(t)$ is the water demand at the i^{th} withdrawal point, after which the residual discharge is 0 m^3 s^{-1}. Accordingly, the incoming discharge at the Tombe Morte node (Q_{G03}) could be computed as follows:

$$Q_{G03}(t) = Q_{G05}(t) - Q_{G04}(t) - Q_{G06}(t) + Q_{DS,TM}(t) \tag{6.11}$$

It is worth to mention that this mass balance doesn't take into account the transfer time from station G04 to G05 (in the order of 2-3 hours) and that the water level at G06 is measured daily. On the other hand the level variation ordinarily are relatively slow, and we believe that the mass balance (Equation 6.11) provides a reasonable evaluation of the inflowing discharge at the Tombe Morte station. Q_{OG} is an outflowing discharge from Naviglio Grande Pallavicino to the Oglio River. Ordinarily, it is zero but it was introduced in the balance for a short period

from 01/07/2024 to 03/07/2024, the 9/07/2024 and from 6/09/2024 to 19/09/2024. Figure 6.36 provides a visual aid for locating the measured and estimated discharges involved in the mass balance.

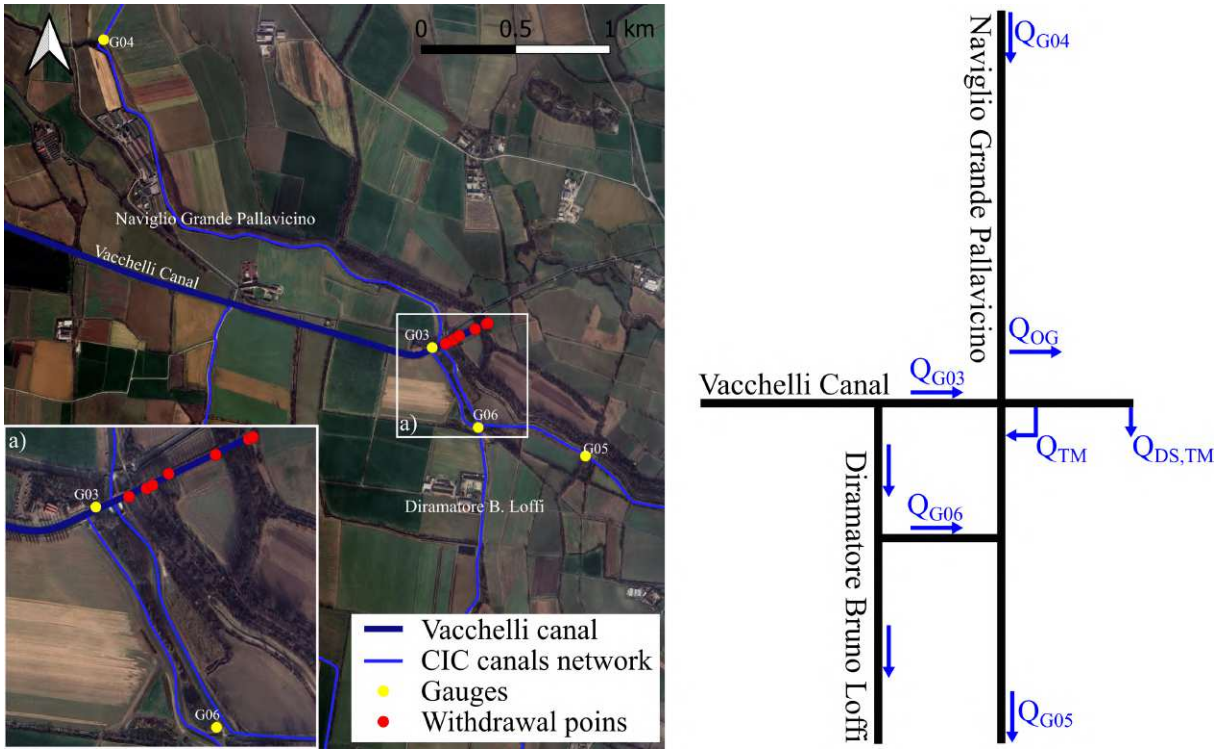

Figure 6.36: Location of the sections used to compute the mass balance at the Tombe Morte node (G03).

Figure (6.32) shows the effect of vegetation on roughness observed in 2022. These measurements underline the fundamental role of vegetation. Considering that one of the main driver of the vegetation growth is the water temperature, two thermistors were placed at the beginning (G01) and at the end (G03) of the Vacchelli canal, where water temperature was measured for the 2023 and 2024 irrigation seasons. As seen in the previous chapter, a temperature model requires some meteorological data and they are retrieved from the ARPA meteorological station at Crema. When nodata values for long periods were present within the time series, they were replaced using the corresponding data of the ARPA meteorological station at Persico Dosimo (Cremona). The hydrodynamic model of the Vacchelli canal was built considering a mean spacing of the cross section of around 21.6 m (1576 cross section); the Manning roughness coefficient was kept fixed for the banks whereas for the bottom of the channel it was changed daily according to the values shown in Figures 6.32, 6.33, 6.34. The downstream boundary condition was provided by the time series of the water depth measured at G03. The 27 withdrawals points located along the Vacchelli canal were introduced in the equation of the conservation of mass at the corresponding i-th cell, respecting the timetable of the water shifts. Along the channel 44 internal boundary conditions have been used to model the bridges and the siphon crossing the Vacchelli Canal so that the inclusion of routines specifically designed to deal with bridges is fundamental. As described in Chapter 4 the bridges modeling requires stage discharge curve implemented in the model that in this case were obtained from HEC-RAS 1D. Moreover, as mentioned previously, being the incoming discharge related to the water availability of the water volume stored in the pre-alpine

lakes, when needed the consortium applied the same reduction coefficient to each withdrawal, in order to equally reduce the discharge supplied to the secondary channels. As far as the discharge delivered from the Vacchelli Canal to the Geronda Canal and to the Diramatore Bruno Loffi is concerned (see previous description of the different branches along the Vacchelli canal), the corresponding amount and timetable were computed by summing the delivered discharges at each time at all the withdrawals points along these two branches. The temperature model was built considering a mean length of the CSTRs of around 110 m. Accordingly, the Vacchelli canal was discretized with 310 CSTRs.
The irrigation season of 2022 was simulated from 1/6/2022 to 2/08/2022 and the results are reported in Figure 6.37, where the discharge computed at the end of the channel is compared with the reference discharge compute using Equation 6.11.

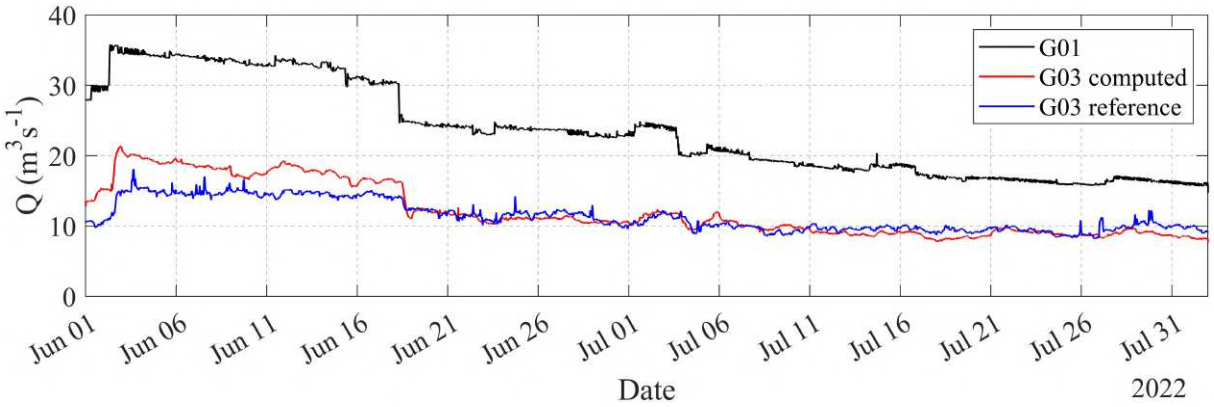

Figure 6.37: Results obtained with the implemented numerical model; the black line is the reconstructed time series of the inflow in the Vacchelli canal, the red and blue line are respectively the discharge computed and reconstructed at the end of the channel during the summer season 2022.

In Figure 6.38 the time series of the reduction factor adopted for the Vacchelli Canal during the irrigation season of 2022 is shown. As can be observed, in order to cope with the extremely dry season and the scarce availability of water volume in the Como Lake, in 2022 a reduction factor as low as 0.3 had to be introduced from July 21.

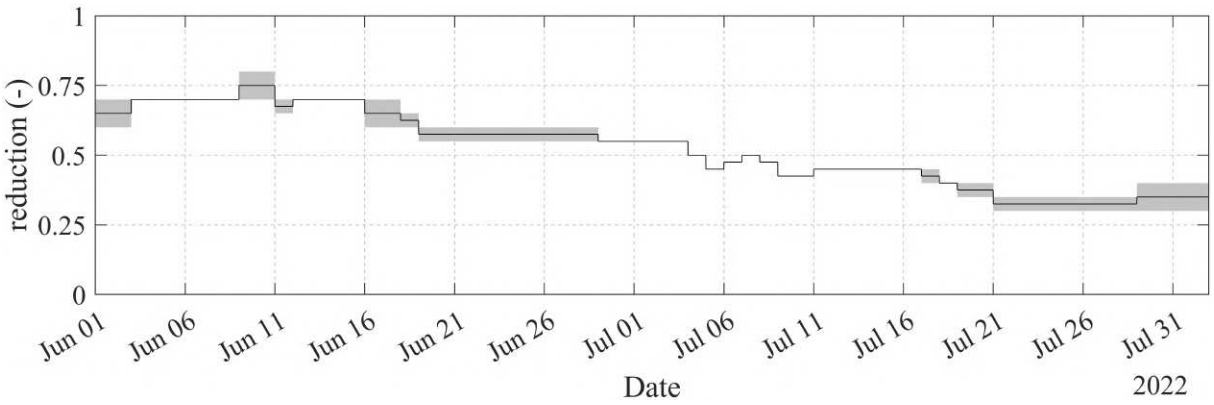

Figure 6.38: Reduction applied to the delivered discharge at the withdrawal points during the irrigation season of 2022; the gray band represents the range of the reduction coefficient.

The irrigation season of 2023 was simulated from 1/06/2023 to 31/08/2023; and the results are reported in Figure 6.39 and the time series of the reduction coefficient is reported in Figure 6.40

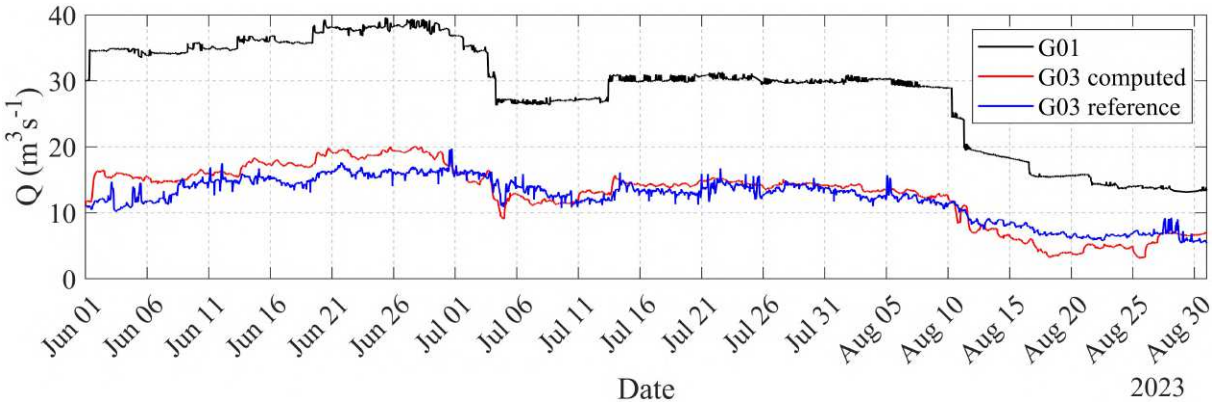

Figure 6.39: Results obtained with the implemented numerical model; the black line is the reconstructed time series of the inflow in the Vacchelli canal, the red and blue line are respectively the discharge computed and reconstructed at the end of the channel during the summer season 2023.

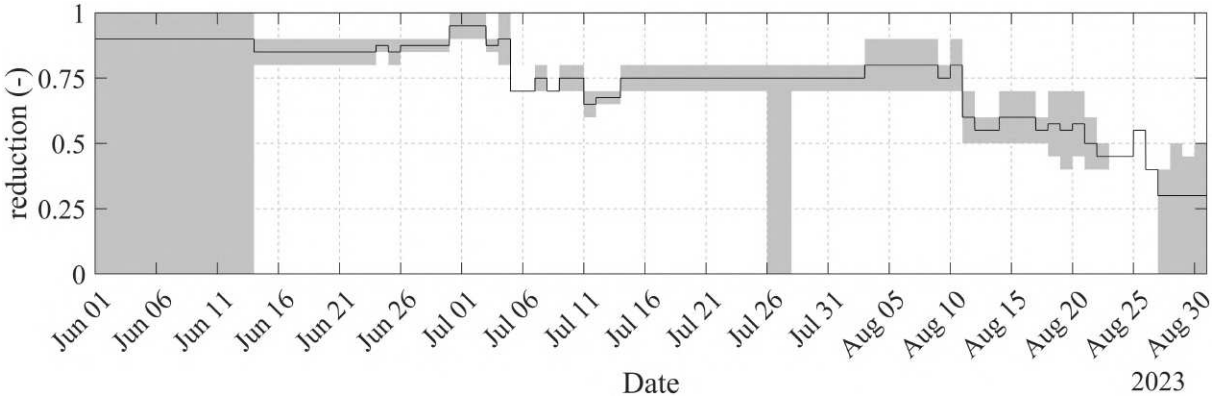

Figure 6.40: Reduction applied to the delivered discharge at the withdrawal points during the irrigation season of 2023; the gray band represents the range of the reduction coefficient.

As mentioned before, during the 2023 irrigation season we measured the water temperature at inlet (G01) and at the end of the channel (G03). The G01 time series was used as the upstream boundary condition for the temperature model, and the G03 time series was used for testing the accuracy of the model. The results of the temperature model are shown in Figure 6.41. The match between observed and computed temperature at Tombe Morte is very good.

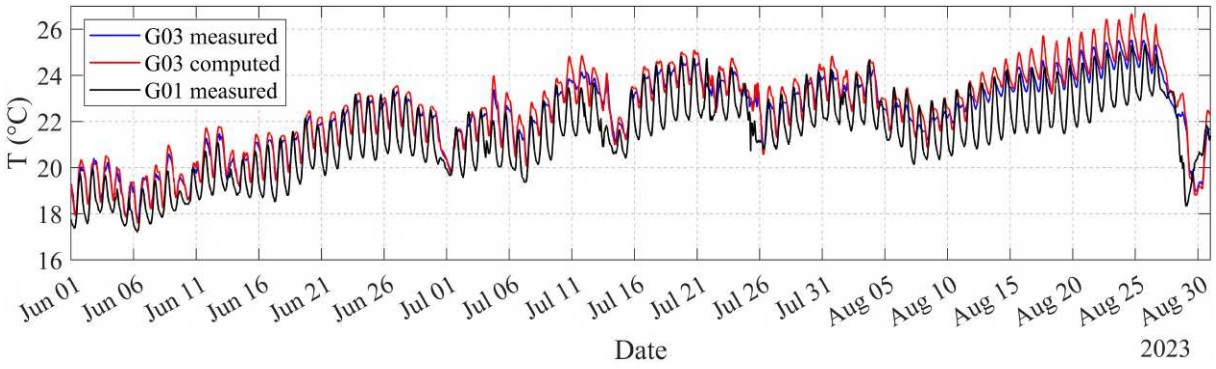

Figure 6.41: Results obtained with the temperature module. The black line is the measured time series of the water temperature at the inlet of the Vacchelli canal whereas the red and blue line are respectively the time series of temperature computed and measured at the end of the Vacchelli canal for the 2023 irrigation season.

Finally, the 2024 irrigation season was characterized by a rainy June, during which irrigation was not necessary. Accordingly, the irrigation started regularly at the 10-15th of July and was simulated in the period between 3/07/2024 to 19/09/2024. The results are reported in Figure 6.42 and the time series of the reduction coefficient is shown in Figure 6.43. The results of the temperature model are shown in Figure 6.44.

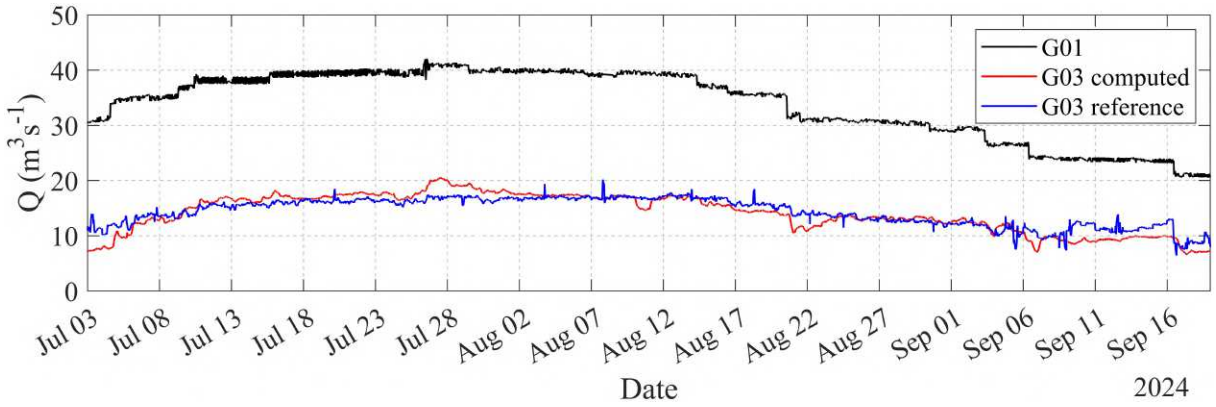

Figure 6.42: Results obtained with the implemented numerical model; the black line is the reconstructed time series of the inflow in the Vacchelli canal, the red and blue line are respectively the discharge computed and reconstructed at the end of the channel during the summer season 2024.

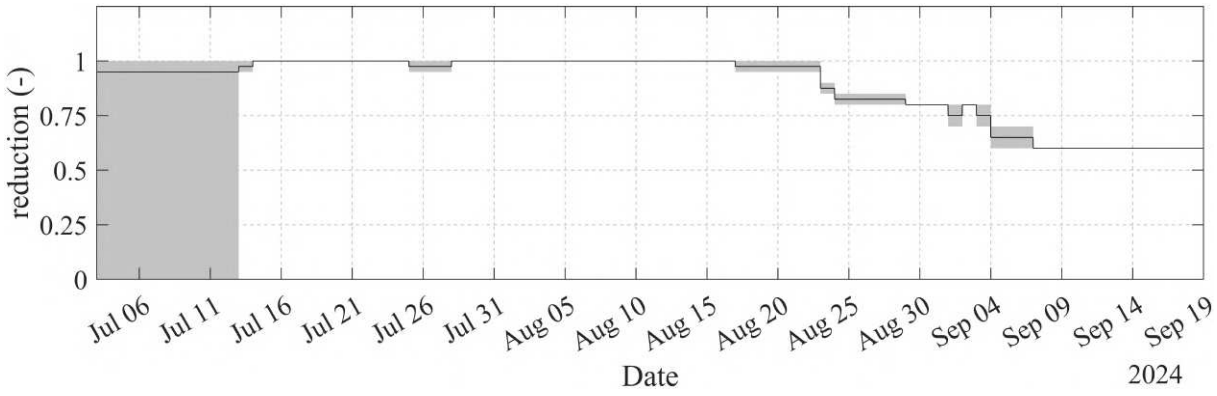

Figure 6.43: Reduction applied to the delivered discharge at the withdrawal points during the irrigation season of 2024,the gray band represents the range of the reduction coefficient.

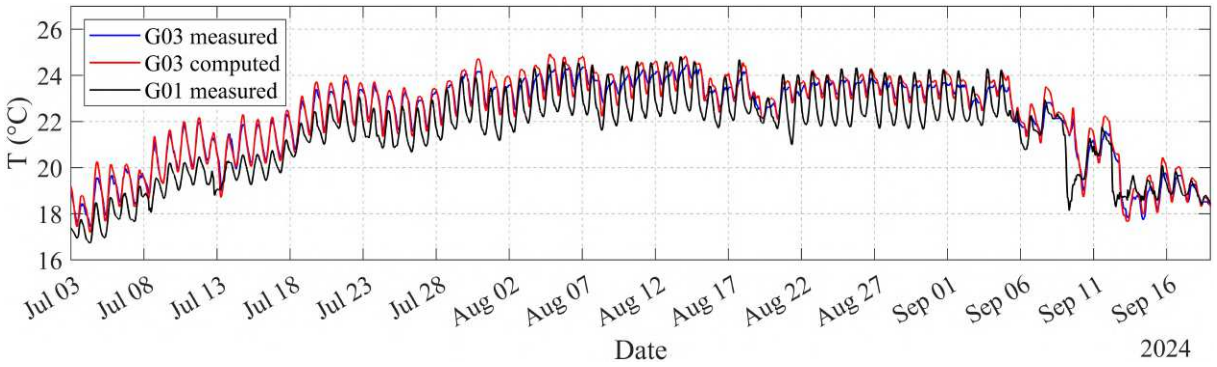

Figure 6.44: Results obtained with the temperature module. The black line is the measured time series of the water temperature at the inlet of the Vacchelli canal, the red line and blue line are respectively the time series of temperature computed and measured at the end of the Vacchelli canal for the 2024 irrigation season.

6.6 Adjustment of the model roughness on the basis of the coupled biomass, hydrodynamic and temperature models

In the following we show the results provided by the simulations with the coupled model that take into account the hydrodynamics, the temperature variation and the biomass growth. The coupling arises because the biomass growth governs the hydraulic roughness that, in turn, governs the momentum equation. The channel roughness update was done on a daily basis. It is important to underline that the friction due to vegetation should be computed using appropriate resistance formulation (e.g., Luhar & Nepf, 2013; Walter Box & Västilä, 2024). In our case, the implemented biomass model is affected by the uncertainty associated with parameters which would require a specific calibration on the basis of the biological characteristic of the macrophyte which grows on the bottom of the Vacchelli canal. Within the Thesis this calibration, that would require an extensive field work, was not possible and, accordingly, the selected parameters were chosen on the basis of the values suggested in the literature. Accordingly, we believe that the obtained results should be deemed as preliminary. However, they also look very promising, showing the effectiveness of the chosen roadmap and another clear connection with the topic of climate change.
In the following, we made the simplifying assumption that both the macrophyte stems number and diameter located in each CSTR don't change in time. Accordingly, we made the assumption that the weed growth affects only the stem length: consequently, the ratio $\frac{h_v(t)}{h_{v0}}$ is equal to the ratio $\frac{C(t)}{C_0}$, where $h_v(t)$ is the length of the vegetation, h_{v0} is the initial length of the vegetation, $C(t)$ is the biomass concentration and C_0 is the initial concentration.
In the following, we made the assumption that the Manning roughness coefficient depends on the relative roughness $\frac{h_v(t)}{h(t)}$, according to a power law:

$$\frac{n(t)}{n_0} = A\left(\frac{C(t)}{C_0}\frac{h_{v,0}}{h(t)}\right)^B \tag{6.12}$$

where n_0 is the initial Manning roughness coefficient for the bottom of the bed, $n(t)$ is the Manning roughness coefficient at the time t, $h(t)$ is the mean water depth in the stretch of the canal where $n(t)$ is computed. By imposing $n(0) = n_0$ and consequently $h(0) = h_0$ it is possible to obtain the value of the coefficient A:

$$A = \left(\frac{h_0}{h_{v,0}}\right)^B \tag{6.13}$$

Accordingly Equation 6.13 can be written as:

$$n(t) = n_0\left(\frac{C(t)}{C_0}\frac{h_0}{h(t)}\right)^B \tag{6.14}$$

that depends on the unknown exponent B. This Equation was used to update the roughness coefficient of the bottom every new day on the basis of the computed biomass concentration. In Table 6.2 the values of the parameter used to calibrate the biomass model are provided. Note that this set of parameters is equal to the recommended values. Only $\mu_{\mathrm{m,max}}$ (day^{-1}), K_{mr} (day^{-1}) and the parameters of the reaction rate multiplier for temperature have been slightly changed.

Table 6.2: Values of the coefficient used in the biomass model

Parameter	***Value***	***Parameter***	***Value***
k_e (m^{-1})	0.45	K_3 (-)	0.98
β (-)	0.45	K_4 (-)	0.1
$\mu_{m,max}$ (day^{-1})	0.28	T_1 (°C)	5
K_{mr} (day^{-1})	0.06	T_2 (°C)	20
K_{mm} (day^{-1})	0.05	T_3 (°C)	25
K_1 (-)	0.1	T_4 (°C)	40
K_2 (-)	0.98	I_h ($W\ m^{-2}$)	30

To complete the calibration of Equation 6.14 , $h_0 = 1.63$ m was selected as the mean water level in the Vacchelli canal for $t = t_0$ and B was set to 0.9 after a short calibration. In order to test the effectiveness of the model, we focused on the first 10 km of the Vacchelli canal. The same discretization previously adopted for the whole Vacchelli canal was used and the normal depth with a slope of the bottom ($S_o = 0.00035$) was used as the downstream boundary condition. The results are reported in Figure 6.45. In place of showing a comparison between the observed and computed water depth at the G01 station, we directly show the results in terms of the match between the Manning's n measured by the stage-discharge curve and the ones provided by the coupled model. The match looks extremely good. It's interesting to observe that Equation 6.14 that accounts for relative submergence of the vegetation, is also able to describe the reduction of resistance at the end of August due to the rising of the incoming discharge and consequently of the water depth.

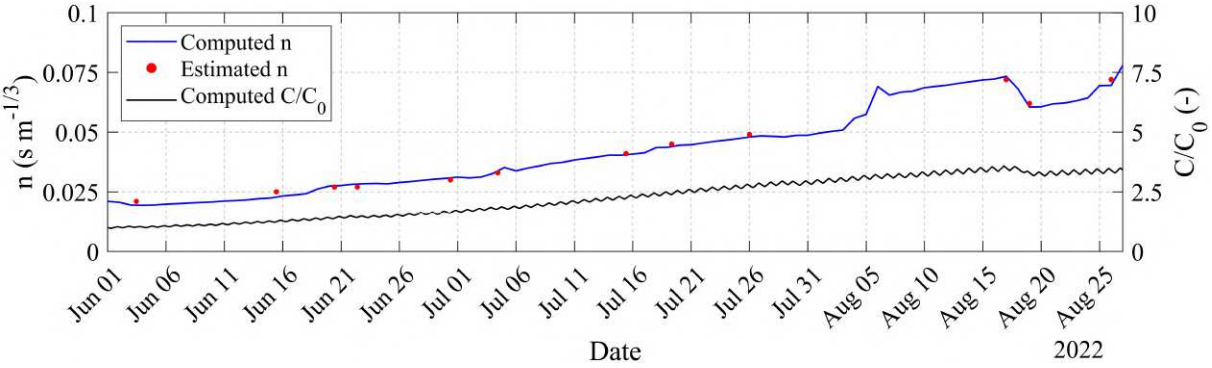

Figure 6.45: Comparison between the Manning's coefficients for the 2022 irrigation season computed by the model and the estimated values provided by the stage-discharge measurements in the previous section. In black the ratio C/C_0 computed using the biomass model.

6.7 Conclusions

The Consorzio di Irrigazioni Cremonesi considered in this Chapter provides an exemplary case study of the relevance of water management in a changing climate and of the potential of the implemented model. It also highlights a series of aspects that could constitute possible directions for further study beyond this doctoral research. Although the lack of precise data on the overall geometry of the network has made it impossible to extend the model to all branches of the network (a limitation that will certainly be overcome over the next years), the studied case of the Canale Vacchelli represents its most significant part. Many features make this case remarkable, only a partial list of which is presented in the following. The presence of many delivery points along the route, with a complex pattern of water withdrawal shifts, shows the operative complexity of this kind of irrigation canal. Taking inspiration from this complexity we compared the differences between a simple way to estimate the water discharge at a point on the basis of a simple mass balance and a more refined approach to do this task using the implemented model. The comparison between the two methods provides insights that can be useful for other cases. The terminal point at Tombe Morte node, where water depth and temperature are measured and discharge can be evaluated, allows the positive verification of the implemented model. Despite the hydraulic model computes the water discharge at the node of Tombe Morte with good agreement with the observations, at the beginning of the irrigation of the season 2022 and 2023 the differences between observed and computed discharge are not negligible. In these periods the numerical model overestimate the discharge with respect to the observed one. Assuming that the incoming discharge, and the delivered discharge at the delivery points are well described, the difference between the results and the observations could be attributed at the infiltrations which are not accounted by the numerical model. We believe that the seepage loss at the beginning of the irrigation season could be related to two different processes:

- at the beginning of the irrigation season, the discharge diverted from the Adda River and consequently the water level in the Vachelli Canal is increased. This increase has two effects: an infiltration in the unsaturated porous media which characterized the embankment of the Vacchelli canal and an increase of the saturated infiltration process through the bottom due to the increase of the hydraulic gradient.

- This effect gradually decrease moving forward in the irrigation season due to the combined effects of the embankments saturation, the reduction of the hydraulic gradient caused by the reduction of the water level (in accordance with the availability of the water stocked in the Como Lake) and the possible increase of the groundwater table level due to the aquifer feeding by the surface irrigation largely used in the study area.

Modeling this complex phenomenon requires field observations in order to quantify the infiltration for different stretch of the channel network. Accordingly, different methods could be followed to measure the seepage losses (Lund et al., 2023):

- Inflow-outflow measurements: this method is based on a mass water balance on a control volume, where the only unknown is the seepage loss. Indeed, once a stretch of the river is selected (it should be sufficiently long in order to ensure that the infiltration losses are larger than the error and uncertainties of the methodology), the water balance allows to compute the seepage loss considering the measured inflow discharge, the measured outflow discharge, possible measured inflows and withdrawals along the control volume of the reach, evaporation losses and any changes in the stored volume occurring during the inflow-outflow measurements (neglected in steady state). The main advantage of this method

is that the channel remains fully operative. Considering the instrumentation availability at CIC, ADCP discharge measurements could effectively be used for this method (Kinzli et al., 2010).

- Pounding measurements: this method requires the creation of a pond between two dams built within the channel. Accordingly, a water mass balance is performed on the stored volume. This method doesn't require the measurements of the inflowing and outflowing discharge as for the inflow-outflow method but only the measurement of the water level in the pond. All the other inflow and outflow should be considered (e.g. evaporation, withdrawals) in the water balance. A disadvantage of this method, is the difficulty to keep the channel fully operative.

- Point measurements by meas of seepage meter (Rosenberry et al., 2020).

From a numerical point of view this complex phenomenon could be addressed by several approaches characterized by different level of complexities. Once the mean infiltration rate or the time series of seepage during the irrigation season is known it could be integrated directly in the mass conservation. Considering that the infiltration process happens in saturated soils for the bottom of the channel the Darcy law can be used to estimate the infiltration in the mass conservation equation. Using the Darcy law the increase/decrease of the hydraulic gradient would be automatically taken into account by the model once the level of the groundwater table is known.
Finally, the presence of a stage-discharge curve carefully measured and recalibrated over the years, makes evident the summer variation of this curve, providing a quantitative measure of the role of vegetation growth in terms of Manning's n variation. This observation was supported by the water temperature measurement campaign, which lasted for about 2 years in two points 35 km apart, allowing us to observe the interesting water thermal dynamics during time span taken by water to move from Merlino to Tombe Morte. The coupling between these information sets provided the starting point for the development of a thermal model of the flow and of a coupled weed growth model. In turn, these two models provided the modeled seasonal variation of the Manning's n that matched very well the observed variation of the channel roughness. The numerical application of the model has also shown the relevance of some phenomena that would be worthy of further study in the future: such as the role of infiltration along some of the stretches of the canal.

Conclusions

This doctoral research presents the steps followed for the implementation, validation and application of a mathematical model of unsteady open channel flow in irrigation networks. The topic was suggested by the relevance of optimal water management in agriculture in the framework of a changing climate, that will inevitably lead to the search for more sophisticated approaches to manage water delivery.

The 6 chapters of the Thesis present different aspects emerged along my three year research period, that can be summarized as follows:
Implementation and validation of a mathematical model for an irrigation channel network.
The implementation was primarily based on the numerical method proposed by Casulli and Stelling (2013). This method, was selected because it can handle different topology of the network without increasing the complexity of the implementation. Moreover the semi-implicit numerical method allows to relax the CFL condition, this can useful in case of long time-span simulation. The implemented numerical model was tested for a set of steady test cases considering different bathymetries in different flow regimes (MacDonald test cases, Flow over a bump test cases) providing a good correspondence with analytical solution. Similarly, the implemented model was tested with some cases presented in the literature for open channel network (e.g., Islam et al., 2005; Sen & Garg, 2002) in unsteady condition, with a good match with the results provided by Zhu et al. (2011). In future, the numerical model could be completed introducing the effects of infiltration, a type of process that was not implemented in the model due to the lack of specific data.

Numerical tests on the Conceptual Schemes Adopted in the Code for Bridge Modeling
For hydraulic structure modeling, and for bridges in particular, there is not a standard reference for the conceptual equations to be used for a general layout. However, HEC-RAS, that is becoming a worldwide standard for 1D and 2D solution of SWE, includes different schemes to compute flow through different hydraulic works. Accordingly, we started from the careful analysis of the different conceptualization implemented in HEC-RAS. In particular, we tested the effectiveness of the adopted methods to model bridge in a 2D domain, using a recent and extensive experimental dataset provided by Ratia et al. (2014). The results showed a good match of the model results with the experimental measurement both in steady and unsteady conditions for two different schematizations (Energy method and Pressure and Weir method). Accordingly, the same conceptual methods were introduced in the implemented model.

Terrain modification to DEM derived from LiDAR surveys
In general, one stumbling block in hydraulic modeling is the availability of bathymetric data for a careful representation of the water course. We explored the possibility of using LiDAR surveys for this purpose. LiDARs are increasingly used to detect landforms and provide data with an accuracy that can reach the order of 10 cm. However, although LiDAR data provides a careful representation of the water course and the floodplain areas, they lack in the reproduction of the bed bottom covered by water during the survey. Accordingly, they provide an inaccurate representation of the submerged portion of the cross section that looks fictitiously higher due to the presence of water. In the search for a solution to this problem, in this chapter we have proposed an original methodology to tackle it. The procedure is physically based because it takes advantage from a preliminary hydraulic simulation which provides a simple method to identify with a reasonable approximation the DTM subset of cells that were flooded during the LiDAR

survey. This information is later used in the procedure to compute the offset to be applied to reconstruct the correct bed topography.

Coupling water channel temperature and hydrodynamic: implementation and validation
The measured data taken during the irrigation season, coupled with some preliminary simulations accomplished for the Vacchelli Canal have shown the role of the aquatic weed growth on the variation of the hydraulic roughness of the bed, as documented in Chapter 6. Accordingly, this is a fundamental process that proved necessary to accomplish seasonal simulations. Considering that the aquatic weed growth is strongly governed by water temperature, solar radiation and availability of nutrients (e.g., Carr et al., 1997), we deployed two thermistors at the beginning and at the end of the Vacchelli Canal, measuring around two years long series of water temperature and observing interesting peculiarities of the temperature variation during the transfer from the channel inlet to the end of the channel. The methodology presented by Pilotti et al. (2019) to compute the energy balance was coupled with the hydrodynamic model to test whether the coupled model was able to capture the observed dynamics. The implementation was validated by comparing the results for a simplified case with the results provided by HEC-RAS, providing remarkably close results despite different equations are implemented in HEC-RAS (e.g., longwave radiation, sensible heat and latent heat). Finally, the modeled temperature pattern was used by implementing weed growth model presented by Berger and Wells (2008) on the basis of some simplification (e.g., extinction coefficient for light attenuation, infinite availability of nutrients). This aspect is very complex and further investigation will be inevitable, requiring a botanic competence.

Application to a real Irrigation Channel Network
Finally, the numerical model was implemented for a real test case. The Vacchelli Canal managed by Consorzio Irrigazioni Cremonesi (CIC), was considered. This case is a remarkable one for its historical importance, its dimension and complexity. The numerical model proved effective in reproducing the discharge at the end of the Vacchelli Canal when compared with the reference discharge. Regarding the uncertainty, it's here important to remark that the inflowing discharge in the Vacchelli canal is estimated using a stage discharge curve variable in time calibrated with the measurements accomplished during the irrigation season. The discharge at the end of the Vacchelli canal is estimated considering different control section around the Tombe Morte node. Moreover, the reduction coefficient applied to the different offtaking structure is provided daily in a range. Regarding the model, the values of the Manning coefficient assumed for the bottom is the same for the entire Vacchelli Canal (except for the zone where the Canal has a concrete-lined bottom). This is a limitation of the model because the macropythe growth probably is not the same along the canal. The offtaking structure which fed the secondary channel has been considered in the mass conservation equation this led to a simplification of the real operation done at the gate by the operators of the consortium that frequently regulates the gate on the basis of the contemporary level in the main and in the secondary channel. Despite these uncertainties which require further analysis, the 2022 and 2023 seasons show infiltration at the beginning of the irrigation season which cannot be accounted by the model. This aspect was not observed in the 2024 season probably as an effect of the rainy month of June. Regarding the temperature model, it has shown the capability to model the daily variation of temperature at different progressive along the channel. At the end of August 2023 the model overestimate the temperature.

The different modeling aspects addressed in the Thesis have been finally combined to pro-

duce a reasonably complete and state-of-the-art model that can be used in perspective to adapt the management rules of an irrigation consortium on the basis of the changed climatic conditions, which may impose changes in the space-time structure of the water shifts. Of course, the developed model is not perfect and directions along which it could be improved in the future have emerged right from the start. First of all, it' s future use as a digital twin will require its integration within a water balance system of the irrigation district where it will be implemented. Furthermore, it will be necessary to address the problem of infiltration, introducing it in the mass balance equations as a term that depends on the simultaneous level in the channel and in the surrounding aquifer. Furthermore, the algal growth model will have to be adapted to the specific needs of the case, on the basis of specific measurements and possibly more complete conceptual schemes than the one adopted in the Thesis. From a numerical point of view, the current code, implemented in a MATLAB environment, can certainly be optimized and will have to be improved with the introduction of feedbacks that link in real time the settings of the hydraulic structures (for example, the opening of the gates) to the measurements in the field. Regarding these aspect, currently, the implemented model can work for off-line simulation only and for scenarios with given boundaries and initial conditions. It is therefore possible, for given scenarios, to evaluate certain operational choices, such as the effects of a reduced inflow at the inlet of the network or a different scheduling discharges delivered to the various withdrawal points. In this way, it becomes possible to assess the impacts of different management choices in advance. One possible development of the model could include the automatic updating of boundary conditions based on the monitoring network introduced in the Paragraph 6.3. This type of integration would enable the creation of a digital twin of the network, in order to have a real-time model of the system. The inflowing discharges monitored at the inlet of the network would provide the boundary conditions for the model, while sensors installed within the network could offer data for the model's calibration. For instance, measured water levels along the network could give insights for the calibration of the roughness coefficients; on the other hand, the discharges monitored along the network could be used to detect seepage or infiltration into the canal. Such information would allow for a real-time modeling of the network. Although all these and other aspects can be improved, we believe that this work, developed in a geographical and technical context where these methodologies are not yet a consolidated standard, can offer a contribution to the achievement of the increasingly important objectives of optimization of the management of water resources in the agricultural field.

List of Research Outputs

Scientific Publications

- Bonomelli, R., Farina, G., Pilotti, M., Molinari, D. and Ballio, F., (2023). Historical comparison of the damage caused by the propagation of a dam break wave in a prealpine valley,*Journal of Hydrology-Regional Studies,* Volume 48, August 2023, 101467.
- Arosio, M., Arrighi, C., Bonomelli, R., Domeneghetti, A., Farina, G., Molinari, D., Monteleone, B., Scorzini, A. R., and Martina, M. (2024). Unveiling the assessment process behind an integrated flood risk management plan, *International Journal of Disaster Risk Reduction*, Volume 112, October 2024, 104755.
- Farina, G., Pilotti, M., Milanesi, L. and Valerio G., (2025). A simple method for the enhancement of river bathymetry in LiDAR DEM, *Environmental Modelling & Software*, Volume 186, March 2025, 106354.

Scientific Publication under review

- Farina, G., Pilotti, M., Bonomelli, R., Martínez-Aranda, S., García-Navarro, P. Modeling bridges in HEC-RAS 2D: comparison with flume experiments. Technical note under review *Journal of Hydraulic Engineering ASCE.*
- Bonomelli, R., Pilotti, M., Farina, G. Use of simple analytical solutions in the calibration of Shallow Water Equations debris flow models, EGUsphere [preprint], https://doi.org/10.5194/ egusphere-2024-2267, 2024.

Conferences Contributions

- Farina, G., Bonomelli, R., Pilotti, M. (2022). Effects of Anthropic Changes on the Propagation of the Gleno Dam Break Wave in the Valle Camonica Floodplain, Proceedings of the 39th IAHR World Congress, 19-24 June, 2022 Granada, Spain.
- Ballio, F., Armaroli, C., Arosio, M., Arrighi, C., Borgogno Mondino, E., Carisi, F., Castelli, F., Ciavola, P., De Biaggi, S., Di Pietro, G., Domeneghetti, A., Duo, E., Farina, G., Gallazzi, A., Ghilardi, F., Giusti, R., Hammouti, M., Luino, F., Martina, M., Molinari, D., Monteleone, B., Petruccelli, N., Pilotti, M., Scorzini, A.R., Simonelli, T., Sterlacchini, S., Turconi, L., Vasini, C., Zazzeri, M., Zoppi, L. (2022). The Movida Project to Support the Update of Flood Risk Maps in the Po River District: Methodology for Flood Damage Assessment, Proceedings of the 39th IAHR World Congress, 19-24 June, 2022 Granada, Spain
- Pilotti, M., Farina, G., Bonomelli, R., Milanesi, L. (2022). Physically Based Vulnerability Functions for flood risk mapping in mountain area, Proceedings of the 39th IAHR World Congress, 19-24 June, 2022 Granada, Spain.
- Farina, G., Pilotti, M., Milanesi, L. (2022). A simple method for the enhancement of river bathymetry in LIDAR DEM, Proceedings 7th IAHR Europe Congress, September 7– 9, 2022, Athens, Greece.
- Bonomelli R., Farina, G., Pilotti, M. (2023). Far field simulation of a landslide-generated tsunami in Lake Iseo, International workshop on Physical Processes in Natural Waters, 19– 23 June, 2023, Brescia, Italy.

- Farina, G., Pilotti, M., Milanesi, L., (2023). Modeling a historical lowland irrigation channel network in northern Italy, Proceedings of the 40th IAHR World Congress, 21-25 August 2023, Vienna, Austria.
- Bonomelli, R., Farina, G. and Pilotti, M. (2024). Far-field simulation of a landslide-generated tsunami in Lake Iseo, Proceedings of the 45th edition of the Italian Conference on Integrated River Basin Management, Cosenza, Calabria, 17-18 June 2024
- Farina, G., Pilotti, M., Milanesi, L. (2024). A mathematical model for unsteady flow in regulated irrigation channel networks, XXXIX Convegno Nazionale di Idraulica e Costruzioni Idrauliche, Parma, 15-18 Settembre 2024.
- Farina, G., Bacchi, V., Pilotti, M. (2024). Implementation and validation of a new friction vegetation law in TELEMAC-2D, XXXth TELEMAC User Conference, Chambéry, France.

References

Afrasiabikia, P., Rizi, A. P., & Javan, M. (2017). Scenarios for improvement of water distribution in doroodzan irrigation network based on hydraulic simulation. *Computers and Electronics in Agriculture*, *135*, 312–320. https://doi.org/10.1016/j.compag.2017.02.011

Barkhordari, S., & Hashemy Shahdany, S. M. (2022). A systematic approach for estimating water losses in irrigation canals. *Water Science and Engineering*, *15*(2), 161–169. https://doi.org/10.1016/j.wse.2022.02.004

Berger, C. J., & Wells, S. A. (2008). Modeling the effects of macrophytes on hydrodynamics. *Journal of Environmental Engineering*, *134*(9), 778–788. https://doi.org/10.1061/(ASCE)0733-9372(2008)134:9(778)

Bhuyian, M. N. M., Kalyanapu, A. J., & Nardi, F. (2015). Approach to digital elevation model correction by improving channel conveyance. *Journal of Hydrologic Engineering*, *20*(5), 04014062. https://doi.org/10.1061/(ASCE)HE.1943-5584.0001020

Bonomelli, R., Farina, G., Pilotti, M., Molinari, D., & Ballio, F. (2023). Historical comparison of the damage caused by the propagation of a dam break wave in a pre-alpine valley. *Journal of Hydrology: Regional Studies*, *48*, 101467. https://doi.org/10.1016/j.ejrh.2023.101467

Bradley, J. N. (1978). *Hydraulics of bridge waterways*. US Department of Transportation Federal Highway Administration.

Brunner, G. W. (2016). *Hec-ras user's manual*. Davis CA: U.S. Army Corps of Engineers.

Brunner, G. W. (2020). *Hec-ras, river analysis system hydraulic reference manual*. Davis CA: U.S. Army Corps of Engineers.

Brunner, G. W. (2024a). *Hec-ras 2d, user's manual. exported march 2024*. Davis CA: U.S. Army Corps of Engineers.

Brunner, G. W. (2024b). *Hec-ras user's manual*. Davis CA: U.S. Army Corps of Engineers.

Brunner, G. W., Sanchez, A., Molls, T., & Parr, D. A. (2020). *Hec-ras verification and validation tests*. Davis CA: U.S. Army Corps of Engineers.

Bures, L., Roub, R., Sychova, P., Gdulova, K., & Doubalova, J. (2019). Comparison of bathymetric data sources used in hydraulic modelling of floods. *Journal of Flood Risk Management*, *12*(S1), e12495. https://doi.org/10.1111/jfr3.12495

Carr, G. M., Duthie, H. C., & Taylor, W. D. (1997). Models of aquatic plant productivity: A review of the factors that influence growth. *Aquatic Botany*, *59*(3), 195–215. https://doi.org/10.1016/S0304-3770(97)00071-5

Castellarin, A., Baldassarre, G. D., Bates, P. D., & Brath, A. (2009). Optimal cross-sectional spacing in preissmann scheme 1d hydrodynamic models. *Journal of Hydraulic Engineering*, *135*(2), 96–105. https://doi.org/10.1061/(ASCE)0733-9429(2009)135:2(96)

Casulli, V. (1988). Eulerian-lagrangian methods for hyperbolic, and convection dominated parabolic problems. Computational Methods for Nonlinear Problems(Taylor, C., Owen, D.R.J., Hinton, E.), Pineridge, Swansea.

Casulli, V. (2023). *Lecture notes: Advanced numerical methods for free-surface hydrodynamics*.

Casulli, V. (1990). Semi-implicit finite difference methods for the two-dimensional shallow water equations. *Journal of Computational Physics*, *86*(1), 56–74. https://doi.org/10.1016/0021-9991(90)90091-E

Casulli, V., & Stelling, G. S. (2013). A semi-implicit numerical model for urban drainage systems. *International Journal for Numerical Methods in Fluids*, *73*(6), 600–614. https://doi.org/10.1002/fld.3817

Casulli, V., & Zanolli, P. (2022). A review on advanced numerical methods for free-surface hydrodynamics. *Annali dell'Università di Ferrara*, *68*(2), 621–643. https://doi.org/10.1007/s11565-022-00406-9

Catella, M., Paris, E., & Solari, L. (2008). Conservative scheme for numerical modeling of flow in natural geometry. *Journal of Hydraulic Engineering*, *134*(6), 736–748. https://doi.org/10.1061/(ASCE)0733-9429(2008)134:6(736)

Caviedes-Voullième, D., Morales-Hernández, M., López-Marijuan, I., & García-Navarro, P. (2014). Reconstruction of 2d river beds by appropriate interpolation of 1d cross-sectional information for flood simulation. *Environmental Modelling & Software*, *61*, 206–228. https://doi.org/10.1016/j.envsoft.2014.07.016

Cea, L., & López-Núñez, A. (2021). Extension of the two-component pressure approach for modeling mixed free-surface-pressurized flows with the two-dimensional shallow water equations. *International Journal for Numerical Methods in Fluids*, *93*(3), 628–652. https://doi.org/10.1002/fld.4902

Cea, L., Vila, G., García-Alén, G., Puertas, J., & Pena, L. (2022). Hydraulic modeling of bridges in two-dimensional shallow water models. *Journal of Hydraulic Engineering*, *148*(8). https://doi.org/10.1061/(ASCE)HY.1943-7900.0001992

Chanson, H. (2004). *The hydraulics of open channel flows: An introduction*. 2nd ed. Oxford, UK: Elsevier.

Chapra, S. C. (1997). *Surface water-quality modeling*. Waveland press.

Chaudhry, M. (2008). *Open-channel flow second edition*. 2nd ed. New York: Springer.

Clemmens, A. J. (1993). Editorial. *Journal of Irrigation and Drainage Engineering*, *119*(4), 613–614. https://doi.org/10.1061/(ASCE)0733-9437(1993)119:4(613)

Conde, G., Quijano, N., & Ocampo-Martinez, C. (2021). Modeling and control in open-channel irrigation systems: A review. *Annual Reviews in Control*, *51*, 153–171. https://doi.org/ https://doi.org/10.1016/j.arcontrol.2021.01.003

Conner, J. T., & Tonina, D. (2014). Effect of cross-section interpolated bathymetry on 2d hydrodynamic model results in a large river. *Earth Surface Processes and Landforms*, *39*(4), 463–475. https://doi.org/10.1002/esp.3458

Connor, R. (2015). *The united nations world water development report 2015: Water for a sustainable world* (Vol. 1). UNESCO publishing.

Costabile, P., Costanzo, C., Ferraro, D., & Barca, P. (2021). Is hec-ras 2d accurate enough for storm-event hazard assessment? lessons learnt from a benchmarking study based on rain-on-grid modelling. *Journal of Hydrology*, *603*, 126962. https://doi.org/10.1016/j.jhydrol.2021.126962

Dai, A. (2013). Increasing drought under global warming in observations and models. *Nature climate change*, *3*(1), 52–58. https://doi.org/10.1038/nclimate1633

Dalin, C., Wada, Y., Kastner, T., & Puma, M. J. (2017). Groundwater depletion embedded in international food trade. *Nature*, *543*(7647), 700–704. https://doi.org/10.1038/nature21403

Dazzi, S., Vacondio, R., & Mignosa, P. (2020). Internal boundary conditions for a gpu-accelerated 2d shallow water model: Implementation and applications. *Advances in Water Resources*, *137*. https://doi.org/10.1016/j.advwatres.2020.103525

De Marchi, G. (1977). *Nozioni di idraulica con particolare riguardo ai problemi delle bonifiche e delle irrigazioni*. EDAGRICOLE.

Delestre, O., Lucas, C., Ksinant, P.-A., Darboux, F., Laguerre, C., Vo, T.-N.-T., James, F., & Cordier, S. (2014). Swashes: A compilation of shallow water analytic solutions for

hydraulic and environmental studies. *International Journal for Numerical Methods in Fluids*, *74*(3), 229–230. https://doi.org/10.1002/fld.3865

Deltares, D. (2024). Delft3d-flow user manual. *Deltares Delft, The Netherlands*.

Dietterich, L. H., Rosa, S. O., Charbonneau, B. R., & McKay, S. K. (2024). A systematic review of mechanistic models of riverine macrophyte growth. *Aquatic Botany*, *190*, 103724. https://doi.org/10.1016/j.aquabot.2023.103724

Döll, P., Müller Schmied, H., Schuh, C., Portmann, F. T., & Eicker, A. (2014). Global-scale assessment of groundwater depletion and related groundwater abstractions: Combining hydrological modeling with information from well observations and grace satellites. *Water Resources Research*, *50*(7), 5698–5720. https://doi.org/10.1002/2014WR015595

Dysarz, T. (2018). Development of riverbox—an arcgis toolbox for river bathymetry reconstruction. *Water*, *10*(9). https://doi.org/10.3390/w10091266

FAO. (2017). *Water for sustainable food and agriculture*. Food and Agriculture Organization of the United Nations, Rome.

Ghetti, A. (1998). *Idraulica*. Edizioni Libreria Cortina Padova.

Henderson-Sellers, B. (1986). Calculating the surface energy balance for lake and reservoir modeling: A review. *Reviews of Geophysics*, *24*(3), 625–649. https://doi.org/10.1029/RG024i003p00625

Islam, A., Raghuwanshi, N. S., & Singh, R. (2008). Development and application of hydraulic simulation model for irrigation canal network. *Journal of Irrigation and Drainage Engineering*, *134*(1), 49–59. https://doi.org/10.1061/(ASCE)0733-9437(2008)134:1(49)

Islam, A., Raghuwanshi, N., Singh, R., & Sen, D. (2005). Comparison of gradually varied flow computation algorithms for open-channel network. *Journal of Irrigation and Drainage Engineering*, *131*(5), 457–465. https://doi.org/10.1061/(ASCE)0733-9437(2005)131:5(457)

Jamal, J. F., & Bhallamudi, S. M. (2020). Efficient solution algorithm for unsteady flow in channel networks using subtiming technique. *Journal of Irrigation and Drainage Engineering*, *146*(6), 04020012. https://doi.org/10.1061/(ASCE)IR.1943-4774.0001474

Järvelä, J. (2004). Determination of flow resistance caused by non-submerged woody vegetation. *International Journal of River Basin Management*, *2*(1), 61–70. https://doi.org/10.1080/15715124.2004.9635222

Karimi Avargani, H., Hashemy Shahdany, S. M., Hashemi Garmdareh, S. E., Liaghat, A., Guan, G., Behzadi, F., Milan, S. G., & Berndtsson, R. (2023). Operational loss estimation in irrigation canals by integrating hydraulic simulation and crop growth modeling. *Agricultural Water Management*, *288*, 108478. https://doi.org/10.1016/j.agwat.2023.108478

Keupers, I., Thanh, T. N., & Willems, P. (2015). Modelling the time variance of the river bed roughness coefficient for improved simulation of water levels. *International Journal of River Basin Management*, *13*(2), 167–178. https://doi.org/10.1080/15715124.2014.999782

Kinzel, P. J., Legleiter, C. J., & Nelson, J. M. (2013). Mapping river bathymetry with a small footprint green lidar: Applications and challenges. *JAWRA Journal of the American Water Resources Association*, *49*(1), 183–204. https://doi.org/10.1111/jawr.12008

Kinzli, K.-D., Martinez, M., Oad, R., Prior, A., & Gensler, D. (2010). Using an adcp to determine canal seepage loss in an irrigation district. *Agricultural Water Management*, *97*(6), 801–810. https://doi.org/https://doi.org/10.1016/j.agwat.2009.12.014

Knighton, D. (1998). *Fluvial forms and processes*. Edward Arnold, London.

Lai, R., Wang, M., Yang, M., & Zhang, C. (2018). Method based on the laplace equations to reconstruct the river terrain for two-dimensional hydrodynamic numerical modeling. *Computers & Geosciences*, *111*, 26–38. https://doi.org/10.1016/j.cageo.2017.10.006

Lai, R., Wang, M., Zhang, X., Huang, L., Zhang, F., Yang, M., & Wang, M. (2021). Streamline-based method for reconstruction of complex braided river bathymetry. *Journal of Hydrologic Engineering*, *26*(5), 04021012. https://doi.org/10.1061/(ASCE)HE.1943-5584.0002080

Lee, K., Ho, H.-C., Marian, M., & Wu, C.-H. (2014). Uncertainty in open channel discharge measurements acquired with streampro adcp. *Journal of Hydrology*, *509*, 101–114. https://doi.org/https://doi.org/10.1016/j.jhydrol.2013.11.031

Legleiter, C. J. (2012). Remote measurement of river morphology via fusion of lidar topography and spectrally based bathymetry. *Earth Surface Processes and Landforms*, *37*(5), 499–518. https://doi.org/10.1002/esp.2262

Leopold, L. B., & Maddock, T. (1953). *The hydraulic geometry of stream channels and some physiographic implications* (Vol. 252). US Government Printing Office.

Levidow, L., Zaccaria, D., Maia, R., Vivas, E., Todorovic, M., & Scardigno, A. (2014). Improving water-efficient irrigation: Prospects and difficulties of innovative practices. *Agricultural Water Management*, *146*, 84–94. https://doi.org/10.1016/j.agwat.2014.07.012

Luhar, M., & Nepf, H. M. (2013). From the blade scale to the reach scale: A characterization of aquatic vegetative drag [35th Year Anniversary Issue]. *Advances in Water Resources*, *51*, 305–316. https://doi.org/https://doi.org/10.1016/j.advwatres.2012.02.002

Lund, A. R., Gates, T. K., & Scalia, J. (2023). Characterization and control of irrigation canal seepage losses: A review and perspective focused on field data. *Agricultural Water Management*, *289*, 108516. https://doi.org/https://doi.org/10.1016/j.agwat.2023.108516

Luppi, M., Malaterre, P.-O., Battilani, A., Di Federico, V., & Toscano, A. (2018). A multi-disciplinary modelling approach for discharge reconstruction in irrigation canals: The canale emiliano romagnolo (northern italy) case study. *Water*, *10*(8). https://doi.org/10.3390/w10081017

Macdonald, I. (1996). *Analysis and computation of steady open channel flow* [Doctoral dissertation, University of Reading].

Maranzoni, A., & Mignosa, P. (2018). Numerical treatment of a discontinuous top surface in 2d shallow water mixed flow modeling. *International Journal for Numerical Methods in Fluids*, *86*(4), 290–311. https://doi.org/10.1002/fld.4418

Martínez-Aranda, S., Fernández-Pato, J., Caviedes-Voullième, D., García-Palacín, I., & García-Navarro, P. (2018). Towards transient experimental water surfaces: A new benchmark dataset for 2d shallow water solvers. *Advances in Water Resources*, *121*, 130–149. https://doi.org/10.1016/j.advwatres.2018.08.013

Mazzoleni, M., Paron, P., Reali, A., Juizo, D., Manane, J., & Brandimarte, L. (2020). Testing uav-derived topography for hydraulic modelling in a tropical environment. *Natural Hazards*, *103*, 139–163. https://doi.org/10.1007/s11069-020-03963-4

Mckenna, J., Glenis, V., & Kilsby, C. (2023). A new riemann solver for modelling bridges in flood flows - development and experimental validation. *Applied Mathematics and Computation*, *447*. https://doi.org/10.1016/j.amc.2023.127870

Mersel, M. K., Smith, L. C., Andreadis, K. M., & Durand, M. T. (2013). Estimation of river depth from remotely sensed hydraulic relationships. *Water Resources Research*, *49*(6), 3165–3179. https://doi.org/10.1002/wrcr.20176

Merwade, V., Cook, A., & Coonrod, J. (2008). Gis techniques for creating river terrain models for hydrodynamic modeling and flood inundation mapping. *Environmental Modelling & Software*, *23*(10), 1300–1311. https://doi.org/10.1016/j.envsoft.2008.03.005

Mihalevich, B. A., Neilson, B. T., & Buahin, C. A. (2022). Evaluation of the era5-land reanalysis data set for process-based river temperature modeling over data sparse and topographically complex regions. *Water Resources Research*, *58*(7), e2021WR031294. https://doi.org/10.1029/2021WR031294

Milanesi, L., & Pilotti, M. (2021). Coupling flood propagation modeling and building collapse in flash flood studies. *Journal of Hydraulic Engineering*, *147*(12). https://doi.org/10.1061/(ASCE)HY.1943-7900.0001941

Mueller, D. S. (2016). *Qrev—software for computation and quality assurance of acoustic doppler current profiler moving-boat streamflow measurements—technical manual for version 2.8* (tech. rep.). US Geological Survey.

Mueller, D. S., Wagner, C. R., Rehmel, M. S., Oberg, K. A., & Rainville, F. (2013). *Measuring discharge with acoustic doppler current profilers from a moving boat* (tech. rep.). US Geological Survey.

Octavio, K. A. H. (1977). *Vertical heat transport mechanisms in lakes and reservoirs* [Doctoral dissertation, Massachusetts Institute of Technology].

Perret, E., Renard, B., & Le Coz, J. (2021). A rating curve model accounting for cyclic stage-discharge shifts due to seasonal aquatic vegetation. *Water Resources Research*, *57*(3), e2020WR027745. https://doi.org/10.1029/2020WR027745

Pilotti, M. (2016). Extraction of cross sections from digital elevation model for one-dimensional dam-break wave propagation in mountain valleys. *Water Resources Research*, *52*(1), 52–68. https://doi.org/10.1002/2015WR017017

Pilotti, M., Chapra, S. C., & Valerio, G. (2019). Steady-state distributed modeling of dissolved oxygen in data-poor, sewage dominated river systems using drainage networks. *Environmental Modelling & Software*, *111*, 153–169. https://doi.org/10.1016/j.envsoft.2018.08.027

Pilotti, M., Maranzoni, A., Tomirotti, M., & Valerio, G. (2011). 1923 gleno dam break: Case study and numerical modeling. *Journal of Hydraulic Engineering*, *137*(4), 480–492. https://doi.org/10.1061/(ASCE)HY.1943-7900.0000327

Pilotti, M., Milanesi, L., Bacchi, V., Tomirotti, M., & Maranzoni, A. (2020). Dam-break wave propagation in alpine valley with hec-ras 2d: Experimental cancano test case. *Journal of Hydraulic Engineering*, *146*(6). https://doi.org/10.1061/(ASCE)HY.1943-7900.0001779

Ratia, H., Murillo, J., & García-Navarro, P. (2014). Numerical modelling of bridges in 2d shallow water flow simulations. *International Journal for Numerical Methods in Fluids*, *75*(4), 250–272. https://doi.org/10.1002/fld.3892

Reil, A., Skoulikaris, C., Alexandridis, T., & Roub, R. (2018). Evaluation of riverbed representation methods for one-dimensional flood hydraulics model. *Journal of Flood Risk Management*, *11*(2), 169–179. https://doi.org/10.1111/jfr3.12304

Richards, R. A., Rebetzke, G. J., Condon, A. G., & van Herwaarden, A. F. (2002). Breeding opportunities for increasing the efficiency of water use and crop yield in temperate cereals. *Crop Science*, *42*(1), 111–121. https://doi.org/10.2135/cropsci2002.1110

Rosatti, G., Bonaventura, L., Deponti, A., & Garegnani, G. (2011). An accurate and efficient semi-implicit method for section-averaged free-surface flow modelling. *International Journal for Numerical Methods in Fluids*, *65*(4), 448–473. https://doi.org/10.1002/fld.2191

Rosatti, G., Cesari, D., & Bonaventura, L. (2005). Semi-implicit, semi-lagrangian modelling for environmental problems on staggered cartesian grids with cut cells. *Journal of Computational Physics*, *204*(1), 353–377. https://doi.org/10.1016/j.jcp.2004.10.013

Rosenberry, D. O., Duque, C., & Lee, D. R. (2020). History and evolution of seepage meters for quantifying flow between groundwater and surface water: Part 1 – freshwater settings. *Earth-Science Reviews*, *204*, 103167. https://doi.org/https://doi.org/10.1016/j.earscirev.2020.103167

Roub, R., Hejduk, T., & Novák, P. (2012). Automating the creation of channel cross section data from aerial laser scanning and hydrological surveying for modeling flood events. *Journal of Hydrology and Hydromechanics*, *60*(4), 227–241. https://doi.org/10.2478/v10098-012-0020-5

Scheffer, M., Bakema, A. H., & Wortelboer, F. G. (1993). Megaplant: A simulation model of the dynamics of submerged plants. *Aquatic Botany*, *45*(4), 341–356. https://doi.org/10.1016/0304-3770(93)90033-S

Sen, D., & Garg, N. (2002). Efficient algorithm for gradually varied flows in channel networks. *Journal of Irrigation and Drainage Engineering*, *128*(6), 351–357. https://doi.org/10.1061/(ASCE)0733-9437(2002)128:6(351)

Tarpanelli, A., Camici, S., Nielsen, K., Brocca, L., Moramarco, T., & Benveniste, J. (2021). Potentials and limitations of sentinel-3 for river discharge assessment [25 Years of Progress in Radar Altimetry]. *Advances in Space Research*, *68*(2), 593–606. https://doi.org/10.1016/j.asr.2019.08.005

Teledyne RD Instruments. (2021). *Winriver iisoftware user's guide* (tech. rep.). Teledyne RD Instruments,P/N 957–6231–00.

Thornton, K. W., & Lessem, A. S. (1978). A temperature algorithm for modifying biological rates. *Transactions of the American Fisheries Society*, *107*(2), 284–287.

Wada, Y., van Beek, L. P. H., Viviroli, D., Dürr, H. H., Weingartner, R., & Bierkens, M. F. P. (2011). Global monthly water stress: 2. water demand and severity of water stress. *Water Resources Research*, *47*(7). https://doi.org/10.1029/2010WR009792

Wahlin, B., & Zimbelman, D. (2014). *Canal automation for irrigation systems*. American Society of Civil Engineers. https://doi.org/10.1061/9780784413685

Walker, W. R. (1989). Guidelines for designing and evaluating surface irrigation systems.

Walter Box, J. J., & Västilä, K. (2024). New formulas addressing flow resistance of floodplain vegetation from emergent to submerged conditions. *International Journal of River Basin Management*, *22*(3), 333–349. https://doi.org/10.1080/15715124.2022.2143512

Wanyama, J., & Bwambale, E. (2024). Hydraulic modelling of irrigation canals for improved flow conditions in surface irrigation systems. *ISH Journal of Hydraulic Engineering*, *30*(1), 7–17. https://doi.org/10.1080/09715010.2023.2245785

Website SIC2. ( ). https://sic.g-eau.fr/?lang=en

WMO. (2010). *Manual on stream gauging volume i – fieldwork* (Vol. 1044).

Yin, X., Goudriaan, J., Lantinga, E. A., Vos, J., & Spiertz, H. J. (2003). A flexible sigmoid function of determinate growth. *Annals of Botany*, *91*(3), 361–371. https://doi.org/10.1093/aob/mcg029

Yuan, S., Zhou, J., Hu, D., & Zhu, S. (2020). An integral 1-d eulerian-lagrangian method and its application to a hydrodynamic river network. *Water (Switzerland)*, *12*(2). https://doi.org/10.3390/w12020542

Zhu, D., Chen, Y., Wang, Z., & Liu, Z. (2011). Simple, robust, and efficient algorithm for gradually varied subcritical flow simulation in general channel networks. *Journal of Hydraulic Engineering*, *137*(7), 766–774. https://doi.org/10.1061/(ASCE)HY.1943-7900.0000356